# Search for new physics in the scalar sector using advanced $\tau$ lepton reconstruction and identification techniques in the ATLAS experiment


## Monika Juzek


**Thesis presented in fulfillment of the requirements for the degree of Doctor of Philosophy**

**Supervisor:** Dr. hab. Paweł Brückman de Renstrom

**Co-Supervisor:** Dr. Magdalena Sławińska


Division of Particle and Astroparticle Physics
Henryk Niewodniczański Institute of Nuclear Physics
Polish Academy of Sciences

Kraków, 2025

# Acknowledgements

First and foremost, I would like to express my deepest gratitude to my supervisor, Dr. hab. Paweł Brückman de Renstrom, for his invaluable guidance, scientific insight, and continuous support throughout the course of this PhD. His mentorship helped me a lot during my development as a researcher and has greatly influenced the direction and quality of this work.

I would like to thank the members of the ATLAS Tau Working Group and the $H^+ \to \tau\nu$ analysis team for many productive discussions and for generously sharing their expertise. Special thanks are due to Dr. hab. Anna Kaczmarska for her steady support and collaboration during the extensive $\tau$ Monte Carlo validation work - her help, quick feedback, and encouragement made a big difference. I also gratefully acknowledge support from the Polish National Science Centre (NCN) under grant number 2022/47/B/ST2/03059.

I am further grateful to Dr. hab. Ewa Stanecka for her guidance and advice during my work on the Detector Control Systems, particularly in the SCT and ITk detectors projects, which allowed me to grow beyond the scope of pure analysis. Furthermore, I am grateful to the SCT detector and ITk upgrade teams; their dedication to precision, safety, and knowledge-sharing made my detector service contributions invaluable. I also acknowledge financial support provided by the Polish National Agency for Academic Exchange NAWA under the Programme STER- Internationalisation of doctoral schools, Project no BPI/STE/2023/1/00027/U/00001.

I am sincerely thankful to all the scientists and colleagues at the Institute of Nuclear Physics, Polish Academy of Sciences, and within the ATLAS Collaboration for fostering a supportive and intellectually stimulating environment. The opportunity to contribute to various aspects of the ATLAS experiment has been both a challenge and a privilege. I would also like to thank Dr. Magdalena Sławińska for her helpful comments and support during the writing of this thesis.

Finally, I want to express my deepest appreciation to my husband Piotr and my family. Your unwavering love, patience, and belief in me, especially when I doubted myself, have been the foundation of my resilience.

# Abstract

While the Standard Model (SM) of particle physics has been validated in many experiments, most notably with the discovery of the Higgs boson in 2012, it remains an incomplete theory. It does not account for phenomena such as neutrino masses, dark matter, and the cosmic matter–antimatter asymmetry. Various extensions of the SM have been proposed, introducing new physics processes beyond the SM (BSM), most notably the Two-Higgs-Doublet Model (2HDM) and the Minimal Supersymmetric Standard Model (MSSM), both predicting an extended scalar sector containing particles such as a charged Higgs boson. This thesis presents a search for new physics in the scalar sector using $\tau$ leptons in proton–proton collision data recorded by the ATLAS detector at the LHC. Due to their distinct decay signatures, $\tau$ leptons are powerful tools for discriminating potential BSM signals from SM backgrounds.

The main goal of the thesis is the search for charged Higgs bosons ($H^{\pm}$) decaying via $H^{\pm} \to \tau^{\pm}\nu_{\tau}$, using proton–proton collision data at $\sqrt{s} = 13$ TeV collected with the ATLAS detector during Run-2 of the LHC, corresponding to an integrated luminosity of 140 fb$^{-1}$. The analysis targets two final state signatures: $\tau+$jets and $\tau+$lepton (electron or muon), covering a wide mass range of 80–3000 GeV. The author's primary task was the estimation of backgrounds from jets misidentified as hadronically decaying $\tau$ leptons ($\tau_{\text{had-vis}}$). This background estimation remains among the leading sources of systematic uncertainty across the full $H^{\pm}$ mass range. A data-driven Fake-Factor (FF) method was developed and optimized for the new $\tau$ identification algorithm based on recurrent neural networks employed by the ATLAS experiment. A template-fit method was applied to derive combined FFs reflecting the gluon/quark jet composition in the signal regions. These FFs were validated in control regions enriched with fake $\tau_{\text{had-vis}}$ backgrounds, demonstrating good modeling. Systematic uncertainty studies identified heavy-flavour jets misidentified as $\tau_{\text{had-vis}}$ as the dominant contribution. No significant excess above the SM background was observed. Upper limits at the 95% confidence level were set on the production cross-section times branching ratio $\mathcal{B}(H^{\pm} \to \tau^{\pm}\nu_{\tau})$, with values ranging from 4.51 pb to 0.4 fb across the $H^{\pm}$ mass range. For low masses (80–130 GeV), this corresponds to limits on $\mathcal{B}(t \to bH^{\pm}) \times \mathcal{B}(H^{\pm} \to \tau^{\pm}\nu_{\tau})$ of 0.27%–0.04%.

The author also contributed to the Detector Control System for the current ATLAS Semiconductor Tracker (SCT) and to the upgrade of the Inner Tracker (ITk) for the High-Luminosity LHC (HL-LHC) phase. In addition, supporting studies were conducted, including validation of $\tau$ lepton polarization and spin correlations in Monte Carlo samples, as well as development of Rivet tools for validation of MC simulations with $\tau$ leptons in final states, now used by the ATLAS Collaboration.

Each component of the presented work contributes to the broader ATLAS physics programme, spanning detector operations and advanced data analysis in the ongoing quest for new physics.

# Streszczenie

Model Standardowy (SM) fizyki cząstek elementarnych, pomimo licznych potwierdzeń doświadczalnych, a w szczególności odkrycia bozonu Higgsa w 2012 roku, pozostaje teorią niepełną. Nie wyjaśnia on takich zjawisk jak masy neutrin, ciemna materia czy asymetria między materią a antymaterią we Wszechświecie. Liczne proponowane rozszerzenia SM, takie jak np. Two-Higgs-Doublet Model (2HDM) oraz Minimalny Supersymetryczny Model Standardowy (MSSM), przewidują istnienie dodatkowych cząstek, w tym naładowanych bozonów Higgsa.

Celem niniejszej rozprawy jest poszukiwanie sygnałów nowej fizyki w sektorze skalarnym z wykorzystaniem leptonów $\tau$ w danych zderzeń proton-proton zebranych przez detektor ATLAS podczas Run-2 akceleratora LHC przy energii w środku masy $\sqrt{s} = 13$ TeV, odpowiadających łącznej zcałkowanej świetlności 140 fb$^{-1}$. Analiza koncentruje się na poszukiwaniach naładowanych bozonów Higgsa ($H^{\pm}$) w kanale rozpadu $H^{\pm} \to \tau^{\pm}\nu_{\tau}$, badając dwie sygnatury stanów końcowych: $\tau$+dżety oraz $\tau$+lepton (elektron lub mion), w zakresie mas 80–3000 GeV.

W ramach pracy opracowano i zoptymalizowano metodę szacowania tła pochodzącego od dżetów błędnie identyfikowanych jako hadronowe rozpady $\tau$ ($\tau_{\text{had-vis}}$), opartą na współczynnikach Fake-Factor (FF). Niepewność wyznaczenia tego tła stanowi jedno z głównych źródeł niepewności systematycznej poszukiwania $H^{\pm}$ w całym zakresie masy. Zastosowano metodę dopasowania do kształtu (template-fit method) do uwzględnienia składu dżetów gluonowych i kwarkowych w obszarach sygnałowych. Otrzymane współczynniki FF zostały zweryfikowane w obszarach kontrolnych, uzyskując dobrą zgodność z danymi. Analiza niepewności systematycznych wykazała, że główne źródło niepewności stanowią ciężkie dżety kwarkowe błędnie klasyfikowane jako $\tau_{\text{had-vis}}$. Nie stwierdzono istotnych odchyleń od przewidywań Modelu Standardowego. Ustalono górne ograniczenia na poziomie 95% przedziału ufności dla iloczynu przekroju czynnego i częstości rozpadu $\mathcal{B}(H^{\pm} \to \tau^{\pm}\nu_{\tau})$, w zakresie od 4.51 pb do 0.4 fb, w zależności od masy $H^{\pm}$. Dla niskich mas (80–130 GeV) odpowiada to ograniczeniom na $\mathcal{B}(t \to bH^{\pm}) \times \mathcal{B}(H^{\pm} \to \tau^{\pm}\nu_{\tau})$ w zakresie 0.27%–0.04%.

Przedstawiono również wkład autora w rozwój Systemu Kontroli Detektora (DCS) dla Półprzewodnikowego Detektora Śladów (SCT) oraz w prace modernizacyjne nad nowym Detektorem Śladów ITk przygotowywanym na fazę wysokiej świetlności LHC (HL-LHC). Dodatkowo przeprowadzono badania obejmujące walidację polaryzacji i korelacji spinowych leptonów $\tau$ w próbkach Monte Carlo oraz opracowanie narzędzi Rivet do analizy próbek Monte Carlo z leptonami $\tau$ w stanie końcowym, wykorzystywanych w eksperymencie ATLAS.

Wyniki pracy wpisują się w szeroki program badawczy eksperymentu ATLAS, obejmujący zarówno rozwój infrastruktury detektora, jak i zaawansowane analizy danych w poszukiwaniu fizyki wykraczającej poza Model Standardowy.

# Table of Contents

# 1 Introduction

Our current understanding of the fundamental constituents of matter and their interactions is described by a single framework known as the Standard Model (SM) of particle physics. The final missing component that would complete the theory, the Higgs boson, was discovered in 2012 by the ATLAS [1] and CMS [2] Collaborations at the Large Hadron Collider (LHC) [3] at CERN. Although the SM has been thoroughly tested in a wide range of experiments and provides remarkably accurate predictions for many subatomic processes, it does not address several fundamental phenomena, such as neutrino masses, dark matter, dark energy, and the matter, antimatter asymmetry observed in the Universe. These unresolved issues strongly suggest the need for a more comprehensive theoretical framework. Proposed extensions of the SM that attempt to address these open questions are usually referred to as physics beyond the SM (BSM) or new physics. Many such extensions, notably the generic Two-Higgs-Dublet Models (2HDM) [4] and the Minimal Supersymmetric Standard Model (MSSM) [5, 6], postulate the existence of the second scalar dublet of the $SU_{(2)}$, hence the existence of additional Higgs bosons, among others the charged Higgs bosons ($H^{\pm}$). While the discovery of a charged Higgs boson would constitute direct evidence of BSM physics, even the exclusion of specific regions in the parameter space provides valuable constraints on theoretical models. In either outcome, the current state of scientific knowledge is expanded, which is why research in this area is so important. Many BSM theories predict the existence of additional, often heavier, scalar bosons that preferentially decay into $\tau$ leptons [7], particularly in models involving an extended Higgs sector.

The primary goal of this thesis is to search for signs of new physics in the Higgs sector using $\tau$ leptons in data recorded by the ATLAS detector. The $\tau$ lepton provides a powerful probe in searches for BSM events due to its rich physics and unique properties enabling more effective separation of the signal from background processes.

The first component of the work focuses on the ATLAS detector infrastructure, which is fundamental for successful data-taking. In particular, the inner tracking system reconstructs charged particle tracks and interaction vertices in $pp$ collisions. Its stable and safe operation is ensured by a dedicated Detector Control System (DCS) [8]. As the LHC prepares for its High-Luminosity phase (HL-LHC) [9], which will increase the instantaneous luminosity by a factor of 10, it is essential to maintain and upgrade this infrastructure. My contributions include maintenance and operational support of the current Semiconductor Tracker (SCT), as well as development and testing of the readout system for the preproduction power supplies of the future Inner Tracker (ITk) [10] Strip detector in Cracow, under HL-LHC conditions.

The second part of this thesis addresses the reconstruction and modeling of $\tau$ leptons in simulated datasets. Proper identification of $\tau$ leptons and accurate simulation of their properties, including polarization and decay modes, are critical for ATLAS physics analyses. The thesis includes validation studies using Monte Carlo (MC) simulations and the development of tools to improve the modeling of $\tau$ leptons in ATLAS datasets.

The final and central part of this thesis focuses on the direct search for a charged Higgs boson, a key prediction in many BSM theories. The analysis targets the $H^{\pm} \to \tau^{\pm}\nu_{\tau}$ decay channel, where hadronically decaying $\tau$ leptons ($\tau_{\mathrm{had-vis}}$) are reconstructed. A major challenge in this search is the accurate estimation of background events, particularly those where hadronic jets mimic $\tau_{\mathrm{had-vis}}$ signatures. Since Monte Carlo predictions are unreliable for such backgrounds, a dedicated data-driven Fake-Factor (FF) method was implemented and optimized as part of this work.

Each of these components-detector operations, object reconstruction, and physics analysis-represents a critical stage in the ATLAS workflow. Together, they support a precise and robust search for new physics phenomena, culminating in the search for the charged Higgs boson decaying to a $\tau$ lepton and a neutrino.

The thesis is organized as follows. Chapter 2 delivers a brief introduction to the Standard Model and BSM theories, followed by the experimental aspects of high-energy particle physics studied by the ATLAS Experiment at the LHC, which are mentioned in Chapter 3. Next, the development of the Detector Control System for the SCT detector, as well as the ITk detector for future HL-LHC upgrade, is presented in Chapter 4. The description of Monte Carlo generators and a summary of $\tau$ lepton validation tests in different MC samples conducted for the Tau Working Group at the ATLAS Experiment are shown in Chapter 5. The final part is dedicated to the search for a charged Higgs boson decaying to $\tau\nu$ and the data-driven FF method for background estimation in the dataset collected by the ATLAS Experiment Run-2 period.

### Author contribution statement

The author's involvement in the studies presented in this thesis is outlined as follows:

- **Chapter 4**: The author was involved in service work on the currently operational Detector Control System of the SCT detector, which is a component of the Inner Detector. The task required adapting the control system to align with the latest version of the back-end software responsible for communication with the detector hardware. Additionally, the author contributed to the development of the readout system for the pre-production modules, which are part of the power supply system of the ITk Strip Detector tested in Cracow.
- **Chapter 5**: As a part of the ATLAS authorship qualification for the ATLAS Experiment, the author conducted a series of $\tau$ lepton validation tests performed in the Tau Working Group, which involved monitoring $\tau$ lepton properties such as polarization, spin correlations and branching ratio in various MC samples used by the experiment. In addition, the new validation software was developed, which enables fast and detailed validation tests of $\tau$ lepton properties for all groups responsible for generating Monte Carlo samples. Results were documented in an internal note written by the author.
- **Chapter 6**: The author was responsible for the fake $\tau$ leptons background estimation using the data-driven FF method in the search for $H^{\pm} \to \tau^{\pm}\nu_{\tau}$ using the full Run-2 dataset. The FF method required re-implementation and adjustment to a new algorithm for $\tau$ lepton identification based on recurrent neural networks (RNN), validation of the method using MC samples and a comprehensive analysis of all systematic uncertainties. The results are presented in the ATLAS Collaboration's publication [11].

### Notation conventions

Throughout this thesis, several conventions are adopted for clarity and consistency. The symbol $H^+$ is used to denote the charged Higgs boson, with the understanding that it represents both charge states, $H^+$ and $H^-$, unless specified otherwise. Hereafter, the terms $\tau^+$ and $\tau^-$ will be denoted as $\tau$, unless a distinction is necessary. This convention also applies to other charged particles. The generic symbol $\ell$ is used to indicate a light charged lepton, referring collectively to electrons ($e$) and muons ($\mu$).

Natural units are employed, wherein the proton is assigned a positive unit of charge and the speed of light is normalized to unity (c=1).

# 2 Theoretical Background

## 2.1 The Standard Model of Particle Physics

The elegant theory of the Standard Model [12, 13, 14, 15, 16, 17, 18] describes the world of the fundamental constituents of matter in the Universe and the interactions between them. It is the result of numerous theoretical and experimental advancements made throughout the 20th century. The elementary particles and three out of four known fundamental forces - the electromagnetic, weak, and strong forces - are categorized based on their distinctive properties described by the SM. Despite the lack of explanation of the gravitational force, the SM represents the most precise framework currently available for describing the unification of fundamental forces and it has been broadly tested by a series of experiments. The elementary particles can be classified into two primary groups - matter constituents (known as fermions) with a spin of $\frac{1}{2}$ controlled by the Fermi-Dirac statistics [19, 20], and integer-spin carriers of their interactions, bosons, that obey the Bose-Einstein statistics [21, 22].

The SM framework is based on the Quantum Field Theory (QFT), which combines properties of quantum mechanics and special relativity. In the QFT, each fundamental particle is defined as a quantum field excitation that exists throughout spacetime and the behavior of these fields is determined by quantum field equations. The theoretical foundation of the SM within QFT is controlled by a Lagrangian, which is renormalizable and invariant under local gauge transformation, as well as describes the theory dynamics. The SM is a non-abelian gauge theory that demonstrates invariance under a particular gauge symmetry group:

$$SU(3)_C \times SU(2)_L \times U(1)_Y \tag{1}$$

Here, the $SU(3)_C$ group represents the symmetry group of the strong interaction and is associated with the color charge $C$. The $SU(2)_L \times U(1)_Y$ refers to the electroweak interaction gauge group with the hypercharge $Y$, in which $SU(2)_L$ group couples to the left-handed fermions $L$, while $U(1)_Y$ to both right- and left-handed fermions. Each of the mentioned gauges will be discussed in detail in the coming sections.

The fundamental particles of the SM with its key properties are shown in Figure 1.

### 2.1.1 The Fundamental Particles

As mentioned above, the particles that make up fundamental matter are called fermions. They are classified as either leptons or quarks, which are organized into three distinct generations, with each generation containing two quarks, one lepton, and one neutrino. Fermions belonging to different generations share the same quantum properties, but their masses steadily increase across successive generations. The ordinary matter around us is made up of the first-generation particles. Additionally, each fermion possesses an antiparticle counterpart with equivalent mass but opposite electric charge.

Quarks carry both electric and color charges, enabling them to undergo electromagnetic, strong, and weak interactions. The primary generation of quarks is composed of up ($u$) and down ($d$) quarks, the second generation of charm ($c$) and strange ($s$) quarks, and the third generation of top ($t$) and bottom ($b$) quarks. Quarks possess fractional EM charges - the up-type quarks of $+\frac{2}{3}$ and the down-type quarks of $-\frac{1}{3}$. Since quarks cannot exist as free particles, they combine into hadrons - mesons formed by a quark and antiquark pair, or barions made up of three quarks. Examples of barions are proton ($uud$) and neutron ($udd$). The formed bound states are colorless and have an integer-value of electric charge. More complicated hadron structures, composed of four or five quarks, have also been observed and are called exotic hadrons [24].

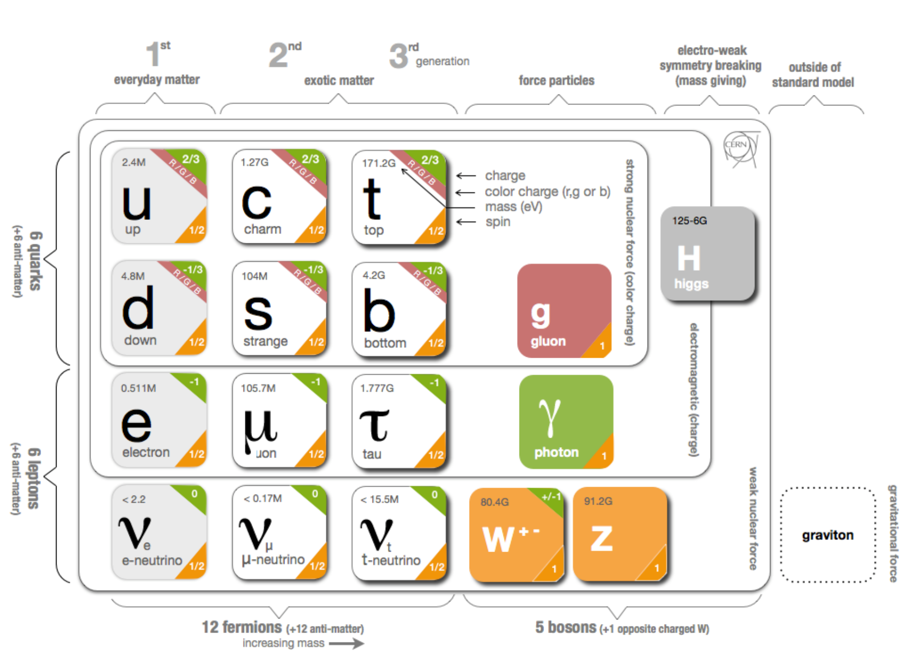


Figure 1: The SM theory particles with their charge, mass and spin properties [23].

There are three lepton generations that include the electron ($e$), muon ($\mu$) and tau ($\tau$), which possess the electromagnetic charge of -1, and corresponding electrically neutral neutrinos: electron neutrino ($\nu_e$), muon neutrino ($\nu_\mu$), and tau neutrino ($\nu_\tau$). All charged leptons interact through weak and electromagnetic forces, while neutrinos only interact weakly.

All above-mentioned fundamental SM particles as point-like and elementary, which implies there is no observed evidence of internal structures associated with these particles.

### 2.1.2 Electromagnetic interaction

Quantum electrodynamics (QED) is an important component of the Standard Model and describes the interaction between electrically charged particles including each generation of quarks and $e$, $\mu$, $\tau$ leptons. The force carrier of the EM interaction with a local symmetry $U(1)$ is the massless photon ($\gamma$), which possesses the EM charge 0 and does not self-interact.

The coupling of a charged fermion field $\psi$ with the EM field $A_\mu$ is defined by the Lagrangian density of the QED interaction as follows:

$$\mathcal{L}_{QED} = \bar{\psi}(i\gamma^\mu D_\mu - m)\psi - \frac{1}{4}F_{\mu\nu}F^{\mu\nu} \tag{2}$$

where $\gamma^\mu$ refers to Dirac gamma matrices, $m$ represents the particle's mass, $D_\mu = \partial_\mu - ieA_\mu$ is a covariant derivative, $e$ relates to elemental electrical charge. The final part of the Lagrangian describes the photon kinetic energy and $F_{\mu\nu}$ represents the field strength tensor:

$$F_{\mu\nu} = \partial_\mu A_\nu - \partial_\nu A_\mu \tag{3}$$

A key parameter in the QED framework that determines the strength of the electromagnetic interaction between charged fermions and photons is the fine-structure constant, $\alpha$, defined as:

$$\alpha = \frac{e^2}{4\pi\hbar c\epsilon_0} \tag{4}$$

Although it is often treated as a constant, $\alpha$ actually depends on the energy scale due to vacuum polarization effects - a phenomenon known as the running of the coupling constant. Experimental measurements reveal that $\alpha$ increases with energy: it is approximately 1/137 at low energies relevant to atomic physics, but rises to about 1/127 at the energy scale of the $Z$ boson [25].

### 2.1.3 Electroweak interaction

The electroweak theory, which unified the electromagnetic and weak interactions was introduced by Glashow, Salam and Weinberg [12, 13, 14]. It is based on the $SU(2)_L \times U(1)_Y$ gauge group, whose generators are the weak isospin $I$ (along with third isospin component $I_3$) and the weak hypercharge $Y$, respectively.

Empirical investigations have demonstrated that the weak interactions exclusively engage left-handed fermions, and equally importantly, the charge-parity (CP) conservation is not respected. Under the $SU(2)_L$ transformation left-handed fermions are represented as left-chiral doublets and right-handed ones as right-chiral singlets:

$$\begin{aligned} \psi_L &= \frac{1-\gamma_5}{2}\psi \\ \psi'_R &= \frac{1+\gamma_5}{2}\psi' \end{aligned} \tag{5}$$

where $\frac{1-\gamma_5}{2}$ and $\frac{1+\gamma_5}{2}$ are the left- and right-handed projection operators, respectively. The third isospin component value is $I_3 = \frac{1}{2}$ for the up-type quarks and the neutrinos, while $I_3 = -\frac{1}{2}$ for the charged leptons and the down-type quarks. The EM charge ($Q$) is linked to $I_3$ and $Y$ according to the following Gellmann-Nishijama formula [26, 27, 28]:

$$Q = I_3 + Y \tag{6}$$

As a result of the local gauge invariance requirement, there is a generation of three gauge fields $W_\mu^{1,2,3}$ corresponding to $SU(2)$ and one gauge field $B_\mu$ from $U(1)$, which interacts with both the left- and right-handed fermions. Combinations of these gauge boson fields create the fields of the EW bosons: the photons and the $Z$ bosons are associated with a linear combination of $A_\mu$ and $W_\mu^3$ fields, whereas the $W^\pm$ bosons are associated with a linear combination of $W_\mu^1$ and $W_\mu^2$, as follows:

$$A_\mu = \frac{g' B_\mu + g W_\mu^3}{\sqrt{g^2 + g'^2}} \tag{7}$$

$$W_\mu^\pm = \frac{W_\mu^1 \pm i W_\mu^2}{\sqrt{2}} \tag{8}$$

$$Z_\mu = \frac{g' B_\mu - g W_\mu^3}{\sqrt{g^2 + g'^2}} \tag{9}$$

The electroweak Lagrangian density can be written as:

$$\mathcal{L}_{\text{EW}} = \bar{\psi_L}(i\gamma^\mu(D_\mu))\psi_R - \frac{1}{4}W_{\mu v}^i W^{i\mu\nu} - \frac{1}{4}B_{\mu\nu}B^{\mu\nu} \tag{10}$$

Here, the covariant derivative $D_\mu$, gauge fields $W_{\mu\nu}^i$ and $B_{\mu\nu}$ are:

$$D_\mu = \partial_\mu + \frac{1}{2}\sigma_{L,R}W_\mu^i - \frac{1}{2}ig'Y_{L,R}B_\mu \tag{11}$$

$$W_{\mu\nu}^i = \partial_\mu W_\nu^i - \partial_\nu W_\mu^i + g\epsilon^{ijk}W_\mu^j W_\nu^k, \tag{12}$$

$$B_{\mu\nu} = \partial_\mu B_\nu - \partial_\nu B_\mu \tag{13}$$

where $\sigma_i$, being the three 2×2 Pauli matrices, the coupling parameters $g$ and $g'$ correspond to the gauge groups $SU_L$ and $U_Y$, respectively. The relative strengths of electromagnetism and the weak forces are quantified by electroweak mixing angle $\theta_W$, which is defined using the coupling constants:

$$\cos(\theta_W) = \frac{g}{\sqrt{g^2 + g'^2}}, \quad \sin(\theta_W) = \frac{g'}{\sqrt{g^2 + g'^2}}, \tag{14}$$

In addition, it enables to express the electric charge in relation to the gauge couplings:

$$e = g\sin(\theta_W) \tag{15}$$

Due to the local gauge invariance principle, SM force carriers (bosons) cannot bear mass. Likewise, parity violation of the $SU(2)_L$ precludes existence of massive fermions in the theory. It is true for the gluons and the photons, due to the conservation of EM charge and the eight color charges as the corresponding symmetry generators. However, experiments clearly have shown evidence that electroweak gauge bosons $W^\pm$ and $Z$, as well as fermions, possess mass. The solution to the riddle of mass generation for the elementary particles in the theory will be discussed in Section 2.1.5.

### 2.1.4 Strong interaction

Strong interactions govern the binding of atomic nuclei and other entities known as hadrons. They are described by Quantum Chromodynamics (QCD) theory [29, 30] and are based on the local gauge invariance of the $SU(3)_C$. In this framework, a new quantum number called the color charge ($C$) is the conserved quantity under the corresponding gauge transformations. Color charge is a counterpart to the QED electric charge. Only quarks and antiquarks are engaged in strong interactions, which are mediated by massless spin-1 gauge bosons known as gluons.

The QCD Lagrangian is represented by the following equation:

$$\mathcal{L}_{\text{QCD}} = -\frac{1}{4}G_{\mu\nu}^a G^{a,\mu\nu} + \sum_f \bar{q}_f(i\gamma^\mu D_\mu - m_f)q_f \tag{16}$$

where $q_f$ represents to quark field, which possesses a mass of $m_f$, $f$ is a flavour index and $\gamma^\mu$ denotes the Dirac matrices. The tensor $G_{\mu\nu}^a$ of the gluon field strength can be written as:

$$G_{\mu\nu}^a = \partial_\mu G_\nu^a - \partial_\nu G_\mu^a - g_S f^a bc \partial_\mu G_\mu^b \partial_\mu G_\nu^c \tag{17}$$

Incorporating the term $\frac{1}{4}G_{\mu\nu}^a G^{a,\mu\nu}$ in the Lagrangian guarantees local gauge invariance, which subsequently results in self-interactions among the gluons.

The covariant derivative $D_\mu$ represents the coupling between quarks and gluons:

$$D_\mu = \partial_\mu - ig_S\frac{\lambda_i}{2}G_\mu^i(x) \tag{18}$$

where $G_\mu^i(x)$ strength tensors relate to the eight gluon fields and $g_s$ represents the coupling constant, which is directly connected with the coupling constant $\alpha_s$ of the strong coupling:

$$g_s = \sqrt{4\pi\alpha_s} \tag{19}$$

Unlike in QED, where the photon does not self-interact, the self-interactions of gluons lead to a different energy scaling behavior in QCD. As mentioned in Section 2.1.3, coupling constants in quantum field theories generally depend on the energy scale, a behavior known as the "running of the coupling". In the case of the low energy scales, the phenomenon known as color confinement is observed - as the effective coupling between quarks increases, those particles have to be grouped in colourless bound states (hadrons). On the other hand, high energy scales result in the $\alpha_S$ starting to asymptotically approach zero, hence quarks can exist outside the bound states. Such a behavior in QCD is called asymptotic freedom [31]. This phenomenon stands in contrast to QED theory, in which interaction rates diminish significantly for particles that are far away from each other or when the energy scale decreases [32].

### 2.1.5 The Higgs Mechanism and Mass Generation

As mentioned earlier, gauge theories forbid the gauge bosons to be massive as their mass term breaks gauge invariance. On the other hand, the experimental results have provided evidence for finite masses of the fermions, alongside the $W^{\pm}$ and $Z$ bosons, clearly contradicting the SM theory so far.

A solution was proposed by Brout, Englert and Higgs [16, 17] in the 60s (also called as "BEH mechanism") based on the spontaneous electroweak symmetry breaking (EWSB) of a local gauge field. The origin of masses of fermions and bosons is explained through the incorporation of a complex doublet scalar $\Phi(x)$ (known as the Higgs field) to the Lagrangian, which consists of complex scalar fields under $SU(2)_L$ transformation:

$$\Phi = \frac{1}{\sqrt{2}} \begin{pmatrix} \phi_1(x) + i\phi_2(x) \\ \phi_3(x) + i\phi_4(x) \end{pmatrix} = \begin{pmatrix} \phi^+ \\ \phi^0 \end{pmatrix} \tag{20}$$

Here $\phi_1$, $\phi_2$, $\phi_3$ and $\phi_4$ represent normalized real scalar fields.

The lagrangian related to the Higgs field is:

$$\mathcal{L}_{\text{Higgs}} = |(D_\mu \Phi)|^2 - V(\Phi) \tag{21}$$

This includes the kinetic term $|(D_\mu \Phi)|^2$ and the potential term $V(\Phi)$ for the Higgs field $\Phi$. The interaction of the Higgs field with the electroweak gauge bosons is represented by the covariant derivative $D_\mu$:

$$D_\mu = \partial_\mu + \frac{ig}{2}\sigma^i W_\mu^i + \frac{ig'}{2} Y B_\mu \tag{22}$$

The scalar Higgs potential is written as follows:

$$V(\Phi) = \mu^2 \Phi^\dagger \Phi + \lambda(\Phi^\dagger \Phi)^2 \tag{23}$$

with scalar parameters $\mu$ and $\lambda$.

In the case of $\mu^2 > 0$ and $\lambda > 0$ situation, the $V(\Phi)$ potential minimum is equal to 0. On the other hand, when $\mu^2 < 0$ the $V(\Phi)$ minimum can be defined by a variety of possible solutions that fulfill:

$$\Phi^\dagger \Phi = \frac{1}{2}(\phi_1^2 + \phi_2^2 + \phi_3^2 + \phi_4^2) = \frac{\nu^2}{2} = -\frac{\mu^2}{2\lambda} \tag{24}$$

Here $\nu = \sqrt{\frac{\mu^2}{\lambda}}$ represents the vacuum expectation value (VEV) of the scalar potential $V(\Phi)$. Figure 2 presents the characteristic "Mexican hat" form of the Higgs field potential $V(\Phi)$.

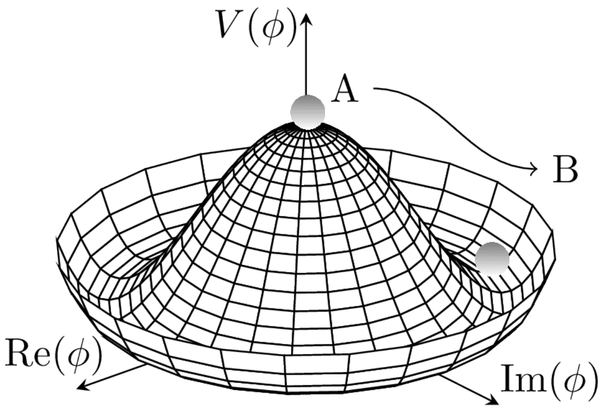


Figure 2: The shape of Higgs potential with its nonzero vacuum expectation value [33].

Due to the spontaneous symmetry breaking, the system settles into one of many possible ground states, for instance:

$$\Phi_0 = \frac{1}{\sqrt{2}}\begin{pmatrix}0\\ v\end{pmatrix} \tag{25}$$

If one expands the $\Phi(x)$ around the ground state, the Higgs field itself is obtained as:

$$\Phi_0 = \frac{1}{\sqrt{2}}\begin{pmatrix}0\\ v+H\end{pmatrix} \tag{26}$$

Here, Higgs boson $H$ is a massive (real) excitation of the Higgs field. As a result, the Higgs field's Lagrangian, which defines the Higgs boson's mass and self-interaction, becomes:

$$\mathcal{L}_{\text{Higgs}} = \frac{1}{2}\partial H \partial^{\mu} H - \lambda \nu^2 H^2 - \lambda \nu H^3 - \frac{\lambda}{4} H^4 \tag{27}$$

The discovery of the scalar boson with a mass of ~125 GeV in 2012, which matches the characteristics of the SM Higgs boson, was announced by the ATLAS and CMS collaborations at CERN [34, 35].

The Higgs particle interacts with all massive particles, including itself. This self-coupling is of significant theoretical interest, and extensive experimental efforts have been devoted to investigate it [36, 37]. The Goldstone theorem [38] demonstrates that spontaneous breaking of a local global symmetry results in massless scalar particles called Goldstone bosons ($G^{\pm}$ and $G^0$), which are absorbed by the gauge fields. This gives mass to the $W^{\pm}$ and $Z$ bosons, and a longitudinal polarization, unifying spontaneous symmetry breaking with gauge invariance in the Standard Model. The mass terms obtained by the $W^{\pm}$, $Z$ and $H$ bosons are as follows:

$$m_W = \frac{1}{2}\nu g, \quad m_Z = \frac{1}{2}\nu\sqrt{g^2 + g'^2}, \quad m_H = \sqrt{2\mu^2} \tag{28}$$

As far as fermion masses are concerned, they are acquired through the Yukawa interaction with the Higgs field [39]. This is not covered in detail in this dissertation, but the general principle is:

$$m_f = \frac{h_f \nu}{\sqrt{2}} \tag{29}$$

Here the $h_f$ represents the coupling between a particular fermion and Higgs boson. One can notice that fermion masses are directly proportional to fermion-Higgs coupling and boson masses are proportional to the squared value of boson-Higgs coupling. Consequently, the most likely production and decay processes of the Higgs boson are characterized by couplings to the $W^{\pm}$ and $Z$ gauge bosons, as well as the heavy third-generation fermions, which are the heaviest fundamental particles in the Standard Model.

## 2.2 Beyond Standard Model - Supersymmetry Models

Regardless of the Standard Model's success in explaining the fundamental particles' properties, it falls short of being an ultimate theory of matter and forces in the Universe due to the challenges outlined below:

- **Lack of quantum description of the gravity:**

  In the SM framework, only three of four known fundamental forces are included, excluding gravity. It is significantly weaker than the other forces and is described by the classical field theory of General Relativity proposed by Einstein [40]. However, the gravitational quantum effects cannot be disregarded at the Plank scale, as gravity is expected to be as impactful as the other fundamental forces. Despite many successes of general relativity (for instance making accurate predictions about gravitational waves observed in 2016 [41]), no sufficient quantum theory of gravity, which would be unified with the SM, has been proposed after a century of research [42].

- **Massive neutrinos:**

  The SM predicts the mass of neutrinos to be 0. On the other hand, the experimental results clearly show the existence of phenomena known as neutrino oscillations, which contradicts this theory by demanding that no less than two generations of neutrinos possess mass [43, 44]. This issue can be resolved by adding the right-handed neutrinos and introducing a Dirac mass term. The neutrinos obtained in this manner would be, however, sterile, meaning they would interact with other particles only gravitationally. Different approach postulates the Majorana nature of neutrinos indicating the neutrino and antineutrino may be the same particle [45]. This theory, contrary to Dirac's view on neutrinos, provides the opportunity to be experimentally tested, for instance searching for the double $\beta$ decay with no neutrino emission [46].

- **Matter-antimatter asymmetry:**

  Within the Standard Model theory there is no mechanism that explains why, as of now, matter clearly dominates in the visible Universe. Right after the creation of the Universe, the production and annihilation of matter and antimatter ran at the same pace. The expansion of the Universe broke down this thermal equilibrium. The asymmetry in baryon production can be achieved by a mechanism with sufficiently strong CP-violation, known as baryogenesis [47]. On the other hand, the phase in the CKM mixing matrix is the only observed source of CP-violation in the SM, and this amount of CP-violation is not enough to explain the baryon density [48].

- **Dark matter and dark energy:** Based on the observed evidences from astrophysics of the rotation curves of galaxies [49], the anisotropy of the cosmic microwave background (the thermal radiation being the leftover from the Big Bang) [50] and gravitational lensing [51], clearly indicate the existence of an additional type of matter, which does not emit light (hence it is called dark matter) and can be studied exclusively via the gravitational effects it has on normal "visible" matter. Dark matter is responsible for about 27% of the Universe's energy, while SM's baryonic matter is only 4.8% [52]. The rest, 68% of energy relates to so-called dark energy, which is the cause of the observed accelerating expansion of the Universe [53].

- **Hierarchy problems:** The hierarchy problems address the question of why there are large discrepancies between values of the model parameters that theory is unable to account for or that would require extensive fine-tuning of the model parameters to align with experimental observations. One of the biggest puzzles is the significant difference between the electroweak scale and the Planck scale (approximately $10^{17}$ GeV in magnitude). The observed Higgs boson mass depends on the bare mass value in Lagrangian and the radiative corrections, which are expected to become immense, nearly 30 orders of magnitude larger if the Planck scale is a cutoff, when compared to the observed mass of the Higgs boson of $\sim$125 GeV. This situation requires a significant degree of fine-tuning between the SM parameters and the anticipated contribution of an unknown heavy particle existing between the electroweak and Planck scales, even if it interacts with the Higgs boson only indirectly [54].

In order to address those issues and provide answers to numerous questions, theorists have developed a variety of theoretical physics models extending the Standard Model. They incorporate ideas such as extra dimensions, alternative gravity theories, an introduction of new particles (for example extended Higgs sector), proposing a new symmetry like Supersymmetry (SUSY), or some kind of combination of them in a single framework. The two of most appealing scenarios, which are widely studied at the LHC, are the Two-Higgs-Doublet Models (2HDMs)[4] and SUSY models [55].

The family of 2HDMs propose the existence of an additional Higgs doublet to the SM one within EW breaking sector. It would effectively describe the SM-like Higgs boson and any new scalar particles, as well as their production and decay rates, in an elegant manner.

The SUSY frameworks, on the other hand, would provide an explanation to several shortcomings of the SM by introducing an additional symmetry between bosons and fermions, called Supersymmetry. However, to allow for a successful EW Symmetry Breaking mechanism, SUSY needs more than one Higgs doublet. For two Higgs doublets as for a generic 2HDMs, one obtains the simplest version of the SUSY framework, the Minimal Supersymmetric Standard Model (MSSM) [5, 6].

These models provide straightforward and testable predictions, like additional Higgs bosons and, in MSSM, the existence of supersymmetric particles, what makes them experimentally accessible at the hadronic accelerators at TeV scale. The details of the 2HDMs and MSSM theories mentioned above are discussed in the subsequent sections.

### 2.2.1 2HDM Models

The 2HDMs extend the SM in the simplest manner by introducing two Higgs scalar doublets $\phi_1$ and $\phi_2$ of hypercharge equal to +1. The most general and $SU(2)_L \otimes U(1)_Y$ invariant form of the 2HDM scalar potential $V(\phi_1, \phi_2)$ is [56]:

$$\begin{aligned} V(\phi_1,\phi_2) = {} & m_{11}^2\phi_1^\dagger\phi_1 + m_{22}^2\phi_2^\dagger\phi_2 - \left[m_{12}^2\phi_1^\dagger\phi_2 + h.c.\right] + \frac{1}{2}(\phi_1^\dagger\phi_1)^2 \\ & + \frac{1}{2}\lambda_2(\phi_2^\dagger\phi_2)^2 + \lambda_3(\phi_1^\dagger\phi_1)(\phi_2^\dagger\phi_2) + \lambda_4(\phi_1^\dagger\phi_2)(\phi_2^\dagger\phi_1) \\ & + \frac{1}{2}\lambda_5(\phi_1^\dagger\phi_2)^2 + \left[\lambda_6(\phi_1^\dagger\phi_1) + \lambda_7(\phi_2^\dagger\phi_2)\right](\phi_1^\dagger\phi_2) + h.c. \end{aligned} \tag{30}$$

The factors $m_{11}^2, m_{22}^2, \lambda_1, \ldots, \lambda_4$ are real numbers, while $m_{12}^2, \lambda_5, \lambda_6, \lambda_7$ may potentially be complex. Presence of the complex parameters with non-zero imaginary terms, which cannot be eliminated, provide additional CP-violation processes in the 2HDM scalar potential - explicit violation via the complex phase $\phi$ present in the part $(\phi_1^\dagger\phi_2 + h.c.)$ or through spontaneous violation as a result of the relative phase between the two Higgs doublets VEVs. This feature of the 2HDM theories could explain the baryon asymmetry observed today. If the tree-level flavor-changing neutral currents (FCNCs) are constrained, the parameters $\lambda_6$ and $\lambda_7$ equal 0 [57].

Minimization of the scalar potential provides vacuum expectation values:

$$\langle\phi_1\rangle_0 = \frac{1}{\sqrt{2}}\begin{pmatrix}0\\ v_1\end{pmatrix}, \quad \langle\phi_2\rangle_0 = \frac{1}{\sqrt{2}}\begin{pmatrix}0\\ v_2\end{pmatrix}. \tag{31}$$

with $\sqrt{\nu_1^2+\nu_2^2} = 246$ GeV.

After the symmetry breaking, two Higgs doublets give eight degrees of freedom. Goldstone bosons, introduced in Section 2.1.5, correspond to three degrees of freedom. The remaining five Higgs physical states are: the CP-even $h$ and $H$ (fulfilling the requirement $m_h \leq m_H$), the CP-odd pseudo-scalar $A$ and an electrically charged pair of Higgs bosons ($H^+$).

Given the minima above, the mass terms for neutral scalars $\rho$, pseudo-scalars $\eta$ and charged scalars $\phi^{\pm}$ can be written as follows [4]:

$$\mathcal{L}_{\rho\ \mathrm{mass}} = -\begin{pmatrix}\rho_1 & \rho_2\end{pmatrix}\begin{pmatrix}\frac{m_{12}^2 v_2}{v_1} + \lambda_1 v_1^2 & -m_{12}^2 + \lambda_{345} v_1 v_2\\ -m_{12}^2 + \lambda_{345} v_1 v_2 & \frac{m_{12}^2 v_1}{v_2} + \lambda_2 v_2^2\end{pmatrix}\begin{pmatrix}\rho_1\\ \rho_2\end{pmatrix} \tag{32}$$

$$\mathcal{L}_{\eta\ \mathrm{mass}} = \frac{m_A^2}{v_1^2+v_2^2}\begin{pmatrix}\eta_1 & \eta_2\end{pmatrix}\begin{pmatrix}v_2^2 & -v_1 v_2\\ -v_1 v_2 & v_1^2\end{pmatrix}\begin{pmatrix}\eta_1\\ \eta_2\end{pmatrix} \tag{33}$$

$$\mathcal{L}_{\phi^{\pm}\ \mathrm{mass}} = \left[m_{12}^2 - (\lambda_4+\lambda_5)v_1 v_2\right]\begin{pmatrix}\phi_1^- & \phi_2^-\end{pmatrix}\begin{pmatrix}\frac{v_2}{v_1} & -1\\ -1 & \frac{v_1}{v_2}\end{pmatrix}\begin{pmatrix}\phi_1^+\\ \phi_2^+\end{pmatrix} \tag{34}$$

Here $\lambda_{345} = \lambda_3+\lambda_4+\lambda_5$ and the terms for physical mass-squared of pseudoscalar $A$ and charged Higgs $H^+$ bosons can be written as, respectively:

$$m_A^2 = \left[m_{12}^2/(v_1 v_2) - 2\lambda_5\right](v_1^2+v_2^2) \tag{35}$$

$$m_{H^+}^2 = \left[m_{12}^2/(v_1 v_2) - \lambda_4 - \lambda_5\right](v_1^2+v_2^2) \tag{36}$$

In Equations 32 and 33 zero eigenvalues occur, which relate to Goldstone bosons absorbed to give mass to the $W^{\pm}$ and $Z^0$, while the rest correspond to the five Higgs bosons.

The mass-squared matrices of scalars shown above can be diagonalized using two mixing angles $\alpha$ and $\beta$ - the $\alpha$ angle performs rotation of the scalar mass matrix, while the $\beta$ angle diagonalizes the mass matrix of charged and pseudoscalar Higgs bosons, and is defined as:

$$\tan\beta = \frac{v_2}{v_1} \tag{37}$$

Both mixing angles are crucial parameters of the 2HDMs phenomenology, as they specify various Higgs field interactions with fermions and vector bosons. As for the SM theory, in the 2HDMs the masses of each particle are not defined. A specific selection of the Higgs boson masses ($m_h$, $m_H$ , $m_A$ and $m_{H^+}$), the soft breaking parameter $m_{12}^2$, the $\alpha$ mixing angle between $h$ and $H$ states, and $\tan\beta$ describes a specific model [4].

**Yukawa Coupling in the 2HDMs:** The general property of the 2HDMs scenarios is that they allow the FCNCs at the tree level, which is strongly prohibited by the experimental observations. The existence of FCNCs imposes an additional obstacle for any theories with scalar multiplets. A solution was proposed by Glashow and Weinberg's theorem [58] by postulating a discrete symmetry $Z_2$ to the right-hand fermions:

$$\phi_1 \to \phi_1, \quad \phi_2 \to -\phi_2. \tag{38}$$

which forces a given fermion not to couple to more than one Higgs doublet, hence forbidding the unwanted tree-level FCNC. If the same quantum number $Z_2$ is shared by a group of certain fermions (up-quarks, down-quarks, and leptons), there are several available 2HDM scenarios with different Yukawa couplings. The list of four allowed 2HDM realizations (Type I, Type II, Type X and Type Y) can be seen in Tab.1.

Table 1: Different coupling scenarios of $\phi_1$ and $\phi_2$ doublets to up-type ($q^u$) and down-type ($q^d$) quarks, as well as charged leptons, introduced by various 2HDM models. According to convention, the $\phi_2$ doublet couple to the up-type quarks [4].

| Type | $q^u$ | $q^d$ | $\ell$ |
|---|---|---|---|
| I: Fermiophobic | $\phi_2$ | $\phi_2$ | $\phi_2$ |
| II: MSSM-like | $\phi_2$ | $\phi_1$ | $\phi_1$ |
| X: Lepton-specific | $\phi_2$ | $\phi_2$ | $\phi_1$ |
| Y: Flipped | $\phi_2$ | $\phi_1$ | $\phi_2$ |

### 2.2.2 Minimal Supersymmetric Standard Model as a Type-II 2HDM

Firstly formulated in the 1970s [59, 60, 61, 62], the Supersymmetry postulates the existence of the additional symmetry between fermions and bosons:

$$Q|fermion\rangle = |boson\rangle, \quad Q|boson\rangle = |fermion\rangle, \tag{39}$$

Here $Q$ represents the new fermionic operator, which enables conversion between fermionic and bosonic states. As a result, each SM particle should possess a supersymmetric counterpart (also called sparticle) with a difference of $\frac{1}{2}$ in spin but the rest of the quantum numbers remain identical for both particles. Pairs composed of one SM fermion (boson) and a SUSY boson (fermion), called superpartners of each other, are arranged in supermultiplets.

Nowadays, the "SUSY" term refers to a vast group of theories with the above mentioned symmetry and remains one of the most compelling proposals for the BSM physics, despite that no evidence for additional SUSY particles has been found so far. The absence of the superpartners indicates that there must be spontaneous breaking of the supersymmetry, resulting in different masses of the corresponding particles and sparticles.

The simplest version of SUSY is called the Minimal Supersymmetric Standard Model, which postulates the minimal number of particles fulfilling the supersymmetry conditions. The SM particles and their superpartners would be arranged into supermultiplets as follows: gauge bosons of the SM theory with corresponding gauginos (gluino, wino and bino), the quarks and leptons with the squarks and sleptons, while the Higgs boson with higgsino. The existence of only one higgsino would result in gauge symmetry breaking because of the chiral anomaly [63]. To prevent this, one has to introduce the second Higgs supermultiplet $H_u$.

As for the 2HDMs, two Higgs supermultiplets provide five Higgs bosons after electroweak symmetry breaking - neutral scalars $h$ and $H$, the pseudoscalar $A$ and charged scalars $H^+$. In addition, the mixing of the winos, the bino and the higgsinos together results in the creation of the four neutral massive neutralinos $\tilde{\chi}_a^0$ ($a$=1,2,3,4), as well as two charged massive charginos $\tilde{\chi}_a^\pm$ ($a$=1,2). The chiral and gauge supermultiplets described above with two Higgs supermultiplets are presented in Tables 2 and 3, respectively.

In the MSSM theory, the Higgs sector represents the type-II 2HDM mentioned in Section 2.2.1, where one Higgs doublet couples to up-type fermions and the second one only to down-type fermions. An appealing feature of the MSSM Higgs sector is that it

Table 2: Chiral supermultiplets in the MSSM based on [55].

| **Supermultiplet** | **Spin 1/2** | **Spin 0** | $SU(3)_C, SU(2)_L, U(1)_Y$ |
|---|---|---|---|
| Quarks and squarks (×3 generations) | $(u_L, d_L)$ | $(\tilde{u}_L, \tilde{d}_L)$ | $(\mathbf{3}, \mathbf{2}, \frac{1}{6})$ |
| | $u_R^\dagger$ | $\tilde{u}_R^*$ | $(\bar{\mathbf{3}}, \mathbf{1}, -\frac{2}{3})$ |
| | $d_R^\dagger$ | $\tilde{d}_R^*$ | $(\bar{\mathbf{3}}, \mathbf{1}, \frac{1}{3})$ |
| Leptons and sleptons (×3 generations) | $(\nu, e_L)$ | $(\tilde{\nu}, \tilde{e}_L)$ | $(\mathbf{1}, \mathbf{2}, -\frac{1}{2})$ |
| | $e_R^\dagger$ | $\tilde{e}_R^*$ | $(\mathbf{1}, \mathbf{1}, 1)$ |
| Higgsinos and Higgs | $(\tilde{H}_u^+, \tilde{H}_u^0)$ | $(H_u^+, H_u^0)$ | $(\mathbf{1}, \mathbf{2}, \frac{1}{2})$ |
| | $(\tilde{H}_d^0, \tilde{H}_d^-)$ | $(H_d^0, H_d^-)$ | $(\mathbf{1}, \mathbf{2}, -\frac{1}{2})$ |

Table 3: Gauge supermultiplets in the MSSM based on [55].

| **Supermultiplet** | **Spin 1** | **Spin 1/2** | $SU(3)_C, SU(2)_L, U(1)_Y$ |
|---|---|---|---|
| Gluon and gluino | $g$ | $\tilde{g}$ | $(\mathbf{8}, \mathbf{1}, 0)$ |
| $W$ bosons and winos | $W^\pm, W^0$ | $\tilde{W}^\pm, \tilde{W}^0$ | $(\mathbf{1}, \mathbf{3}, 0)$ |
| $B$ boson and bino | $B^0$ | $\tilde{B}^0$ | $(\mathbf{1}, \mathbf{1}, 0)$ |

can be characterized by merely two independent parameters at the tree level, whereas a general 2HDM requires seven parameters. At a tree level, the mixing angle $\alpha$ and the neutral Higgs masses can be parametrized as a function of the $\tan\beta$ and mass of the Higgs pseudoscalar $m_A$:

$$m_{H^+}^2 = m_A^2 - m_W^2, \tag{40a}$$

$$m_{H,h}^2 = \frac{1}{2}\left[m_A^2 + m_Z^2 \pm \sqrt{(m_A^2 + m_Z^2)^2 - 4m_Z^2 m_A^2 \cos^2 2\beta}\right], \tag{40b}$$

$$\cos(2\alpha) = -\cos(2\beta)\frac{m_A^2 - m_Z^2}{m_H^2 - m_h^2}, \quad \sin(2\alpha) = -\sin(2\beta)\frac{m_H^2 + m_h^2}{m_H^2 - m_h^2}. \tag{40c}$$

In the case of the $m_A^2 \gg m_Z$ in the MSSM scenarios the equations above become:

$$m_A \approx m_H, \quad \beta - \alpha \approx \frac{\pi}{2}. \tag{41}$$

Unfortunately, it is a well-established fact that radiative corrections to the MSSM Higgs sector [64, 65] significantly alter the tree-level relationships. The considerable number of SUSY parameters complicate the characterization of the Higgs potential, resulting in a much more complicated phenomenological analysis and elevating the $h$ boson mass above the $m_Z$.

One solution is to use benchmark scenarios that accurately represent the model's phenomenology. In these scenarios, the two primary input parameters (such as $\tan\beta$ and $m_A$) are left unconstrained, while all other parameters contributing to the loop corrections are maintained at fixed values. This approach has been extensively utilized by both theorists and experimentalists to investigate the MSSM Higgs sector, especially prior to the discovery of the $h$ Higgs boson.

This fact had a massive influence on the MSSM study. Several benchmark scenarios have been constructed with a mass of $h$ boson below 130 GeV, for instance the so-called $m_h^{\text{mod}+}$ and $m_h^{\text{mod}-}$ scenarios, that ensure a minimal number of free parameters in the theoretical model, even if high-order corrections are considered [66]. In addition, a decade ago the hMSSM scenario [67, 68] was proposed. This model avoids the varying of relevant input parameters, which would provide the experimentally measured $h$ mass, and instead uses the observed $m_h$ value as an input parameter from the outset. This approach enables the parameterization of the CP-conserving and "model-independent" MSSM Higgs sector using only two input parameters, without the need to fix any other SUSY parameters.

These frameworks are extensively studied by the ATLAS and CMS collaborations to investigate the MSSM Higgs sector parameter space and its constraints. The direct searches carried out at the LHC have revealed that the masses of all SUSY particles are significantly higher than the measured Higgs boson mass. The limits on the masses of the strongly interacting superparticles, such as gluinos and squarks, are constrained to be greater than 2 TeV, while the weakly interacting superparticles are expected to have masses (at least) around 1 TeV.

### 2.2.3 Production of Charged Higgs Boson

As discussed earlier, there are many BSM theories extending the Higgs sector like MSSM and four main types of the 2HDMs (Type I, Type II, Type X and Type Y) usually considered in the physics programme of the multi-purpose LHC experiments, which predicts the existence of the charged Higgs boson.

Regardless of which BSM theory is considered, the mass of the $H^+$ is a key factor in defining its production process. Three principal mass ranges can be distinguished:

- Low-mass region ($m_{H^+} < m_{top}$): the charged Higgs boson is produced mainly via the decay of the top quark, $t \to bH^+$, in a double-resonant production of the $t\bar{t}$ pairs. Although for the type-II 2HDM, the dominant decay process of $H^+$ is $H^+ \to \tau\nu$, at low values of $\tan\beta$ also $H^+ \to cs$ and $cb$ can reach considerable proportions.

- High-mass region ($m_{H^+} > m_{top}$): $H^+$ production happens simultaneously with top quark as a result of the single-resonant top-quark production $gg \to tbH^+$ or $gb \to tH^+$.

- Intermediate-mass region ($m_{H^+} \simeq m_{top}$): the creation of $H^+$ takes place through the interference of non-resonant, single-resonant and double-resonant top-quark production processes. Theoretical predictions for $H^+$ production at the mass window near the $m_{top}$ are given in [69].

Feynman diagrams corresponding to the main $H^+$ production modes occurring during $pp$ collisions at the LHC are depicted in Figure 3.

Another parameter that influences the production processes of charged Higgs boson and its decay modes is $\tan\beta$. Production cross-sections of $H^+$ during proton-proton collisions as a function of the $m_{H^+}$ and $\tan\beta$ in the 2HDM are shown in Figure 4.

Production cross sections of heavy $H^+$ Higgs bosons times branching fractions for $H^+ \to \tau\nu$, as a function of $m_{H^+}$ and for $\tan\beta = 7$, $\tan\beta = 20$ and $\tan\beta = 40$ values at $\sqrt{s} = 13$ TeV in the hMSSM and the $m_h^{\text{mod}+}$ scenarios of MSSM, are presented in Figure 5.

A summary of the cross-section predictions for multiple production modes and their interference in the intermediate-mass region is given in [71]. The branching fractions for $H^+$ decays into SM particles, as a function of $m_{H^+}$, for $\tan\beta = 10$ and $\tan\beta = 50$, in the $m_h^{\text{mod}+}$ scenario, are shown in Figure 6. Although the $H^+$ decays to superparticles are not displayed in the plots, their effects can be seen as kinks in the lines of other channels (especially in case of $\tan\beta = 10$). The leading decay process of light $H^+$ for $\tan\beta > 3$ is $H^+ \to \tau\nu$ [7]. It also becomes sizeable for $m_{H^+}$ above the top-quark mass (BR($H^+ \to \tau\nu$) at level $\geqslant$10% depending on the value of $\tan\beta$).

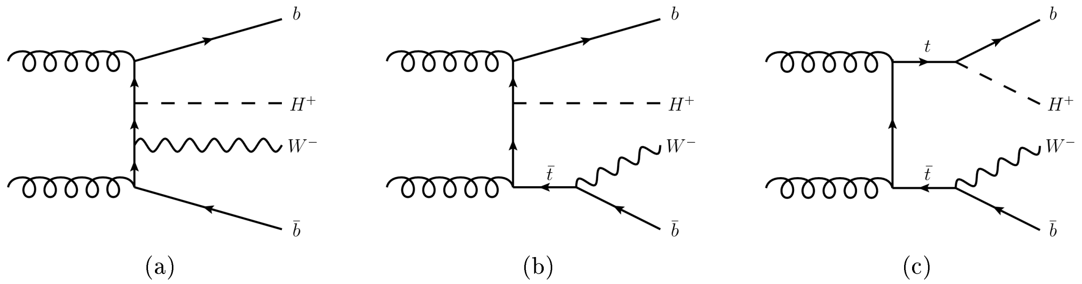


Figure 3: Major leading-order Feynman diagrams for the charged Higgs boson production processes in the $pp$ collisions: (a) non-resonant top-quark production, (b) single-resonant top-quark production dominating at large $H^+$ masses, (c) double-resonant top-quark production dominating at low $H^+$ masses. In the intermediate-mass region, those three modes interfere with each other [70]

.

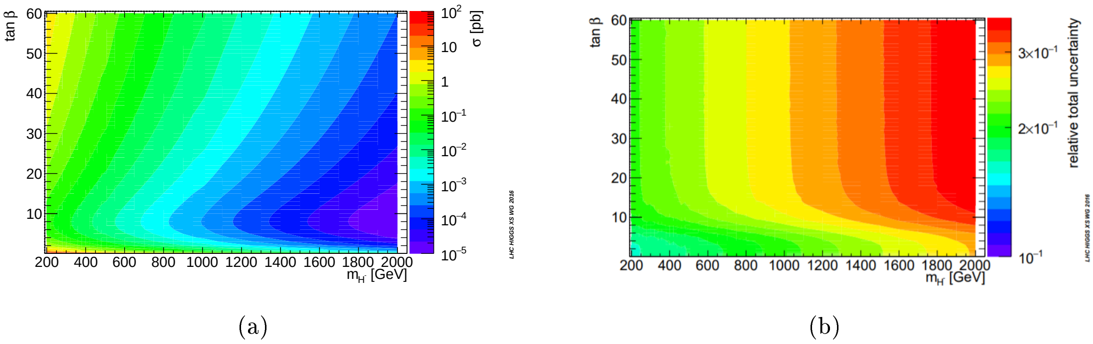


Figure 4: Two-dimensional plot of the charged Higgs boson production cross-section (a) and average relative uncertainty (b) depending on the $\tan\beta$ and $m_{H^+}$ values in the type-II 2DHM [70].

## 2.3 $\tau$ Lepton Properties

Investigation of the processes with $\tau$ leptons in final states is an important part of the nowadays HEP research programme. These particles enable the identification and measurement of electroweak processes and top quark production, and they also provide high sensitivity to new physics searches, such as the charged Higgs boson production mentioned in Section 2.2.3.

As the first particle from the 3rd generation of leptons, the $\tau$ lepton was discovered while studying $e-\mu$ at the Stanford Linear Accelerator in 1975 [72]. It has a spin of $\frac{1}{2}$ and carries an electric charge of $-1$. The $\tau$ is the heaviest observed lepton with the mass of $m_\tau = (1776.82 \pm 0.16)$ MeV [73] hence it can decay to light hadrons. The mean $\tau$ lifetime is $(290.3 \pm 0.5) \times 10^{-15}$ s and the mean $\tau$ decay length is 87 $\mu$m. As a result, usually in the HEP experiments the $\tau$ decays well before it can reach the innermost part of particle detectors, which significantly complicates its detection from the experimental data.

In general, the $\tau$ decay channels can be grouped into to two categories: leptonic decays to lighter $e$ or $\mu$ with corresponding neutrinos, and hadronic decays to charged and neutral hadrons with a $\nu_\tau$. Branching ratios for different modes of $\tau$ decays are shown in Table 4. While the most frequently observed hadronic decay is to $\pi^\pm$, $\tau$ also decays to other charged hadrons such as $K^\pm$. Depending on the number of charged hadronic decay products (so-called "daughters"), we distinguish 1-prong (85% of the decays), 3-prong (14% of the decays)

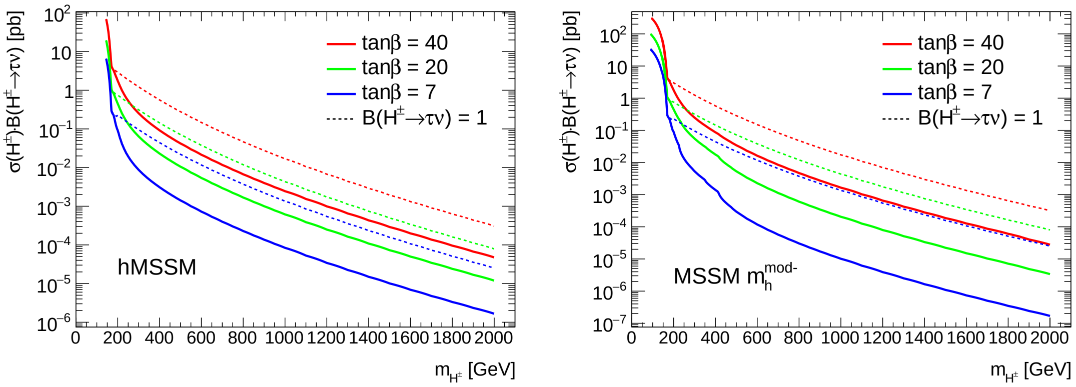


(a) (b)

Figure 5: Branching ratios of $H^+$ as a function of charged Higgs boson mass in $pp$ collisions at $\sqrt{s} = 13$ TeV, for $\tan\beta$ values of 7, 20 and 40, in (a) the hMSSM scenario and (b) the $m_h^{\text{mod-}}$ scenario of the MSSM [70].

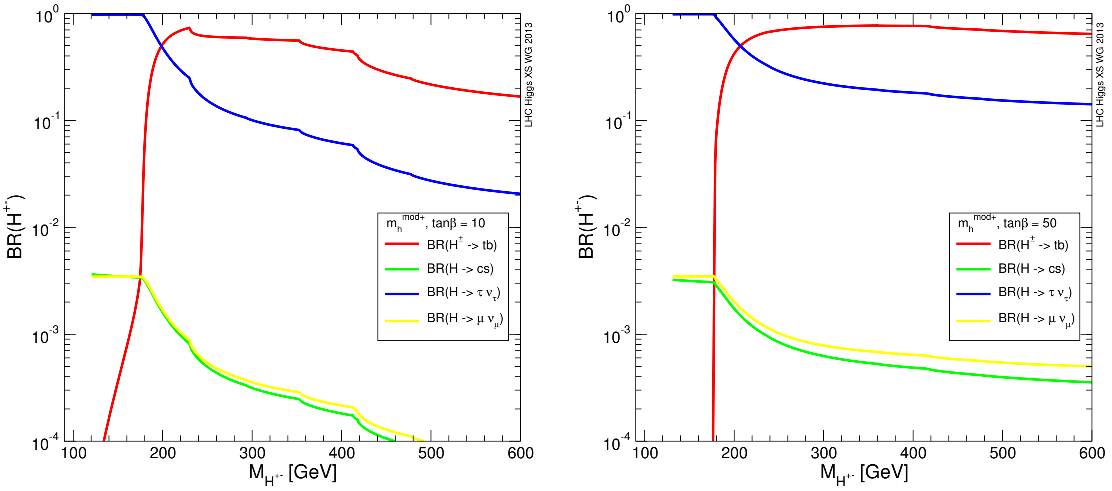


(a) (b)

Figure 6: Branching fractions of the charged Higgs boson depending on $m_{H^+}$, for $\tan\beta$ values of 10 (a) and 50 (b), in the $m_h^{mod+}$ scenario of the MSSM [70].

or rare 5-prong $\tau$ decays [73].

### 2.3.1 Polarization of the $\tau$ Lepton

The $\tau$ polarization ($P_\tau$) is defined as the assymetry in production cross-sections for left-handed ($\sigma_L$) and right-handed ($\sigma_R$) $\tau$ leptons as follows:

$$P_\tau = \frac{\sigma_R - \sigma_L}{\sigma_R + \sigma_L} \tag{42}$$

for $\tau$ production. This quantity reflects the degree of parity violation, offering insight into the underlying Lorentz structure of the studied interaction [74]. The most precise measurement of the $P_\tau$ in $Z \to \tau\tau$ decays was provided by LEP in the $e^-e^+$ annihilation process at the $\sqrt{s} = m_Z$, where results of different experiment at LEP were combined to calculate $\tau$ production asymmetry ($A_\tau$). It is a quantity with the opposite sign to the $\tau$ polarization, extracted from angular distributions of $\tau$ decay products, and with small

Table 4: Branching ratios for most frequent $\tau$ decay modes [73].

| Decay mode | Resonance | $\mathcal{B}\,(\%)$ |
|---|---|---|
| **Leptonic decays** | | |
| $\tau^- \to e^-\bar{\nu}_e\nu_\tau$ | | 17.8 |
| $\tau^- \to \mu^-\bar{\nu}_\mu\nu_\tau$ | | 17.4 |
| **Hadronic decays** | | |
| $\tau^- \to h^-\nu_\tau$ | | 11.5 |
| $\tau^- \to h^-\pi^0\nu_\tau$ | $\rho(770)$ | 25.9 |
| $\tau^- \to h^-\pi^0\pi^0\nu_\tau$ | $a_1(1260)$ | 9.5 |
| $\tau^- \to h^-h^+h^-\nu_\tau$ | $a_1(1260)$ | 9.8 |
| $\tau^- \to h^-h^+h^-\pi^0\nu_\tau$ | | 4.8 |
| Other | | 3.3 |

($\mathcal{O}(0.005)$) corrections reflecting the influence of the interference of the $Z$ boson and photon propagators, as well as the contribution of the pure photon. The final result was $A_\tau = 0.1439 \pm 0.0043$ [75].

The $\tau$ decay products' angular distribution is strongly connected with the $\tau$ spin orientation as a result of the angular momentum conservation. The most convenient way to determine the spin orientation of the $\tau$ is by investigating the $\tau$ hadronic decays, which in the final state contain only one meson. Measuring the polarization in the experimental data may enable to discriminate between the SM and BSM processes, especially those having identical final decay products, including $\tau$ leptons with similar kinematics. As an example of such processes, one can consider $W^- \to \tau_L^-\bar{\nu_\tau}$ and $H^- \to \tau_L^-\bar{\nu_\tau}$ decays with different handedness of 1-prong $\tau$ leptons.

Although the chiral states, contrary to the helicity states, cannot be probed in the experiment, the right-handed (left-handed) chiral states coincide with the positive (negative) helicity, under the assumption of the relativistic limit. In other words, the $\tau$ handedness is its helicity. The SM postulates the existence of only left-handed $\tau$ neutrinos and right-handed $\tau$ antineutrinos. If $W^\pm \to \tau^\pm\nu_\tau$ decay is considered, one can expect exclusively left-handed $\tau$ leptons and right-handed anti-$\tau$ leptons, which corresponds to $P_\tau$ of -1. On the other hand, BSM theories with $H^+$ boson predict decays to solely right-handed $\tau$ or left-handed anti-$\tau$, as a result of lepton number, angular momentum and the boson spin conservation. In that case, the expected $P_\tau$ would be $+1$. Diagrams for both mentioned decays are presented in Figure 7.

To access the information about the $P_\tau$ from the experimental data the observable $\theta$ angle is used, which in the relativistic approximation ($m_\tau \ll E$) is defined as the ratio of the decay products' energy from hadronic $\tau$ decay to the energy of $\tau$ in the laboratory frame. However, due to the lack of direct neutrino detection in the experiment a precise $\tau$ energy reconstruction from $W \to \tau\nu$ decays is not possible. A common approach uses the hadronic decay of $\tau$ to one neutral and one charged pions via $\rho$ meson, which makes $\sim$25% of all $\tau$ decays [73], and introduces the $\cos\psi$ observable with the $\psi$ angle measured between the $\rho$ and the $\pi^+$ flight directions in the $\rho$ rest frame [77, 78]:

$$\cos\psi = \frac{m_\rho}{\sqrt{m_\rho^2 - 4m_\pi^2}}\frac{E_\pi^- - E_{\pi^0}}{|\mathbf{p}_{\pi^-} + \mathbf{p}_{\pi^0}|}, \tag{43}$$

Here, the $E$ and $\mathbf{p}$ of each particle are measured in the laboratory frame. As a result of the angular momentum conservation in $\tau \to \rho\nu$ decays, the $\rho$ mesons are polarized

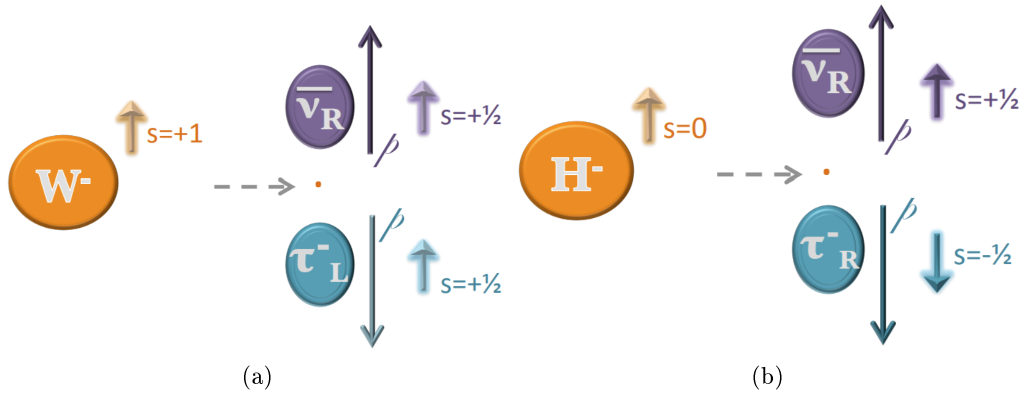


Figure 7: Diagrams of the $W^- \to \tau_L^- \bar{\nu}_\tau$ (a) and $H^- \to \tau_L^- \bar{\nu}_\tau$ (b) decays with spin directions of each particle displayed, in the rest frame of the $W^-$ and $H^-$ bosons, respectively [76].

depending on the handness of $\tau$ lepton - preferred option is transversely polarized $\rho$ in the left-handed $\tau$ decays and longitudinally polarized $\rho$ in the right-handed $\tau$ decays. There is no significant energy asymmetry between decay products of the transversely polarized $\rho$, while for longitudinally polarized $\rho$ the energies of the charged and neutral pions differ. Direct experimental measurement of the $\cos\psi$ is demanding, hence a more accessible observable is introduced called charged asymmetry ($\Upsilon$), which measures the energy distribution between the charged and neutral pions produced in the decay of the $\tau$, with respect to the $\tau$ observable momentum. The energy of the charged pion is approximated using the transverse momentum of the associated track ($p_{\mathrm{T}}^{\tau\text{-track}}$), as reconstructed by the calorimeter subdetector. The neutral pion energy is estimated as the difference between the reconstructed $\tau$ transverse momentum ($p_{\mathrm{T}}^{\tau}$) and that of the charged track, as presented below [74]:

$$\Upsilon = \frac{E_{\mathrm{T}}^{\pi^\pm} - E_{\mathrm{T}}^{\pi^0}}{E_{\mathrm{T}}^{\tau}} \approx \frac{p_{\mathrm{T}}^{\tau\text{-track}} - (p_{\mathrm{T}}^{\tau} - p_{\mathrm{T}}^{\tau\text{-track}})}{p_{\mathrm{T}}^{\tau}} = 2\frac{p_{\mathrm{T}}^{\tau\text{-track}}}{p_{\mathrm{T}}^{\tau}} - 1.$$

Initially, the charged asymmetry variable was defined for $\tau \to \rho\nu$ decays, but in the physics analyses with hadronically decaying $\tau$ leptons it can be applied inclusively to all decays with one charged particle in the final state.

### 2.3.2 Spin Effects of the $\tau$ Lepton

Another useful characteristic of the $\tau$ lepton in the HEP analyses is the spin-spin correlation in the $\tau$ lepton pair. In addition to mitigating irreducible backgrounds to the processes with a pair of $\tau$ leptons in the final states at the LHC (for instance MSSM Higgs bosons decays), these properties can also assist in determining the CP-mixing angle of the Higgs boson in processes like $H \to \tau\tau$. Access to the mixing angle $\phi_\tau$ is provided by examining the differential decay width of $H \to \tau\tau$ process, which in the rest frame of the Higgs boson is given by [79]:

$$d\Gamma_{H\to\tau^+\tau^-} \sim 1 - s_z^- s_z^+ + |\mathbf{s}_{\mathrm{T}}^-||\mathbf{s}_{\mathrm{T}}^+| \cos(\varphi_s - 2\phi_\tau) \quad (44)$$

Here the $\mathbf{s}^\pm$ are defined as the normalized $\tau^\pm$ spin vectors in their respective $\tau$ rest frames (determined through a Lorentz boost along the $\tau^\pm$ momenta from the Higgs boson rest frame). The indices "$z$" refer to $\mathbf{s}^\pm$ components parallel to the beamline (longitudinal spin correlation), while $\mathbf{s}_{\mathrm{T}}^\pm$ denotes their respective transverse components (transverse spin correlation). The angle $\varphi_s$ is defined as the angle between the transverse spin vectors $\mathbf{s}_{\mathrm{T}}^+$

and $\mathbf{s}_\mathrm{T}^-$ in a right-handed coordinate system. The longitudinal spin correlation results from helicity conservation and is not connected with the mixing angle $\phi_\tau$, hence all CP-sensitive information can be accessed through the transverse spin correlation measurement.

Contrary to longitudinal $\tau$ lepton spin correlation, which is based on the energy spectra of the $\tau$ visible decay product, the transverse spin correlations are investigated by analyzing the angular distribution of the decay products of the $\tau$ lepton pair by CP-sensitive observable called the acoplanarity angle ($\phi_{CP}$) [79]. It is an angle between the planes spanned by $\tau$ leptons and their decay products (charged pions for $\tau^\pm \to \pi^\pm \nu_\tau$ decay) measured in the rest-frame of the Higgs boson. For $\phi_{CP}$ calculation, angle $\phi^*$ and $\mathcal{O}^*_{CP}$ can be defined as [79]:

$$\phi^* = \cos^{-1}\left(\frac{\vec{n_+} \cdot \vec{n_-}}{|\vec{n_+}||\vec{n_-}|}\right) , \quad 0 \leq \phi^* \leq \pi \tag{45}$$

$$\mathcal{O}^*_{CP} = \frac{\vec{p_-} \cdot (\vec{h_+} \times \vec{h_-})}{|\vec{p_-} \cdot (\vec{h_+} \times \vec{h_-})|} \tag{46}$$

where $\vec{n_\pm}$ is the normal vector to the plane spanned by the $\tau^\pm$ lepton and $\pi^\pm$, $\vec{p_-}$ is the momentum vector of $\tau^-$ lepton and $\vec{h_\pm}$ is a 4-momentum of the charged pion. The variable $\mathcal{O}^*_{CP}$ represents the right-hand rule convention: it selects cases where the cross product of the two vectors is either parallel or anti-parallel with the $\tau^-$ lepton direction of flight.

From $\phi^*$ and $\mathcal{O}^*_{CP}$, the $\phi_{CP}$ is reconstructed in a range $[0, 2\pi]$ according to the formula:

$$\phi_{CP} = \begin{cases} \phi^* & \text{for } O^*_{CP} \geq 0 \\ 2\pi - \phi^* & \text{for } O^*_{CP} < 0 \end{cases} \tag{47}$$

With this formulation, the differential decay width of the process $H \to \tau\tau, \tau^\pm \to \pi^\pm + \nu_\tau$ can be expressed as a function of the $\phi_{CP}$ variable at LO [79]:

$$d\Gamma_{h \to \tau^+\tau^-} \approx 1 - \frac{\pi^2}{16} \cos\left(\phi_{CP} - 2\phi_\tau\right) \tag{48}$$

The obtained normalized distributions of $\phi_{CP}$ for the Higgs bosons of $m_H$ =125 GeV with different CP characteristics from simulated $pp$ collisions at $\sqrt{s} = 14$ TeV are presented in Figure 8. The CP-even SM-like Higgs boson is represented by the dashed blue line, the CP-odd version by the dotted black line and the CP-mixture Higgs boson is shown by the dot-dashed black line.

It is crucial to discuss the behavior of the $\phi_{CP}$ distribution for the $Z \to \tau\tau$ process. This represents a major background with the same final state as Higgs boson decays to $\tau$ leptons and a comparable mass of $m_Z \approx 91$ GeV. Contrary to the production of $H$ boson, the matrix element for a process $q + \bar{q} \to \gamma^*, Z^* \to \tau^- + \tau^+ \to a^- + a^+ + X$ does not decompose into the separate components of $pp \to Z^*/\gamma^* + X$ production and the subsequent $Z^*/\gamma^* \to \tau\tau$ decay, as studied in Reference [79].

After calculation of the spin density matrix of $\tau$ pair, one can write a differential cross-section for double $\tau^\pm \to \pi^\pm \nu_\tau$ decay in the $\tau^+\tau^-$ zero-momentum-frame, which is integrated over the polar angles of the $\pi^-$ and $\pi^+$ momenta, as:

$$\frac{d\sigma^{(0)}}{d\varphi_+ d\varphi_-} \sim 1 + \frac{\pi^2}{32} \kappa(B_1, B_2) \cos(\phi_+ + \phi_-) \tag{49}$$

Here $\kappa(B_1, B_2) = (\pi_\tau^B, \pi_\tau^{B_2} - v_\tau^B v_\tau^{B_2})/(\pi_\tau^B \pi_\tau^{B_2} + v_\tau^B v_\tau^{B_2})$ and $\phi_\pm$ are the azimuthal angles of the $\pi^-$ and $\pi^+$ momenta in a coordinate system where the direction of the $\tau^-$ momentum is set to be the $z$-axis, and the initial quark momentum lies within the $x, z$-plane [79]. Integrating over the two azimuthal angles in Equation 49 by applying the trigonometric

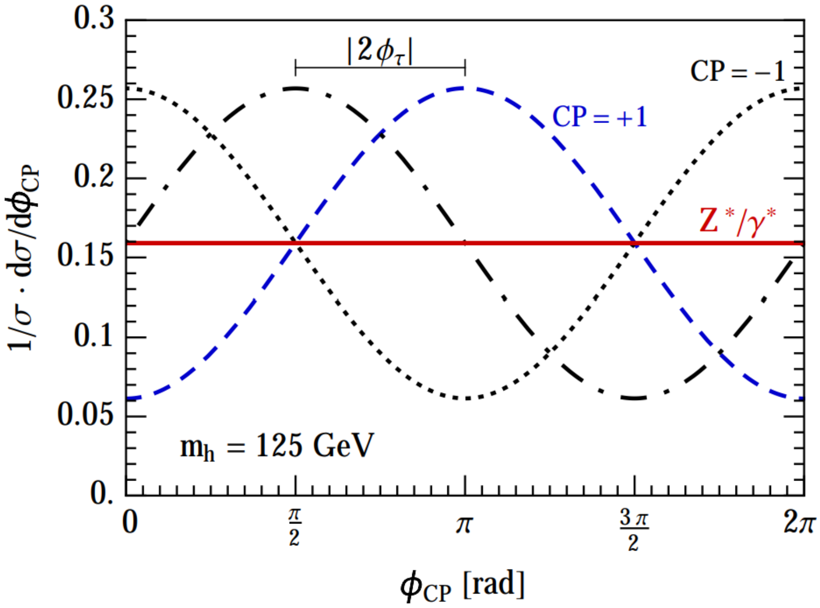


Figure 8: Normalized distribution of $\phi_{CP}$ for a double $\tau^{\pm} \to \pi^{\pm}\nu_{\tau}$ decay. The CP-even SM-like Higgs boson is shown by the dashed blue line, the CP-odd version by the dotted black line and the example CP-mixture Higgs boson is represented by the dot-dashed black line. The solid red line presents the distribution of the $Z^*/\gamma^* \to \tau^+\tau^-$ background [79].

identity $\varphi = \phi_- + \phi_+$ results in a flat $\phi_{CP}$ distribution, as depicted by the red line in Figure 8. This flat distribution persists even when next-to-leading order QCD corrections are included. Validation of $\tau$ polarization, as well as the longitudinal and transverse $\tau$ spin correlations, in the simulated ATLAS samples is presented in Section 5.

The two introduced BSM models in this chapter, the 2HDM and MSSM theories, predict the existence of a charged Higgs boson. To test these predictions, the subsequent chapters focus on a search for the $H^+ \to \tau\nu$ decay over a wide mass range. A critical element of this analysis is the accurate modeling of background processes involving $\tau$ leptons, which heavily relies on Monte Carlo simulations. Therefore, the most important aspect of this chapter is the theoretical foundation for validating tau MC samples, particularly through $\tau$ polarization studies (Equation 42), which will be thoroughly tested and applied in the analysis presented in the following parts of the thesis.

# 3 The ATLAS Experiment as a part of the Large Hadron Collider Accelerator Complex

One of the key characteristics of the high-energy physics (HEP) experiments, which enables the scientists to make discoveries of new particles, is the energy of the colliding particles. This fact favours hadronic colliders over leptonic ones. While electron-electron colliders offer high precision in the collision energy available to produce specific particles of interest, synchrotron radiation poses a significant technological challenge to access new energy bands. Hadronic colliders, with a synchrotron radiation magnitudes smaller, remain the preferred choice for discovery-oriented machines in HEP. In the present times, the biggest machine of this type is the Large Hadron Collider [3].

In this chapter, special attention is given to the ATLAS Experiment, the largest experiment at the LHC. It is hosted by the European Organization for Nuclear Research (CERN) situated near Geneva in Switzerland, which is the world's biggest center for HEP research. ATLAS is a general-purpose detector designed to investigate a broad spectrum of physics phenomena, from the precision SM measurements to searches for any signs of BSM physics. This chapter gives a brief description of the LHC facility, the ATLAS detector and its main components, and the strategy for the physics object reconstruction, which are employed by the $H^+ \to \tau\nu$ analysis described in Section 6.

## 3.1 The Large Hadron Collider

The Large Hadron Collider, situated in close proximity to Geneva and occupying a site that extends across the border between France and Switzerland, is recognized as the world's largest particle accelerator facility, operated by CERN. It is located in the 26.7 km circular tunnel, which was originally built for the Large Electron-Positron (LEP) collider [80]. The LHC project with ultimate centre-of-mass energy ($\sqrt{s}$) of 10 TeV was approved in 1994, redefined in 1996 to reach the $\sqrt{s}$ of 14 TeV and completed and finalized in 2008 [3]. Reusing the LEP tunnel offered the advantage of having access to the established LEP injection system, which was subsequently utilized by the LHC. The superconducting magnets are used to control the hadronic beams - dipole magnets steer and accelerate the particles, while quadrupole magnets focus them.

The LHC has experienced numerous operational cycles and enhancements since its first collisions. The initial operational period (Run-1) began in 2009 and involved collisions at $\sqrt{s}$ ranging from 7 to 8 TeV, after which in 2013 an upgrade was implemented during the first Long Shutdown (2013-2015). The subsequent data-tacking period (Run-2) reached a $\sqrt{s}$ of 13 TeV in 2015-2018 and ended with the Long Shutdown 2 (2018-2022). The ongoing operational phase (Run-3) started in 2022 and obtained centre-of-mass energy of 13.6 TeV. Substantial quantities of data produced by the LHC (approximately 1 EB/year) have to be processed by a sophisticated computing infrastructure. The next planned upgrade to the High Luminosity-LHC (HL-LHC) [9], discussed in Section 3.4, is scheduled to start in 2030.

### 3.1.1 The Design of the LHC

The proton acceleration operation for the LHC starts with the source of the hydrogen gas, which is ionized to extract protons using a duoplasmatron device [81]. Subsequently, the protons are gradually boosted to higher energies by a sequence of accelerator systems: the LINAC 4 (160 MeV) [82], the Proton Synchrotron Booster (1.4 GeV) [83], the Proton Synchrotron (25 GeV) [84], and the Super Proton Synchrotron (SPS) before reaching the LHC with the energy of 450 GeV [85]. Ultimately, the protons at the LHC are further accelerated to an energy of 6.8 TeV, resulting in a $\sqrt{s}$ of 13.6 TeV. The numerous high-intensity proton bunches (up to 2,808 per LHC ring) have tightly controlled transverse and longitudinal emittance to maintain beam stability and maximize collision efficiency [3]. The layout of the CERN accelerator infrastructure, presenting the primary LHC experiments, is depicted in Figure 9.

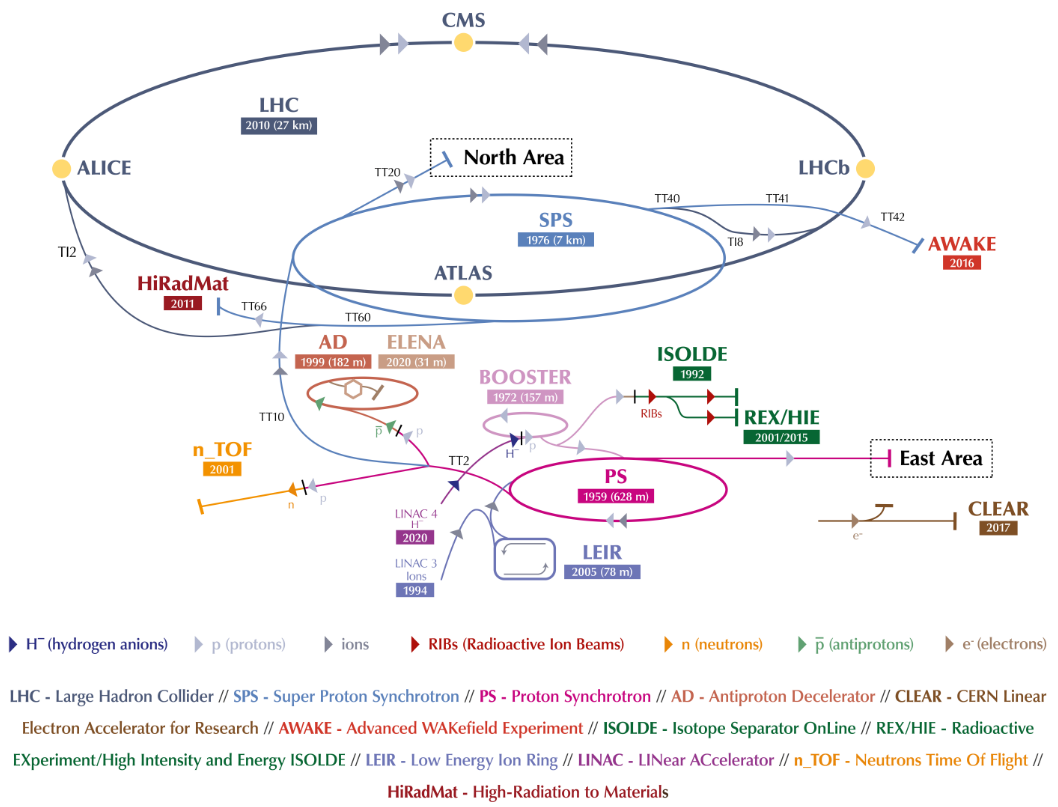


Figure 9: Scheme of the CERN accelerator complex and its experimental facilities [86].

The proton beams within the LHC, guided by a dual-core magnet system, circulate in two opposite directions. This system uses 1,232 superconducting dipole magnets that produce a magnetic field of approximately 8.4 T to steer the beams, as well as 474 quadrupole magnets to focus the particle trajectories. A cross-section scheme of the dipole magnet is presented in Figure 10. Additional multipole magnets, including sextupole, octupole, and decapole configurations, are utilized to stabilize the proton beam. The injected protons travel in discrete bunches of approximately $10^{11}$ particles each, separated by intervals of 25 ns. The bunches' acceleration is enabled by sixteen radio-frequency cavities, which also serve to preserve its structure.

The LHC design also enables the heavy ion collisions using fully stripped lead ions ($^{208}Pb^{82+}$) at a beam energy of 2.76 TeV per nucleon. Compared to protons, ion beams confront difficulties arising from their robust nuclear and electromagnetic interactions, which can influence parameters such as beam lifetime and number of interactions. The performance of ion beams is difficult to forecast due to uncertainties about vacuum conditions and beam stability. The heavy ion injection process starts with LINAC 3 [88], where lead ions are accelerated to an energy of 4.2 MeV per nucleon. These ions are then transported to the Low Energy Ion Ring (LEIR) [89], which transforms the initially lengthy ion pulses into compact, dense bunches. This compression technique ensures the high particle intensities necessary for heavy ion collisions within the LHC. Then, the heavy ion bunches follows the same accelerator path up to the LHC as the proton bunches. [3]

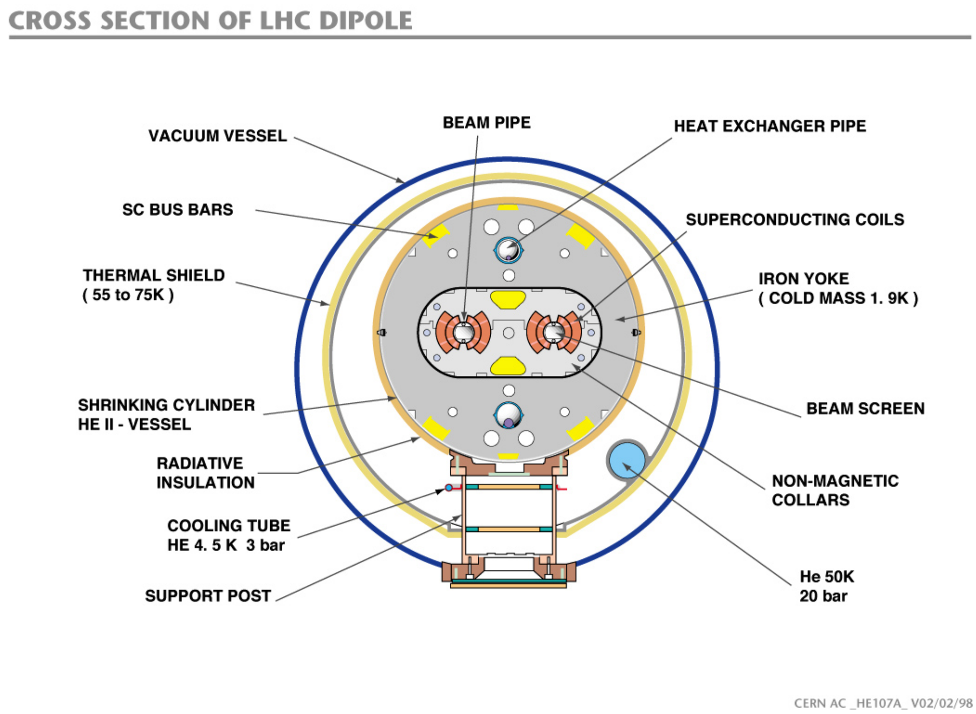


Figure 10: Cross-section scheme of the LHC dipole [87].

LHC facility has four interaction points, which correspond to four major detectors: ATLAS [1], CMS [2], ALICE [90] and LHCb [91]. There are a total of seven distinct detectors, which collectively enable the investigation of particle collisions from diverse perspectives and provide a comprehensive physics research agenda. The two biggest experiments, the ATLAS (A Toroidal LHC ApparatuS) and CMS (Compact Muon Solenoid), are general-purpose detector systems constructed to investigate multiple collision processes. Both allowed for the Higgs boson discovery in 2012 and are actively investigating BSM phenomena. The ALICE detector focuses on the study of heavy-ion collisions in order to provide more information about the characteristics of quark-gluon plasma (a proposed high-energy, hot state of matter when quarks and gluons move freely in a dense medium, existing shortly after the Big Bang). It offers valuable insights into the properties of matter under conditions of extreme temperature and density. The LHCb detector focuses on the study of heavy-flavor physics, particularly examining the properties and decays of $B$ and $D$ hadrons exploring the matter-antimatter asymmetry visible in the Universe, as well as searching for indirect evidence of BSM physics. There are other five smaller experiments located on the LHC. TOTEM (TOTal, Elastic and diractive cross-section Measurement) [92] and LHCf (LHC-forward experiment) [93] specialize in investigating protons or heavy ions, that are scattered at extremely narrow angles in relation to the beamline (so-called "forward particles"). The MoEDAL (Monopole and Exotics Detector At the LHC) [94], is dedicated to the magnetic monopole searching, a hypothetical particle possessing a singular magnetic pole. The two most recent LHC experiments situated in proximity to the ATLAS collision point, namely FASER [95] and SND@LHC [96], are focused on the detection of light, weakly-interacting exotic particles and neutrino physics research.

### 3.1.2 The LHC Performance Goals

The LHC experiments are focused on uncovering and investigating highly uncommon processes, hence an immense volume of data is required to generate statistically robust samples for physics analyses. The rate of particle collision events produced at the LHC is described by the following expression:

$$\mathrm{d}N_{\text{event}} = L\sigma_{\text{event}}\mathrm{d}t \tag{50}$$

Here the cross-section for the specific process under investigation is denoted as $\sigma_{\text{event}}$ and $\mathcal{L}$ represents the machine luminosity. The $\mathcal{L}$ quantity characterizes the machine performance and the beam parameters, which for a Gaussian beam profile is given by the formula:

$$\mathcal{L} = \frac{N_b^2 n_b f_{\text{rev}} \gamma_r F}{4\pi\epsilon_n \beta^*} \tag{51}$$

where the number of particles in each bunch is denoted as $N_b$ and $n_b$ represents the number of bunches per beam. The revolution frequency of $\sim$11.2 kHz is given by $f_{\text{rev}}$, and $\gamma_r$ is the relativistic gamma factor. The normalized transverse beam emittance is represented by $\epsilon_n$, $\beta^*$ is the beta function at the collision point and $F$ denotes the geometric luminosity reduction factor [3].

The initial LHC design allowed to reach an instantaneous luminosity of $\mathcal{L} = 10^{34}$ cm$^{-2}$s$^{-1}$ during $pp$ collision at the $\sqrt{s} = 14$ TeV with the average interactions number of 25 per bunch crossing. Additionally, the planned centre-of-mass energy for heavy ion collisions was expected to be 5.5 TeV per nucleon pair with a luminosity of $\mathcal{L} = 10^{27}$ cm$^{-2}$s$^{-1}$. Eventually, the peak instantaneous luminosity exceeded the design value, reaching a maximum of $\mathcal{L} = 2.1 \times 10^{34}$ cm$^{-2}$s$^{-1}$ during Run-2. The average number of interactions per bunch crossing measured during Run-2 was 33.7, with a maximum value above 60 interactions per bunch crossing documented in 2017 and 2018. In this thesis, the analysis using the full Run-2 dataset is presented, which corresponds to the integrated luminosity of 140 fb$^{-1}$. The Run-3 period with proton-proton collisions at $\sqrt{s} = 13.6$ TeV is anticipated to provide a peak instantaneous luminosity of around $\mathcal{L} = 2. \times 10^{34}$ cm$^{-2}$s$^{-1}$ and the total integrated luminosity of 250 fb$^{-1}$ [97]. The total integrated luminosity for $pp$ collisions collected by the ATLAS detector during full Run-2 and the ongoing Run-3 phase are presented in Figures 11a and 11b.

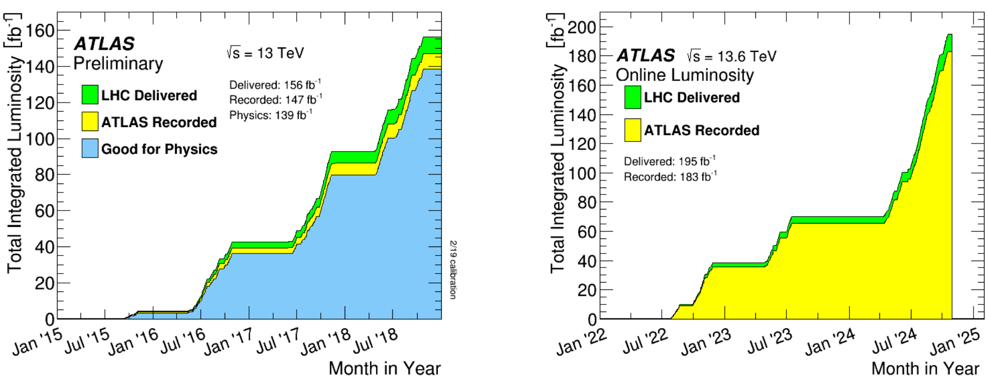


(a) (b)

Figure 11: Total Integrated Luminosity recorded during stable beams for $pp$ collisions at $\sqrt{s} = 13$ during Run-2 (a) and $\sqrt{s} = 13.6$ during Run-3 (b). Cumulative luminosity is presented as a function of time for three categories: delivered by the LHC (green), recorded by ATLAS detector (yellow), and good quality data used for analyses (blue) [98].

## 3.2 The ATLAS Detector

The ATLAS is one of the four principal experiments situated at the LHC, the largest of them all. The ATLAS detector is a general-purpose instrument, measuring 44 meters in length and 25 meters in diameter. The overall weight of the detector is approximately 7000 tonnes [1]. Its aim is to collect data for a range of physics studies, including precision evaluations of the SM, as well as investigations into the Higgs boson and BSM phenomena. The high-energy, high-collision-rate environment of hadron-hadron collisions poses significant challenges in the design of the ATLAS detector. To detect the diverse range of produced physical objects different subdetectors are required, each constructed to suit the unique characteristics of the respective objects. The ATLAS detector consists of four major concentric sub-systems: the Inner Detector, the Calorimeters, the Muon Spectrometer and the Magnet system. The cross-sectional view of the ATLAS detector is shown in Figure 12. This section provides a detailed description of each of the mentioned subsystems, along with the Trigger and Data Acquisition systems responsible for data selection through the implementation of a combination of hardware and software algorithms.

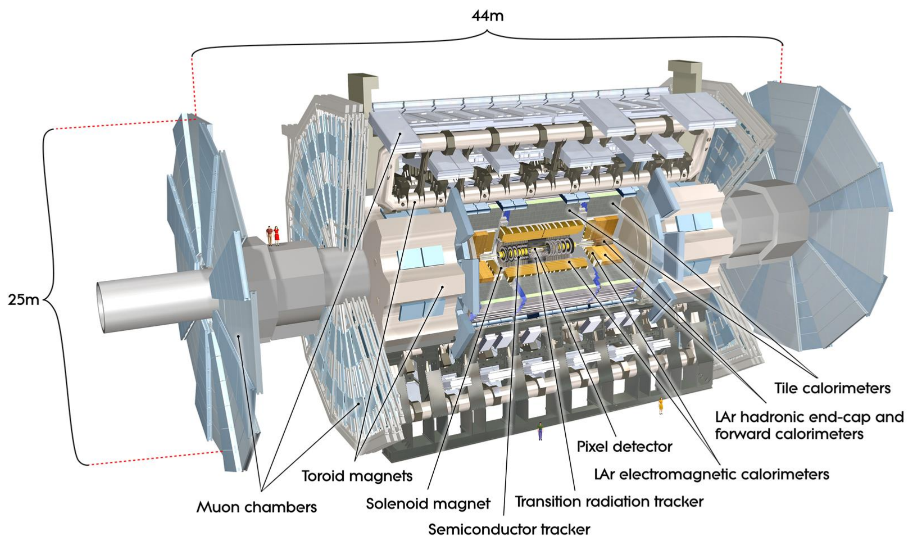


Figure 12: Cross-sectional view of the ATLAS detector [1].

### 3.2.1 Coordinate System of the ATLAS Detector

The ATLAS detector's cylindrical geometry has resulted in the use of right-handed polar cylindrical coordinates. The coordinate system's origin is defined at the nominal interaction point, which is the detector's geometric center. The x-axis extends from the IP towards the center of the LHC ring, while the y-axis is oriented in the upward direction and the z-axis is aligned with the direction of the particle beam. The region of the detector with positive $z$-coordinates is known as the "A-side", while the opposing half is called the "C-side". In the transverse plane, the cylindrical coordinates $(r, \phi)$ are utilized, where $\phi$ represents the azimuthal angle measured around the beam axis. Transverse momenta of the particles are calculated from the three-momenta $\vec{p}$ as $p_{\mathrm{T}} = |\vec{p}|\ sin\theta$. In the field of hadron collider physics, the pseudorapidity variable $\eta$ is frequently used to express the angle between a particle's trajectory and the beam axis as follows:

$$\eta = -ln[\tan(\frac{\theta}{2})] \tag{52}$$

Here $\theta$ is the polar angle measured from the y-axis. Illustration of the ATLAS coordinate system is presented in Figure 13.

If a particle travels in the transverse direction relative to the beam axis, its pseudorapidity $\eta$ is zero. Conversely, a particle with high pseudorapidity values travels along the beamline and may not be fully detected by the detector. The pseudorapidity is the preferred metric for particles without a mass, whereas the rapidity ($y$) is the corresponding quantity employed for massive particles, calculated as:

$$y = \frac{1}{2} \ln \left( \frac{E + p_z}{E - p_z} \right) \tag{53}$$

where $E$ refers the particle's energy and $p_z$ represents the momentum of the particle along the z-axis. The difference $\delta y$ between particles is a Lorentz-invariant property, which is independent of the longitudinal frame of reference. Another quantity, which also is Lorentz-invariant, is the angular distance $\Delta R$ in $(\eta - \phi)$ space, calculated from the formula:

$$\Delta R = \sqrt{\Delta\eta^2 + \Delta\phi^2} \tag{54}$$

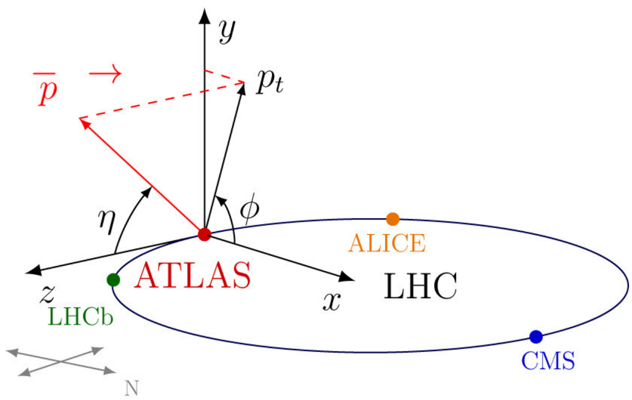


Figure 13: Coordinate systems illustration used at the ATLAS experiment in the geographical context of the LHC [99].

### 3.2.2 Inner Detector

The closest subsystem to the interaction point is the ATLAS Inner Detector (ID). It is designed to perform precise measurements of the momentum and vertex positions of EM charged particles, as well as comprehensive tracking of their trajectories, with full coverage in $\phi$ in the pseudorapidity range of $|\eta| < 2.5$. The ID utilizes a strong 2 T solenoidal magnetic field described in Section 3.2.5. It has dimensions of 7 meters in length surrounding the beam pipe and a total radius of 1.2 meters, as depicted in Figure 14a. The ID system consists of three main subsystems: the Pixel Detector, the Semiconductor Tracker (SCT) and the Transition Radiation Tracker (TRT) [1]. The ID scheme and its cross-sectional view, along with the diameters of each subdetector layer, are presented in Figures 14a and 14b.

**Pixel Detector:**

The Pixel detector is the subdetector positioned nearest to the interaction point and possesses the highest level of granularity using silicon pixel sensors. It features a barrel geometry with three layers of silicon pixel detectors with a radius of around 5 cm, 9 cm, and 12 cm. In addition, this system incorporates three end-cap disks positioned on each side at a distance of approximately 50 cm, 55 cm and 80 cm from the IP, which expand the coverage for particles traversing at higher pseudorapidity regions. In order to improve the efficiency of tracking and enhance the reliability of measurement procedures, the Insertable B-Layer (IBL) was added in 2014 during LS 1 [100] as the innermost detector component at a radius of 33.3 mm. The dimensions of pixels are $50\times250$ $\mu$m$^2$ in the IBL and $50\times400$ $\mu$m$^2$ in the other layers. The detector's robust design, with 1,744 modules and nearly 92 million pixels, enables the precise interaction point and vertex reconstruction.

**Semiconductor Tracker:**

The second subdetector of the ATLAS ID is the Semiconductor Tracker. The SCT employs silicon microstrip sensors to precisely track the charged particles. It comprises four barrel layers located radially between approximately 30 cm and 51.5 cm distances from the IP, complemented by nine end-cap disks on each side, which are positioned at radial distances from 80 cm to 280 cm. The SCT architecture uses around 15,900 silicon strip sensors, which are organized into 4,088 double-sided modules. This system covers an approximate area of 63 m$^2$ and includes around 6.3 million readout channels. The SCT detector modules are composed of two microstrip detector layers each measuring 12.8 cm in length and glued in a back-to-back configuration at a slight angular offset "stereo angle" of 40 mrad. This design approach guarantees that a minimum of four detector layers will be crossed by each charged particle, thereby enabling the acquisition of four spatial measurement points for each track. The SCT exhibits spatial measurements with a resolution of 17 $\mu$m in the transverse plane to the beamline and 580 $\mu$m in the z-direction thanks to the stereo angle solution. This results in the high tracking precision within the acceptance coverage $|\eta| < 2.5$, which is comparable to the performance of the Pixel Detector.

**Transition Radiation Tracker:**

The TRT serves as the outermost layer of the ATLAS ID, which is placed radially between approximately 55.5 cm and 108 cm from the beamline. As an alternative to silicon sensors, the subdetector utilizes the straw drift tubes with a diameter of 4 mm, which are filled with a gaseous blend composed of 70% Xe, 27% $CO_2$, and 3% $O_2$ along with 5-10 mbar over-pressure [1]. The ionization of the gas within the straws, induced by the passage of charged particles, generates an electrical signal as the free electrons move towards the centrally-located, high-voltage gold-plated tungsten wire. The TRT is composed of 350,000 readout channels in total - a barrel section with 50,000 straws and 18 end-cap wheels containing an additional 250,000 straws. Each individual straw offers a spatial resolution ranging from around 130 to 170 $\mu$m. In addition, the subdetector contributes to the discrimination of particle types by exploiting the transition radiation X-rays that are produced when highly relativistic particles pass through the boundaries of different materials. The integration of the precision tracking sensors at the innermost layers and the TRT at the outer layer provides a powerful pattern identification, enhances the track reconstruction, as well as improves the resolution of momentum measurements.

### 3.2.3 Calorimetry

The calorimeters of the ATLAS detector provide the particles' energy measurement by completely absorbing their energy through the formation of electromagnetic and hadronic showers. They can detect most particles, but muons and neutrinos pass through. The Muon Spectrometer is used to identify muons, while neutrinos transverse the detector and result in the "missing energy" signature. The calorimetry subsystem consists of two principal components: the Liquid Argon (LAr) calorimeter and the Tile calorimeter. The calorimetry system's sampling detectors offer comprehensive $\phi$-symmetry and coverage around the beam axis (up to $|\eta| < 4.9$). The calorimeters are crucial for gathering information utilized by the Trigger System. An overview of the ATLAS calorimetry system is presented in Figure 15.

**The Liquid Argon Calorimeters:**

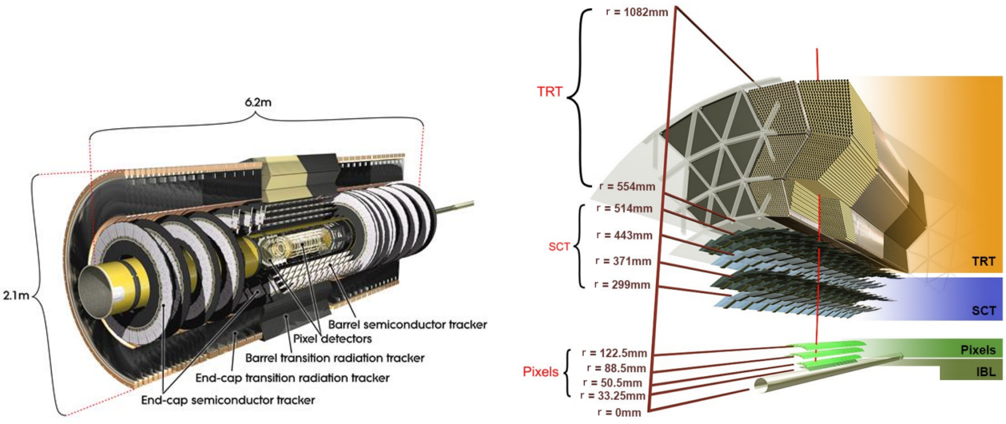


(a) (b)

Figure 14: The Inner Detector scheme (a)), as well as its cross-sectional overview with sensors and structural elements traversed by a charged track (b)) [101].

The LAr calorimeters in the ATLAS detector utilize liquid argon as the active material to perform the energy measurement of electrons, photons, and hadrons. The ionization of the LAr by traversing charged particles results in the generation of free electrons, which then drift to the electrodes, producing an electrical signal. The LAr calorimeters in ATLAS utilize around 180,000 readout channels, enabling detailed energy and spatial measurements of particles. This LAr technology was selected for linear response characteristics, its stability of response over time and its robust radiation tolerance [1].

The system has four Liquid Argon calorimeters that measure energy across different regions of pseudorapidity. The region with $|\eta| < 1.475$ is covered by the Electromagnetic Barrel Calorimeter (EMB), whereas the Electromagnetic End-Cap Calorimeter (EMEC) provides additional coverage up to $|\eta| < 3.2$. Those two subdetectors utilize an absorber made from lead-stainless steel and have an accordion-shaped electrode structure. This design ensures complete azimuthal coverage without any gaps. The next component, the Hadronic End-Cap Calorimeter (HEC), spans the pseudorapidity range of $1.5 < |\eta| < 3.2$ and employs copper-based absorbers for hadronic shower detection. Finally, the Forward Calorimeter (FCAL) further extends the coverage to $|\eta| < 4.9$. It consists of one module optimized for the EM measurements, and the remaining two modules are dedicated to hadronic energy deposition, utilizing copper and tungsten absorbers, respectively. The EMB and EMEC calorimeters employ a multi-layer design. The initial layer offers precise spatial measurements, the second layer accumulates the majority of the particle energy due to its thickness, and the final layer records the tails of the particle showers with a coarser level of granularity. Furthermore, a LAr presampler is incorporated into the EMB in order to account for energy deposits occurring before the particle enters the calorimeter area.

**The Tile Calorimeter:**

The goal of the Tile calorimeter (TileCal) is the total hadronic shower absorption. It is located between the radial distance of approximately 2.3 m and 4.3 m from the IP and provides the pseudorapidity coverage up to $|\eta| < 1.7$. Contrary to the LAr calorimeters design, the TileCal technology is based on steel absorbers, where the scintillating plastic tiles are utilized as the active material. The scintillating medium is excited by the transversing charged particles, resulting in photon production. This light is then detected by fibers capable of wavelength shifting, which subsequently transmit the photons to Photomultiplier Tubes (PMTs). The cell of the TileCal is composed of two PMTs, with a total number of 256 detector modules and more than 10,000 readout channels.

The electrical signals generated by the PMTs undergo shaping and amplification at two different gain levels before being digitized at a sampling rate of 40 MHz using 10-bit analog-to-digital converters. The TileCal includes three subsystems: a central barrel component and two extended barrel components. It operates in conjunction with the HEC and FCAL to deliver precise measurements of missing transverse energy. It is essential for the ATLAS calorimetry system, as it guarantees the complete absorption of hadronic particle showers by spanning over a range of approximately 7.4 interaction lengths (the average distance needed for a particle to interact with the detector medium).

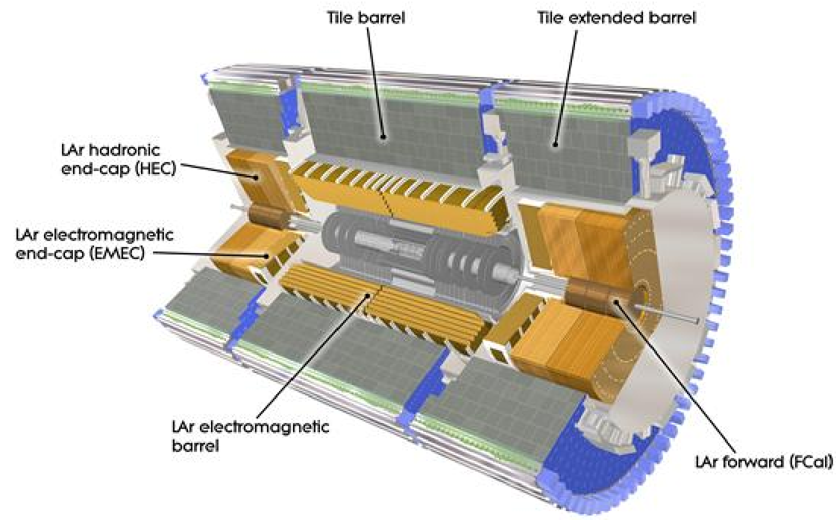


Figure 15: The overview of the calorimeter system in the ATLAS experiment [1].

### 3.2.4 Muon Spectrometer

The outermost layer of the ATLAS detector is the Muon Spectrometer (MS), which is shown in Figure 16. As a specialized subdetector, it is dedicated to precisely measuring the properties of muons, which typically traverse the whole detector material by interacting minimally with matter. Muons, unlike other particles, are not absorbed but rather their trajectories are measured using high-precision chambers, when they are deflected by the toroidal magnetic field. The covered pseudorapidity ranges by the MS subdetector are as follows: $|\eta| < 2.7$ for momentum measurements and $|\eta| < 2.4$ for triggering. The MS barrel section (with coverage $|\eta| < 1.4$) consists of three concentric cylindrical shells positioned at radial distances of 5 m, 7.5 m, and 10 m. In the end-cap region ($1.6 < |\eta| < 2.7$) the large wheels transverse to the beam axis are located at $|z| \approx 7.4$ m, 10.8 m, 14 m, and 21.5 m [1]. The MS uses precision-tracking chambers, which ensure precise trajectories and position measurements of muons. There are two types: Monitored Drift Tubes (MDTs) and Cathode Strip Chambers (CSCs). MDTs, located in both the barrel and end-cap regions of the MS, provide the pseudorapidity range coverage of $|\eta| < 2.7$. However, in the forward region, where the particle flux is higher ($2.0 < |\eta| < 2.7$), CSCs are utilized instead of MDTs. The MDTs use approximately 354,000 tubes filled with gas to measure the ionized electrons' drift time for muon detection. Its design enables to achieve a high spatial resolution - 80 $\mu$m/tube and 35 $\mu$m/chamber. CSCs design relies on multi-wire proportional chambers, which employ the cathode planes divided into perpendicular strips, enabling precise reconstruction of particle trajectories. Its spatial resolution is at level of 40 $\mu$m in the parallel plane to the beam axis and 5 mm in the transverse plane. For a rapid bunch crossing identification and precise muon tracking the other two chambers are used: Resistive Plate Chambers (RPCs) in the barrel ($|\eta| < 1.05$) and Thin Gap Chambers (TGCs) in the end-cap ($|\eta| < 2.4$). In the barrel section, the RPCs identify muons by detecting ionization in a gas gap, whereas in the end-cap region, the TGCs provide the time measurements with high resolution for muon tracking. This multi-layered system employs three detector shells to differentiate between low- and high-momentum muons (with the transition region exclusion of $1.3 < |\eta| < 1.65$ to ensure precision). The magnetic fields produced by the air-core toroids in both the barrel and the end-caps bend the trajectories of muons, providing the measurement of their transverse momentum across a wide energy range.

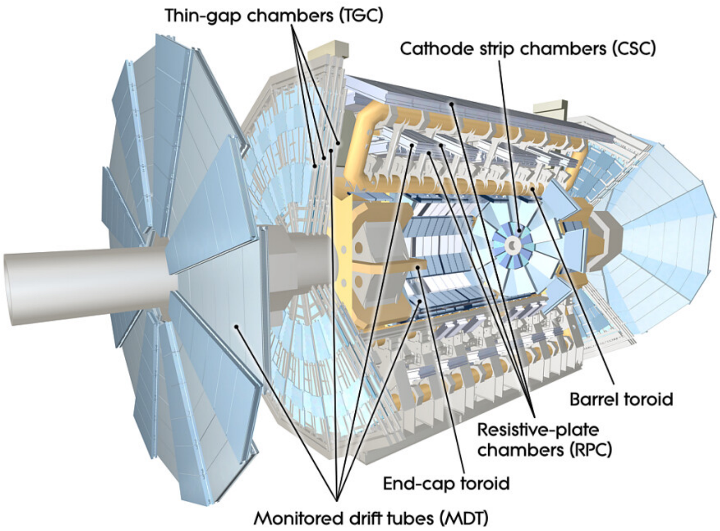


Figure 16: An overview of the Muon Spectrometer system [1].

#### 3.2.5 Magnet System

The ATLAS detector is composed of four superconducting magnets: a central solenoid located around the ID, one toroidal magnet installed in the barrel region, and two toroidal magnets situated in the end-cap regions. The complete magnet system configuration, which is presented in Figure 17, measures 22 meters in diameter and 26 meters in length. Each magnet ensures that magnetic fields are large enough to curve the trajectories of charged particles. The objects' curvatures can be utilized to determine their EM charge, which subsequently enables the measurement of their momentum. When a charged particle moves through a magnetic field, it experiences a Lorentz force that causes it to follow a curved path. The transverse momentum $p_{\mathrm{T}}$ of the particle is related to the strength of the magnetic field $B$, the particle's electric charge $q$, and the radius of curvature $R$ of its trajectory according to the formula:

$$p_{\mathrm{T}} = qBR \tag{55}$$

The superconducting solenoid magnet generates a 2 T axial magnetic field to permeate the inner detector region. As a result of such a powerful magnetic field, the high-momentum particle trajectories can be curved. The solenoidal magnet is situated upstream of the calorimeter, so its design must be as compact as possible to minimize its impact on the calorimeter's performance.

The toroidal magnet located within the barrel section of the detector is the largest of its kind worldwide. It consists of eight sizable coils and measures 25.3 m in length. It provides 3.5 T magnetic field to bend the muons trajectories and achieves such performance in the superconductive state by being cooled to the temperature of 4.5 K using liquid helium. The construction of the end-cap toroids is very similar to the barrel ones. They are composed of eight coils and can generate a magnetic field of up to 1 T. The barrel magnets possess a total cold mass of 370 tonnes, while the individual end-cap magnets each have a cold mass of 160 tonnes.

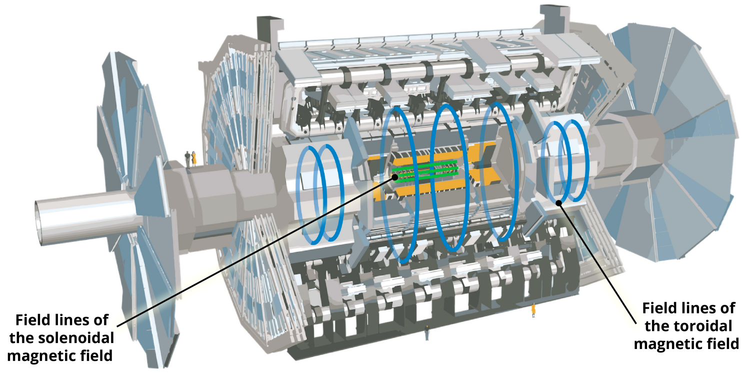


Figure 17: Schematic view of the ATLAS detector Magnet System [102].

### 3.2.6 Trigger System

In order to meet the challenge of the immense volume of data generated in $pp$ collisions at the rate of 40kHz, the ATLAS experiment utilizes an advanced Trigger and Data Acquisition system (TDAQ). Given that not all collision events are of scientific interest and the overwhelming data amount is impractical for storage and analysis, the ATLAS experiment employs a multi-tiered trigger system to selectively preserve and record only the most significant phenomena for physics studies. The ATLAS trigger system operates in two stages: the Level-1 (L1) Trigger and the High-Level Trigger (HLT) [103]. Each level introduces more refined selection criteria than the previous stage. The structure of the TDAQ system is illustrated in Figure 18.

The L1 trigger level, which is hardware-based, is used for the selection of particles with high $p_{\mathrm{T}}$ like photons, electrons, muons, $\tau$ leptons, and jets, in addition to events exhibiting significant missing or total transverse energy. It operates by using data with reduced resolution from a calorimeters system (L1Calo), muon trigger chambers (L1Muon) and L1 topological trigger modules (L1Topo), which are then processed by the Central Trigger Processor (CTP), to make decisions within 2.5 $\mu$s. It employs pre-established selection criteria and applies dead time to protect the readout system. The L1 trigger also identifies Regions-of-Interest (RoIs), highlighting detector areas with notable activity for further processing.

Subsequently, the HLT is a software-based system, which is operating by using advanced offline-like reconstruction algorithms. For the computing operations, it employs a farm of around 40,000 Processing Units (PUs), designed for quick decision-making. The HLT processes either high-resolution event data or data within the RoIs, diminishing the event rate from 100 kHz to around 1.5 kHz, with each event size a little over 1 MB [104]. This concluding selection process guarantees that solely the most significant $pp$ collisions are preserved for further physics analyses. The substantial data reduction by a factor of approximately 40,000 enables the feasibility of data storage and analysis [103].

Following the passing selection of the TDAQ system, the recorded events are archived on magnetic media and are additionally processed at the Tier-0 computing center. To accommodate the growing LHC luminosity, the ATLAS trigger system has been regularly upgraded. These improvements enable the system to process data at higher rates without greatly raising trigger thresholds. As a result, the system maintains sensitivity to important physics phenomena in the face of rising event rates.

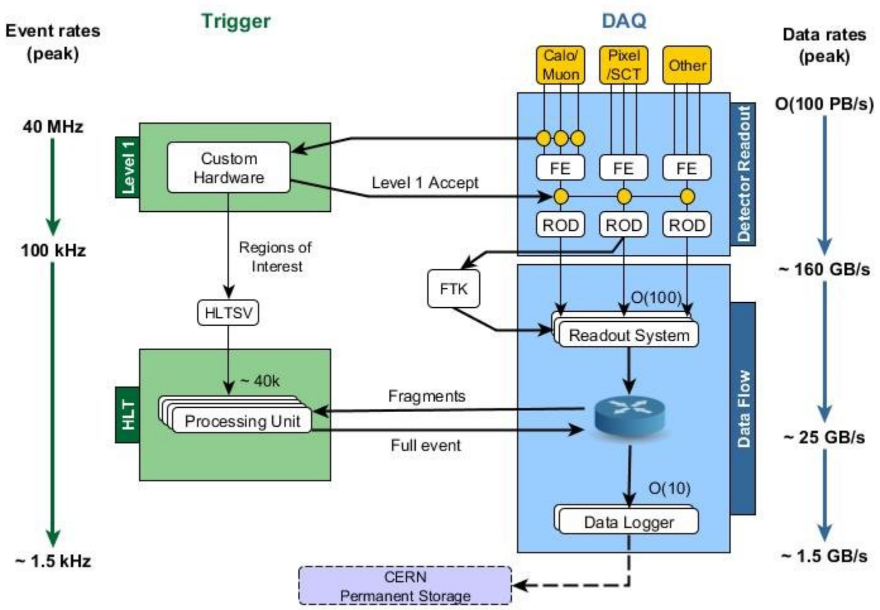


Figure 18: The scheme of the ATLAS TDAQ system's event processing chain during LHC Run-2 [103].

## 3.3 Physics Objects Reconstruction and Identification used in the $H^+ \to \tau\nu$ Analysis

Once the $pp$ collision data are collected by various components of the ATLAS detector, the data must be analyzed to identify physics objects of interest. Due to the excessively short mean lifetime of the sought rare particles, the evidence of such events must be derived from their decay products. ATLAS physics analyses use different selection categories called "working points" (usually set to *loose*, *medium* or *tight* settings), which assess the quality of reconstructed and identified physics objects. These categories provide increasingly rigorous object selection, with higher purity but lower efficiency. The reconstruction and identification processes of physics objects, including electrons, muons, jets, hadronically decaying $\tau$ leptons, and missing transverse energy, are described in this section. A diagram of the particles' signatures left in different subdetectors is shown in Figure 19. These identified objects are then utilized by the various physics analyses, such as $H^+ \to \tau\nu$ search. In addition, the strategy for the removal of geometric overlaps between objects is presented.

### 3.3.1 Reconstruction of Primary Particle Information

Charged particle trajectories (also referred to as "tracks"), primary vertex reconstruction and topoclusters are the crucial steps for any physic object reconstruction in the ATLAS detector.

**Tracks**:

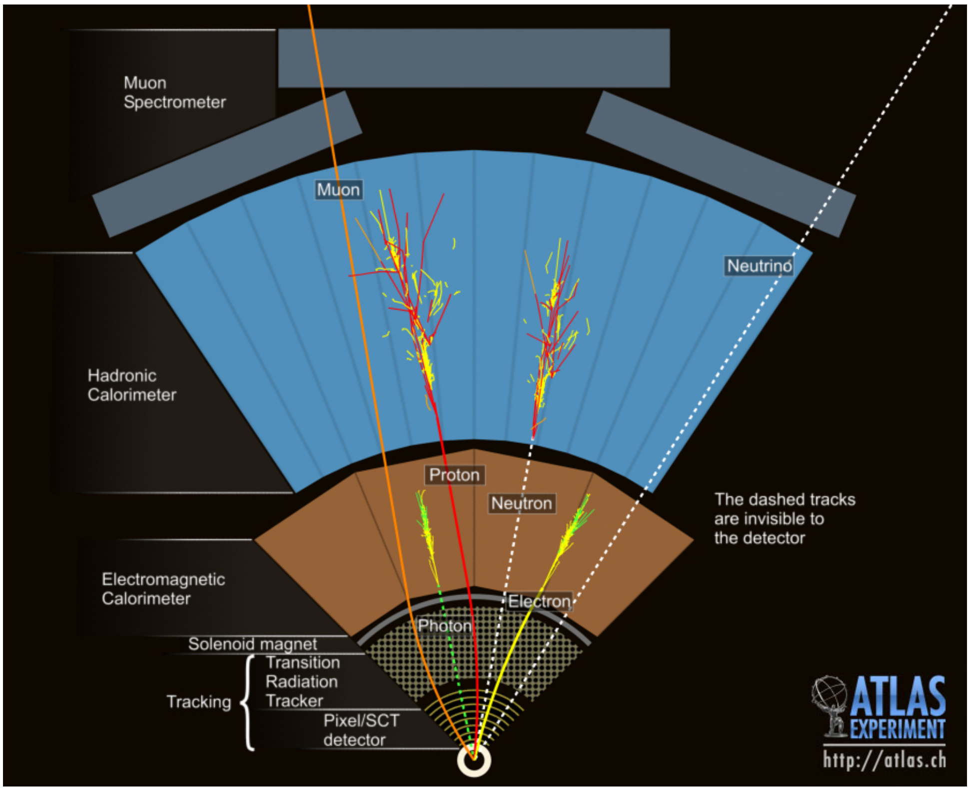


Figure 19: Diagram of particle signatures in the ATLAS detector [105].

As a result of the $pp$ collision, multiple charged particles cross the detector, leaving signals in the material of subsequent subdetectors. By combining these signals, one can reconstruct the path of the produced particle. To provide a comprehensive description of charged particle trajectories five parameters are used: ratio of the particle charge to its momentum, angular variables ($\phi$ and $\theta$), as well as transverse and longitudinal impact parameters ($d_0$ and $z_0$). The reconstruction algorithm starts by forming a track seed (three hits matching predefined curvature shape) called "space-points" in the silicon subdetector [106]. A fourth compatible hit in an additional layer validates the seed, whereupon a combinatorial Kalman filter continues and refines the track by incorporating nearby clusters. The calorimeter data within the seed's Region of Interest is utilized to further refine and validate the track. Then, the quality of the track candidates is evaluated based on the hit topology and their parameters, like the number of missing measurements in the ID layer or the goodness-of-fit of the track ($\chi^2$). If a track does not meet the score requirements it is rejected to minimize combinatorics. In the last stage, the tracks' parameters are refined by taking into account the data from the TRT. If a particle is produced away from the beamline, for instance, electrons are generated in photon conversions, the outside-in algorithm is employed for track reconstruction. In dense high-energy jet cores with $p_T$ between 200 and 1600 GeV, the ATLAS track reconstruction efficiency was measured using a data-driven dE/dx method, showing a slight decrease from approximately 93.9% to 90.7% as jet energy increases [106].

**Primary Vertex**:

The origin point of the incident particles in the ATLAS detector, which is reconstructed through the utilization of selected particle trajectories, is called the primary vertex. In case of more than one reconstructed primary vertex, the selection is looking for the one with the highest total sum of particles' $p_T$. The tracks must meet the requirements of $p_T$ >400 MeV and pseudorapidity $|\eta| < 2.5$. High accuracy is maintained by the minimum hit criteria in the silicon detector. The vertexing algorithm starts with finding a vertex by looking for the initial seed position (in relation to the primary interaction point) of the selected tracks. Then, an iterative process is adopted to refine the vertex position by utilizing the tracks and seeds, and in each interation, the less compatible tracks are eliminated. The process stops when all vertices with two or more associated tracks are found [107].

**Topoclusters**:

A similar process to the track reconstruction by merging signals in the ATLAS ID is performed for the calorimeters, where topological clusters, referred to as "topoclusters", are employed to characterize the energy deposition of individual particles within the calorimeters. By passing through the calorimeter layers the particle leaves energy deposits in calorimeter cells along its path. These small depositions from multiple calorimeter cells can be consolidated into one reconstructed entity - topoclusters. They are seeded if the deposited energy of a local cell exceeds the absolute signal-to-noise ratio by a level of $4\sigma$ (the level varies for different calorimeter components), where noise is defined as a sum of electronic noise and the pile-up.

Once the topocluster seed is created, the cells in the vicinity with a signal-to-noise ratio above $2\sigma$ are included in the topocluster. As a final step, the topocluster is extended by all cells close to the already incorporated cells. The topocluster can be divided into two if it poses two distinct maxima. The calibration of topoclusters from electron- or photon-induced electromagnetic showers is applied to provide the equivalent response for both [108].

### 3.3.2 Electrons

As electrons pass through the detector components, they interact with the cells of the ID, leaving behind signals for track reconstruction. They then continue to traverse the EM calorimeter, generating Bremsstrahlung photons that subsequently convert into electron-positron pairs. This leads to the formation of electromagnetic showers. A similar process occurs when photons are produced and propagated to the EM calorimeter, creating an analogous shower through the conversion into an electron-positron pair. Electrons are reconstructed by matching the tracks reconstructed in the Pixel detector, SCT, and TRT to the clustered energy deposits in the electromagnetic calorimeter [109, 110]. Electron candidates must fulfill quality criteria derived from the properties of their electromagnetic showers, as defined by a loose likelihood-based identification selection point. Candidates should possess the transverse energy $E_{\mathrm{T}} > 20$ GeV and the pseudo-rapidity range of $|\eta| < 2.47$ (with the exclusion of $1.37 < |\eta| < 1.52$).

### 3.3.3 Muons

The tracks reconstructed from muons in the ID are combined with stand-alone tracks reconstructed in the Muon Spectrometer [111]. The muon spectrometer tracks are short, linear segments derived from the hit patterns within each muon subsystem component. In addition, muon candidates must fulfill $p_{\mathrm{T}} > 25$ GeV and $|\eta| < 2.5$ criteria. Only muons satisfying loose identification and tight isolation working points[1] are accepted. To ensure that muons originate from the primary vertex, the track linked to the lepton must have a longitudinal impact parameter and a transverse impact parameter significance that satisfy $|z_0 sin(\theta)| < 0.5$ and $|d_0/\sigma d_0| < 3$, respectively.

[1] Set of criteria employed for identification of particles spatially separated from surrounding detector activity, helping to distinguish prompt signal particles from the background.

### 3.3.4 Jets

Jets originate from the hadronization process of quarks or gluons, resulting in a narrow, particle-filled cone structure. The goal of jet reconstruction is to capture the direction and energy of hadronic showers. Candidates for jets are reconstructed from clustered particle flow objects [108] employing the anti-$k_T$ algorithm [112] with a radius parameter of $R = 0.4$. The particle flow and anti-$k_T$ reconstruction algorithms utilize inputs comprising selected Inner Detector tracks and calorimeter energy deposits. Calibration of the jets is performed with the MCJES+GSC calibration scheme, in which jets candidates must fulfill the requirement of a transverse momentum $p_T > 25$ GeV and $|\eta| < 2.5$. The calorimeter measurements of hadronic jets, which are composed of topologically linked deposits of energy, are significantly impacted by pile-up effects regarding the estimated jet energy and structure. Proper identification and selection of hard-scatter interaction jets is provided by Jet Vertex Tagger (JVT) [113] algorithm for jets meeting the criteria of $p_T < 60$ GeV and $|\eta| < 2.4$.

**The $b$-tagged jets:**

The jets originating from the hard scattering of $b$-quarks play a crucial role in HEP experiments, especially in the $H^+ \to \tau\nu$ analysis with a significant amount of $b$-quarks background events from $t\bar{t}$ processes. The hadronization of an initial state $b$-quark into long-lived $B$-hadrons allows these particles to decay and produce a hadronic shower at a significant distance from the interaction point. This process results in the formation of a measurable secondary vertex. A schematic view is presented in Figure 20.

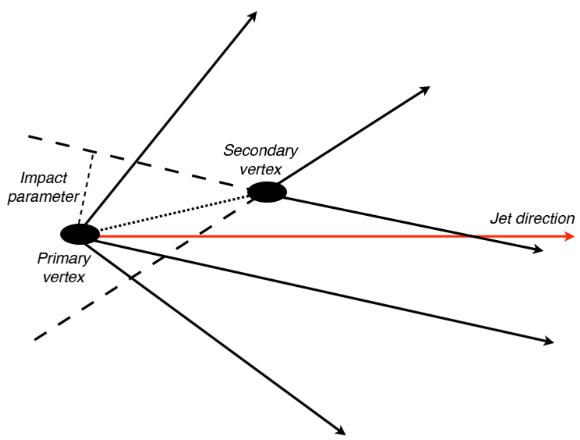


Figure 20: Schematic view of a displaced vertex coming from a $b$-jet [114].

The algorithm is built upon an artificial deep neural network architecture that utilizes over 20 input variables, encompassing the $p_T$ and $\eta$ of reconstructed jets [115]. In addition, the $b$-tagged jets must satisfy the same criteria mentioned earlier, specifically in terms of $p_T$, $\eta$ and the selection for JVT. A predefined working point is selected, referring to an average identification efficiency of 70% for $b$-jets in $t\bar{t}$ events.

### 3.3.5 Hadronically Decaying $\tau$ Leptons

As discussed in Section 2.3, $\tau$ leptons can decay into either an electron, muon, or hadrons, in all cases accompanied by at least one associated neutrino. This thesis considers only hadronically decaying $\tau$ leptons ($\tau_{\text{had-vis}}$) in the later described studies ($H^+ \to \tau\nu$ analysis), and thus focuses solely on the reconstruction of those events. Typical products of the hadronic $\tau$ decays are either one or three tracks of the charged particles, accompanied by the neutrino and potentially neutral pions. This leads to a narrow, collimated energy deposition profile in the calorimeter system and only a few nearby charged particle tracks.

Proper identification of $\tau_{\mathrm{had-vis}}$ objects in $pp$ collisions poses a significant challenge for scientists during the data analysis. Quark- and gluon-initiated jets represent the primary background events for the identification of hadronically decaying $\tau$ leptons, due to their substantial production cross-section, orders of magnitude greater than that of $\tau_{\mathrm{had-vis}}$.

As a first stage of the ATLAS $\tau_{\mathrm{had-vis}}$ reconstruction, the products of a $\tau_{\mathrm{had-vis}}$ decay are seeded by anti-$k_{\mathrm{T}}$ jets with energy deposition $E_{\mathrm{T}} > 10$ GeV in the calorimeter. The $\tau_{\mathrm{had-vis}}$ candidate is associated with all clusters and tracks within a core cone of $\Delta R = 0.2$. Then, the $\tau_{\mathrm{had-vis}}$ momentum direction is utilized to redefine the axis, and the energy scale is calibrated to the $\tau_{\mathrm{had-vis}}$ scale. To make sure the electrons and muons are properly rejected, dedicated rules for overlap removals are employed as described in Section 3.3.6. The $\tau_{\mathrm{had-vis}}$ candidates must meet the following requirements: either one or three associated tracks reconstructed in the Inner Detector, a visible transverse momentum of $< 20$ GeV and presence within the range of $|\eta| < 2.5$ (exclusion region is $1.37 < |\eta| < 1.52$ ). In the specific region selection for the analysis, after overlap removal treatment, the $\tau_{\mathrm{had-vis}}$ criteria are tightened to events with the leading $\tau_{\mathrm{had-vis}}$ candidate possessing $|\eta| < 2.3$ and a transverse momentum of at least 30 GeV.

Secondly, a multivariate analysis is applied. The $\tau$ identification algorithms must be highly robust and perform well across a wide range of transverse momentum for $\tau$ leptons, spanning at least two orders of magnitude ($p_{\mathrm{T}}$ from 15 GeV up to above 1 TeV). Additionally, excellent energy resolution and minimal energy scale error are crucial, especially in analyses where resonances decay to the pair of $\tau$ leptons (for instance $H \to \tau\tau$ and $Z \to \tau\tau$) and their good separation is needed. Furthermore, given that the trigger identification is predicated on an incomplete event reconstruction, it must nonetheless fulfill bandwidth and time-related constraints [116].

The default $\tau$ identification algorithm employed by the ATLAS Experiment for LHC Run-2 is based on track and calorimeter information in a recurrent neural network (RNN) [117] to separate true $\tau_{\text{had-vis}}$ and misidentified $\tau_{\text{had-vis}}$ originating from quark- and gluon-initiated jets. Previously, a set of Boosted Decision Trees BDTs [118] was used for $\tau$ identification.

The RNN employs a mixture of low-level and high-level input variables. The low-level inputs utilize information about individual tracks and clusters associated with the $\tau_{\mathrm{had-vis}}$ candidate, while the high-level inputs are reconstructed from calorimeter and track quantities. These high-level features are analogous to those utilized in the BDT-based $\tau$ identification algorithm reported in the referenced work [118].

The high-level observables are listed below [117]:

1. **Transverse momentum at the LC scale** ($p_T^{\mathrm{uncalib}}$): $p_{\mathrm{T}}$ of the $\tau_{\mathrm{had-vis}}$ candidate at the local cluster scale, which is calculated from the sum of cluster 4-momenta within $\Delta R < 0.2$ of the $\tau_{\mathrm{had-vis}}$ candidate axis, prior to $\tau$ energy scale calibration.

2. **Central energy fraction** ($f_{\mathrm{cent}}$): The ratio of transverse energy at the electromagnetic scale deposited within a region of $\Delta R < 0.1$ to the total energy deposited within $\Delta R < 0.2$ around the axis of the $\tau_{\mathrm{had-vis}}$ candidate, calculated by summing the energy in all cells with a barycentre in these regions.

3. **Inverse momentum fraction of the leading track** ($f^{-1}_{\mathrm{leadtrack}}$): The sum of $E_{\mathrm{T}}$ deposited in all cells belonging to topoclusters in the core region of the $\tau_{\mathrm{had-vis}}$ candidate, divided by the $p_{\mathrm{T}}$ of the core track with the highest $p_{\mathrm{T}}$.

4. **Maximum track $\Delta R$** ($\Delta R_{\mathrm{max}}$): The maximum $\Delta R$ between a core track associated with the $\tau_{\mathrm{had-vis}}$ candidate and the $\tau_{\mathrm{had-vis}}$ direction.

5. **Transverse impact parameter significance of the leading track** ($|\mathrm{S}_{\mathrm{leadtrack}}|$): The transverse impact parameter of the highest-$p_{\mathrm{T}}$ core track associated with the $\tau_{\mathrm{had-vis}}$ candidate, calculated with respect to the $\tau$ vertex, and divided by its estimated uncertainty.

6. **Transverse flight path significance** ($S_T^{\mathrm{flight}}$): The transverse distance between the secondary vertex and the $\tau$ lepton's vertex, divided by the estimated uncertainty of this distance.

7. **Momentum fraction of isolation tracks** ($f_{\mathrm{iso}}^{\mathrm{track}}$): The ratio of the scalar sum of the $p_{\mathrm{T}}$ of the isolation tracks associated with the $\tau_{\text{had-vis}}$ candidate to the sum of the $p_{\mathrm{T}}$ of all the associated core and isolation tracks.

8. **Ratio of EM energy and track momentum** ($f_{\mathrm{track}}^{\mathrm{EM}}$): The ratio of the total energy deposited in the electromagnetic component of the topoclusters to the total momentum of the core tracks. The topoclusters are calibrated at the local cluster energy scale.

9. **Fraction of track-plus-EM-system $p_{\mathrm{T}}$** ($p_{\mathrm{T}}^{\mathrm{EM+track}}/p_{\mathrm{T}}$): The ratio of the $\tau_{\mathrm{had-vis}}$ $p_{\mathrm{T}}$, calculated as the vector sum of core track momenta and up to the two most energetic electromagnetic clusters in the core region, to the calorimeter-only measurement of the $\tau_{\mathrm{had-vis}}$ $p_{\mathrm{T}}$.

10. **Mass of the track-plus-EM-system** ($m_{\mathrm{EM+track}}$): The invariant mass of the system is calculated using the core tracks and up to two most energetic electromagnetic clusters in the core region. The four-momentum of each electromagnetic cluster is computed assuming zero mass and utilizing the topocluster seed direction.

11. **Mass of the track system** ($m_{\mathrm{track}}$): The invariant mass is calculated by summing the four-momenta of all core and isolation tracks, with each track assumed to have the pion mass.

The BDT algorithm utilized two additional variables, not employed in the RNN infrustructure - the track radius ($R_{\mathrm{track}}^{0.2}$) and the fraction of EM energy from charged pions ($f_{\mathrm{EM}}^{\text{track-HAD}}$ ). The $R_{\mathrm{track}}^{0.2}$ variable is defined as the $p_{\mathrm{T}}$-weighted $\Delta R$ distance of the associated tracks to the $\tau_{\mathrm{had-vis}}$, while the $f_{\mathrm{EM}}^{\text{track-HAD}}$ variable represents the ratio of energy deposited in the electromagnetic calorimeter to the energy of charged tracks in the core region [118]. The $\tau$ identification is performed separately for 1- and 3-prong hadronic decays of $\tau_{\mathrm{had-vis}}$ candidate due to different signatures of these two decay channels. Comparison of the variables used by the RNN- and BDT-based $\tau$ ID algorithms, separately for used in 1-track or 3-track $\tau_{\mathrm{had-vis}}$ candidates, is displayed in Table 5.

The RNN architecture enables the $\tau_{\mathrm{had-vis}}$ identification algorithm to process reconstructed objects in the ATLAS detector by treating them as ordered sequences (of an initially undetermined length) based on their physical properties, such as particle $p_{\mathrm{T}}$. This approach is particularly suited for analyzing $\tau$ leptons due to the sequential nature of their decay products. The network is organized into three branches, which are processed separately - charged particle tracks, calorimeter clusters, and high-level variables described above. Within each branch, the model utilizes fully connected layers with shared weights to transform the sequences of tracks and clusters (shared dense layer), before passing them through long short-term memory (LSTM) layers to extract the relevant features.

The LSTM architecture enables the model to maintain information from earlier parts of the sequence and summarize it into a compact representation. The outputs from the three branches are combined in a Merge Layer and further processed through fully connected layers, ultimately generating the $\tau$ identification score using a sigmoid activation function.

Table 5: Summary of high-level variables used in 1- and 3-prong configurations in RNN-based and BDT-based identification algorithms.

| | **RNN** | | **BDT** | |
|---|---|---|---|---|
| **High-level Observable** | **1-prong** | **3-prong** | **1-prong** | **3-prong** |
| $p_T^{\text{uncalibrated}}$ | • | • | | |
| $f_{\text{cent}}$ | • | • | • | • |
| $f_{\text{leadtrack}}^{-1}$ | • | • | • | • |
| $\Delta R_{\text{max}}$ | • | • | | • |
| $\lvert S_{\text{leadtrack}} \rvert$ | • | | • | |
| $S_T^{\text{flight}}$ | | • | | • |
| $f_{\text{iso}}^{\text{track}}$ | • | • | • | |
| $f_{\text{track}}^{\text{EM}}$ | • | • | • | • |
| $p_T^{\text{EM+track}}/p_T$ | • | • | • | • |
| $m^{\text{EM+track}}$ | • | • | • | • |
| $m^{\text{track}}$ | | • | | • |
| $f_{\text{EM}}^{\text{track-HAD}}$ | | | • | • |
| $R_{\text{track}}^{0.2}$ | | | • | • |

The final RNN model contains around 56,000 adjustable parameters optimized to maximize the algorithm's discriminative power.

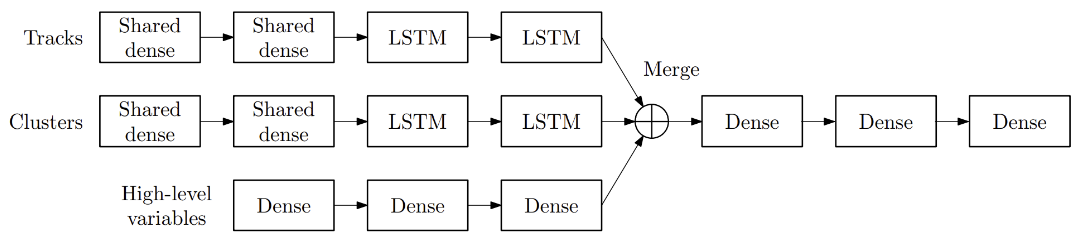


Figure 21: Scheme of the RNN network architecture utilized for $\tau$ identification in the ATLAS Experiment [117].

The RNN architecture was trained using MC-generated samples - Pythia8.212 was used to simulate the signal samples $\gamma^* \to \tau\tau$ and Pythia8.186 simulated the background samples with dijet events.

The RNN-based (as was done for BDT-based) $\tau$ identification output score for true $\tau_{\text{had-vis}}$ candidates is constructed to be uniform within $[0, 1]$ range in each bin of $\tau_{\text{had-vis}}$ $p_T$, pseudorapidity and the number of pile-up interactions per bunch crossing. The value of the transformed score, presented in Figure 22, reflects the fraction of true $\tau_{\text{had-vis}}$, which were rejected.

The rejection power, which is the inverse of the background selection efficiency, for misidentified $\tau_{\text{had-vis}}$ candidates as a function of the true $\tau_{\text{had-vis}}$ selection efficiency is presented in Figure 23. The results are illustrated separately for 1-prong and 3-prong $\tau_{\text{had-vis}}$ candidates, and for both the RNN-based and BDT-based classifiers. The RNN-based model demonstrates significantly better (approximately improved by the factor of 2) rejection power compared to the BDT-based model across the range of signal selection efficiencies. On that basis, four (*Very loose*, *Loose*, *Medium* and *Tight*) $\tau$ identification working points are established, corresponding to different values of the transformed score, which results in varying levels of signal selection efficiency and background rejection. Table 6 displays the performance of each working point for both RNN- and BDT-based classifiers.

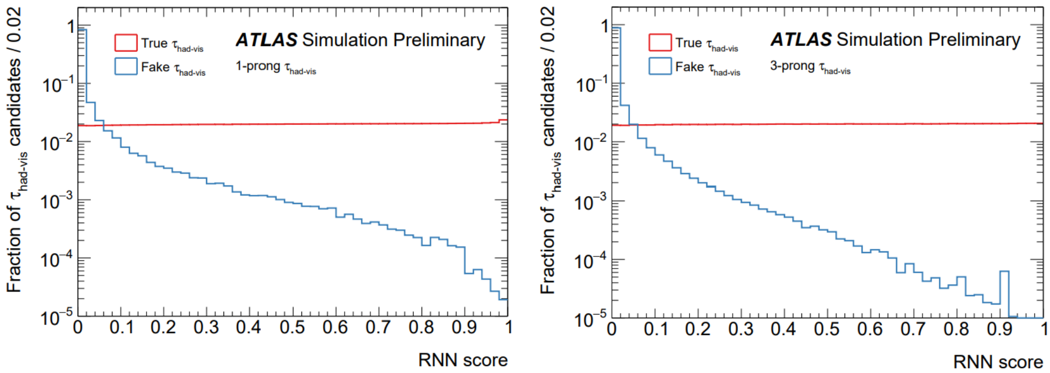


(a) (b)

Figure 22: The RNN score distribution for true (red) and misidentified (blue) $\tau_{\mathrm{had-vis}}$ candidates, separately for 1-prong (a) and 3-prong (b) cases [117].

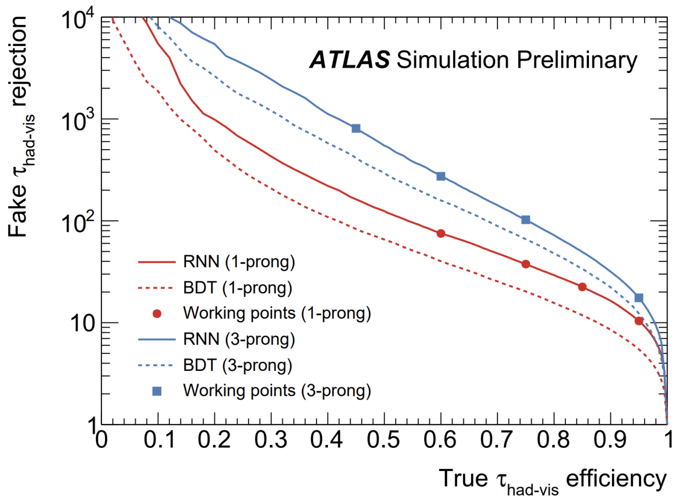


Figure 23: Rejection power for the fake $\tau_{\mathrm{had-vis}}$ candidates as a function of the true $\tau_{\mathrm{had-vis}}$ efficiency for 1-prong (red curve) and 3-prong (blue curve) $\tau_{\mathrm{had-vis}}$ candidates using the RNN-based (full line) or the BDT-based (dashed line) classifiers [117].

Table 6: The performance of different working points, as defined by the true $\tau_{\mathrm{had-vis}}$ selection efficiencies and the corresponding background rejection factors for misidentified $\tau_{\mathrm{had-vis}}$ candidates, compared between the BDT-based and RNN-based models [117].

| Working point | Signal efficiency | | Background rejection BDT | | Background rejection RNN | |
|---|---|---|---|---|---|---|
| | 1-prong | 3-prong | 1-prong | 3-prong | 1-prong | 3-prong |
| *Tight* | 60% | 45% | 40 | 400 | 70 | 700 |
| *Medium* | 75% | 60% | 20 | 150 | 35 | 240 |
| *Loose* | 85% | 75% | 12 | 61 | 21 | 90 |
| *Very loose* | 95% | 95% | 5.3 | 11.2 | 9.9 | 16 |

### 3.3.6 Removal of Geometric Overlaps Between Objects

When there are geometrical overlaps between selected candidates for different physics objects, the ATLAS analyses employ an overlap removal (OLR) procedure. The "heavy-flavor" approach is used with the following criteria:

- if a muon or electron with loose identification criteria contains a pre-selected $\tau_{\mathrm{had-vis}}$ object within its $\Delta R < 0.2$, the $\tau_{\mathrm{had-vis}}$ object is rejected;
- if a log-likelihood matching value of a pre-selected $\tau_{\mathrm{had-vis}}$ object and a reconstructed electron exceeds a pre-established limit, which preserves a *loose* identification performance, the $\tau_{\mathrm{had-vis}}$ object is rejected;
- if an electron shares any track with calorimeter-tagged muons in the Inner Detector part, the muons are removed;
- if remaining muons share any track with electrons in the Inner Detector part, the electrons are removed;
- if the highest-$p_{\mathrm{T}}$ pre-selected $\tau_{\mathrm{had-vis}}$ candidate contains any jets within its $\Delta R < 0.2$, the jets are removed;
- if any selected electron contains non-$b$-tagged jets within its $\Delta R < 0.2$, the jets are removed;
- if any muon contains non-$b$-tagged jets within its $\Delta R < 0.2$, the jets are removed;
- if the remaining non-pile-up jets contain electrons and muons within its $\Delta R < 0.4$, the electrons and muons are rejected.

### 3.3.7 Missing Transverse Momentum $E_{\mathrm{T}}^{\mathrm{miss}}$

The last reconstruction approach corresponds to neutrinos and any other weakly interacting particles. Although these objects cannot be detected in the ATLAS detector, their information can be accessed through the conservation of momentum. In collisions at the LHC, the composite nature of the proton-proton system means the longitudinal part of the initial momentum is not directly accessible. However, the transverse momentum with respect to the beamline is approximately zero ($p_{\mathrm{T}} \simeq 0$). As a result, the missing transverse momentum observable ($E_{\mathrm{T}}^{\mathrm{miss}}$) can be introduced, which is reconstructed from the sum of the transverse momenta of the reconstructed objects. It can also be referred to as the missing transverse energy, due to the negligibly small neutrino mass. By definition, the $E_{\mathrm{T}}^{\mathrm{miss}}$ is calculated according to the formula:

$$E_{\mathrm{T}}^{\mathrm{miss}} = \sum p_{\mathrm{T}}^{e} + \sum p_{\mathrm{T}}^{\mu} + \sum p_{\mathrm{T}}^{\tau} + \sum p_{\mathrm{T}}^{\gamma} + \sum p_{\mathrm{T}}^{\mathrm{jets}} + \sum p_{\mathrm{T}}^{\mathrm{soft}} \tag{56}$$

Here the soft tracks $p_{\mathrm{T}}^{\mathrm{soft}}$ corresponds to the tracks from the hard scattering primary vertex, which are not linked to any physics objects. In the $H^{+} \to \tau\nu$ analysis the $E_{\mathrm{T}}^{\mathrm{miss}}$ is reconstructed using the `METMaker` utility [119].

## 3.4 Planned Upgrades of the LHC - High Luminosity LHC

When this thesis was written, the Run-3 operational period of the LHC was still ongoing, with the planned end date being June 2026. To enhance further the potential of LHC, the High-Luminosity LHC upgrade was proposed in 2010 and approved by the CERN Council in 2016 [120]. The accelerator and detector infrastructure will be adjusted to the new

HL-LHC environment during the Long Shutdown 3 (LS3), which will start after Run-3. The HL-LHC is expected to begin operations in 2030, as can seen in Figure 24.

The goal of the HL-LHC is to achieve luminosity levels 5-7 times higher than a nominal LHC value of about $1 \times 10^{34} \text{cm}^{-2}\text{s}^{-1}$. After approximately 10 years of operation, the overall integrated luminosity is expected to be 3000 $\text{fb}^{-1}$ at a center-of-mass energy of 14 TeV. The levels of expected luminosity for HL-LHC $pp$ collisions during Run-4, Run-5 and Run-6 periods up to 2042, with the assumption of nominal peak luminosity, are presented in Figure 25.

Such a luminosity increase can be achieved by manipulating the beam parameters presented in Equation 3.1.2. The higher beam intensity will be provided by a higher number of bunches per beam ($N_b$) and utilizing the crab cavities, which adjust the orientation of the proton bunches to mitigate the crossing angle of the colliding beams. In addition, the new quadrupole magnets will improve the focusing of the beam, reducing the $\beta^*$ parameter and enhancing collision probability. Also, the LHC Injector Upgrade (LIU) project is developed to provide the lower transverse normalized emittance $\epsilon_n$ [121].

The high instantaneous luminosity, resulting from significantly more interactions per bunch crossing, provides an enormous amount of data, although it also creates harsh conditions for the detector infrastructure. The expected pile-up number will increase from $\langle\mu\rangle \approx 34$ during LHC Run-2 to $\langle\mu\rangle \approx 200$ at the HL-LHC era.

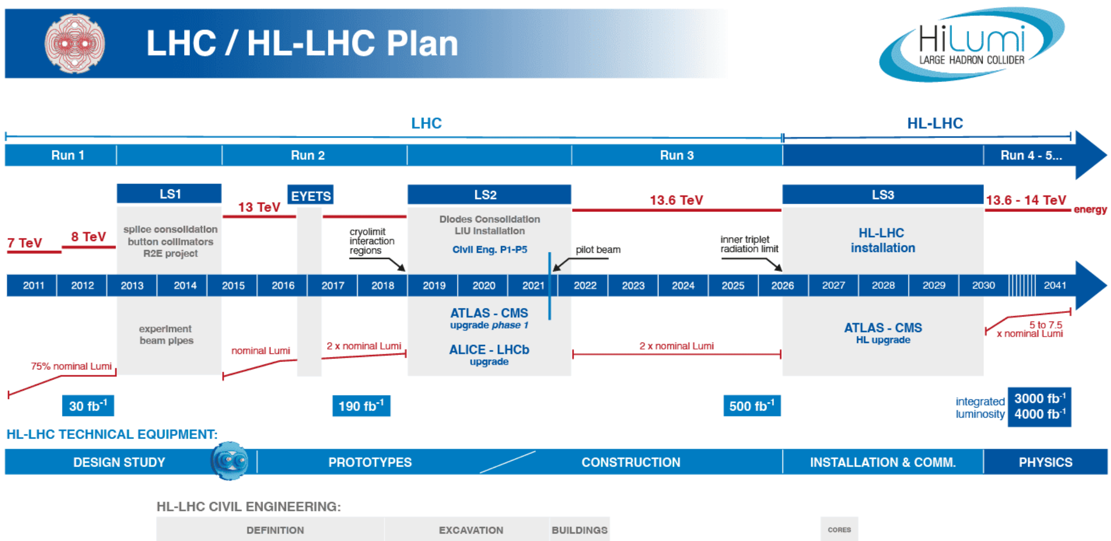


Figure 24: Schedule of the planned LHC/ HL-LHC upgrades and data-taking phases (last update January 2025) [122].

A much larger dataset offered by the HL-LHC upgrade will substantially extend the discovery potential of the LHC. It will enable the precise measurements of already known SM phenomena and will broaden the scope of the current LHC's reach in mass and coupling parameters by 20-50% across a wide range of the new physics scenarios. Furthermore, it will enhance the ability to constrain, or even reveal, novel phenomena that currently remain beyond the reach of existing datasets [124].

The main areas of physics interest at HL-LHC are as follows [124]:

- **Standard Model measurements:** Enhancing precision tests of the QCD and electroweak interactions. Also study of top-quark physics, rare vector boson processes and heavy-ion collisions in the context of quark-gluon plasma.

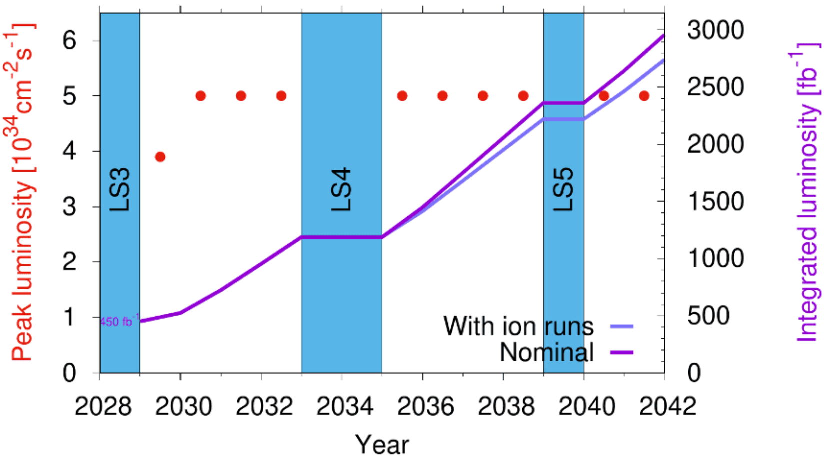


Figure 25: The expected luminosity of HL-LHC $pp$ collisions with and without ion runs out up to 2041 with the assumption of nominal peak luminosity [123].

- **Higgs Boson studies:** High-precision measurements of Higgs couplings to SM particles, testing for deviations from the SM and Higgs self-coupling through double Higgs production.

- **BSM searches:** Improving limits on supersymmetric particles (including charged Higgs boson), heavy resonances ($Z', W'$), and sensitivity to dark matter candidates (eg. WIMPs and axion-like particles).

- **Flavour physics:** Refining the measurements of rare $B$-meson decays, CP-violation, matter-antimatter asymmetry and lepton-flavor violating processes.

### 3.4.1 Phase-II Upgrade of the ATLAS Detectors

To meet the challenge of the intense HL-LHC environment, detectors must be highly granular, radiation-hard, and capable of fast response times to provide high-precision particle reconstruction and efficient background suppression under high track density conditions. The current design of the ATLAS detector could not stand such an increased luminosity. Solely in the context of the Inner Detector, the strip and pixel technology of the first layers would not be able to provide the readout bandwidth needed during the increased detector occupancy, as well as the TRT subdetector would saturate at this pile-up level. Furthermore, the radiation damage at the level of up to $2 \times 10^{16} n_e q \text{cm}^{-2}$ and a total ionizing dose of 10 MGy would be disastrous to the ID components [125].

The ATLAS Experiment plans a list of major Phase-II upgrades during LS3 phase to meet the demanding requirements of the HL-LHC. Some of these upgrades are presented below [126]:

- **The ATLAS Inner Tracker Detector:** The current ATLAS Inner Detector system will be replaced by a new all-silicon Inner Tracker (ITk) [10], which will cope with extreme radiation levels and a high tracking rate.

- **Calorimeter Electronics:** The complete replacement of the LAr detector on- and off-electronics to cope with the increased radiation levels and satisfy the trigger and readout performance criteria. Also, the Tile Calorimeter will receive new electronics for improved precision and full radial granularity requirements, enabling higher data bandwidth and improved radiation hardness.

- **Muon Systems:** Improvement of tracking and performance with lower operating voltages, as well as reduction of detector thickness. New electronics will be installed in MDTs, with small-diameter MDTs (sMDTs) replacing them in selected regions. For the RPCs and TGCs the thinner designs and upgraded readout systems are planned. Overall, the environmental impact will be reduced.

- **Trigger and Data Acquisition System:** To meet the requirements of the increased data rate at the HL-LHC, a single-level hardware trigger will be used with 1 MHz operation frequency. The Front-End Link eXchange (FELIX) board [127] design will provide detector readout at 10 $\mu$s latency and a 5 TB/s data rate. The speed of the optical links will be increased up to 25 Gb/s.

A more detailed description of the ATLAS ITk detector, particularly regarding the development work on the Detector Control System for the ITk Strip Detector, is provided in Section 4.4.

# 4 Development of Detector Control System for ATLAS Silicon Strip Detectors

The efficient and safe operation of all sub-detectors and the technical infrastructure of the ATLAS experiment is impossible without a stable and reliable Detector Control System (DCS) [8]. It is responsible for handling a wide range of essential tasks such as control of power supplies, interlock management, temperature monitoring, and real-time data logging, all of which are vital for detector longevity and its optimal performance. A well-designed DCS is crucial to ensure the high quality of collected data, as fluctuations in environmental or operational conditions can introduce systematic uncertainties. Consequently, an accurate and dependable DCS not only protects the detector components, but also provides the high-precision measurements necessary for physics analyses such as $H^+ \to \tau\nu$ described in this thesis.

This chapter is focused on the ATLAS silicon subdetectors responsible for tracking the produced charged particles - the currently working SCT detector and its successor, the ITk detector for HL-LHC upgrade. The maintenance work for the SCT detector is presented in Section 4.3, which involved the migration of SCT Environmental DCSs to a new generation of OPC UA Servers [128] based on the quasar framework [128]. In addition, drawing on the experience gained with the SCT DCS, I contributed to the development of the readout system for pre-production modules of the ITk Strip power supply system in Cracow, as described in Section 4.4.3.

## 4.1 Introduction to ATLAS DCS

As presented in Section 3.2, the ATLAS detector is composed of many individual subdetectors, each with the capability to operate independently, collectively serving a specific purpose for the integrated system. To enable their harmonious and safe operation as a whole, the DCS was created. It monitors and controls detector processes, maintains optimal operating conditions, archives operational data, and reports abnormal situations. The DCS also handles communication with external systems, including the LHC accelerator, CERN technical services, ATLAS magnets, and the Detector Safety System (DSS) [129].

The architecture of the ATLAS DCS is composed of Front-End (FE) equipment and a Back-End (BE) system, as presented in Figure 26, which are connected mainly by the industrial Controller Area Network (CAN) fieldbus [130] (a small fraction of devices is connected using Ethernet or Modbus). The FE comprises the hardware elements, including power supplies, cooling infrastructure and environmental monitoring sensors. The BE part has the hierarchical architecture of computers (or servers), with different control stations organized into a tree structure. The lowest layer, the Local Control Stations (LCS), is directly linked to the hardware layer and is responsible for transferring information about process control of subsystems to higher levels. Next, the Subdetector Control Stations (SCS) provide high-level control of each sub-detector enabling stand-alone operations. The top layer is called the Global Control Stations (GCS), which summarize data from the lower nodes and allow full ATLAS detector control by server applications and human interfaces in the ATLAS control room [8]. All the BE layers, comprising over 150 individual computer systems, are configured as distributed systems, where the industrial Supervisory Controls And Data Acquisition (SCADA) [131] programme WinCC Open Architecture (WinCC OA) [132] provided by Siemens manages the communication between the various processes over the local area network. Additionally, a connection to DAQ using DAQ to DCS Communication (DDC) is established in order to distribute information regarding power and monitoring parameters that are relevant for run control. The BE hierarchy is based on a distributed Finite State Machine (FSM) system [133] to standardize operation and error management across its components. The DCS serves as a key component of the safety framework, collaborating with interlocks and the Detector Safety System (DSS) to safeguard the detector equipment throughout the experiment's duration.

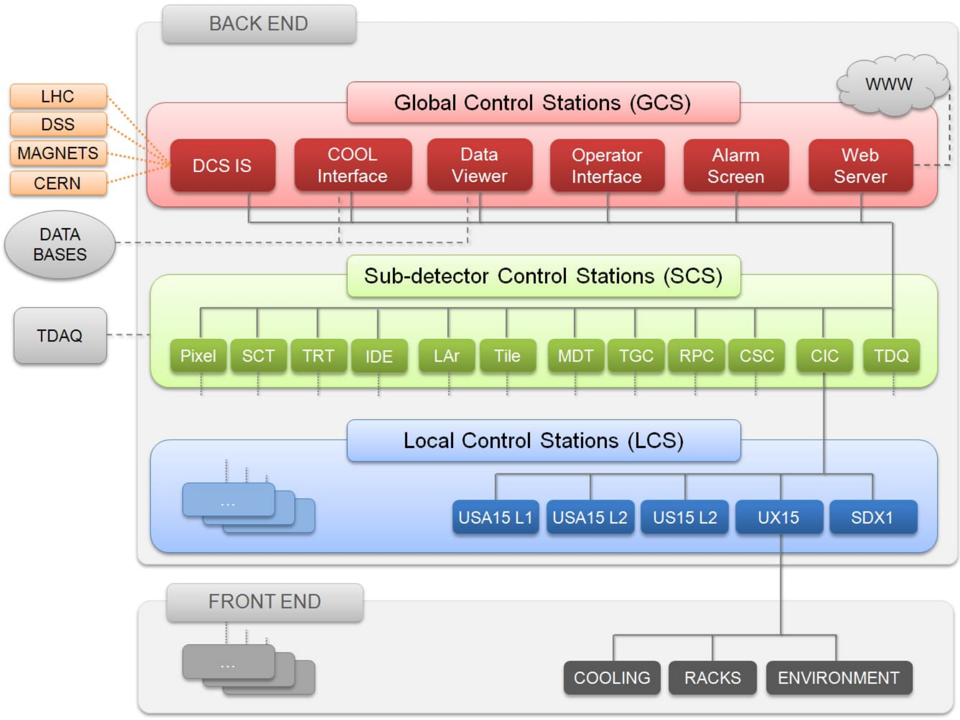


Figure 26: Scheme of the DCS architecture [8].

The primary goal in designing the control system is to ensure its roboust and stable operation from the early stages of the hardware installation up to the last days of data-taking period. Consequently, a well-designed strategy for the system's technical methods and development is crucial. Joint forces of different LHC experiments groups resulted in creating the Joint Controls Project (JCOP) [134], which goal is to find common solutions that minimize the costs and manpower needed to build and operate the experiment control systems. This helps to maintain consistency and expertise across the entire experiment lifetime.

### 4.1.1 Front-End Components of the ATLAS Detector

The DCS FE hardware must meet a set of requirements - low power consumption, high density of I/O channels and minimal overall cost. Also due to the harsh collision environment, the detector electronics must be capable of remote firmware updates, resistant to magnetic fields, and able to withstand the substantial radiation doses anticipated throughout the detector's operational lifetime.

**CAN protocol:** The DCS employs the CAN fieldbus with the CANopen protocol, allowing up to 127 nodes to be connected on a single CANbus, wherever appropriate. Its main advantages are low cost, flexibility, and immunity to strong magnetic fields, unlike Ethernet. CAN is commonly used for controlling power supplies, monitoring environmental conditions such as humidity and temperature, as well as configuring and supervising FE electronics. This makes CAN a reliable choice for operations in the magnetically intense environment of the ATLAS detector.

**ELMB:** The ATLAS DCS is mainly based on custom design devices often integrated through the use of the Embedded Local Monitoring Board (ELMB) [135]. It was developed in order to reduce duplicative research, development, and maintenance efforts, as no commercial solution satisfied all the required specifications. The ELMB serves as a general-purpose plug-on I/O module based on the CAN bus interface, which has 24 digital and 64 analog channels, along with an 8-bit 4 MHz microcontroller, providing analog signal reading (for instance voltage, temperature sensors) and digital input/output control. These modules connect the sensors and/or electronics with higher layers of DCS architecture and are radiation resistant to up to 50 Gy of integrated doses. The overall number of ELMB devices used in the ATLAS DCS is over 5000 [8].

**Standardized commercial systems:** The ATLAS DCS relies also on standardized commercial systems to reduce the manpower needed for development and maintenance. The VME crates are employed to house electronics in shielded areas and ensure monitoring and control features. CAN-based power supply units (PSUs) distribute power to ELMBs, with per-bus monitoring and switching. A modular power system addresses the different power needs of detector electronics. It places control units in safe zones and power modules near the detector, using radiation-tolerant components. Industrial control PCs with remote management are used at various system levels.

### 4.1.2 Back-End Components of the ATLAS Detector

The role of the BE components is to complement the FE hardware by managing the logic and control software, providing supervision and interfacing with users and other systems. The BE system employs industrial, rack-mounted server machines. Two distinct standard configurations are employed: one optimized for applications demanding robust I/O capabilities and another for processing-intensive tasks with Ethernet I/O connectivity. Both models have redundant, hot-swappable power supplies and disk shadowing [8].

**WinCC OA:** Given the specific conditions of the large HEP experiments such as ATLAS, where the DCS must read and process data from over 200,000 sensors, a scalable and flexible solution was required. As a pillar of the ATLAS BE applications the commercial SCADA package, WinCC OA supervisory control software toolkit, was chosen to handle the distributed computing and diverse control application tasks. WinCC OA is a modular SCADA system, which provides visualization and processes control across various industries. Its distributed architecture, as presented in Figure 27, is built from components called “Managers” communicating via a platform-independent protocol over TCP/IP. At the lowest layer, Driver Managers connect to hardware using standard protocols. Communication between different managers, user authorization, as well as message distribution is managed by the Event Manager. The Database Manager is responsible for handling the runtime database, alarms, and parameter archiving, with support for local or Oracle databases. Control Managers (scripts) or API Managers (compiled code) enable running the custom logic by users. The top-level UI layer offers graphical tools for configuration and visualization. Its versatile design provides a range of possible architectural arrangements, from standalone to fully distributed and redundant configurations. WinCC OA is a SCADA tool used to build control systems, rather than an autonomous control system itself.

**CANopen OPC-UA:** The Open Platform Communications Unified Architecture (henceforth OPC-UA) standard, developed by the OPC Foundation and standardized as IEC 62541 [136], is a comprehensive, secure, and adaptable framework for machine-to-machine data exchange, which is well-suited for the ATLAS DCS. It supports customizable data models, various communication methods, and multiple data formats (binary or XML),

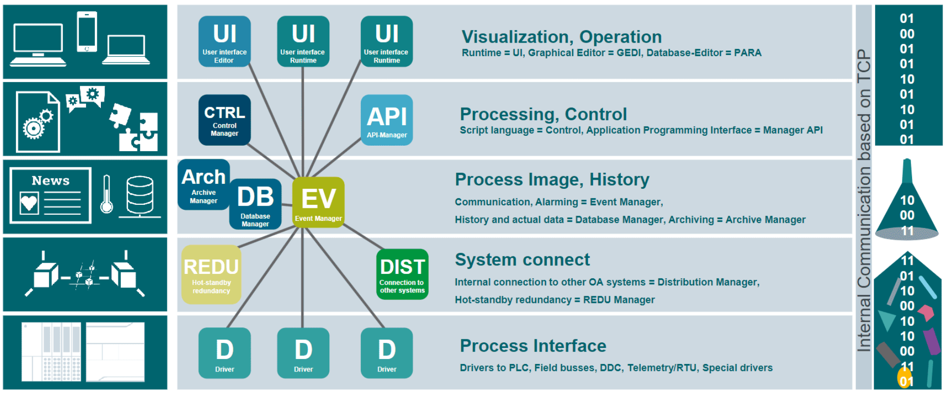


Figure 27: Scheme of the WinCC OA system composed of function-specific units called managers [132].

as well as provides firewall-friendly and secure design [137]. The ATLAS DCS uses the CANopen protocol for data transmission, which provides support for different communication modes and supervision of both the bus and connected devices. The server processes multiplexed messages, such as those originating from the ELMBs, and converts them into individual data objects that are compatible with the WinCC OA software. The OPC UA toolkits are available across a variety of programming languages and OS platforms.

**JCOP Framework:** The CERN community developed the JCOP framework in order to unify and simplify control system development across LHC experiments. This framework offers a set of standard tools and components designed to integrate seamlessly with the WinCC OA package. It enables communication protocols, data storage, and control of common devices like PLCs, ELMBs, and power crates (CAEN, Wiener). The framework enhances the capabilities of the WinCC OA system through additional tools like configuration databases and a centralized installation mechanism. Each component consists of configuration files, libraries and interface panels, which can be added or removed as needed. The framework, developed collaboratively by the JCOP team and experiment-specific teams, also helps to implement and standardize practices across the LHC community, including naming conventions and visual coding, across the control systems. This minimizes the effort required for development and maintenance tasks.

### 4.1.3 Operations

The crucial role of the ATLAS DCS is to ensure the safe operations of the detector with a limited number of shift crew, which involves maintaining well-defined operational states and rapidly recognizing and responding to any errors. The DCS is a complex system with several hundred thousand parameters (corresponding to power, cooling, temperature etc.) to be managed, thus a hierarchical FSM model provided by the JCOP framework was employed. The DCS components, encompassing both physical hardware and logical groupings, are depicted as FSM nodes with pre-defined states and commands. The FSM architecture has three distinct unit classifications: control units for handling operations, logical units for organizing groupings and device units for managing hardware components. The status information is propagated upwardly through the hierarchical structure, while directives are transmitted in a downward direction from control to device units. This hierarchical FSM framework facilitates the centralized control of the entire ATLAS detector, thereby simplifying operational tasks for the shift personnel. The FSM differentiates between a state, which denotes the system's current activity (for instance READY, STANDBY, SHUTDOWN), and a status, which reflects the system's performance (OK, WARNING, ERROR, FATAL). The status of each element is connected to the active alarm conditions, which can be suppressed to prevent an overwhelming display interface. Each FSM element holds a status indicator that presents the most critical active alarm, as well as transmits it upward through the hierarchy for a fast error identification. Although sub-detectors may use their own internal state configurations, they are ultimately obliged to adjust to the standards of the ATLAS community. Additionally, the JCOP framework requires the implementation of consistent color coding and visual indicators, which helps to promote safe and straightforward operation during active physics data-taking periods. An example of ATLAS DCS user interface during a regular LHC fill operation is shown in Figure 28. Automatic procedures are implemented wherever possible to mitigate the risk of operational errors, such as maintaining the detector subsystems in a secure state during LHC physics runs. DIM-based protocol is used for communication with external systems through dedicated DCS Information Servers, which contain built-in mechanisms to monitor data integrity across multiple providers [138].

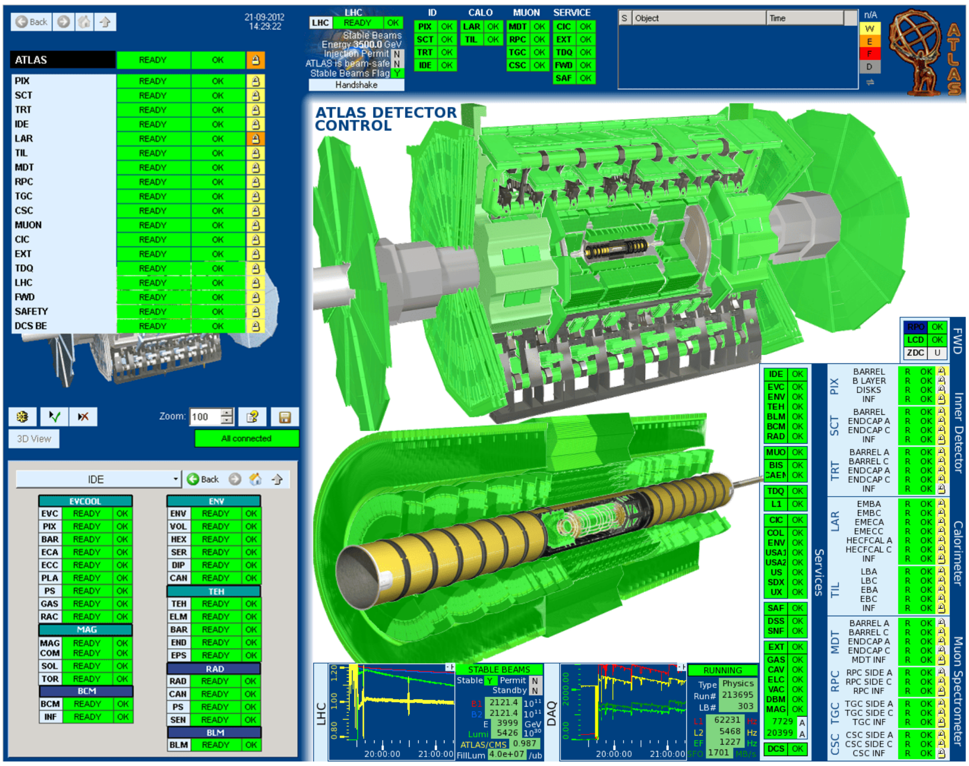


Figure 28: The overview of the DCS user interface (FSM Screen) during a standard LHC fill operation [138].

## 4.2 The SemiConductor Tracker DCS

The main goal of the ATLAS SCT DCS is to ensure safe control and monitoring of the power and control signals transmitted to the detector modules. This guarantees a rapid response to any malfunctions in the SCT system (as described in Section 3.2.2) through the implementation of software and hardware interlocks. The SCT DCS operates in co-ordination with the overall ATLAS DCS and the SCT DAQ system by managing system states and reporting errors. It is divided into two functional blocks: one focused on power supply control, and another responsible for environmental monitoring, providing tracking of temperature, humidity, and dew point measurements [139].

The SCT Power Supply (PS) system is the core of the SCT DCS, providing power supply and configuration to the detector modules. It delivers two voltage levels - the high voltage (HV, 150–480 V) for sensor depletion and low voltage (LV) for the readout electronics, including powering and reading out temperature sensors. The modules have independent HV and LV channels, with automated firmware interlocks to disable power in case of hybrid temperatures above a specified limit with built-in firmware interlocks automatically cut power if temperatures rise above a specified limit (38°C). The system consists of 88 individual crates, with each crate containing HV and LV cards that are supervised by a Crate Controller (CC) unit built around an ELMB128 module. This CC facilitates communication with the DCS via the CAN bus protocol. The SCT Interlock Card (SIC) manages the hardware interlocks. For performance optimization, the crates are organized into 16 CAN bus branches, with each pair of branches monitored by a dedicated computer. The PS system is governed by the Monitor Power Supply Detector Control System (MoPS) project, which allows for optional integration with the DAQ via the DDC protocol. This organization is achieved through a mapping of the detector's topological layout to the underlying hardware configuration [139].

The SCT Environmental (Envr) DCS monitors and protects the detector against thermal shocks and condensation, which are critical due to its operation in a controlled nitrogen environment and the use of $C_3F_8$ evaporative cooling. The system employs a sensor array comprising over 1000 devices, mainly Negative Temperature Coefficient (NTC) thermistors and two types of humidity probes (radiation-hard Xeritron and more precise Honeywell), distributed throughout the detector volume to maintain safe operating conditions. The sensor signals are channeled through patch panels and directed into Building Block Interlock Monitoring (BBIM) crates. Each crate is equipped with at least one BBIM unit, a power distribution board, and an ELMB. The BBIM unit has a backplane connected to Sensor Bias cards and IBOXes, with the ELMB handling data readout. Ultimately, the sensor data are digitized by the ELMB and transmitted via the CAN bus to the OPC server, where the raw measurements are converted into temperature and relative humidity values through the application of calibration functions. The Envr DCS software, running on PCs in the ATLAS service caverns (US15 and USA15), maps sensor channels to detector locations and displays the data, which include calculated dew points, for monitoring and interlock purposes.

The aim of the SCT interlock system is to protect the SCT silicon modules from thermal damage arising from cooling system failures. It is a hardware-based safety mechanism, which uses temperature sensors positioned at the cooling pipe outlets, with each sensor overseeing multiple detector modules. The temperature sensors are read by ELMB boards and IBOX comparators. If the temperature exceeds a predetermined threshold, the IBOX triggers an interlock immediately. Next, the signal is transmitted through a configurable Interlock Matrix (IMatrix), which locates it with the appropriate power supply channels and then forwards to the SCT Interlock Card the command to cutoff the power supply. Additionally, the system safeguards against optical readout laser hazards and integrates with the DSS [140].

### 4.3 CanOPC UA Server Migration for Environmental SCT DCS

Regularly updating the DCS software is crucial to maintain compatibility with new hardware, enhance reliability in control and configuration, and reduce maintenance workload needed through modern frameworks. During the two decades of operation, certain components have undergone significant replacements and/or upgrades to modern technologies appearing in the field. For instance, CAN bus peripheral interfaces were updated along with host machines and their software, as necessary. In 2021, the new generation of CANopen OPC UA servers was introduced.

The initial CANopen OPC UA server implementation was introduced in 2012 as the first OPC UA project like that at CERN, preceding the availability of frameworks like the quasar framework. This kind of framework significantly lowers the cost of developing and maintaining OPC-UA servers through model-driven code generation and the utilization of shared, OPC-UA-specific code. The quasar framework, introduced in 2014, has become a widely employed platform at CERN for constructing efficient OPC UA-based components. The migration of the CANopen OPC-UA server to quasar brings a number of benefits, the most notable being a simplified development process and the ability for non-expert personnel to perform maintenance work [141].

To create a device-specific OPC-UA server, the process begins with developing an XML design file. This file describes an object-oriented information model adjusted to the target device, such as an ELMB. Next, the framework uses this model to generate an executable OPC-UA server, which presents a standardized interface to access device data like parameters (temperatures, voltages, etc.) status, and controls (e.g. reset functions). The server is connected to WinCC OA by the built-in OPC UA client driver, which enables a mapping between the OPC UA nodes and the internal datapoints within the SCADA system. As a result, the WinCC OA system can directly monitor and control hardware devices, such as ELMBs, through the OPC UA server. Switching to the CANopen OPC-UA servers with the quasar framework provides better modularity and maintainability, as compared to previous manual XML configurations.

The goal of the study was the migration of two Enviroment SCT DCS projects - ATLSCTUSAENV located in the service cavern USA15 and ATLSCTUSENV located in US15 - to the quasar-based Next Generation (NG) CANopen OPC UA servers, which required an additional adjustments. The key differences between the standard and the NG CANopen OPC-UA servers were changes in the architecture of their server configuration files. The hierarchy is generally maintained, but the elements' names and attributes semantics have changed (eg. ITEM → CalculatedVariable). Also, the NG CANopen OPC UA server introduces a concept to modularize the description of types of CANopen device models. The initial approach used ELMB node types, which are XML-based representations of the CANopen model for a device. These node types specify the Service Data Objects (SDOs) used for configuration and diagnostics (their data types and the corresponding names in the OPC-UA address space), in addition to the mapping of Process Data Objects (PDOs), which provide rapid, real-time data exchange between devices on the CAN network. This solution, which assigned a single node type to each device, was initially functional but ultimately lacked flexibility. Extending the node types to support new hardware features or making small adjustments often resulted in inconsistencies. This happened when the base node types were updated, but the derived versions were not. The new idea was applied using XML tools like entity references to build node descriptions in a modular way. As a result, one can reuse and extend basic configurations without repeating or duplicating them in a more reliable and easier way.

For a standard ATLAS DCS project the migration was done by the delivered quasar tools. In the case of the ATLSCTUSAENV and ATLSCTUSENV projects, an expert migration was needed due to its specific node types and solution introduced earlier. Table 7 presents the number of used nodes, items and node types per each project.

Table 7: CAN nodes overview in the ATLAS experiment [141].

| **Project** | **node_types** | **#buses** | **#nodes** | **#items** |
|---|---|---|---|---|
| ATLSCTUSAENV | ELMB, SCT_PPM | 4 | 44 | 1437 |
| ATLSCTUSENV | ELMB, SCT_PPM | 4 | 31 | 876 |

The required work for migration to the NG CANopen OPC-UA servers involved:

1. Adjusting the NG CANopen OPC-UA server configuration file structure to new element names and attributes semantics.

2. Updating the list of standard PDO models used for the new “modularize” node types in the NG CANopen OPC UA server configuration file. Each standard model corresponds to a specific functionality, such as digital or analog inputs and outputs.

3. Both OPC UA server configuration files contained additional parameters defined in the XML structure but not represented as datapoints within the WinCC OA project. One such parameter, BOn, is used in the SCT Environmental DCS system as a global flag indicating the operational status of the ATLAS central solenoid magnet. This flag receives input from the DCS Magnet system connected via the GCSs and is set to 1 when the solenoid is in an operational state, and 0 when the magnet is turned off. Within the humidity sensor calibration formulas, BOn is used to conditionally apply correction factors that account for changes in sensor response or environmental conditions influenced by the presence of the magnetic field. In the updated configuration, intermediate OPC entries (previously used to hold corrected values but not associated with dedicated datapoints in WinCC OA) have been removed and replaced with direct correction formula expressions. The BOn variable is now implemented as a dedicated global datapoint.

4. Validation of the NG CANopen OPC-UA servers, ensuring full compatibility and functional equivalence during SCT operations.

5. The new server configuration files were archived on the GitLab server dedicated to the ATLAS SCT DCS projects.

## 4.4 Particle Tracking in ATLAS Detector for HL-LHC

Simultaneously with maintaining and developing the SCT DCS system, work on the new Tracking Detector for the HL-LHC upgrade is also ongoing. The existing ATLAS Inner Detector will be succeeded by a novel all-silicon Inner Tracker, for which the new detector hardware and the associated DCS will be developed. The new detector is anticipated to be commissioned between 2028 and 2030, and the projected duration of the experiment is approximately 15 years from the point of initial deployment. This section provides an overview of the power supply for ATLAS ITk Strip Detector and my contribution to user interface development for ITk Strips Service Tests in Cracow.

### 4.4.1 Overview of ITk Detector

The design of the ATLAS ITk detector must incorporate the technologies fulfilling the requirements of the harsh HL-LHC environment, including enhanced granularity, radiation resistance, readout speed, and minimized material budget. It enables the detector to maintain or surpass the performance of the current tracking system.

The ITk architecture has a multi-layered design: five pixel detector layers located near the IP and an additional four layers of strip detectors situated at larger radial distances. It uses a total of over 27,000 individual detector modules, representing a significant increase of nearly five times the previous ATLAS ID configuration. The ITk detector will have a substantially larger coverage area, 180 $m^2$ compared to the current 63 $m^2$, and incorporate a greatly increased number of readout channels - over 5 billion in contrast to the 100 million channels in the current detector. The solutions incorporated in the ITk design enables to lower the required cost of detector materials despite its larger scale and increased complexity. These changes included innovations in cooling systems (evaporative $CO_2$ cooling with titanium pipes), the usage of lightweight carbon supports, and the implementation of advanced power schemes such as DC/DC conversion and serial powering [10].

The hardware modifications necessitate a corresponding advancement in the associated DCS. Apart from the more sophisticated power distribution architectures, the new ATLAS ITk DCS is required to implement a higher number of high-precision environmental monitoring sensors, for instance, voltage/current, humidity or temperature measurements.

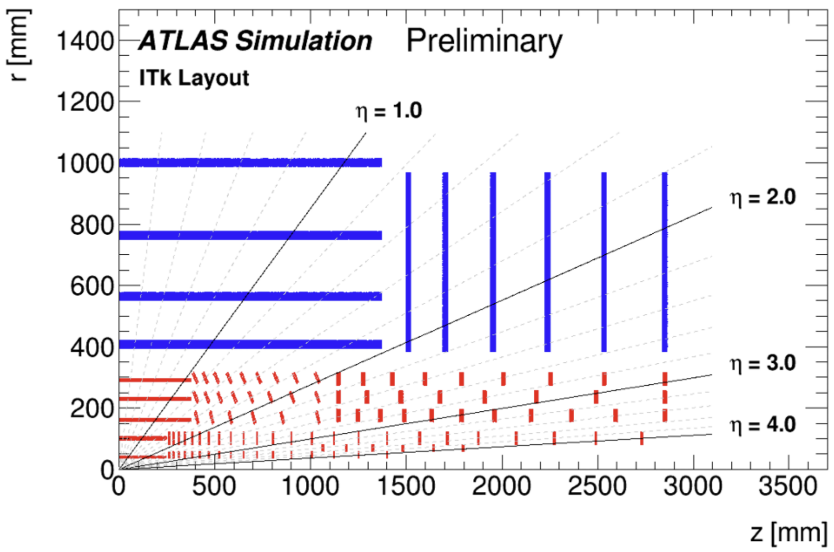


Figure 29: The schematic view of one quadrant of the ATLAS ITk detector. The ITk pixel part is represented by the red color, while the ITk strip detector is depicted by blue components [142].

### 4.4.2 The Power Supply System of ITk Strips

The ITk strip detector [143] is composed of a barrel section and two end-cap regions, with detector modules installed on both sides of the carbon-fiber local support structures ("staves" for the barrel part and "petals" in the end-caps). The various modules that compose the ITk strip detector employ a hierarchical assembly process. Each module consists of one or two hybrid circuits, a silicon sensor, as well as one power board. To fit the different spatial locations within the detector, a total of eight different module types have been designed: two for the barrel section (corresponding to the short stave (SS) and long stave (LS) geometries) and six distinct types optimized for the varying geometries of the end-cap petals (EP).

The ITk Strips detector has a staged power distribution architecture, which is presented in Figure 30. The power is provided by 48 V low-voltage (LV) and 550 V high-voltage (HV) supplies situated in the US15 and USA15 service caverns. The LV is subsequently stepped down to 11 V utilizing custom DC/DC converters installed in the Patch Panel 2 (PP2) regions, with the aim of minimizing power dissipation. In the case of silicon sensors, the HV is directly provided, as the current carried is low. The system utilizes HV multiplexing to divide the HV lines at PP2 in a 1-to-2 ratio for the outer staves and petals, thereby optimizing the use of power supplies. There are two primary DCS components: commercial LV and HV power supplies and active patch panels equipped with DC/DC converters located at PP2.

The LV and HV power supplies are remotely controlled and monitored through the

DCS. If any issues arise, a safety interlock system, integrated with the SCADA monitoring system, will automatically shut down all power channels to protect the detector.

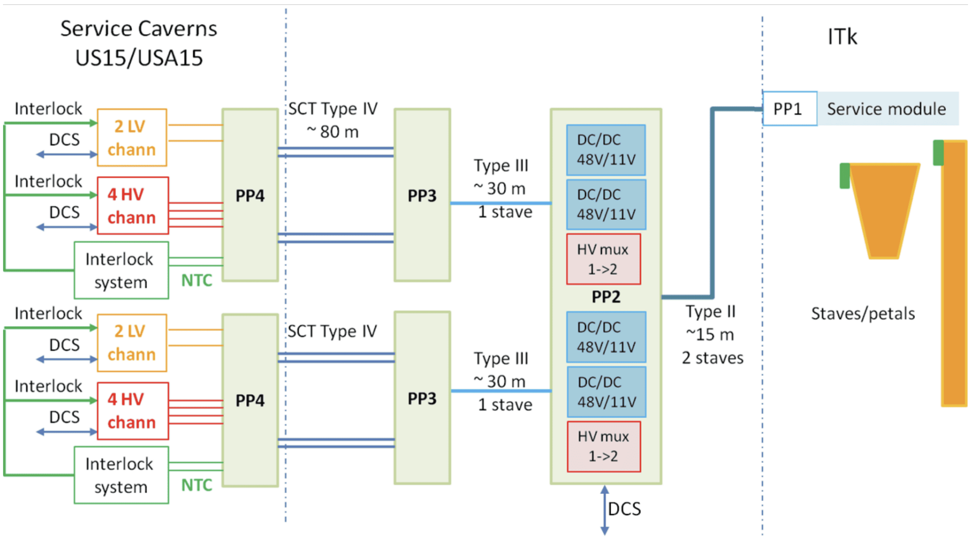


Figure 30: Architecture of the ITk Strips power chain. PP4 and PP3 are passive patch panels; PP2 is an active patch panel with DC/DC converters, located inside the ATLAS detector. The vertical, dashed blue lines represent the boundaries of the service caverns and the ITk respectively [144].

The PP2 subsystem is responsible for distributing the LV power across the ITk Strip detector. This distribution employs custom DC/DC conversion boards (from 48 V to 11 V) and monitoring components (AMACStar chips [145]) that are designed to operate reliably in the presence of higher radiation and magnetic fields [146]. Its modular architecture includes custom frames with a crate controller, embedded cooling plates, and insertable DC/DC boards with two or four output channels. In addition, each DC/DC board provides hardware protection against overcurrent and overvoltage, correction circuitry to mitigate voltage drops along the cabling, and control and monitoring capabilities facilitated by the AMACStar chip. The PP2 DC/DC boards come in two variants - one designed for the short strip staves in the barrel region (SS PP2) and another for the long strip staves in the barrel (LS PP2) and the end-cap petals (EC PP2). The key distinctions between the two board types are their maximum output power capacity and the HV lines distribution. The specifications for these two PP2 DC/DC board variants are shown in Table 8.

Table 8: Comparison of SS PP2 and LS/EC PP2 power parameters.

| **Parameter** | **SS PP2** | **LS/EC PP2** |
|---|---|---|
| N. of channels | 2 | 4 |
| Input voltage $V_{\text{in}}$ | 48 V | 48 V |
| Input current $I_{\text{in}}$ | 4.5 A | 2.5 A |
| Output voltage $V_{\text{out}}$ | 11 V | 11 V |
| Maximum Output current | 10 A | 5 A |
| Conversion efficiency | 85% | 85% |

The simplified view of the PP2 crate with its dimensions is shown in Figure 31. The crate backplane provides the distribution of input and output signals for the DC/DC boards, as well as facilitating e-links communication between the AMACstar chips on the DC/DC channels and the Crate Controller. The Type III cable supplies the 48V input voltage, while the Type II cable delivers the output voltage to the detector. Both cables are connected to the backplane. Different types of cables are designed for various stages of the power and data transmission chain, spanning from the radiation-hard, low-mass connections at the detector modules (Type I), through intermediate routing (Type II), to the long-distance links connecting to off-detector electronics (Type III). The top and bottom crates equipped with cooling plates, optimized for the $C_6F_14$ coolant, remove the additional heat produced by the PP2 electronics.

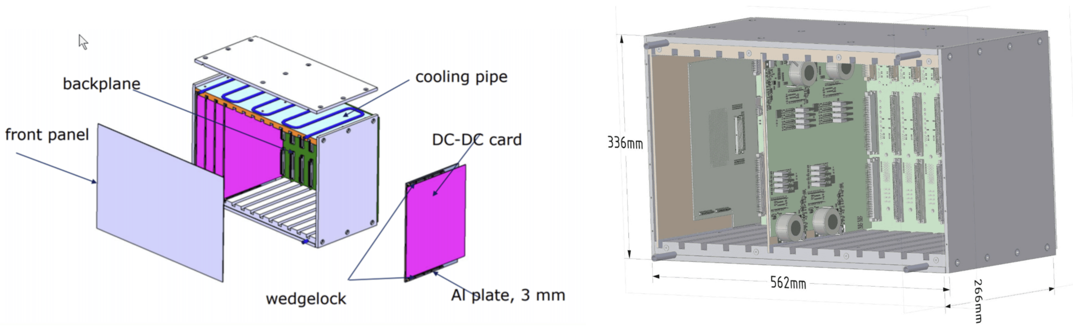


(a) (b)

Figure 31: The simplified view of the PP2 crate (a) with its dimensions (b) [146].

The Crate Controller board, located in the first slot of the crate, is responsible for the monitoring and control of the PP2 DC/DC boards. As the HL-LHC environment puts the demanding requirements for the ATLAS DCS, novel radiation-tolerant interface solutions have been developed for the on-detector FE components: the Embedded Monitoring and Control Interface (EMCI) and the Embedded Monitoring Processor (EMP) boards [147]. The EMCI board serves as the FE interface component, operating close to the detector and transferring slow control data between several FE electronics and the experiment's control system. It is based on the low-power Gigabit Transceiver (lpGBT) [148], which handles configuration, monitoring, and control via its Internal Control (IC) channel. The lpGBT employs custom communication protocols through these e-link interfaces, while the standard lpGBT FPGA IP core is implemented in the programmable logic of the Zynq system-on-chip device [149]. The EMP module, constructed using the TE0807 MPSoC Modules from Trenz Electronic [150], operates in the non-radiation region. It functions as the central processing and routing hub, which can connect up to 12 EMCI devices in a star topology via optical links. It facilitates communication via Ethernet between the SCADA system and the DCS monitoring and control network, functioning as the central infrastructure supporting this interface. The EMP operates the OPC UA server application, providing the data exchange between the hardware and the supervisory layer of the PP2 DCS. As for the current ATLAS ID DCS, the ATLAS ITk Strip DCS is implemented within the WinCC OA framework, which provides a native OPC UA client interface for seamless communication. The new EMCI-EMP system dramatically boosts communication capabilities, providing data transmission rates up to 320 Mbps (the previous standard used for SCT supported 500 kbps). This architecture solution is modular and scalable, thereby improving the reliability, flexibility, and speed of the communication system [151].

The diagram of the ATLAS ITk Strip DCS is shown in Figure 32.

### 4.4.3 Development of Readout System for Pre-Production of PP2 Cracow

The general process of designing and commissioning a new detector in HEP experiments has several phases. It starts with the conceptual design and R&D work, which sets performance

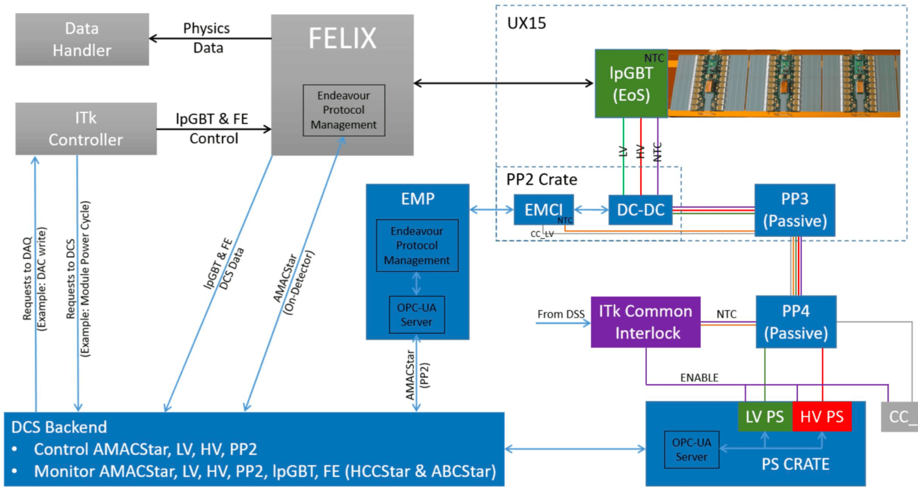


Figure 32: Scheme of the ATLAS ITk Strip DCS [144].

requirements and evaluates the available technology options during small-scale tests. Then, the prototyping and pre-production phase takes place, during which a limited amount of prototype modules are produced and validated in multiple tests concerning the design's properties and final specifications. When everything is ready, the large-scale production of all detector components begins. During system integration, the smaller structures are integrated into the full system and validation of the detector's functionality is performed.

At the time of writing this thesis, the ATLAS ITk detector was in the pre-production phase. This stage plays a crucial role, as the bridge between prototyping and full-scale series production. Each detector component in the final or near-final version is extensively tested on every hand to uncover potential design flaws, making sure the planned manufacturing chains fulfill the set criteria, and provide effective and consistent series production through final documentation and recommendations.

One of the laboratory system tests for the PP2 crate prototype is located in Cracow. As only one crate is used, the cooling system in the test bench employs an industrial water chiller. The overall estimated cooling capacity required for the fully loaded PP2 crate of 48 channels is around 1 kW. For the power supply, an external 48V power generator is employed. Until now, many tests of prototype DC/DC converter modules have been conducted, including characteristics such as the power conversion efficiency and noise [146].

Another phase of the PP2 prototype testing concerns the monitoring and control systems, which are implemented by the Crate Controller on the EMCI board in the first crate slot. Currently, for the Cracow lab test system, the readout chain is based on the prototype EMP board, possessing a reduced number of lpGBT links with 2 SFP+ connectors present (one of them is used for communication with AMACStar chips in the PP2 crate). The scheme and pictures of the test bench of the prototype PP2 system readout in Cracow are presented in Figure 33 and Figure 34, respectively.

The goal of the project was to prepare a DCS readout system for pre-production phase of PP2. The BE software components are the same as for the SCT DCS - the SCADA WinCC OA system, CANopen OPC UA server and JCOP Framework. Firstly, the EMP was configured to launch the AMACStar chip OPC server, which is connected to the WinCC OA monitoring project via OPC UA Client Subscription. This project reflects the architecture of the DC/DC card and provides a tool to control its functionality. The OPC UA server configuration file was adjusted to connect the currently working test bench with the WinCC OA project. The WinCC OA panel has been created, which monitors AMACStar chip parameters (such as temperature, incoming/outcoming voltage, current,

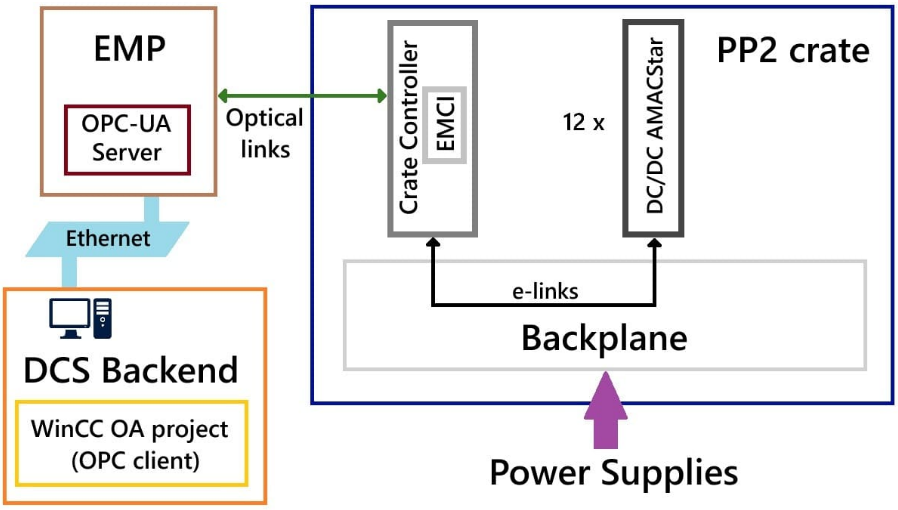


Figure 33: Scheme of the PP2 DCS [152].

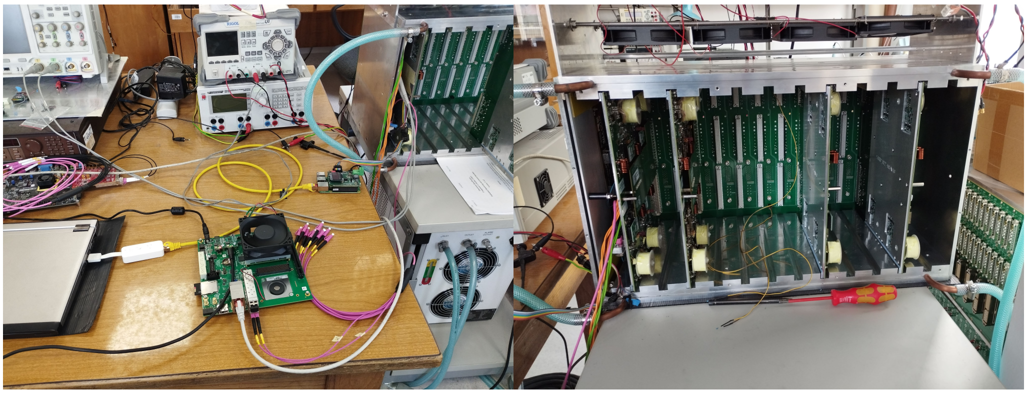

(a) (b)

Figure 34: Test bench of the EMP (a) with the PP2 prototype (b).

and communication status) for each channel in the low-power cards. It also enables to turn on/off the power to a certain detector component.

To enable effective tests of the ITk Strip modules, the monitored parameters are archived using InfluxDB [153], which represents the NextGenArchive (NGA) group of archiving solutions for WinCC OA. Compared to the standard archiving uses (employing internal databases like RAIMA or SQLite), InfluxDB is more suitable for complex systems like those used in the HL-LHC by offering significantly enhanced performance and scalability. In addition NGA archiving is compatible with tools like Grafana [154], which provides flexible, real-time visualization and analysis. It is beneficial during the pre-production stage, where comprehensive monitoring and timely feedback are crucial for validating the reliability of prototype components and verifying that all systems meet design specifications before starting the full-scale production. As part of the work, dedicated Grafana dashboards were developed to monitor the key output parameters of the AMACStar chip and DC/DC converters. Two panels were created: one showing input and output voltages ($V_{in}$, $V_{out}$) and the other focused on output current ($I_{out}$). These plots clearly illustrate the transition behavior of the low-power system - specifically, a voltage step-down from 48 V to approximately 11 V when the DC-DC converter is enabled, and a corresponding increase in output current from 0 A to around 4.5 A. These visualizations provide valuable insight into the operational dynamics of the PP2 readout system and support the qualification of modules under realistic powering conditions. The examples of the two Grafana panels for a specific AMACstar chip used during these tests are presented in Figure 35 and Figure 36.


Figure 35: Grafana panel providing monitoring of the input/output voltage for a specific AMACstar chip before and after enabling the DC/DC converter.

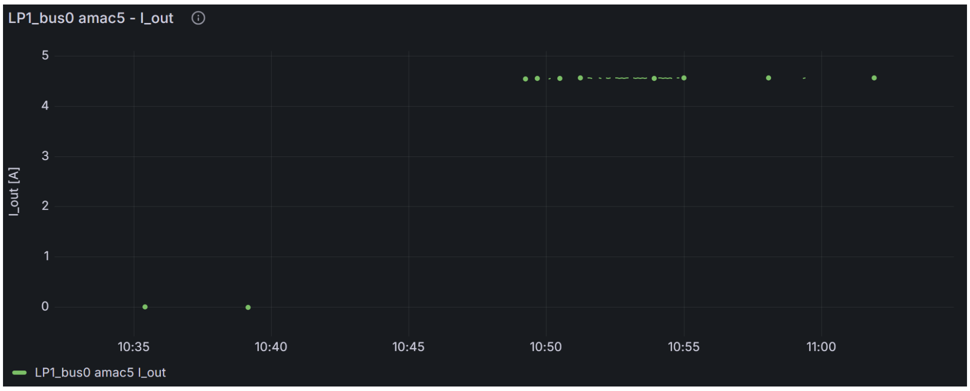


Figure 36: Grafana panel providing monitoring of the output current for a specific AMACstar chip before and after enabling the DC/DC converter.

## 4.5 Summary

Constant maintenance and development of the DCS is crucial for the safe, reliable, and efficient operation of the ATLAS detector under the challenging conditions of the LHC environment. This chapter presented the migration work for the environmental part of the SCT DCS implemented new solutions offered by the quasar-based OPC UA Servers, which reduce maintenance effort and make the system more accessible to new developers. In addition, updated software provides enhanced security, scalability, and readiness.

Over a decade of the experience gathered during ATLAS detector operations, including the SCT detector, is now being applied to develop the DCS for the planned HL-LHC upgrade, when the Inner Detector will be replaced with the ITk detector. The second part of the chapter focused on developing and commissioning of the readout and monitoring system for the ITk Strip detector's pre-production PP2 prototype, tested in Cracow. The system was configured using WinCC OA, OPC UA, and InfluxDB to enable real-time monitoring of AMACStar chips and DC/DC converters under realistic conditions. Customized Grafana dashboards were implemented to visualize voltage and current behavior, ensuring system readiness and reliability before the start of full-scale production.

# 5 Validation of $\tau$ Lepton Properties in Monte Carlo Event Generators

The $\tau$ lepton is a vital component in the rich ATLAS physics programme. It provides unique tools for probing the SM Higgs boson properties and serves as an important element of searches for new physics phenomena at the LHC at CERN, especially when the limit of *pp* collision energy is getting higher and higher with each hardware improvement.

The foundation of these analyses relies on the MC-based estimation of signal and background processes with $\tau$ leptons in the final states. Therefore, it is necessary to obtain an accurate prediction with sufficient statistical precision across a broad phase space. The $\tau$ lepton possesses intriguing phenomenological observables, such as polarization and spin correlations, which are highly effective in separating signal from background or investigating the properties of particles that decay into $\tau$ leptons.

The goal of the following study was to validate the properties of $\tau$ lepton decays in event generators and in the simulation used in ATLAS physics analyses in a single electroweak vector boson ($Z \to \tau\tau$) processes. Studies were carried out at the truth level to avoid any bias from $\tau$ reconstruction using the TauAnalysisTools package [155] or the Rivet (Robust Independent Validation of Experiment and Theory) toolkit [156]. Validation of kinematic distributions sensitive to $\tau$ polarization and spin correlations was performed, as well as the branching ratios of the various decay modes were checked. The reconstruction of $\tau$ RNN input variables compared to the previous BDT version, as well as the treatment of *b*-hadrons and $\tau$ leptons as quasi-stable particles in the Geant4 simulation, were investigated.

## 5.1 Introduction to Monte Carlo Generators in HEP Experiments

The composite inner structure of hadron particles leads to highly complex final states after beam crossing at hadronic colliders, requiring an immensely complicated description. The initial state is undefined, like center-of-mass energy and which types of particles collide. Every hadron-hadron collision usually produces hundreds of particles of various momentum scales, which may be part of the SM or some other framework beyond. The presence of the QCD processes also introduces the problem of running strong coupling depending on the energy scale. Calculating the relevant matrix elements grows in complexity with each order of approximation of the perturbation theory, not to mention the many remaining divergences and near-divergences. In the end, integration of them over the complex final-state phase space is necessary to generate predictions of accessible observables in the experimental data [157].

Keeping this challenge in mind, the Monte Carlo integration remains the only practical solution. Monte Carlo event generators have advanced significantly over the past several decades and are a fundamental computational component in HEP experiments [157]. Especially for the the LHC experiments, they are a vital part of the data processing and analysis pipeline, while consuming substantial computational resources across the Worldwide LHC Computing Grid [158].

One can use the MC generators for several purposes like simulation of a broad spectrum of the most interesting processes in order to perform precise measurements of SM parameters or to search for a new physics signal from the SM processes' background. Furthermore, they are extremely valuable during the design phase of new experiments and enable constant improvement of reconstruction or selection algorithms within a working experiment.

One of the most famous examples that presents the crucial role of the MC predictions in the HEP experiments is the discovery of the Higgs boson by ATLAS and CMS Experiments in 2012. Figure 37 shows the invariant mass distribution of the 4 lepton decay products from the investigated decay channel $H \to Z \to 4\ell$ by the ATLAS Experiment using both

$\sqrt{s}$ = 7 TeV and $\sqrt{s}$ = 8 TeV datasets (black dots), and the MC predictions (red, violet and blue histograms) that are compared with experimental data. A small blue bump near the mass of 125 GeV corresponding to the SM Higgs boson would be irrecognizable from the background processes without the high precision of the MC generators.

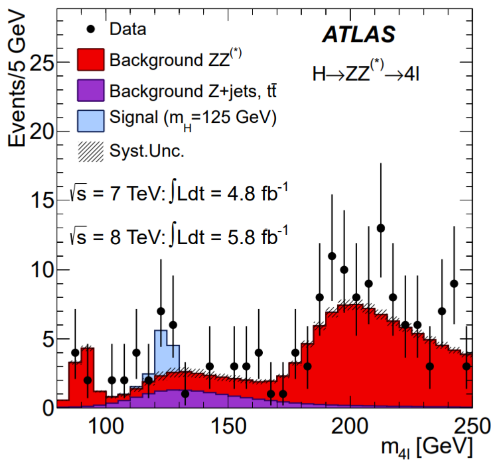


Figure 37: The $m_{4\ell}$ distribution in the channel $H \to Z \to 4\ell$, where experimental data from $\sqrt{s}$ = 7 TeV and $\sqrt{s}$ = 8 TeV ATLAS datasets are compared to the background expectation. The blue signal contribution corresponds to the SM Higgs with $m_H$ = 125 GeV [34].

The MC computation of the process of interest is possible due to the factorization [159], which is a key tool to treat a certain process as different stages of particles' interactions based on the level of momentum transfer between them. Starting from the highest to the lowest momentum scale, five regimes can be distinguished as follows [157]:

1. Hard process - The primary stage starts at the centre of the hadron-hadron collision. To calculate probability distribution and many other features of a specific subprocess with the highest momentum transfer, called "hard scatter", a perturbation theory can be used due to the asymptotic freedom of QCD quanta. It starts with the calculation of the matrix element, which describes the probability amplitude for a given interaction, with a chosen accuracy. The final-state partons' kinematics is derived from integrating over the available phase space while respecting energy-momentum conservation. The momenta of the colliding partons within the protons are sampled from parton distribution functions (PDFs) to account for QCD effects inside the proton.

2. Parton shower - The next phase describes the interactions of the incoming and outgoing partons from the hard scatter. These particles are gluons and quarks, which possess a color charge. Unlike in QED, where scattered charged particles radiate non-interacting photons via the Bremsstrahlung process, in QCD the scattered color-charged partons emit self-interacting gluons both before and after the collision. This results in the prolonged radiation and cascade of (in principle) soft gluons in the phase space. Simluation of the parton shower is done as the ordered, systematic procedure expressed as a progression in momentum transfer scale, starting from the the hard scatter down to the point of the lower momentum scale where the perturbation theory is no longer applicable.

3. Hadronization - So far all calculations have been based on the perturbative model of QCD but at the scale of about 1 GeV, colored particles again begin to strongly

interact. As a result, one has to switch from the perturbative evolution to several non-perturbative hadronization models, which would provide an explanation of how partons are confined into hadrons. A basic idea of these frameworks is that hadronization occurs not at the individual parton level, but rather through the collective process of color-connected parton systems. Although they differ due to various tunable parameters, the fact that a given colored system undergoes hadronization in a consistent manner, regardless of how that system was produced, makes them universal to some extent and applicable to different energy thresholds and new variants of collisions.

4. Underlying event - In the subsequent step, one needs to take into account the remnants of the hadron-hadron collision to fully describe the observed final states. These are particles in a colored state and their very likely interactions, happening in parallel to the hard subprocess, also have to be studied. Such interactions, called "underlying events", generate many soft hadrons throughout the event, which overlay and degrade the hard scatter that had already been simulated. Existing models concentrate on the correlations between hard and underlying events, since they would provide a better understanding of, for instance, jet corrections and high multiplicity soft events.

5. Unstable particle decays - Due to the hadronization of the final-state particles, many of the produced resonances are unstable. As a final procedure, the simulation of secondary particle decays continues until they reach a stable state or would interact with the detector matter, using sophisticated, tunable models. Since many of the observed particles in the detector come from those decays, with different QED radiation effects and electroweak decays happening at the various stages of the event chain, it is essential to obtain the best modeling possible.

The factorized approach allows for gradual improvements to each of the aforementioned stages, through continued advancements in perturbative calculations and more accurate hadronization models.

The typical experimental production chain is as follows: the MC generators produce a huge number of events, which are then processed through detector simulation and reconstruction algorithms. Taking into consideration the two biggest LHC experiments, ATLAS and CMS, the total quantity of simulated events of most relevant processes per each year of data-taking is typically of the order of $10^{10}$ events and is three times bigger than the overall size of the data collected during proton-proton collisions [158]. The basic scheme of the $pp$ collision event at the LHC is shown in Figure 38.

Over the past several decades, a wide variety of Monte Carlo event generators have been developed in the HEP community. A diverse set of independent simulations with potentially various approximations at the different event stages are crucial not only to mutually verify and justify one another, but also each generator is specialized in different types of processes of interest. This ensures to provide the most precise and complete description of the collision as the recorded data by the physics experiments.

One of the features that differentiates the generators is the precision of the QCD coupling constant $\alpha_s$ and the choice of a power in the series expansion - it can be leading-order (LO), next-to-leading-order (NLO), or, getting more accessible, next-to-next-to-leading-order (NNLO). In addition, the developers can select from many hadronization and parton shower models, tools for particle decay simulations, QED radiation corrections and further parameters required as input, including PDFs [161], principally through the LHAPDF library [162]. Such a rich catalogue of MC generators enables numerous software combinations, usually developed by different authors, which represent theoretical approaches through various scientific groups.

The baseline generators used by the LHC experiments are presented below:

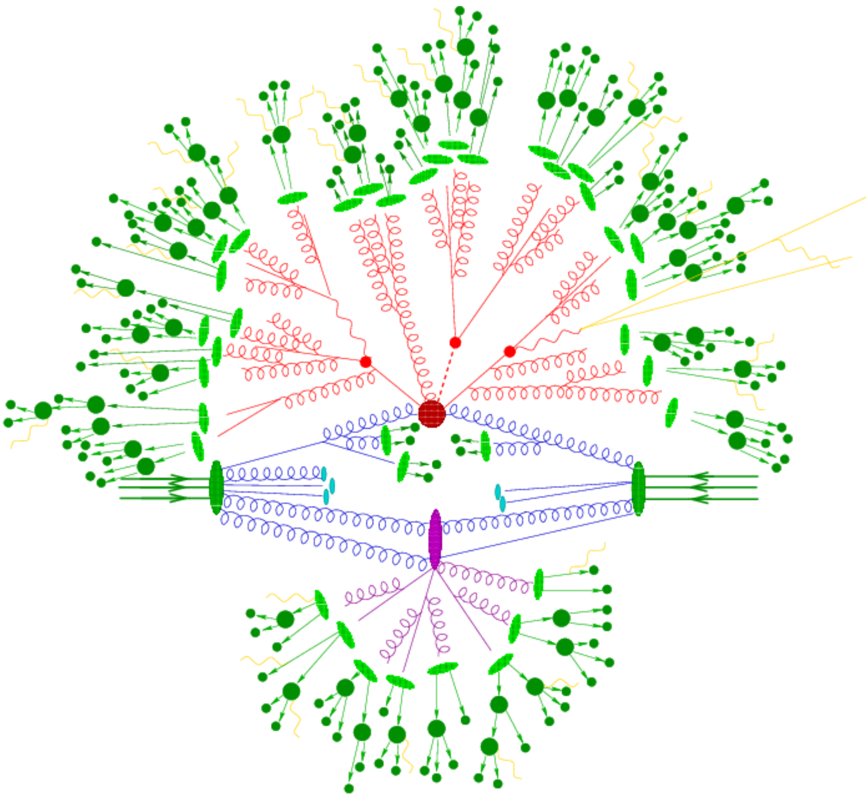

Figure 38: An illustration of a hadron-hadron collision process as simulated by a Monte-Carlo event generator. The different stages of particle interactions are marked with distinct colors: a dark red blob represents the hard subprocess, a red tree-like structure depicts parton showers, a purple blob indicates the underlying event, light green blobs symbolize hadronization, dark green blobs signify the decays of hadrons, and soft photon radiation is visible as yellow lines [160].

- Sherpa [163] - Originally introduced in 2004 [164], this tool is a versatile event generator framework designed for various high-energy collision scenarios including leptons and hadrons. Sherpa provides all essential components to correctly describe a scattering event during a given collision. From the beginning, it was written in C++ with the idea to keep the framework in a clear and straightforward fashion. Sherpa's primary emphasis has been on the perturbative stage of event simulation. In addition, the framework fully models the decays of hadrons and $\tau$ leptons, the QED radiation at the final state, as well as the underlying event.

- MadGraph5_aMCNLO [165] - A general and versatile computer framework that enables computations of SM or BSM processes at all collision stages, from hard events through parton showers and hadronization. MadGraph5_aMCNLO can simulate processes at various perturbative accuracies and final-state descriptions, including the LO precision for all Lagrangians and the NLO for models with QCD and EW corrections applied to SM physics processes. It is also possible to derive tree-level and one-loop-level matrix elements. This feature delivers the possibilty to test multiple simulation scenarios in a single generator framework ensuring their mutual consistency.

- Powheg Box [166] - A computer program based on the POWHEG method, which is designed to enable calculation at the NLO precision in many shower MC frameworks.

Powheg Box also serves as a library with a long list of processes that were previously incorporated and now are accessible to its users. A diverse range of next-to-leading order processes has been implemented, like double vector boson production ($ZZ$, $WZ$ and $W^+W^-$) or $\gamma/Z$ interferences.

- Herwig [167] - A general-purpose simulation framework of highly energetic lepton-lepton, lepton-hadron or hadron-hadron collisions. The generator focuses on the comprehensive modeling of the QCD parton showers and hard/soft scattering. The leading examples of these are first-order matrix elements matching with parton showers, an accurate spin correlations assessment, and the detailed description of heavy quark decays. HERWIG also provides complete spin correlation treatment in automatically generated hard processes and decays across a wide range of BSM scenarios [157]. The code was originally written in Fortran, but has since been further developed and improved in C++ since the start of the LHC experiments.

- Pythia 8 [168] - Pythia is a computer program that simulates processes of hadronic or leptonic high-energy collisions, as well as provides a description of heavy-ion collisions and cosmic ray physics. PYTHIA 8, the next generation of PYTHIA 6, was rewritten from Fortran 77 to C++, but generally, it has been under active development for over 30 years. Depending on the specific needs of the physics group, the simulator is able to provide a huge number of theories and models for different stages of particles' collisions like hard/soft processes, initial- and final-state parton showers or secondary decays of hadronization particles. Pythia is aimed to be an open software designed to enable easy integration with other Monte Carlo frameworks. In contrast to some other simulators, it does not automatically generate code during the process.

The ATLAS experiment uses numerous MC generators for a single physics process to assess theoretical uncertainties, validate parton shower and hadronization models, and also ensure robust matching of matrix elements with parton showers. Different generators focus on various aspects, enabling cross-checks and systematic studies. This approach helps to avoid biases as much as possible, enhance detector response validation, and ensure that results do not excessively rely on a single model.

## 5.2 List of Monte Carlo Generated Samples

The process studied in this chapter is a single electroweak vector boson production in association with jets ($Z$+jets). It is a significant irreducible SM background for various analyses, including BSM searches and measurements of the top quark and Higgs boson.

The Sherpa generator was used to simulate $Z \to \tau\tau$ events with Sherpa 2.2.11 ATLAS configuration [169] with matrix elements for up to two partons at NLO and up to five partons at LO calculated with Comix [170]. This configuration employs the Hessian NNPDF3.0 NNLO PDF set and a modified Catani–Seymour subtraction scheme [171]. In the case of $Z+$ jets configurations the charged leptons invariant mass is set to be >40 GeV.

It introduces multiple improvements and enhancements over the previously utilized Sherpa 2.2.1 [163] prediction, which has been extensively employed by the ATLAS Collaboration for a variety of measurements and the BSM investigations. Sherpa 2.2.1 required a bunch of corrections due to cross-section misprediction in several important phase space regions [169]. Sherpa 2.2.1 $Z \to \tau\tau$, produced with the NNPDF3.0 NNLO PDF set of tuned parameters and the NNPDF30NNLO PDF set for the matrix element, is used in this chapter as a reference for different validation studies.

Usually, the above mentioned $Z$+jets samples are compared with Powheg+Pythia8 (Powheg-Box v1 [166] interfaced to the Pythia 8.186 [172] parton shower model) production

Table 9: List of all validated MC simulated samples.

| **Generator** | **Process** | **Perturbative accuracy** |
|---|---|---|
| Sherpa 2.2.11 | $Z \to \tau\tau$ | NNLO |
| Sherpa 2.2.1 | $Z \to \tau\tau$ | NNLO |
| Powheg+Pythia8 | $Z \to \tau\tau$ | NLO |
| MadGraph+Pythia8 FxFx | $Z \to \tau\tau$ | NNLO |

of $Z \to \tau\tau$ and $DY \to \tau\tau$ samples. The studied Powheg+Pythia8 inclusive $Z \to \tau\tau$ sample was generated using the CT10 PDF set and the AZNLO tune for the underlying event.

The last of the validated MC samples is MadGraph5_aMC@NLO+Pythia FxFx Vjets $Z \to \tau\tau$ sample generated with 0-3jets NLO and HT2bias [173, 169]. Showering and subsequent hadronization processes were simulated using Pythia 8.240 [174], with the A14 tune [175] and the NNPDF2.3 LO parton distribution function (PDF) set with $\alpha_S = 0.130$. To merge the various jet multiplicities the FxFx NLO matrix-element and parton-shower merging prescription [176] is applied with the aim to allow events with hard jets to have their modelling dominated by the matrix element, and for softer jets to be dominated by the parton shower[169].

The TRUTH1 analysis format was used for the analysis of samples with the TauAnalysisTools package. In the case of Rivet analysis files in EVNT format were processed. Both formats provide generator-level information. The EVNT contains the full raw event record in HepMC format, while the TRUTH1 extracts and organizes key truth-level particles, making it more compact and suitable for analysis. A full list of the validated MC simulated samples is displayed in Table 9.

## 5.3 Validation Tests of $\tau$ Properties

### 5.3.1 $\tau$ Polarization Measurement

As mentioned in Section 2.3, the polarization of $\tau$ lepton serves as a valuable characteristic, which provides additional information about the origins of the detected $\tau$ lepton. They can be accessed via the kinematics of all observed decay products, even though some information is missing due to the lack of neutrino(s) detection from $\tau$ lepton decays. This is widely used in physics analyses at the LHC to enhance signals and suppress backgrounds.

If $\tau^{\pm} \to \pi^{\pm}\nu_\tau$ decays from $Z/W$ boson processes are considered, the energy fraction of the $\tau$ lepton carried by the pion, denoted as $x_\pi$, serves as an effective observable for polarization measurements in the laboratory frame:

$$x_\pi = \frac{E_\pi}{E_\tau} \tag{57}$$

Due to the fact, that the fraction $x_\pi$ remains unchanged in the $m_\tau \ll M_Z, M_W$ limit, regardless of the frame of reference (eg. rest frame of the intermediate $Z/W$ boson or the laboratory frame), the $x_\pi$ is usually a good starting point for the spin studies or the spin implementation validation in simulated samples. In addition, a measurement of the $x_\pi$ variable provides a straightforward insight into the decay matrix element properties, which is useful for the Monte Carlo benchmarking [177].

Assuming that QED bremsstrahlung effects can be neglected and $m_\tau \ll M_Z, M_W$, one can obtain the simple analytical formula for the energy spectrum $\frac{dN}{dx_\pi}$ of $\tau^{\pm} \to \pi^{\pm}\nu_\tau$ decay products [178]:

$$\frac{dN}{dx_\pi} = 1 + P \times (2x_\pi - 1) \tag{58}$$

Here $P$ stands for $\tau$ polarization. The analytical description of the particle spectrum presented above can be further developed to incorporate the impacts of radiative corrections [178].

The reference value was derived from precise measurements of the effective weak mixing angle at LEP [179], resulting in the $\tau$ polarization of $P_{LEP} = -14.51 \pm 0.59\%$ for on-shell $Z$ bosons in $Z \to \tau\tau$ decays.

Validation of $\tau$ polarization was performed in various MC-generated samples, which are important for research teams of the ATLAS Experiment. The fit was performed using the `ROOTFit()` function [180] with the first histogram bin omitted, in which mass effects would be the largest.

The validation of $\tau$ polarization in $\tau \to \pi\nu$ decay channel was performed in Sherpa 2.2.11 $Z \to \tau\tau$ sample, Powheg+Pythia8 $Z \to \tau\tau$ sample with $\tau$ decays simulated by Pythia8, as well as MadGraph+Pythia8 FxFx V+jets sample. Obtained polarization for Sherpa setup $P_\pi = -15.2 \pm 1.1\%$ and $P_\pi = -15.6 \pm 0.8\%$ for MadGraph+Pythia8 sample align with expected value $P_{LEP} = -14.51 \pm 0.59\%$, indicating that the modeling of $\tau$ polarization is accurate. It can be observed that in the case of $\tau \to \pi\nu$ polarization in Powheg+Pythia8, $P_\pi = -12.81 \pm 0.59\%$, shows a minor deviation from the benchmark value. Comparison of visible momentum fraction $x_\pi$ distributions for Sherpa 2.2.11 and Powheg+Pythia8 samples with Sherpa 2.2.1 generation is presented in Figure 39, while detailed distributions of $x_\pi$ for Sherpa 2.2.11, Powheg+Pythia8 and MadGraph+Pythia8 setups in $\tau \to \pi\nu$ decay are depicted in Figure 40. All numerical values of measured $\tau$ polarization for various MC samples along with the benchmark values are listed in Table 10.

Table 10: Measured values of $\tau$ polarization for various MC samples along with the benchmark values.

| MC sample | Polarization $\tau \to \pi\nu$ | Reference value |
|---|---|---|
| Sherpa 2.2.11 $Z \to \tau\tau$ | $-15.2 \pm 1.1\%$ | $-14.51 \pm 0.59\%$ |
| Powheg+Pythia8 $Z \to \tau\tau$ | $-12.81 \pm 0.59\%$ | $-14.51 \pm 0.59\%$ |
| MadGraph5+Pythia $Z \to \tau\tau$ | $-15.6 \pm 0.8\%$ | $-14.51 \pm 0.59\%$ |

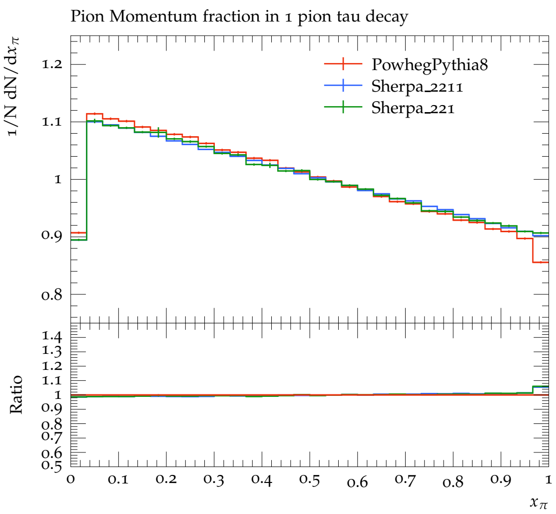


Figure 39: Comparison of $x_\pi$ distributions from $\tau \to \pi\nu$ decay channel between Sherpa 2.2.11 (blue), Powheg+Pythia8 (red) and Sherpa 2.2.11 (green) samples (right-hand side).

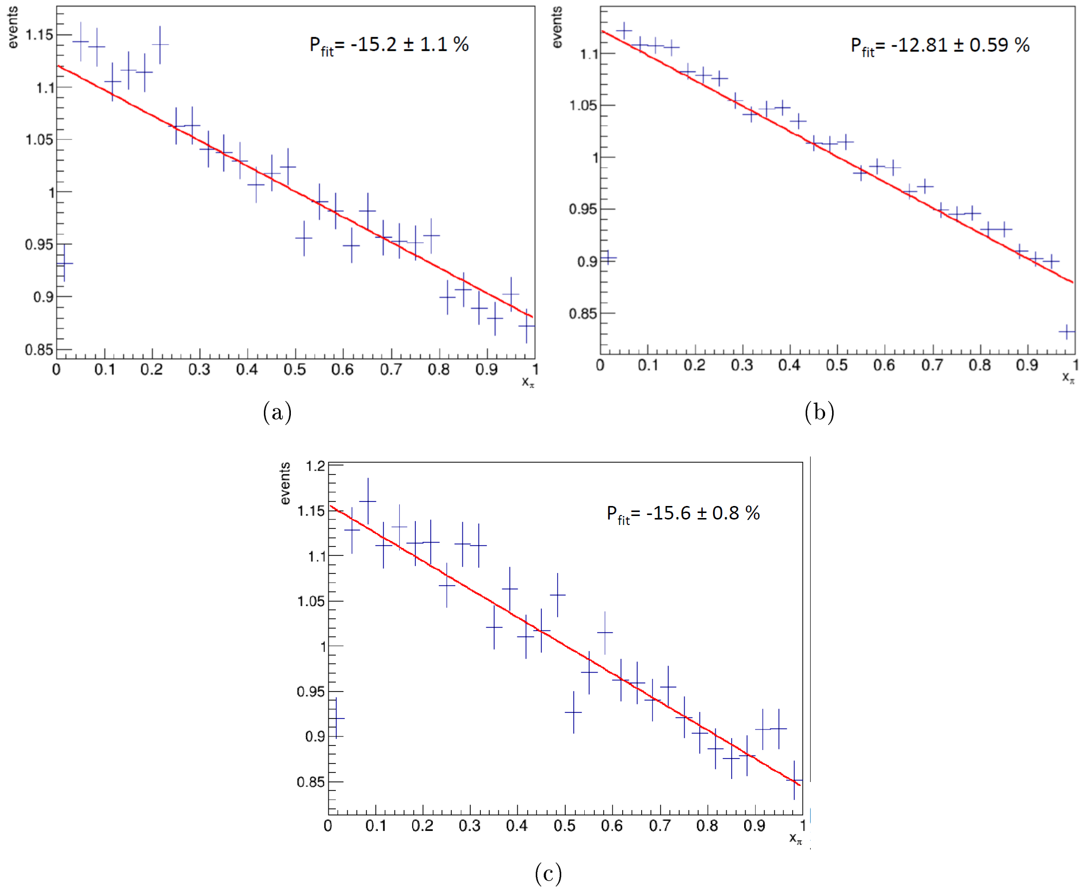


Figure 40: Distributions of visible momentum fraction $x_\pi$ in Sherpa 2.2.11 (a), Powheg+Pythia8 (b) and in MadGraph5+Pythia $Z \to \tau\tau$ sample (c) samples with the polarization fits for $\tau \to \pi\nu$ decay channel.

### 5.3.2 $\tau$ Spin Correlation Measurement

This study aimed to develop an additional validation routine to complement existing methods, such as those measuring $\tau$ lepton kinematics and polarization, and to provide a complete, standardized set of validation plots for $\tau$ lepton properties in MC samples. The goal is to make these tools easily accessible to analysts during data validation. To initiate a standard validation process for $\tau$ leptons in Run-3 MC samples, discussions were started to define common validation metrics. For this purpose, the Rivet toolkit was used. It is a system for the validation of MC event generators and provides a constantly growing set of experimental analyses useful for MC generator development, validation, and tuning, as well as a convenient infrastructure for adding one's own analyses. Rivet is the most widespread way by which analysis code from the LHC and other high-energy collider experiments is preserved for comparison and development of future theory models.

The created routine called `MC_tau_polarization_Zpeak` consists of several standard plots used for the validation of the $\tau$ polarization, as well as introduces observables to monitor $\tau$ spin correlations, which serve as excellent polarimeter probes for the separation of background with $\tau$ leptons decays in the final states. Comparison between these generators is presented in Figures 41 - 43. The different lower cut on invariant mass for various generators is observed in Figure 41.

The longitudinal and transverse spin correlations of the $\tau$ leptons are preserved and encoded in the angular distributions of their visible decay products, enabling measurement

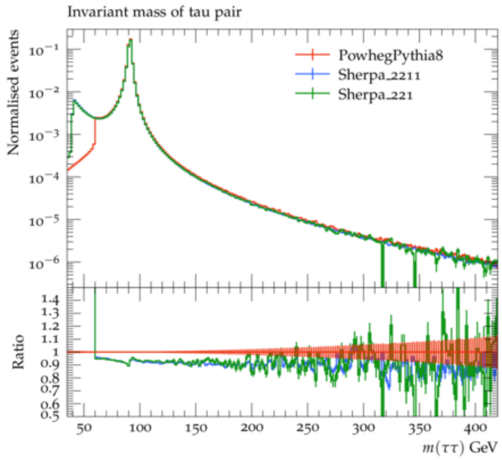


Figure 41: Comparison of the invariant mass of $\tau$ leptons pair between Sherpa 2.2.11 (blue), Powheg+Pythia8 (red) and Sherpa 2.2.11 (green) $Z \to \tau\tau$ samples.

through reconstructed observables. Measurement of the longitudinal $\tau$ lepton spin correlation is mainly based on the energy spectra of the visible decay product - in the case of the $Z \to \tau\tau$, $\tau \to \pi\nu$ decay chain, it is a mass distribution of the charged pions $m_{\pi_+\pi_-}$. For validation of spin correlations the $Z \to \tau\tau$ samples, where polarized and unpolarized $\tau$ leptons decay to charged pion and neutrino, were generated in private stand-alone production using Pythia 8.201 [174] and Tauola++ 1.1.5 [181]. Longitudinal $\tau$ lepton spin correlation check for Sherpa 2.2.1, Sherpa 2.2.11 and Powheg+Pythia8, compared with benchmark plot presenting distributions with and without applied spin correlations, is shown in Figure 42. It is observed that the longitudinal spin correlation of $\tau$ leptons is accurately modeled in the Sherpa 2.2.1 and Powheg+Pythia8 samples.

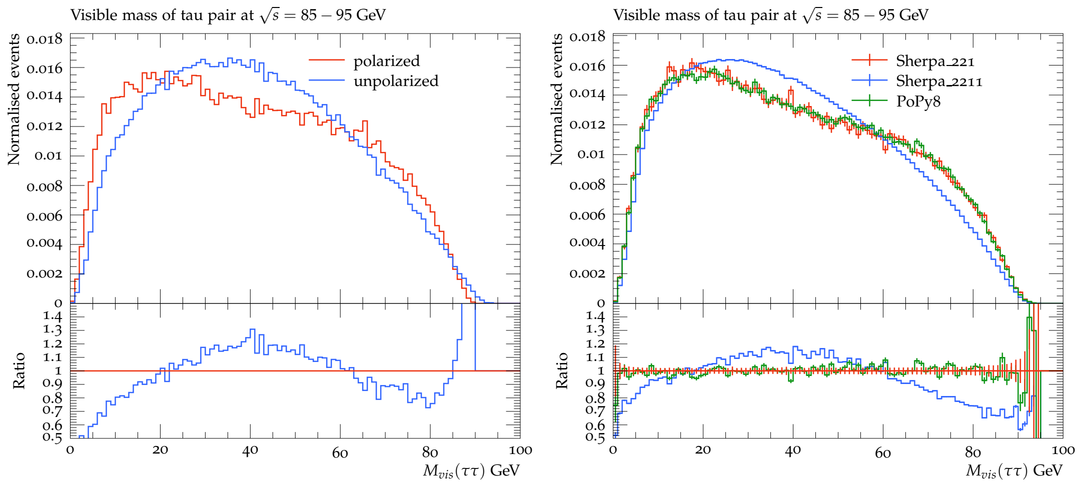


Figure 42: Longnitudal spin correlation comparison between different generators (right-hand side) and benchmark plot for $Z \to \tau\tau$ Pythia+Tauola samples from stand-alone production (left-hand side).

The modelling of transverse $\tau$ lepton spin correlations was validated by analyzing the $\phi_{CP}$ distribution reconstructed in the $Z$ boson rest-frame (as introduced in Section 2.3.2), which is split into two groups. In each group, the $\pi^{\pm}$ is "nearly coplanar" or "nearly perpendicular" with the production plane defined by the beam axis and the $\tau$ lepton momentum in the laboratory frame. The distinction is done by introducing the observable $\alpha$ [79]:

$$\cos\alpha = \left|\frac{\vec{z}\times\vec{p}}{|\vec{z}\times\vec{p}|}\frac{\vec{h}\times\vec{p}}{|\vec{h}\times\vec{p}|}\right| \quad (59)$$

Here, $\vec{z}$ represents the unit vector pointing in the same direction as the direction of one of the proton beams, while $\vec{p}$ and $\vec{h}$ are the unit vectors of the $\tau$ lepton and $\pi^{\pm}$, respectively. A subset of "nearly coplanar" $\pi^{\pm}$ to the production plane of the beam axis is obtained for events meeting the requirement of $\alpha < \pi/4$ and "nearly perpendicular" $\pi^{\pm}$ for $\alpha > \pi/4$. In Figure 43 the comparison of coplanar and perpendicular distributions in the $Z \to \tau\tau$, $\tau \to \pi\nu$ decay channel between Sherpa 2.2.1, Sherpa 2.2.11 and Powheg+Pythia8 samples are displayed, together with expected distributions obtained using the same Pythia+Tauola samples from stand-alone production as for longitudinal $\tau$ lepton spin correlations. Shapes of $\phi_{CP}$ distributions indicate that transverse spin effects are present only in the Sherpa 2.2.1 sample.

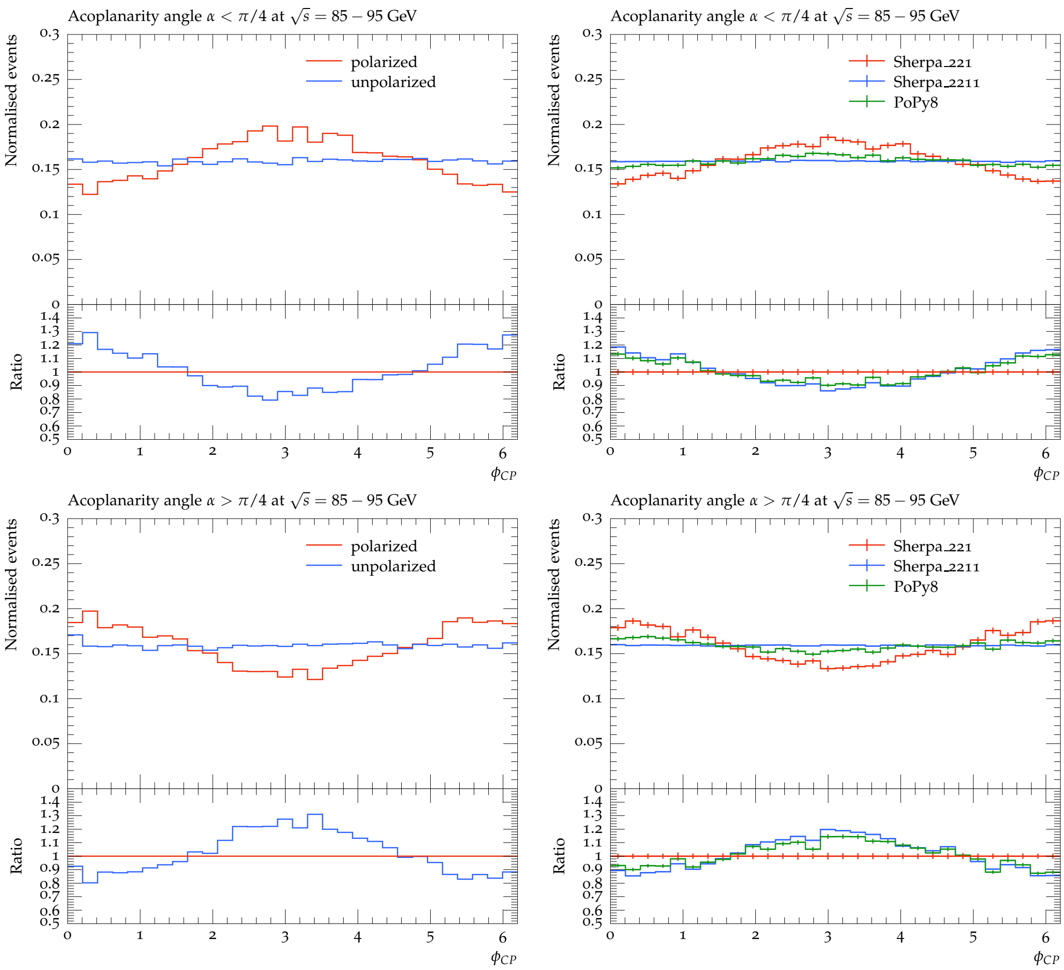


Figure 43: The $\phi_{CP}$ angle distributions for polarized/unpolarized $Z \to \tau\tau$, $\tau \to \pi\nu$ events from stand-alone Pythia+Tauola production (left-hand side) and from various generators (right-hand side). The distributions are analyzed by separating them into subsets based on the orientation of the $\pi^{\pm}$ relative to the production plane, either "nearly coplanar" (top) or "nearly perpendicular" (bottom).

## 5.4 Branching Ratios of $\tau$ Lepton Decays

The branching ratios of various $\tau$ lepton decay modes for Sherpa 2.2.11 and Powheg+Pythia8 $Z \to \tau\tau$ samples, compared to PDG values [182], are presented in Table

11. Listed 1-, 3-, and 5-prong decays include both leptonic and hadronic modes. Hadronic decay modes are described using an X-charged, Y-neutral (XcYn) format, where charged particles are $\pi^{\pm}$ and $K^{\pm}$, and neutral particles are $\pi^0$. The presence of $K^0$ particles is permitted, though they are not counted. Only statistical errors are provided.

The branching ratios generally align with the PDG values within statistical error margins. However, subtle deviations are observed in the hadronic decay branching ratios, where the 1c0n, 1c1n, and 3c0n branching ratios are larger in each sample compared to PDG values, while the remaining branching ratios are slightly smaller. Additionally, in the case of the Powheg+Pythia8 sample, a lack of 3c3n hadronic decays is observed.

Table 11: Branching ratios of $\tau$ lepton decays in Powheg+Pythia8 and Sherpa 2.2.11 sample sorted by the number of prongs (charged decay products), hadronic and leptonic modes, the two leptonic decay modes, and hadronic modes in Xcharged, Y-neutral (XcYn) format. Only statistical errors are presented for Powheg+Pythia8 and Sherpa 2.2.11 samples.

| Decay | Powheg+Pythia8 | Sherpa 2.2.11 | PDG |
|---|---|---|---|
| 1-prong | 84.99 ± 0.07% | 84.75 ± 0.05% | 84.71±0.07% |
| 3-prong | 14.91 ± 0.03% | 15.14 ± 0.02% | 15.20±0.08% |
| 5-prong | 0.083 ± 0.002% | 0.100 ± 0.001% | 0.102±0.004% |
| Leptonic | 35.08 ± 0.04% | 35.09 ± 0.03% | 35.21±0.08% |
| Hadronic | 64.91 ± 0.05% | 64.90 ± 0.04% | 64.8±0.2% |
| $\tau^{\pm} \to e\nu_e\nu_\tau$ | 17.75± 0.03% | 17.78± 0.02% | 17.82±0.04% |
| $\tau^{\pm} \to \mu\nu_\mu\nu_\tau$ | 17.33± 0.03% | 17.31± 0.02% | 17.39±0.04% |
| had 1c0n | 12.7 ± 0.02% | 12.69 ± 0.02% | 12.03±0.05% |
| had 1c1n | 26.63 ± 0.04% | 26.54 ± 0.03% | 25.93±0.09% |
| had 1c2n | 9.31 ± 0.02% | 9.25 ± 0.01% | 9.48±0.10% |
| had 1c3n | 1.09 ± 0.006% | 1.073 ± 0.004% | 1.18±0.07% |
| had 3c0n | 9.78 ± 0.02% | 9.78 ± 0.01% | 9.46±0.05% |
| had 3c1n | 4.62 ± 0.01% | 4.52 ± 0.01% | 4.76±0.05% |
| had 3c2n | 0.48 ± 0.004% | 0.550 ± 0.003% | 0.51±0.03% |
| had 3c3n | 0.00011 ± 0.00001% | 0.277 ± 0.002% | 0.21±0.03% |

## 5.5 Generator-Level RNN Input Comparison

As mentioned in previous sections, the $\tau$ leptons are unstable particles that typically decay before they can reach the detector hardware, hence they must be reconstructed based on their decay products. The primary background to hadronic decays of $\tau$ lepton, which is already observed at the trigger level during event reconstruction, arises from jets of energetic hadrons generated through the strong interactions of gluons and quarks.

Hadronic decays of $\tau$ leptons in final states play a crucial role in the ATLAS physics program, particularly in studies of the Higgs boson and searches for BSM phenomena.

This section presents a follow-up of the study of the BDT input comparison on generator-level for Sherpa 2.2.1 and Powheg+Pythia8 $Z \to \tau\tau$ samples [183]. The study was repeated due to the change in $\tau$ identification method from BDT to RNN, as presented in Section 3.3.5, and the availability of a new version of generated Sherpa 2.2.11 samples.

The comparison between the Powheg+Pythia8 and Sherpa 2.2.11 samples is crucial, as the Powheg+Pythia8 sample is utilized by the Tau CP Group for performance studies, while the Sherpa samples are employed by the majority of ATLAS physics analyses. To mitigate potential biases arising from differences in the $\tau$ lepton $p_{\mathrm{T}}$ spectra between the

Sherpa and Powheg+Pythia8 samples, an additional set of histograms was produced with event weights applied as a function of the true $\tau$ lepton $p_{\mathrm{T}}$. This reweighting enabled a more direct comparison of the two samples by aligning their underlying $\tau$ kinematic distributions. A visual comparison of the tau $p_{\mathrm{T}}$ distribution from on-shell $Z$ boson ($m_{\tau\tau}$ in the range of 88-94 GeV) in Sherpa 2.2.11 and Powheg+Pythia8 samples was conducted (Figure 44), where good agreement can be observed.

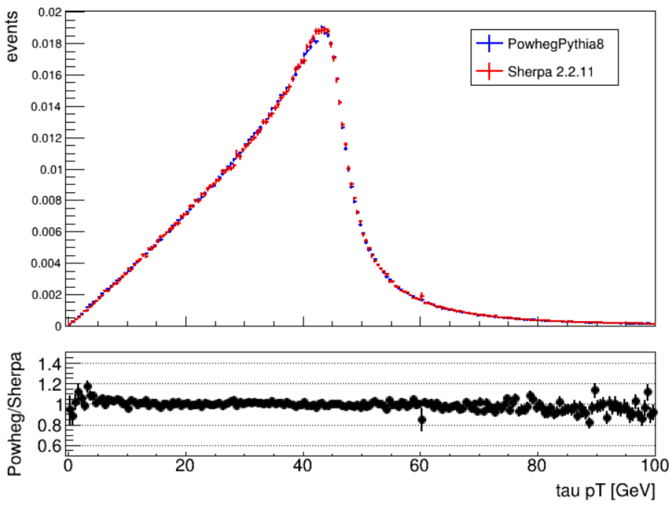


Figure 44: Comparison of $\tau$ $p_T$ distribution between Sherpa 2.2.11 and Powheg+Pythia8 from on-shell $Z$ boson.

The RNN $\tau$ identification utilizes more input variables for discrimination compared to the BDT identification, but a majority of the high-level input variables are the same for both algorithms. Only those RNN input variables whose definitions overlap with the previously used BDT input variables were included in the comparison (a list of the variables is presented in Table 5). In the following study, the $\tau$ RNN variables were reconstructed at the generator level, which means a simulation of detector interaction was not applied. Such events in the TRUTH1 format contain information only about particle four-momenta. Due to the lack of data on e.g. calorimeter cluster energies, certain variables had to be redefined using only the available particle information, in contrast to their original definitions in References [117, 118].

For the construction of $\tau$ RNN variables the TauAnalysisTools framework was used. Only hadronic decays to charged pions were considered. Energies of electromagnetically-interacting particles were used as energy deposits in the EM calorimeter. Pions were associated with "truth" $\tau$ candidates if they passed the requirements of a minimum $p_T$ threshold of 1 GeV and were within $\Delta R < 0.2$ around the truth $\tau$ direction. A number of charged decay tracks for each $\tau$ candidate was derived from the number of associated pions. Depending on the variable, the distributions were compared separately for the 1-prong, 3-prong, or inclusive case.

Figures 45-54 show a comparison of $\tau$ RNN variables' distributions (in either exclusive 1-, 3-prong decays or inclusive $\tau$ events) for Sherpa 2.2.11 and Powheg+Pythia8 samples, Sherpa 2.2.11 and Powheg+Pythia8 samples with $\tau$ $p_{\mathrm{T}}$ event weights, as well as Sherpa 2.2.1 and Powheg+Pythia8 samples (taken from Reference [183]).

In general, a decent agreement is observed across the majority of distributions between the Sherpa 2.2.11 and Powheg+Pythia8 samples, similarly as between Sherpa 2.2.1 and Powheg+Pythia8 samples. The most noticeable differences between the two distributions are seen for the $f^{-1}_{\mathrm{leadtrack}}$ (Figure 46), $p_{\mathrm{T}}^{\mathrm{EM+track}}/p_{\mathrm{T}}$ (Figure 52) and $m_{\mathrm{EM+track}}$ (Figure 53) variables (visible slopes in the corresponding ratio plots), which were not observed in previous Janina Krzysiak's study [183]. Conversely, the Sherpa 2.2.11 and Powheg+Pythia8 samples show better alignment for the $\Delta R_{\mathrm{max}}$ variable distribution (Figure 48). The application of $\tau$ $p_{\mathrm{T}}$ event weights on histograms has a subtle positive impact on the variables' distribution.

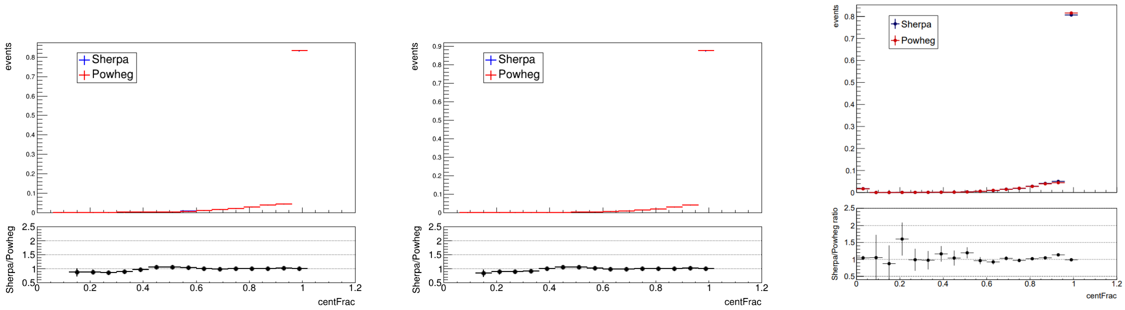


Figure 45: Distribution of the central energy fraction ($f_{\mathrm{cent}}$) variable for inclusive $\tau$ leptons at generator level for Sherpa 2.2.11 and Powheg+Pythia8 samples (left), for Sherpa 2.2.11 and Powheg+Pythia8 samples with $\tau$ $p_{\mathrm{T}}$ event weights (center) and for Sherpa 2.2.1 and Powheg+Pythia8 samples [183] (right).

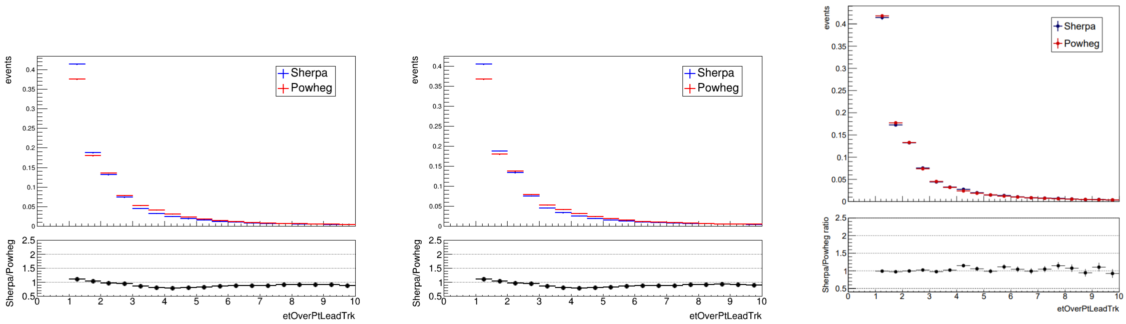


Figure 46: Distribution of the inverse momentum fraction of the leading track ($f^{-1}_{\mathrm{leadtrack}}$) variable for inclusive $\tau$ leptons at generator level for Sherpa 2.2.11 and Powheg+Pythia8 samples (left), for Sherpa 2.2.11 and Powheg+Pythia8 samples with $\tau$ $p_{\mathrm{T}}$ event weights (center) and for Sherpa 2.2.1 and Powheg+Pythia8 samples [183] (right).

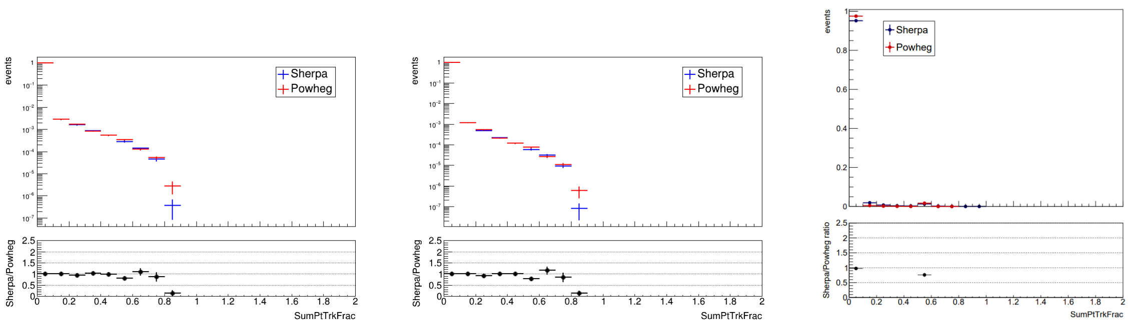


Figure 47: Distribution of the momentum fraction of isolation tracks ($f^{\mathrm{track}}_{\mathrm{iso}}$) variable for 1-prong $\tau$ leptons at generator-level for Sherpa 2.2.11 and Powheg+Pythia8 samples (left), for Sherpa 2.2.11 and Powheg+Pythia8 samples with $\tau$ $p_{\mathrm{T}}$ event weights (center) and for Sherpa 2.2.1 and Powheg+Pythia8 samples [183] (right).

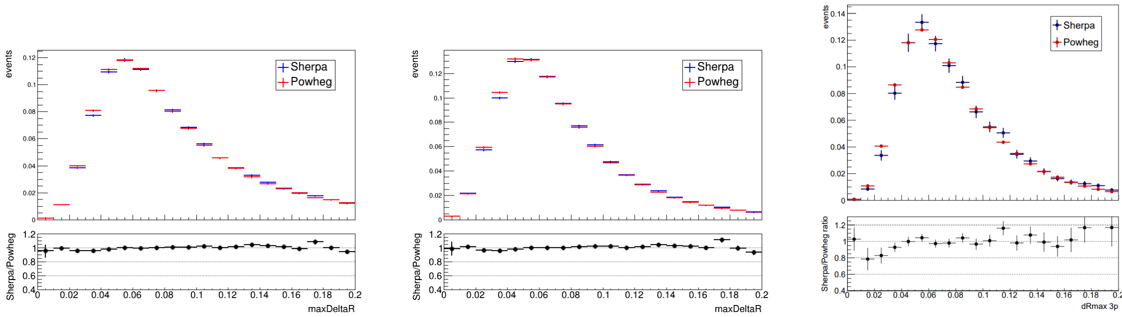


Figure 48: Distribution of the maximum track $\Delta R$ ($\Delta R_{\text{max}}$) variable for 3-prong $\tau$ leptons at generator-level for Sherpa 2.2.11 and Powheg+Pythia8 samples (left), for Sherpa 2.2.11 and Powheg+Pythia8 samples with $\tau$ $p_{\text{T}}$ event weights (center) and for Sherpa 2.2.1 and Powheg+Pythia8 samples [183] (right).

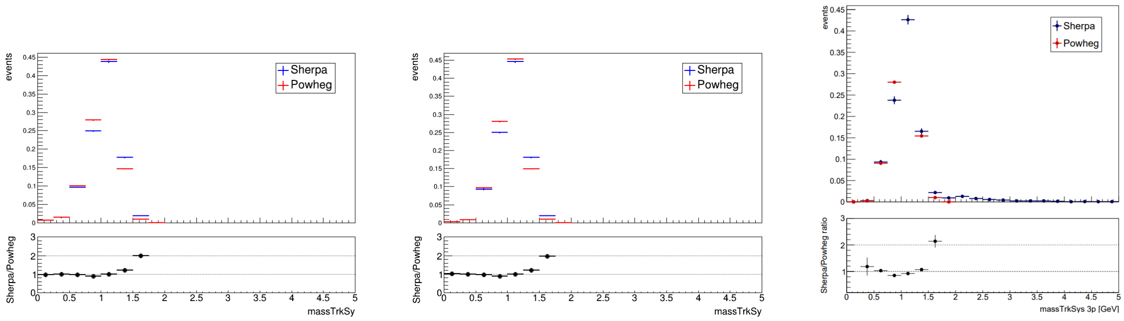


Figure 49: Distribution of the mass of the track system ($m^{\text{track}}$) variable for 3-prong $\tau$ leptons at generator-level for Sherpa 2.2.11 and Powheg+Pythia8 samples (left), for Sherpa 2.2.11 and Powheg+Pythia8 samples with $\tau$ $p_{\text{T}}$ event weights (center) and for Sherpa 2.2.1 and Powheg+Pythia8 samples [183] (right).

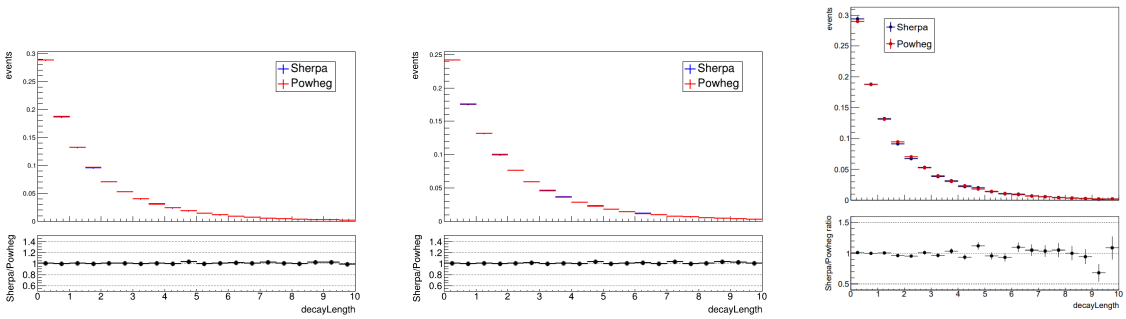


Figure 50: Distribution of the transverse flight path significance ($S_{\text{T}}^{\text{flight}}$) variable for inclusive $\tau$ leptons at generator-level for Sherpa 2.2.11 and Powheg+Pythia8 samples (left), for Sherpa 2.2.11 and Powheg+Pythia8 samples with $\tau$ $p_{\text{T}}$ event weights (center) and for Sherpa 2.2.1 and Powheg+Pythia8 samples [183] (right).

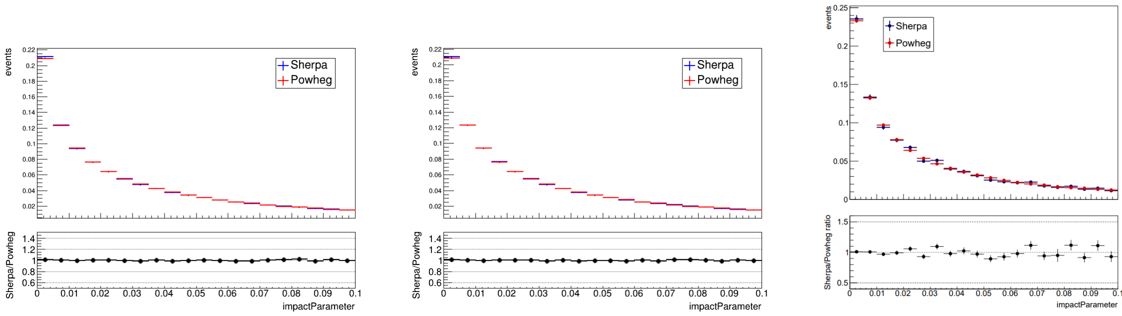


Figure 51: Distribution of the transverse impact parameter significance of the leading track ($|S_{\text{leadtrack}}|$) variable for inclusive $\tau$ leptons at generator-level for Sherpa 2.2.11 and Powheg+Pythia8 samples (left), for Sherpa 2.2.11 and Powheg+Pythia8 samples with $\tau$ $p_{\text{T}}$ event weights (center) and for Sherpa 2.2.1 and Powheg+Pythia8 samples [183] (right).

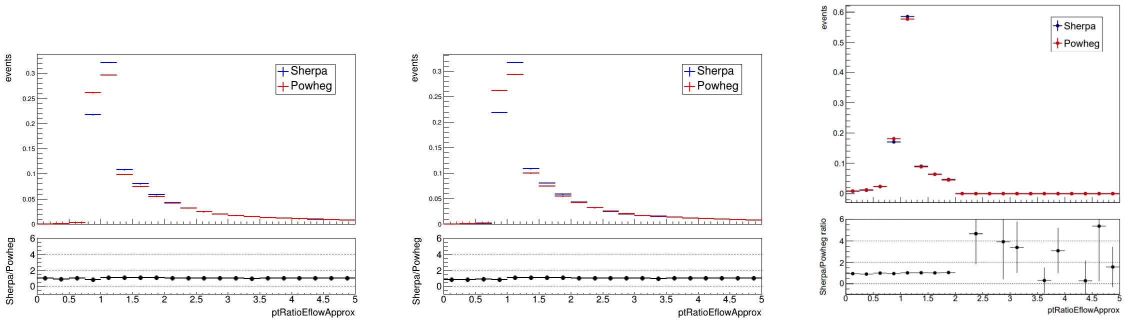


Figure 52: Distribution of the fraction of track-plus-EM-system ($p_{\text{T}}^{\text{EM+track}}/p_{\text{T}}$) variable for inclusive $\tau$ leptons at generator-level for Sherpa 2.2.11 and Powheg+Pythia8 samples (left), for Sherpa 2.2.11 and Powheg+Pythia8 samples $\tau$ $p_{\text{T}}$ event weights (center) and for Sherpa 2.2.1 and Powheg+Pythia8 samples [183] (right).

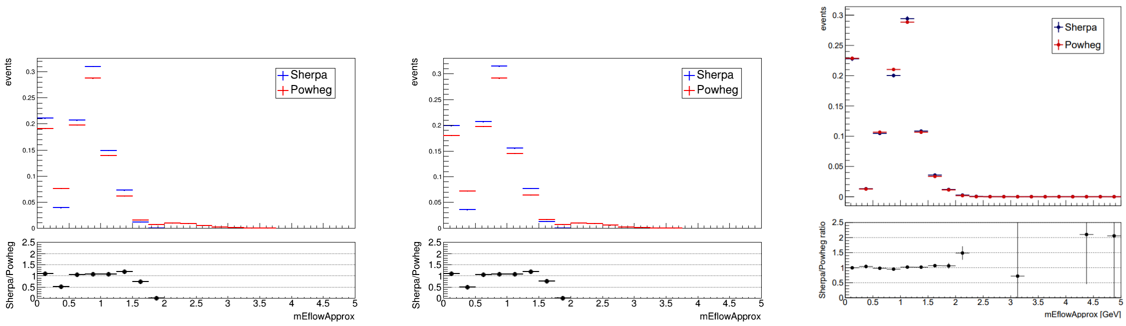


Figure 53: Distribution of the mass of the track-plus-EM-system ($m_{\text{EM+track}}$) variable for inclusive $\tau$ leptons at generator-level for Sherpa 2.2.11 and Powheg+Pythia8 samples (left), for Sherpa 2.2.11 and Powheg+Pythia8 samples with $\tau$ $p_{\text{T}}$ event weights (center) and for Sherpa 2.2.1 and Powheg+Pythia8 samples [183] (right).

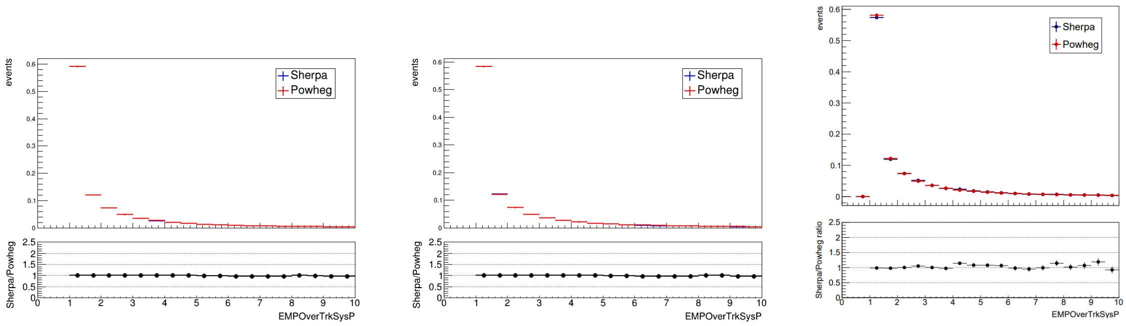


Figure 54: Distribution of the ratio of EM energy and track momentum ($f^{\mathrm{EM}}_{\mathrm{track}}$) variable for inclusive $\tau$ leptons at generator-level for Sherpa 2.2.11 and Powheg+Pythia8 samples (left), for Sherpa 2.2.11 and Powheg+Pythia8 samples $\tau$ $p_{\mathrm{T}}$ event weights (center) and for Sherpa 2.2.1 and Powheg+Pythia8 samples [183] (right).

### 5.6 $\tau$ Leptons and $b$-quarks as Quasi-Stable Particles in the Geant4 Simulation

An accurate simulation of $b$-hadron and $\tau$ leptons properties is a key part of the proper optimization of the particles' identification algorithms in the ATLAS experiment [184, 118, 117]. In the typical Geant4 software [185], the interactions of the $b$-hadrons and $\tau$ leptons with detector material are neglected and only interactions of their decay products are taken into account. Due to the increasing center-of-mass energy during $pp$ collisions at the LHC, more and more high $p_{\mathrm{T}}$ particles are expected, which can transverse the detector material, hence a more precise detector simulation is needed. In order to improve the standard simulation process, the quasi-stable (QS) particle simulation approach was proposed, in which particles considered unstable by the generators are passed to Geant4 to allow them to deposit energy in the tracking layers that they traverse. Particles treated by QS simulation are pre-assigned the lifetime and decay products from the generator, so that the GenEvent truth record is reproduced. A dedicated study of the QS simulation was presented in [186]. Figure 55 presents the difference in the decay length ($d_{\mathrm{diff}}$) for corresponding $\tau$ leptons from the standard ($d_{\mathrm{withoutQS}}$) and quasi-stable particle versions ($d_{\mathrm{withQS}}$) of Geant4 simulation using the Drell-Yan production of 2-3 TeV $\tau$ lepton pairs. The $d_{\mathrm{diff}}$ is calculated as follows:

$$d_{\mathrm{diff}} = d_{\mathrm{withQS}} - d_{\mathrm{withoutQS}} \tag{60}$$

Contrary to the expected reduction in decay length, a symmetric broadening was observed, indicating that the Geant4 is not performing as expected.

A result of the incorrect simulation was an insufficient precision ($10^{-8}$ or higher precision must be employed) in the GEN_EVENT HepMC record for boosted objects, therefore the original calculation from the vertex and momentum 4-vector components did not provide the proper lifetime of a high $p_{\mathrm{T}}$ propagating $\tau$ lepton. A corrected $\tau$ lifetime was calculated from the particle 4-momentum and the 3D distance of the vertices.

Per-$\tau$ comparison of the difference in distance for particles without QS and with corrected QS for $Z \to \tau\tau$ and $DY \to \tau\tau$ validation samples produced with Powheg+Pythia8 generator is shown in Figure 56. It can be observed that the distance change for $\mathcal{O}(100-500)$ GeV $\tau$ leptons in $Z \to \tau\tau$ sample is significantly smaller than for $\mathcal{O}(2-3)$ TeV $\tau$ leptons in $DY \to \tau\tau$ sample. In addition, some differences are present above zero ($10^{-7}$-$10^{-4}$) in $DY \to \tau\tau$ sample.

Another part of the QS simulation study was to test the possibility of an alternative re-processing workflow, in which only events with $b$-hadrons or $\tau$ leptons with decay length

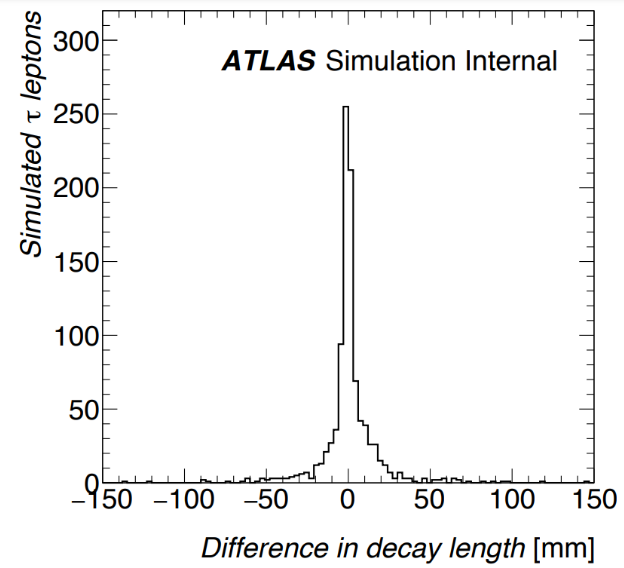


Figure 55: The difference in decay length for corresponding $\tau$ leptons for standard and quasi-stable particle simulations [186].

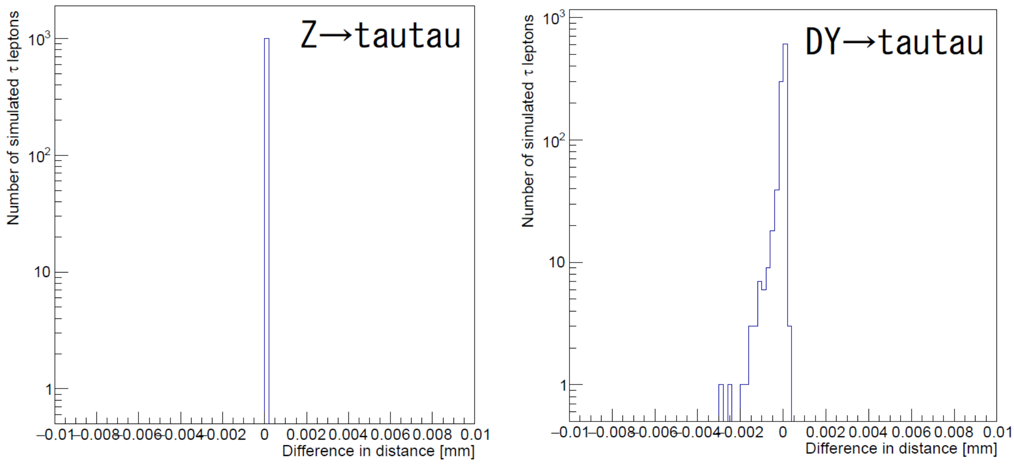


Figure 56: Per-$\tau$ comparison without-QS/with-fixed-QS $Z \to \tau\tau$ (left-hand side) and $DY \to \tau\tau$ (right-hand side) validation samples.

beyond the beam-pipe would be re-simulated, instead of re-simulation of the full sample. Such an approach would accelerate the entire process, given the great number of MC samples used by the ATLAS experiment. In order to estimate the fraction of events that require re-simulation, the events with $b$-hadrons ($B^+$, $B_c^+$), which are actually affected by quasi-stable particle simulation in standard events, were measured.

Figure 57 depicts the decay radius and distance of the $b$-hadrons in the $t\bar{t}$ validation sample produced using the Powheg+Pythia8 generator. The distance refers to the 3D distance to (0,0,0) of the decay vertex. As can be seen, for $b$-hadrons only %-level of events have decayed beyond the beam pipe (above 22 mm).

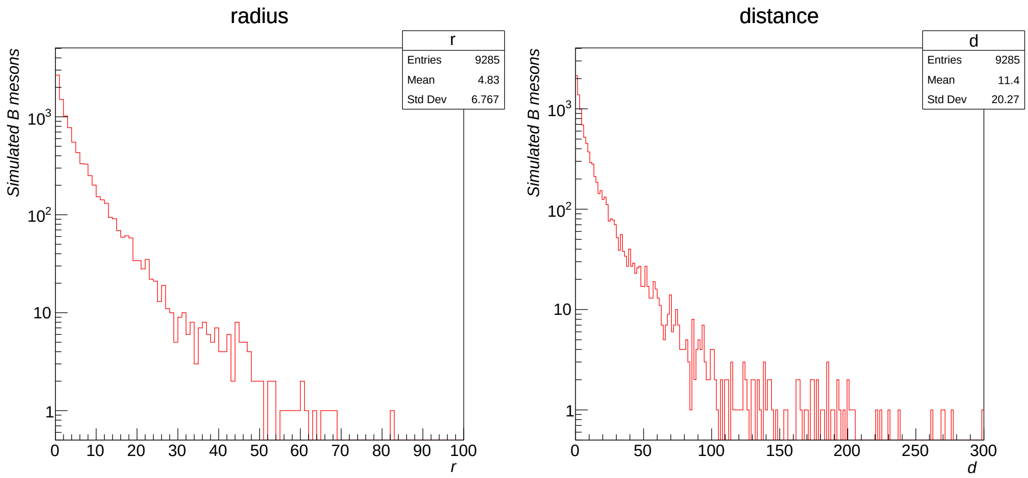


Figure 57: Decay radius (left-hand side) and distance to (0,0,0) of the decay vertex (right-hand side) of $B$ mesons ($B^+$, $B_c^+$) in the $t\bar{t}$ validation sample.

## 5.7 Conclusion

The $\tau$ lepton polarization $Z \rightarrow \tau\tau$ decays was validated in various MC samples utilized by many ATLAS Experiment analyses. In MadGraph+Pytia8 FxFx $Z \rightarrow \tau\tau$ samples observed polarization was a few percent above the expected value, while in Sherpa 2.2.11 and Powheg+Pythia8 $Z \rightarrow \tau\tau$ samples polarization was generally in good agreement with the expected value measured at LEP, $P \cong -0.145$. In addition, the new Rivet routine for MC samples validation with $\tau$ leptons in the final states was created, summarizing previous $\tau$ polarization tests and introducing new observables for $\tau$ spin correlations. It was observed that the longitudinal spin correlations were not implemented in the Sherpa 2.2.11 $Z \rightarrow \tau\tau$ samples, while the absence of the transverse spin correlations was observed for both Sherpa 2.2.11 and Powheg+Pythia8 $Z \rightarrow \tau\tau$ samples. Both issues were reported to ATLAS Tau CP Group for further investigation. Slight differences from the PDG values can be observed in the hadronic decay branching ratios in Sherpa 2.2.11 $Z \rightarrow \tau\tau$ and Powheg+Pythia8 samples, especially for events with the 1c0n, 1c1n, and 3c0n decay configurations. The reconstructed $\tau$ RNN identification input variables from truth information at the generator level for Sherpa 2.2.11 and Powheg+Pythia8 samples were compared with the previous version of $\tau$ BDT identification. Good agreement was observed between the Sherpa 2.2.11 and Powheg+Pythia8 samples, further slightly improved by applying additional $\tau$ $p_{\mathrm{T}}$ event weights, as well as between the distributions of the new $\tau$ RNN input variables and those of the previously used $\tau$ BDT variables. In addition, a corrected quasi-stable particle simulation for highly energetic $b$-hadrons and $\tau$ leptons was validated on $Z \rightarrow \tau\tau$ and $DY \rightarrow \tau\tau$ samples.

# 6 Search for a Charged Higgs Boson in the ATLAS Experiment

This chapter describes a search for charged Higgs bosons, motivated by predictions of multiple BSM theories, using the $H^+ \to \tau\nu$ decay, with a subsequent hadronic decay of the $\tau$-lepton (referred to as $\tau_{\text{had-vis}}$). The investigated mass range is 80–3000 GeV, including the intermediate-mass region described in Section 2.2.3. The analysis focuses on two distinct channels, dependent on the assumed decay mode of the $W$ boson originating from the top-quark produced in association with $H^+$. Specifically, the $\tau_{\text{had-vis}}$+jets channel is considered if the $W$ boson decays into a $q\bar{q}$ pair, whereas the $\tau_{\text{had-vis}}$+lepton channel is targeted if the $W$ boson decays into an electron or muon and neutrino. The dataset utilized in this analysis was collected from $pp$ collisions at $\sqrt{s} = 13$ TeV, recorded by the ATLAS experiment during the LHC Run-2 data-taking period. The integrated luminosity of the dataset corresponds to $140\,\text{fb}^{-1}$.

This chapter starts with the summary of the previous searches of the charged Higgs boson, followed by the data and simulated samples in Section 6.2. Then, the event selection and multivariate discriminant are discussed in Sections 6.3 and 6.4. In Section 6.5 the background modelling is described. In particular, my contribution to implement and optimize the data-driven estimation of events with misidentified $\tau$ objects, crucial to provide high sensitivity to the searched signal, is presented. The modelling of top-quark and $W$+jets backgrounds is shown in Section 6.6. A discussion of the systematic uncertainties and a description of the statistical analysis used to derive exclusion limits on the production of a charged Higgs boson decaying via $H^+ \to \tau\nu$ are presented in Sections 6.7 and 6.8, respectively. Finally, a summary is given in Section 6.9.

The analysis overview is based on the analysis publication [11].

## 6.1 Previous Searches for $H^+$

The charged Higgs boson has been extensively searched for by many experiments. Early efforts at the Large Electron-Positron (LEP) collider considered only two decay modes, $H^+ \to \bar{c}s$ and $H^+ \to \tau\nu$, assuming their branching ratios summed to 1. Based on this assumption, collected data excluded charged Higgs masses below 80 GeV at 95% confidence level [187]. In contrast, the ATLAS and CMS collaborations have conducted a broader set of searches using Run-1 data from $pp$ collisions at $\sqrt{s} = 7$ and 8 TeV, investigating multiple final states corresponding to a wider range of possible branching ratios predicted by various models. They explored the mass regime below the top-quark mass through the $\tau\nu$ [188, 189, 190, 191, 192] and $cs$ [193, 194] final states, along with the mass range exceeding the top-quark mass with the $\tau\nu$, $tb$ and $WZ$ decay modes [190, 190, 195, 196]. The next searches using Run-2 $pp$ collision data at $\sqrt{s} = 13$ TeV probed charged Higgs boson decaying to $\tau\nu$ [70, 197] (the first analysis probing intermediate mass region), $tb$ [198, 199], $WZ$ [200, 201], $HW$ [202, 203], $cb$ [204] and $cs$ [205, 206] decay channels. Furthermore, the ATLAS and CMS experiments have investigated neutral scalar resonances that decay into $\tau$ lepton pairs [207, 208], a process to which the hMSSM is also sensitive in certain parameter regimes. These searches did not provide any evidence of charged Higgs bosons. A recent ATLAS Collaboration analysis of Run-2 data reported an excess over the SM expectation with a global significance of 2.5 $\sigma$ in the search for $H^+ \to cb$ at a mass hypothesis of 130 GeV. This finding, combined with the discrepancies observed in semi-leptonic $B$-meson decays across multiple flavor physics experiments [209], lends support to the 2HDM as a viable theoretical framework accommodating flavor-changing neutral currents [210, 211], and justify further searches for the charged Higgs boson [212].

## 6.2 Data and Samples of Simulated Events

The analysis utilized $pp$ collision data at $\sqrt{s} = 13$ TeV collected during the Run-2 data-taking periods, which consists of a sample of $140.1 \pm 1.2$ fb$^{-1}$. This sample was selected to include only events recorded with all ATLAS sub-systems in full operational status, as well as with stable beam conditions [213].

The Monte Carlo simulated data samples were employed to formulate and validate the analysis methodology, compute the signal selection efficiency and certain background contributions, as well as assess the systematic uncertainties. These samples are based on the ATLAS full GEANT4 [185, 214] simulation and are reconstructed utilizing the identical analytical framework as the experimental data. The SM background processes, outlined in Table 12, consist of top-quark pair and single-top production, which were generated using the POWHEG-BOX v2 [215, 216] framework and NNPDF3.0 NLO PDF [217]. Additionally, the top quark decays were modeled with MADSPIN [218] to preserve the associated spin correlations. Parton shower, fragmentation, and underlying event modeling is done using the PYTHIA v8.230 [219] event generator with the A14 tune, while heavy-flavor hadron decays are handled by the EVTGEN [220] package. The top-quark pair and single-top production samples are scaled to their corresponding NNLO [221] and approximate NNLO cross-sections [222, 223, 224], respectively. Additionally, systematic uncertainties are evaluated using alternative samples interfaced with the HERWIG v7.0.4 event generator. $W/Z+$ jets processes are simulated using the SHERPAv2.2.1 [225] and their cross-sections are normalized to NNLO [217] calculations performed with FEWZ [226, 227, 228]. Diboson processes, on the other hand, are generated with POWHEG-BOX v2 and PYTHIA v8.210, employing CT10NLO and CTEQ6L1 parton distribution functions, and modeling non-perturbative effects with the AZNLO tune [229].

All simulated background samples are scaled using $k$-factors normalization factors to ensure the estimated background yields align with the most recent theoretical predictions calculated at NNLO or NLO. Furthermore, all events are combined with additional minimum-bias events generated using Pythia v8.186 [220], employing the A3 set of tuned parameters and the NNPDF2.3lo set of PDFs to emulate the effects of multiple $pp$ collisions per bunch crossing, which occur at a variable rate. The combined simulated events are then weighted to align with the pile-up distribution observed in the data.

Simulated $H^+$ signal samples were generated across three different mass ranges, utilizing the narrow-width approximation for all values of $H^+$ mass. The event generation was performed with MADGRAPH5_AMCNLO [227], either at LO or NLO, employing the corresponding NNPDF3.0 PDF set. The selection of renormalization and factorization scale settings was motivated by References [230, 69].

For different $m_{H^+}$ masses, different production channels dominate:

1. For the low mass domain ($m_{H^+} < 140$ GeV), $t\bar{t}$ events featuring the subsequent decay of a single $t$-quark into a $H^+$ and a $b$-quark are generated with MADGRAPH+AMCNLO using LO computations exclusively and the NNPDF3.0 LO set. One can neglect the $t\bar{t}$ events with both top quarks decaying to $bH^+$ and single-top-quark events with a subsequent $t \to bH^+$ decay, as their contribution is insignificant.

2. For the intermediate mass range (140 GeV $\leq m_{H^+} < 200$ GeV), non-resonant, single- and double-resonant top-quark processes featuring a $W$ boson, a $H^+$ and two bottom-quarks in the final state are generated at LO employing the four-flavor scheme (4FS).

3. For the high-mass regime ($m_{H^+} \geq 200$ GeV), the $H^+$ production in association with a single top-quark is generated using NLO calculations in the 4FS.

Table 12: Different SM background processes included in the analysis with the specification of how they were generated [11].

| **Background process** | **Generator and parton shower** | **Cross section [pb]** | **ME order** |
|---|---|---|---|
| $t\bar{t}$ | POWHEG-BOX v2 and Pythia 8 | 832 | NLO |
| Single top quark $t$ channel | POWHEG-BOX v2 and Pythia 8 | 217 | NLO |
| Single top quark $s$ channel | POWHEG-BOX v2 and Pythia 8 | 10.3 | NLO |
| Single top quark $Wt$ channel | POWHEG-BOX v2 and Pythia 8 | 72 | NLO |
| $W(\ell\nu)+$ jets | Sherpa 2.2.1 | $2.0 \times 10^4$ | NNLO |
| $Z/\gamma^*(\ell\ell, \nu\nu)+$ jets | Sherpa 2.2.1 | $2.1 \times 10^3$ | NNLO |
| $WW$ | POWHEG-BOX v2 and Pythia 8 | 55 | NLO |
| $WZ$ | POWHEG-BOX v2 and Pythia 8 | 26 | NLO |
| $ZZ$ | POWHEG-BOX v2 and Pythia 8 | 8.4 | NLO |

## 6.3 Event Selection

This analysis considered a charged Higgs boson decaying via $H^+ \to \tau\nu$ in topologies where it is produced either in top-quark decays or in association with a top-quark. Depending on whether the top-quark produced with the $H^+$ decays hadronically or semileptonically, two channels are targeted: $\tau_{\text{had}-\text{vis}}$+jets or $\tau_{\text{had}-\text{vis}}$+lepton, respectively. The corresponding signal regions are described below.

All events are required to have a good-quality primary vertex with a minimum of two associated tracks ($p_{\text{T}} > 400$ MeV), collected during periods when all detector subsystems were functioning correctly. Details on the physics objects used or vetoed in this analysis were discussed in Section 3.3.

### 6.3.1 $\tau_{\text{had}-\text{vis}}$+jets Channel

The $\tau_{\text{had}}$+jets channel analysis uses events selected by $E_{\text{T}}^{\text{miss}}$ triggers [231] with thresholds at 70, 80, 90 or 110 GeV, with consideration of the data-taking period to account for varying pile-up conditions. The simulation does not perfectly model the trigger efficiency, therefore it is fitted using a Gaussian error function in both the data and simulation. Their efficiency ratio is then employed to reweight the simulated events.

The selection criteria for $\tau_{\text{had}}$+jets channel signal region (SR) are as follows:

- at least one $\tau_{\text{had-vis}}$ candidate, fulfilling *medium* working point criteria, with $p_{\text{T}} >$ 40 GeV and $|\eta| < 2.3$,
- no loose leptons with $p_{\text{T}} > 20$ GeV,
- at least three jets with $p_{\text{T}} > 25$ GeV, of which at least one is $b$-tagged,
- $E_{\text{T}}^{\text{miss}} > 150$ GeV,
- $m_{\text{T}} > 50$ GeV.

The above mentioned $m_{\text{T}}$ refers to the transverse mass of the highest-$p_{\text{T}}$ $\tau_{\text{had-vis}}$ candidate and $E_{\text{T}}^{\text{miss}}$, defined as:

$$m_{\text{T}}(\tau_{\text{had-vis}}, E_{\text{T}}^{\text{miss}}) = \sqrt{2p_{\text{T}}^{\tau} E_{\text{T}}^{\text{miss}}(1 - \cos\Delta\phi_{\tau,\text{miss}})} \quad (61)$$

Here, $\Delta\phi_{\tau,\text{miss}}$ is the azimuthal angle between the $\tau_{\text{had-vis}}$ and the missing transverse momentum.

### 6.3.2 $\tau_{\mathrm{had-vis}}$+lepton Channel

The analysis also investigates the $\tau_{\mathrm{had-vis}}$+lepton channel, comprising the $\tau_{\mathrm{had-vis}}$+electron and $\tau_{\mathrm{had-vis}}$+muon sub-channels, which uses events selected by single-lepton triggers. A combination of electron and muon triggers is employed with different thresholds and isolation requirements [232, 233, 234]. Low $E_{\mathrm{T}}$ or $p_{\mathrm{T}}$ thresholds triggers (20–26 GeV depending on the data-taking period) with stricter isolation criteria are combined in a logical OR with higher $p_{\mathrm{T}}$ threshold (60–120 GeV for electrons, 50 GeV for muons) triggers that have looser isolation or identification requirements. This approach enables maximizing the overall trigger efficiency.

The requirements for $\tau_{\mathrm{had}}$+lepton channel SR events are:

- exactly one *tight* lepton fulfilling *tight* working point criteria, with $p_{\mathrm{T}} > 30$ GeV and $|\eta| < 2.5$ ($|\eta| < 2.47$, excluding $1.37 < |\eta| < 1.52$) for muons (electrons) matched to the single-lepton trigger object,
- exactly one *medium* $\tau_{\text{had-vis}}$ candidate with $p_{\mathrm{T}} > 30$ GeV, $|\eta| < 2.3$ and an electric charge opposite to that of the lepton,
- at least one $b$-tagged jet with $p_{\mathrm{T}} > 25$ GeV,
- $E_{\mathrm{T}}^{\mathrm{miss}} > 50$ GeV.

### 6.3.3 Control Regions

Besides the signal regions, the control regions (CR) are utilized to validate the agreement between data and background simulation, and to derive essential corrections for specific background processes. These regions are designed to be similar to the signal regions in terms of kinematics, but are enriched in background events and largely depleted of signal. This allows for a data-driven evaluation of the modelling accuracy and the application of correction factors (such as scale factors), improving the background estimation. Importantly, these CRs are not incorporated into the final likelihood fit. There are several CRs defined:

- $\tau_{\mathrm{had}}$+jets $t\bar{t}$ CR - a CR with reduced signal content is established to investigate the modeling of the $t\bar{t}$ background. It applies the same event selection criteria as the $\tau_{\mathrm{had}}$+jets SR, but with the requirement of $m_{\mathrm{T}}$ between 50 and 100 GeV and at least two $b$-jets. This region has approximately 90% purity in top-quark backgrounds. In order to ensure orthogonality, events selected for this CR are excluded from the SR.
- $\tau_{\mathrm{had}}$+lepton $t\bar{t}$ CR - a region enriched in $t\bar{t}$ events is selected to derive corrections for the modeling of $t\bar{t}$ processes in $\tau_{\mathrm{had}}$+lepton channel. This follows the same event selection criteria as the $\tau_{\mathrm{had}}$+lepton SR, with the additional requirement of $E_{\mathrm{T}}^{\mathrm{miss}} >$ 80 GeV, $m_{\mathrm{T}} < 70$ GeV and at least two $b$-tagged jets. Events selected for this control region are also excluded from the $\tau_{\mathrm{had}}$+lepton SR, similar to the approach used for the $\tau_{\mathrm{had}}$+jets $t\bar{t}$ CR, to preserve orthogonality.
- $\tau_{\mathrm{had}}+e/\mu$ b-veto CRs - it follows the same event selection criteria as the $\tau_{\mathrm{had}}$+lepton SR, with the additional requirement of vetoing any $b$-tagged jets. Such defined CR is enriched in $W$+jets events containing $e/\mu$ signatures along with a jet misidentified as $\tau_{\text{had-vis}}$, as well as $Z$+jets events where the $Z$ boson decays to a pair of $\tau$ leptons.
- $\tau_{\mathrm{had-vis}}$+jets $b$-veto $\mathrm{m_T}$ >100 CR - a region is defined by the same event selection criteria as the $\tau_{\mathrm{had-vis}}$+jets SR, with additional requirements: a $b$-jet veto and $\mathrm{m_T}(\tau, E_{\mathrm{T}}^{\mathrm{miss}}) > 100$ GeV. This region is enriched in hadronic jets misidentified as $\tau_{\mathrm{had-vis}}$ candidates.

- $e + \mu$ $b$-tag CR - a CR enriched in $t\bar{t}$ event, which employs the same selection requirements as the $\tau_{\text{had}}$+lepton SR, but has additional criteria of a *tight* $e + \mu$ pair instead of a $\tau_{\text{had-vis}}$+lepton pair. This control region is highly enriched (>99.8%) with top-quark background events.

- $W/Z$+jets CR - a CR applying the same selection criteria as $\tau_{\text{had}-\text{vis}}$+jets SR but with $b$-jet veto and $m_T(\tau, E_T^{\text{miss}}) < 100$ GeV.

## 6.4 Multivariate Discriminant

Based on the event selections described, key kinematic variables, which distinguish the signal processes from the background processes, are integrated into a multivariate discriminant using Parameterized Neural Networks [235] part of the multi-variate analysis (MVA). The PNN output is parameterized by an observable — the charged Higgs boson mass — allowing the network to interpolate between discrete mass values and replace the need for training separate classifiers at each point. A single PNN is trained on all signal samples using Keras [236] with TensorFlow [237] as a backend. Since background events are reused across the 32 simulated mass points, they are weighted to the cross-section predictions to avoid statistical bias. This strategy improves efficiency and simplifies the analysis by enabling a single model to evaluate events at any $H^+$ mass.

In this analysis, the $k$-fold training method, with $k = 5$, is used by dividing the input samples into $k$ equally sized subsets. Then, each of the $k$ PNN discriminants is trained on $k - 1$ subsets (with an 80/20% split into training and evaluation) and validated on the remaining subset. This method optimizes statistical usage by ensuring $(k - 2)/k$ part of events is used for training and the $1/k$ part for validation, while reducing the risk of overfitting through independent evaluation on unseen subsets.

The PNNs are trained independently for $\tau_{\text{had}-\text{vis}}$+jets events and $\tau_{\text{had}-\text{vis}}$+lepton events ($\tau_{\text{had}-\text{vis}}$ + electron and $\tau_{\text{had}-\text{vis}}$ + muon channels are combined to increase the training data). Furthermore, the training differs based on the number of associated tracks (one or three) to the leading $\tau_{\text{had}-\text{vis}}$ candidate. The 1-prong $\tau_{\text{had}-\text{vis}}$ PNN model is trained solely on 1-prong $\tau_{\text{had}-\text{vis}}$ events, while the 3-prong $\tau_{\text{had}-\text{vis}}$ PNN model is trained on both 1-prong and 3-prong $\tau_{\text{had}-\text{vis}}$ events to enhance the training statistics. The input variables utilized in the PNN training, summarized in Table 13, varied across the two final state categories considered in this study.

Table 13: Input variables used in the PNN training for the $\tau_{\text{had-vis}}$+jets and $\tau_{\text{had-vis}}$+lepton channels [11].

| **PNN input variable** | $\tau_{\text{had-vis}}$ + jets | $\tau_{\text{had-vis}}$ + lepton |
|---|---|---|
| $p_T^\tau$, $\eta^\tau$, $\phi^\tau$, $E^\tau$ | ✓ | ✓ |
| $p_T^\ell$, $\eta^\ell$, $\phi^\ell$, $E^\ell$ | | ✓ |
| $p_T^{b\text{-jet}}$, $\eta^{b\text{-jet}}$, $\phi^{b\text{-jet}}$, $E^{b\text{-jet}}$ | ✓ | ✓ |
| $p_T^{\text{jet-1}}$, $\eta^{\text{jet-1}}$, $\phi^{\text{jet-1}}$, $E^{\text{jet-1}}$ | ✓ | ✓ |
| $p_T^{\text{jet-2}}$, $\eta^{\text{jet-2}}$, $\phi^{\text{jet-2}}$, $E^{\text{jet-2}}$ | ✓ | ✓ |
| $p_T^{\text{jet-3}}$, $\eta^{\text{jet-3}}$, $\phi^{\text{jet-3}}$ | ✓ | ✓ |
| $p_T^{\text{jet-2}}$ | ✓ | |
| $E_T^{\text{miss}}$, $\phi^{E_T^{\text{miss}}}$ | ✓ | ✓ |
| $\Upsilon^a$ | ✓ | ✓ |
| $m_{\text{truth}}^{\text{H}^+}$ | ✓ | ✓ |

[a] For 1-prong $\tau_{\text{had-vis}}$ only.

Efficient discrimination between signal and background is provided by the transverse mass $m_{\mathrm{T}}$ of the $\tau_{\text{had-vis}}$ candidate and $E_{\mathrm{T}}^{\text{miss}}$, especially for analyses targeting high $H^+$ masses. The MVA strategy decomposes this quantity into its three components: $p_{\mathrm{T}}^{\tau}$, $E_{\mathrm{T}}^{\text{miss}}$, and $\Delta\phi_{\tau,\text{miss}}$. These individual features carry equivalent information to the original quantity, but may potentially provide richer and more nuanced information to the analysis. The other variables, which are based on either transverse momenta or angular separation, provide a detailed examination of the kinematic characteristics of the events under consideration.

At low $H^+$ masses, the kinematics of the $t \to bH^+$ and $t \to bW$ decay products are similar. In that case, the polarization of the $\tau$-lepton is employed as a discriminating variable via $\Upsilon$ variable introduced in Section 2.3.1. It is defined for all $\tau_{\text{had-vis}}$ candidates with only one associated track, and $p_{\mathrm{T}}^{\tau}$ is the transverse momentum of that track. The PNN training is performed separately for events with a selected 1- or 3-prong $\tau_{\text{had-vis}}$ object, and $\Upsilon$ is included in the PNN discriminant only for events where the $\tau_{\text{had-vis}}$ has one associated track. While $\Upsilon$ is one of the most discriminating input variables of the PNN at low $H^+$ masses, the importance of other kinematic variables in the PNN training becomes much greater at large $H^+$ masses, in particular, the three variables entering the computation of the transverse mass, i.e., $E_T^{\text{miss}}$, $p_{\mathrm{T}}^{\tau}$ and $\Delta\phi_{\tau,\text{miss}}$.

The modeling of the PNN input variables and the output score is validated in the CRs. The PNN score distributions are illustrated in Figure 58 for an exemplary $H^+$ mass of 170 GeV in the $t\bar{t}$ enriched $\tau_{\text{had}}$ + jets $t\bar{t}$ CR, as well as in the $W/Z$ + jets enriched $b$-veto CR of the $\tau_{\text{had}} + \mu$ channel. In addition, the PNN scores for two example signal masses (170 GeV and 1000 GeV) are presented in Figure 59 for the $\tau_{\text{had}}$ + jets SR, the $\tau_{\text{had}}$ + electron SR and $\tau_{\text{had}}$ + muon SR.

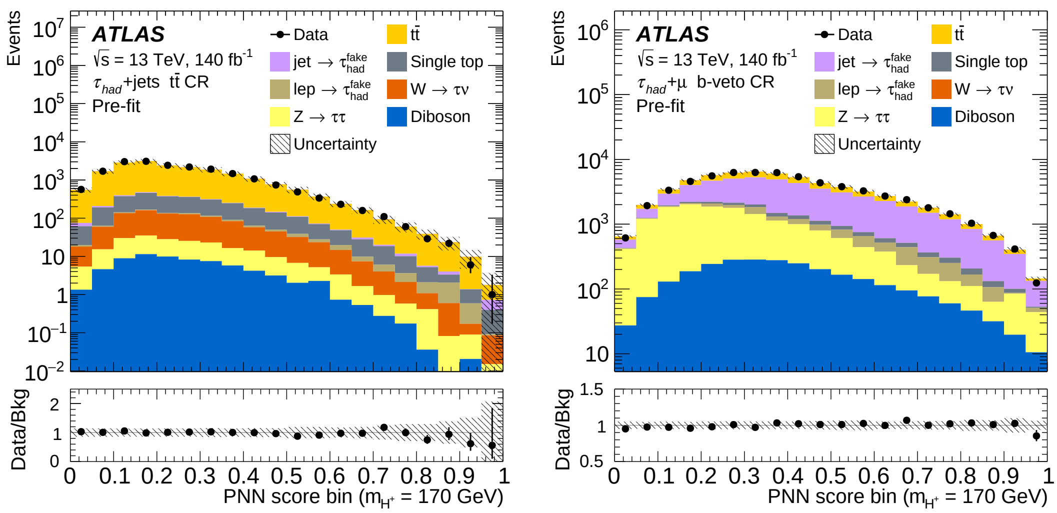


(a) (b)

Figure 58: Predicted and measured PNN score distributions before the fit to data ("Pre-fit") in the $t\bar{t}$ enriched CR of the $\tau_{\text{had}}$ + jets channel (a) and the $b$-veto CR of the $\tau_{\text{had}}$ + muon channel enriched in the $W/Z$ + jets events with jets faking $\tau_{\text{had-vis}}$ (b), for the 170 GeV $m_{H^+}$ hypothesis. The lower panel of each plot shows the ratio of data to the SM background prediction. The uncertainty bands include all statistical and systematic uncertainties. The bin boundaries of these distributions are spaced equally at intervals of 0.05 and do not represent the binning scheme used in the final fits [11].

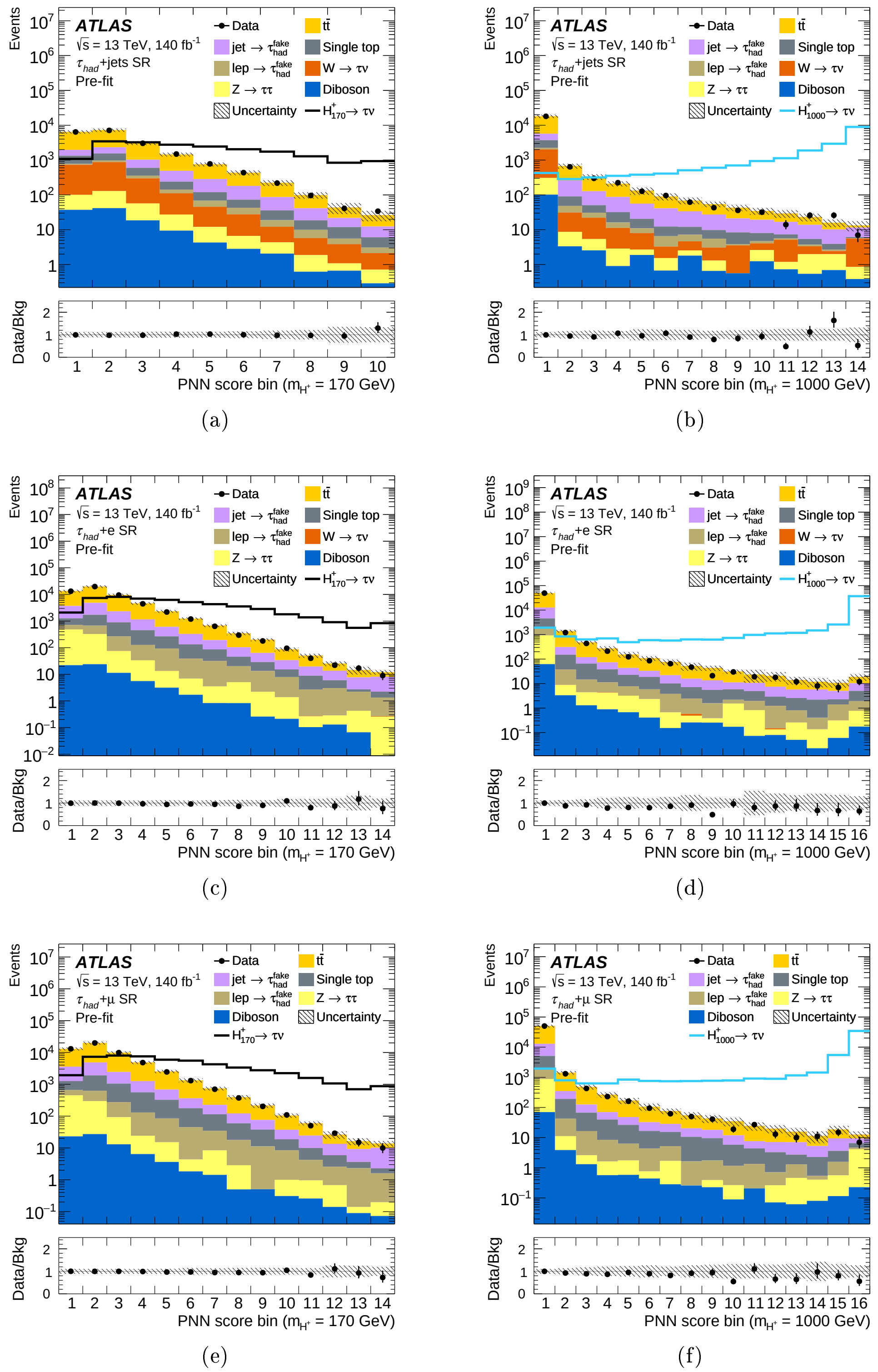


Figure 59: PNN score distributions before the fit to data ("Pre-fit") in the SR of the $\tau_{\text{had}}$+jets for the 170 GeV (a) and 1000 GeV (b) $m_{H^+}$ hypotheses, the $\tau_{\text{had}}$+electron sub-channel for the 170 GeV (c) and 1000 GeV (d) $m_{H^+}$ hypotheses and $\tau_{\text{had}}$+muon sub-channel for the 170 GeV (e) and 1000 GeV (f) $m_{H^+}$ hypotheses. The lower panel of each plot shows the ratio of data to the SM background prediction. The uncertainty bands include all statistical and systematic uncertainties. Bin boundaries are optimized for the best sensitivity of the final fit but are displayed as equidistant for better readability. Also, the expected signal distributions are shown, normalized to the total background yield [11].

## 6.5 Background estimation

The primary background contributions are categorized based on the source object responsible for the identified hadronic $\tau$ candidate. The MC simulated event samples are employed to assess backgrounds where the hadronic $\tau$ candidate is derived from an electron, muon, or hadronically decaying $\tau$ lepton. Conversely, a data-driven methodology is used for all other cases.

### 6.5.1 Electron Faking $\tau_{\text{had-vis}}$ Candidates

To investigate the modeling of electrons misidentified as $\tau_{\text{had-vis}}$ candidates in simulation, a dedicated control region enriched in $Z \to ee$ events is defined, with the following event selection:

- single-electron trigger, the same as used in the $\tau_{\text{had-vis}}$+lepton signal region;
- one *tight* electron with $E_{\text{T}} > 30$ GeV matched to the trigger;
- one *medium* $\tau_{\text{had-vis}}$ candidate with $p_{\text{T}}^{\tau} > 40$ GeV and an electric charge opposite to that of the selected electron;
- no $b$-tagged jets or muons;
- at least one jet with $p_{\text{T}} > 25$GeV;
- the invariant mass of the $\tau_{\text{had-vis}} + e$ system is between 80 GeV and 110 GeV.

The selected events contain a promptly produced electron that is reconstructed and identified as a *medium* $\tau_{\text{had-vis}}$ candidate, rather than being identified as an electron. The $e$-$\tau_{\text{had-vis}}$ visible mass distribution, as well as the transverse mass distribution of the $\tau_{\text{had-vis}} + E_{\text{T}}^{\text{miss}}$ system, in the $Z \to ee$ CR are presented in Figure 60. The simulation of misidentified electrons as $\tau_{\text{had-vis}}$ candidates is satisfactory in the Sherpa $Z \to ee$ samples. Consequently, no further scale factors are applied apart from the recommended $e \to \tau_{\text{had-vis}}$ scale factors.

### 6.5.2 Fake-factor Method for jet$\to \tau_{\text{had-vis}}$ Background Estimation

Hadronic jets originating from quarks or gluons may be falsely reconstructed and classified as $\tau_{\text{had-vis}}$ candidates, allowing them to contaminate the signal region. Accurate modeling of these background processes is challenged by the limited statistical sample of simulated events (e.g. multi-jet processes), as well as the lack of good understanding of the systematic uncertainties associated with those objects. Consequently, a data-driven method is employed to estimate this background contribution.

**Basics of the Method:** The Fake-factor (FF) method estimates the contribution from jets misidentified as $\tau_{\text{had-vis}}$ candidates based on the measured rate at which quark- or gluon-initiated jets are reconstructed and pass the $\tau_{\text{had-vis}}$ identification criteria. The method involves applying weights to a specific subset of so-called anti-$\tau_{\text{had-vis}}$ objects, which are defined as events failing to meet the standard $\tau_{\text{had-vis}}$ identification criteria within the signal region. The fake-factors, serving as weights, are defined as the ratio of the number of fake $\tau_{\text{had-vis}}$ candidates that pass the nominal identification criteria ($N_{\text{CR}}^{\tau-\text{id}}$) to those satisfying the anti-$\tau$ control region criteria ($N_{\text{CR}}^{\text{anti}-\tau-\text{id}}$). They are measured in the control region (CR) enriched with jet$\to \tau_{\text{had-vis}}$ background events and with a similar composition of gluon/quark-initiated jets as the signal region. The FFs in a given control region are:

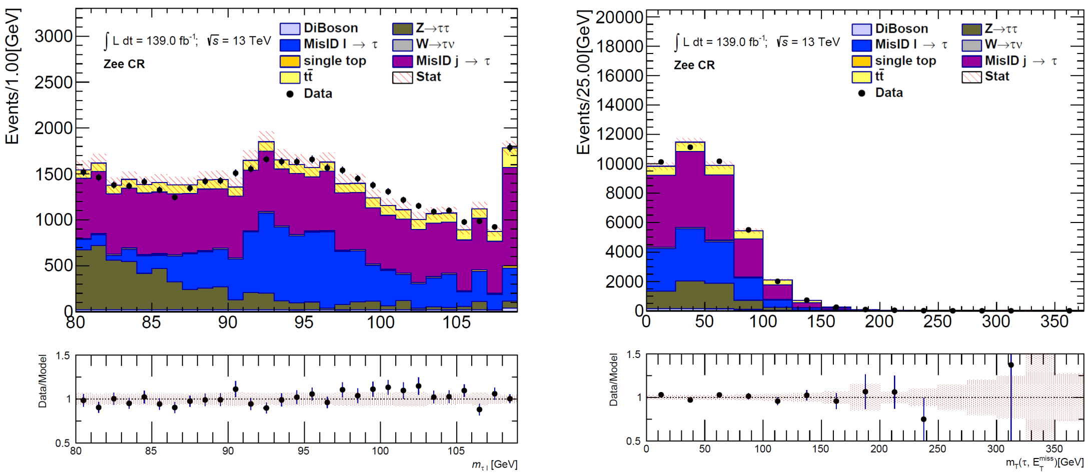


(a) (b)

Figure 60: Distribution of the $e \to \tau_{\text{had-vis}}$ visible mass (a) and transverse mass (b) of the $\tau_{\text{had-vis}} + E_{\text{T}}^{\text{miss}}$ system in the $Z \to ee$ control region. The recommended $e \to \tau_{\text{had-vis}}$ scale factors are applied. Jets misidentified as $\tau_{\text{had-vis}}$ are estimated from data using the FF method. The $l \to \tau$ background includes all processes with e or $\mu$ reconstructed and identified as the $\tau_{\text{had-vis}}$. All other SM backgrounds are derived from MC simulation. Error bars represent statistical uncertainties.

$$\text{FF} = \frac{N_{\text{CR}}^{\tau-\text{id}}}{N_{\text{CR}}^{\text{anti}-\tau-\text{id}}}, \tag{62}$$

In the previous equation, both $N_{\text{CR}}^{\tau-\text{id}}$ and $N_{\text{CR}}^{\text{anti}-\tau-\text{id}}$ are corrected for $\tau_{\text{had-vis}}$ candidates matching a true hadronic $\tau$ events at the generator level:

$$N_{\text{CR}}^{\tau-\text{id}} = N_{\text{CR}}^{\tau-\text{id}}(\text{data}) - N_{\text{CR,true}}^{\tau-\text{id}}(\text{MC}) \tag{63}$$

$$N_{\text{CR}}^{\text{anti}-\tau} = N_{\text{CR}}^{\text{anti}-\tau}(\text{data}) - N_{\text{CR,true}}^{\text{anti}-\tau}(\text{MC}) \tag{64}$$

Ultimately, the number of fake $\tau_{\text{had-vis}}$ objects in the signal region ($N_{\text{SR}}^{\text{fake}-\tau}$) is determined as follows:

$$N_{\text{SR}}^{\text{fake}-\tau} = N_{\text{SR}}^{\text{anti}-\tau} \times \text{FF}, \tag{65}$$

where $N_{\text{SR}}^{\text{anti-}\tau}$ is also corrected by subtracting the contribution from generator-level true hadronic $\tau$ candidates.

### 6.5.3 Fake-factor Method in the $H^+ \to \tau\nu$ Analysis

For the FFs extraction in the in the $H^+ \to \tau\nu$ analysis, the following anti-$\tau$ control region selection criteria are applied to reconstructed $\tau_{\text{had-vis}}$ objects:

- failing the loose $\tau$ RNN-based ID working point,
- RNN score $> 0.01$ (to ensure that the $\tau_{\text{had-vis}}$ object and event topology closely resemble those of the signal region.).

The dominant sources of the jet$\to \tau_{\text{had-vis}}$ background in the signal region are $t\bar{t}$ and multi-jet processes. Within $t\bar{t}$ processes, the misidentified $\tau_{\text{had-vis}}$ candidates come mainly from quark-initiated jets. On the other hand, in multi-jet events, both quark- and gluon-initiated jets contribute substantially.

The rates of the quark- or gluon-initiated fake $\tau_{\text{had}-\text{vis}}$ objects in the signal regions are not known a priori, hence two control regions with different jet compositions are utilized in order to estimate them:

- The first control region is the multi-jet CR. Similar to the $\tau_{\text{had}-\text{vis}}$+jets SR, events are collected using a combination of multijet triggers. The selection criteria are:
  - at least one *medium* $\tau_{\text{had-vis}}$ candidate with $p_{\text{T}} > 30$ GeV,
  - no $b$-jets or leptons (electron or muon),
  - at least three jets with $p_{\text{T}} > 25$ GeV,
  - $E_{\text{T}}^{\text{miss}} < 80$ GeV,
  - $m_{\text{T}}(\tau, E_{\text{T}}^{\text{miss}}) > 50$ GeV.
- The second control region is the $W$+jets CR, where the fake $\tau_{\text{had}-\text{vis}}$ composition is dominated by quark-initiated jets. It has the following requirements:
  - exactly one electron or muon with $p_{\text{T}} > 30$ GeV;
  - zero $b$-tagged jets;
  - at least one reconstructed $\tau_{\text{had}-\text{vis}}$ candidate;
  - 60 GeV$< m_{\text{T}}(\ell, E_{\text{T}}^{\text{miss}}) <$ 160GeV.

The FFs show a strong dependence on the $p_{\text{T}}$ of the $\tau_{\text{had}-\text{vis}}$ candidate, therefore a $\tau_{\text{had}-\text{vis}}$ $p_{\text{T}}$ parametrization is applied. The FFs measured in these two control regions are presented in Figure 61. In the multi-jet CR, the contamination arising from correctly reconstructed and identified $\tau_{\text{had}-\text{vis}}$ objects is small (8%), while in the $W$+jets CR, this contamination is approximately 20%. In the corresponding anti-$\tau$ regions, the fraction of candidates matching a true hadronic $\tau$ events at the generator level is negligible in the multi-jet CR and around 6% in the $W$+jets CR. The contribution from true $\tau$ events in the above mentioned categories is subtracted using simulation. Transverse mass distributions for $\tau$ identification and anti-$\tau$ identification in both CRs are shown in Figure 62.

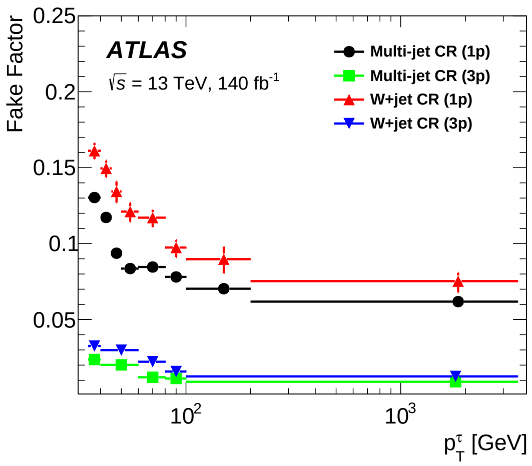


Figure 61: Fake-factors parameterized as a function of $p_{\text{T}}^{\tau}$ and the number of charged $\tau$ decay products (1-prong and 3-prong) obtained in the multi-jet and $W$+jets CRs. Error bars represent the full systematic uncertainties.

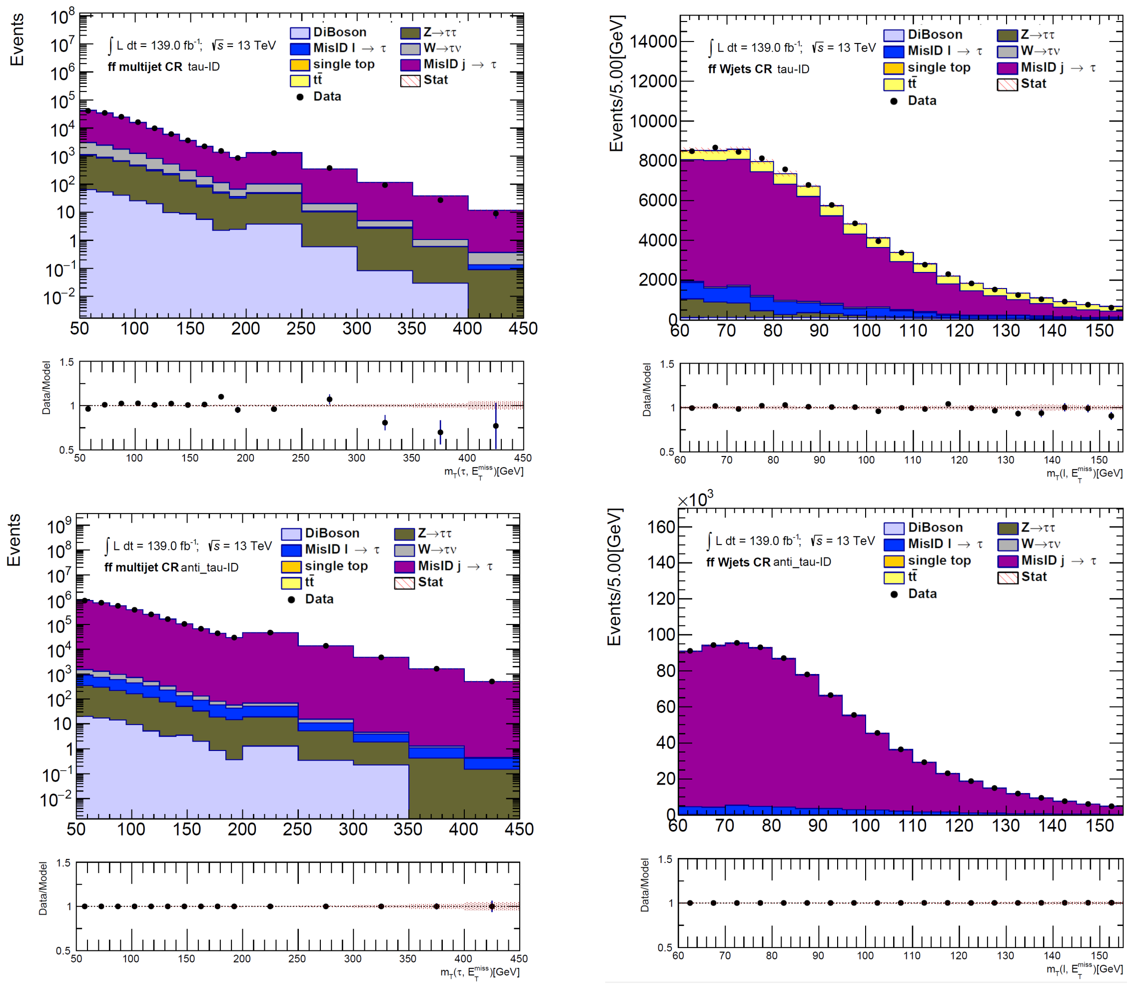


Figure 62: Transverse mass distributions for events passing the $\tau$ identification criteria in the multi-jet CR (a) and the W+jets CR (b), where jets misidentified as $\tau_{\text{had-vis}}$ are estimated from data using the FF method, as well as for events passing the anti-$\tau$ identification criteria in the multi-jet CR (c) and the W+jets CR (d). The $l \to \tau$ background includes all processes with $e$ or $\mu$ reconstructed and identified as the $\tau_{\text{had-vis}}$. All other backgrounds correspond to events where the $\tau_{\text{had-vis}}$ object matches a hadronic $\tau$ decay at the generator level. These backgrounds are derived from simulation. Only statistical uncertainties are presented.

### 6.5.4 Estimation of the Combined Fake-Factors

The signal region is expected to have contributions from both quark- and gluon-initiated jets, but with varying fractions. One can consider two populations of jets with different fake-factors such that the total fake-factors in the SR can be expressed by:

$$\text{FF}_{\text{SR}} = f_g^{\text{SR}} \times \text{FF}_g + \left(1 - f_g^{\text{SR}}\right) \times \text{FF}_q, \tag{66}$$

where $f_g^{\text{SR}}$ refers to the fraction of gluon-initiated jets in the signal region. The $\text{FF}_g$ and $\text{FF}_q$ are the fake-factors of these two populations (denoted by $g$ for gluon-initiated jets and $q$ for quark-initiated jets).

Similarly, the fake-factors in both FF CRs can be written as follows:

$$\text{FF}_{\text{MJ}} = f_g^{\text{MJ}} \times \text{FF}_g + \left(1 - f_g^{\text{MJ}}\right) \times \text{FF}_q, \tag{67}$$

$$\mathrm{FF}_{W+\mathrm{jets}} = f_g^{W+\mathrm{jets}} \times \mathrm{FF}_g + \left(1 - f_g^{W+\mathrm{jets}}\right) \times \mathrm{FF}_q, \tag{68}$$

Here $f_g^{\mathrm{MJ}}$ and $f_g^{W+\mathrm{jets}}$ represent the fractions of gluon-initiated jets in the multi-jet and $W$+jets CRs.

One can introduce the $\alpha_{\mathrm{MJ}}$ parameter as:

$$\alpha_{\mathrm{MJ}} := \frac{f_g^{\mathrm{SR}} - f_g^{W+\mathrm{jets}}}{f_g^{\mathrm{MJ}} - f_g^{W+\mathrm{jets}}}. \tag{69}$$

Ultimately, Equation (66) can be rewritten as a function of $\alpha_{\mathrm{MJ}}$ and the fake-factors extracted from the multi-jet and $W$+jets CRs:

$$\mathrm{FF}_{\mathrm{SR}} = \alpha_{\mathrm{MJ}} \times \mathrm{FF}_{\mathrm{MJ}} + (1 - \alpha_{\mathrm{MJ}}) \times \mathrm{FF}_{W+\mathrm{jets}}. \tag{70}$$

It is worth mentioning that $\alpha_{\mathrm{MJ}}$ can get negative values when the signal region has a larger fraction of quark-initiated jets than in the $W$+jets CR ($f_g^{\mathrm{SR}} \leq f_g^{W+\mathrm{jets}}$), and values greater than one when the signal region has a larger fraction of gluon-initiated jets than the multi-jet CR ($f_g^{\mathrm{SR}} \geq f_g^{\mathrm{MJ}}$).

Estimation of $\alpha_{\mathrm{MJ}}$ is done by utilizing a template-fit method, which uses discriminating variable sensitive to the origin of the jet:

1. The normalized distributions of the discriminating variable (called "templates"), which is sensitive to the fraction of gluon-initiated jets, are created for both multi-jet and $W$+jets CRs. The chosen variable is the $\tau_{\mathrm{had-vis}}$ width for both 1-prong and 3-prong $\tau_{\mathrm{had-vis}}$ candidates, defined as:
$$w_\tau = \frac{\sum \left[p_{\mathrm{T}}^{\mathrm{track}} \times \Delta R\left(\tau_{\mathrm{had-vis}}, \mathrm{track}\right)\right]}{\sum p_{\mathrm{T}}^{\mathrm{track}}} \tag{71}$$
for tracks satisfying $\Delta R\left(\tau_{\mathrm{had-vis}}, \mathrm{track}\right) < 0.4$. These templates for anti-$\tau_{\mathrm{had-vis}}$ candidates are obtained from the experimental data, for different bins of $p_{\mathrm{T}}$ and a number of associated tracks of the fake $\tau_{\mathrm{had-vis}}$ ($P_{\mathrm{bin}}^{\mathrm{multi-jet}}(x)$ and $P_{\mathrm{bin}}^{W+\mathrm{jets}}(x)$).

2. Next, the weighted combination of the two shapes is estimated using $\alpha_{\mathrm{MJ}}$ parameter:
$$P_{\mathrm{bin}}^{\alpha_{\mathrm{MJ}}}(x) = \alpha_{\mathrm{MJ}} \times P_{\mathrm{bin}}^{\mathrm{multi-jet}}(x) + (1 - \alpha_{\mathrm{MJ}}) \times P_{\mathrm{bin}}^{W+\mathrm{jets}}(x). \tag{72}$$

3. The combination is fitted to the shape measured for anti-$\tau_{\mathrm{had-vis}}$ candidates in the signal region $P_{\mathrm{bin}}^{\mathrm{SR}}(x)$, by minimizing the $\chi^2$ as a function of $\alpha_{\mathrm{MJ}}$:
$$\chi^2_{\mathrm{bin}}\left(\alpha_{\mathrm{MJ}}\right) = \sum_{x=0}^{K+1} \frac{\left(P_{\mathrm{bin}}^{\alpha_{\mathrm{MJ}}}(x) - P_{\mathrm{bin}}^{\mathrm{SR}}(x)\right)^2}{\left(\sigma_{\mathrm{bin}}^{\mathrm{template}}(x)\right)^2 + \left(\sigma_{\mathrm{bin}}^{\mathrm{SR}}(x)\right)^2}, \tag{73}$$
where $\sigma_{\mathrm{bin}}(x)$ is the statistical uncertainty and $K+1$ is the number of bins in the $\tau_{\mathrm{had-vis}}$ width in the template distribution (later denoted as the number of degrees of freedom, or ndf). The distribution of $\chi^2_{\mathrm{bin}}$ can be described by a $\chi^2$-function with $K$ degrees of freedom, which has a mean and a variance of $K$ and $2K$, respectively.

The template shapes obtained in the FF control regions ($P_{\mathrm{bin}}^{\mathrm{multi-jet}}(x)$ and $P_{\mathrm{bin}}^{W+\mathrm{jets}}(x)$), the template shape in the region of interest $P_{\mathrm{bin}}^{\mathrm{ROI}}(x)$ together with the fitted shape ($P_{\mathrm{bin}}^{\alpha_{\mathrm{MJ}}}(x)$) minimizing $\chi^2\left(\alpha_{\mathrm{MJ}}\right)$, and the distribution of $\chi^2/\mathrm{ndf}$ as a function of the varying parameter $\alpha_{\mathrm{MJ}}$, are all shown in Figures 63–65 for the $\tau_{\mathrm{had-vis}}$+jets SR and in Figures 66–69 for the $\tau_{\mathrm{had-vis}}$+lepton SR. An uncertainty on the fit is considered by taking a band within $\sqrt{2/\mathrm{ndf}}$ from $\chi^2_{\mathrm{min}}/\mathrm{ndf}$ (the smallest value of the $\chi^2$-function) [238]. The fitted $\alpha_{\mathrm{MJ}}$ numerical values for $\tau_{\mathrm{had-vis}}$+jets and $\tau_{\mathrm{had-vis}}$+lepton signal regions are gathered in Table 14.

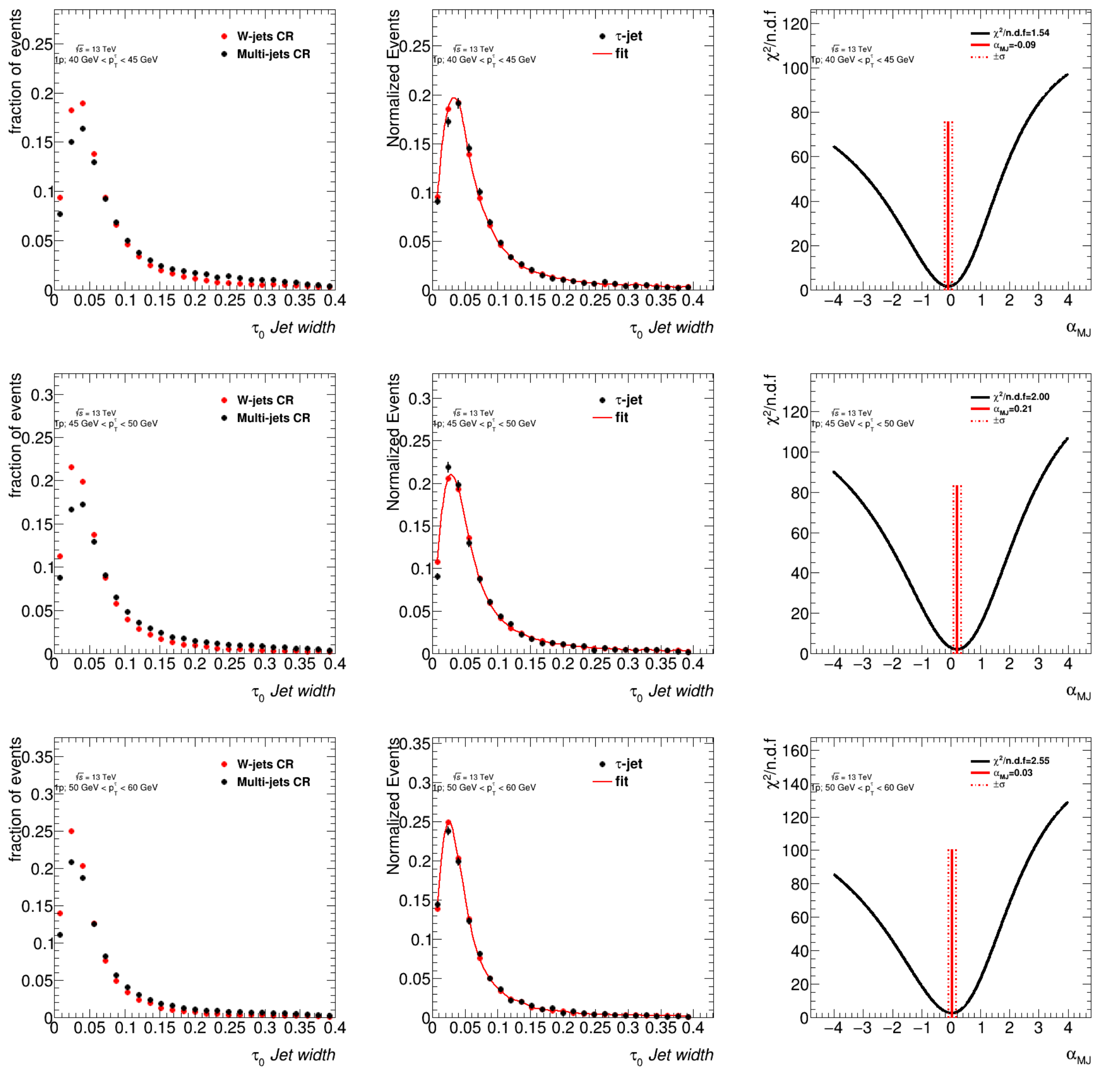


Figure 63: The procedure of $\alpha_{\mathrm{MJ}}$ estimation in the $\tau_{\mathrm{had-vis}}$+jets signal region for $p_{\mathrm{T}} \leq 60$ GeV 1-prong $\tau_{\mathrm{had-vis}}$ candidates. Left-hand side: measured templates of the discriminating variable for multi-jet and $W$+jets CRs in various $\tau_{\mathrm{had-vis}}$ $p_{\mathrm{T}}$ bins. Center: template of the discriminating variable obtained in the SR and fitted combination of the two CRs shapes using $\alpha_{\mathrm{MJ}}$ parameter. Right-hand side: $\chi^2$/ndf of the fit as a function of $\alpha_{\mathrm{MJ}}$, the $\alpha_{\mathrm{MJ}}$ unceratinty is determined by the band at $\chi^2_{\mathrm{min}}/\mathrm{ndf} + \sqrt{\frac{2}{\mathrm{ndf}}}$.

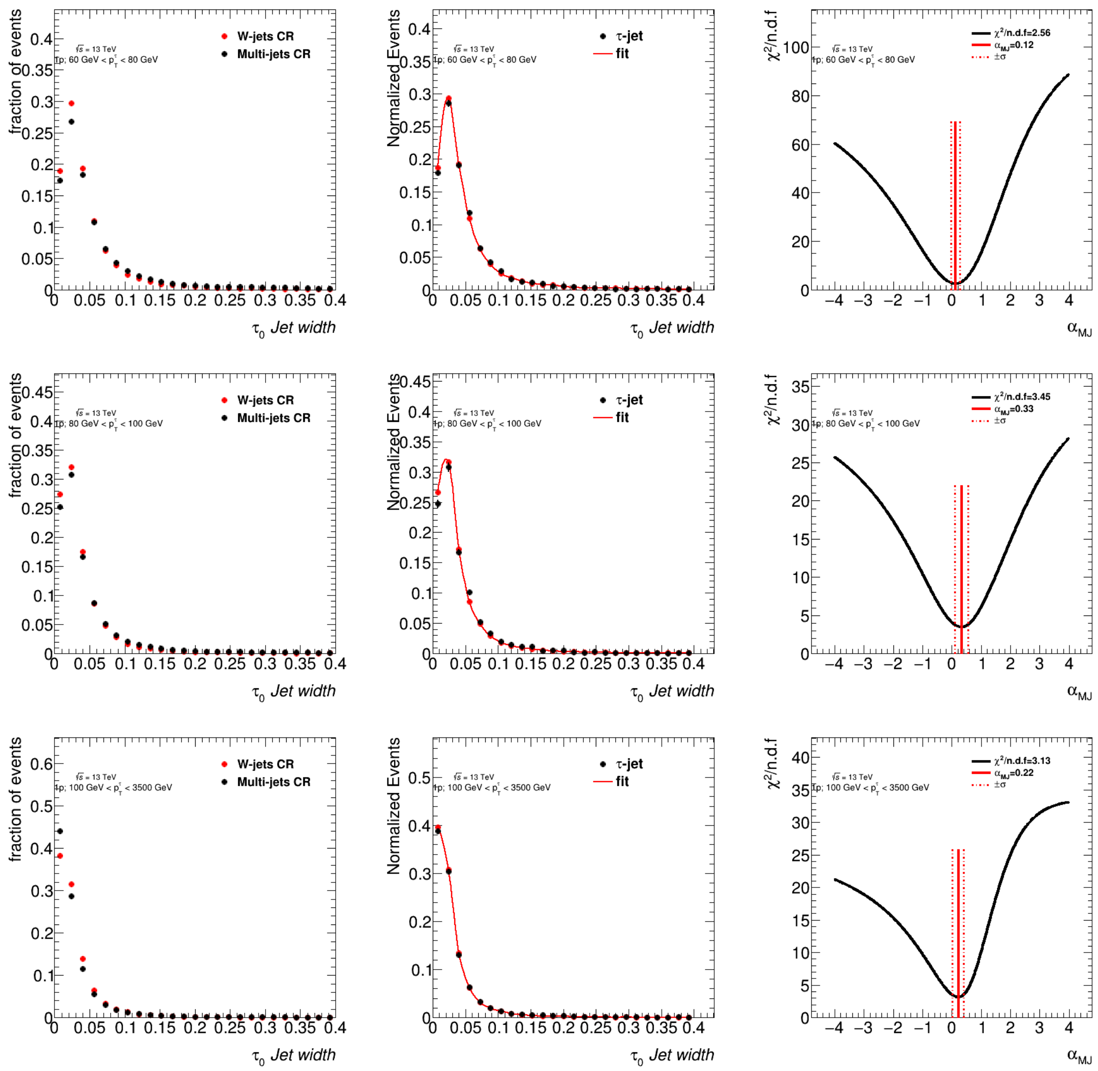


Figure 64: The procedure of $\alpha_{\mathrm{MJ}}$ estimation in the $\tau_{\mathrm{had-vis}}$+jets SR for $p_{\mathrm{T}} \geq 60$ GeV 1-prong $\tau_{\mathrm{had-vis}}$ candidates. Left-hand side: measured templates of the discriminating variable for multi-jet and $W$+jets CRs in various $\tau_{\mathrm{had-vis}}$ $p_{\mathrm{T}}$ bins. Center: template of the discriminating variable obtained in the SR and fitted combination of the two CRs shapes using $\alpha_{\mathrm{MJ}}$ parameter. Right-hand side: $\chi^2$/ndf of the fit as a function of $\alpha_{\mathrm{MJ}}$, the $\alpha_{\mathrm{MJ}}$ uncertainty is determined by the band at $\chi^2_{\mathrm{min}}/\mathrm{ndf} + \sqrt{\frac{2}{\mathrm{ndf}}}$.

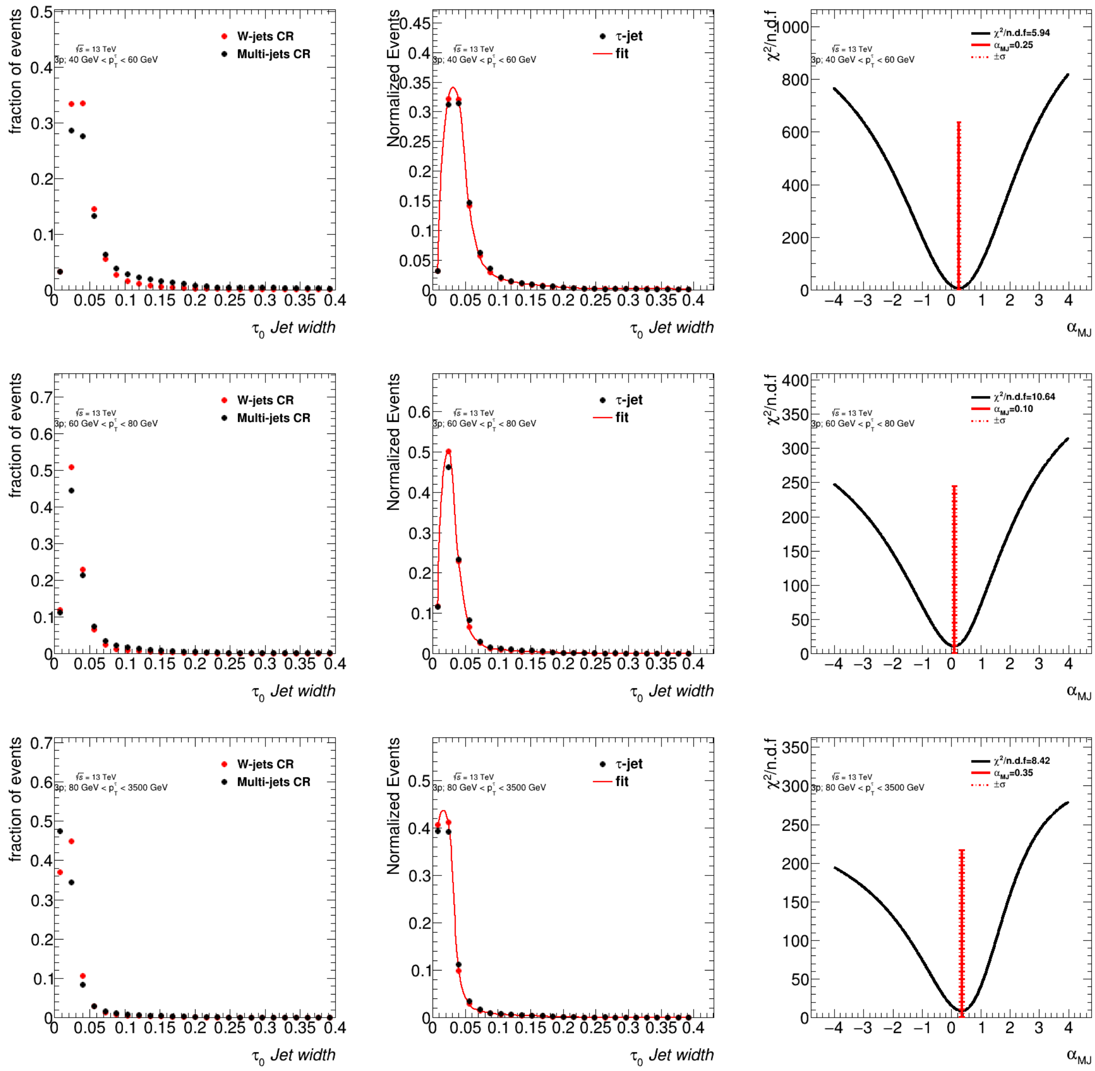


Figure 65: The procedure of $\alpha_{\rm MJ}$ estimation in the $\tau_{\rm had-vis}$+jets SR for 3-prong $\tau_{\rm had-vis}$ candidates. Left-hand side: measured templates of the discriminating variable for multi-jet and $W$+jets CRs in various $\tau_{\rm had-vis}$ $p_{\rm T}$ bins. Center: template of the discriminating variable obtained in the SR and fitted combination of the two CRs shapes using $\alpha_{\rm MJ}$ parameter. Right-hand side: $\chi^2$/ndf of the fit as a function of $\alpha_{\rm MJ}$, the $\alpha_{\rm MJ}$ uncertainty is determined by the band at $\chi^2_{\rm min}/{\rm ndf} + \sqrt{\frac{2}{\rm ndf}}$.

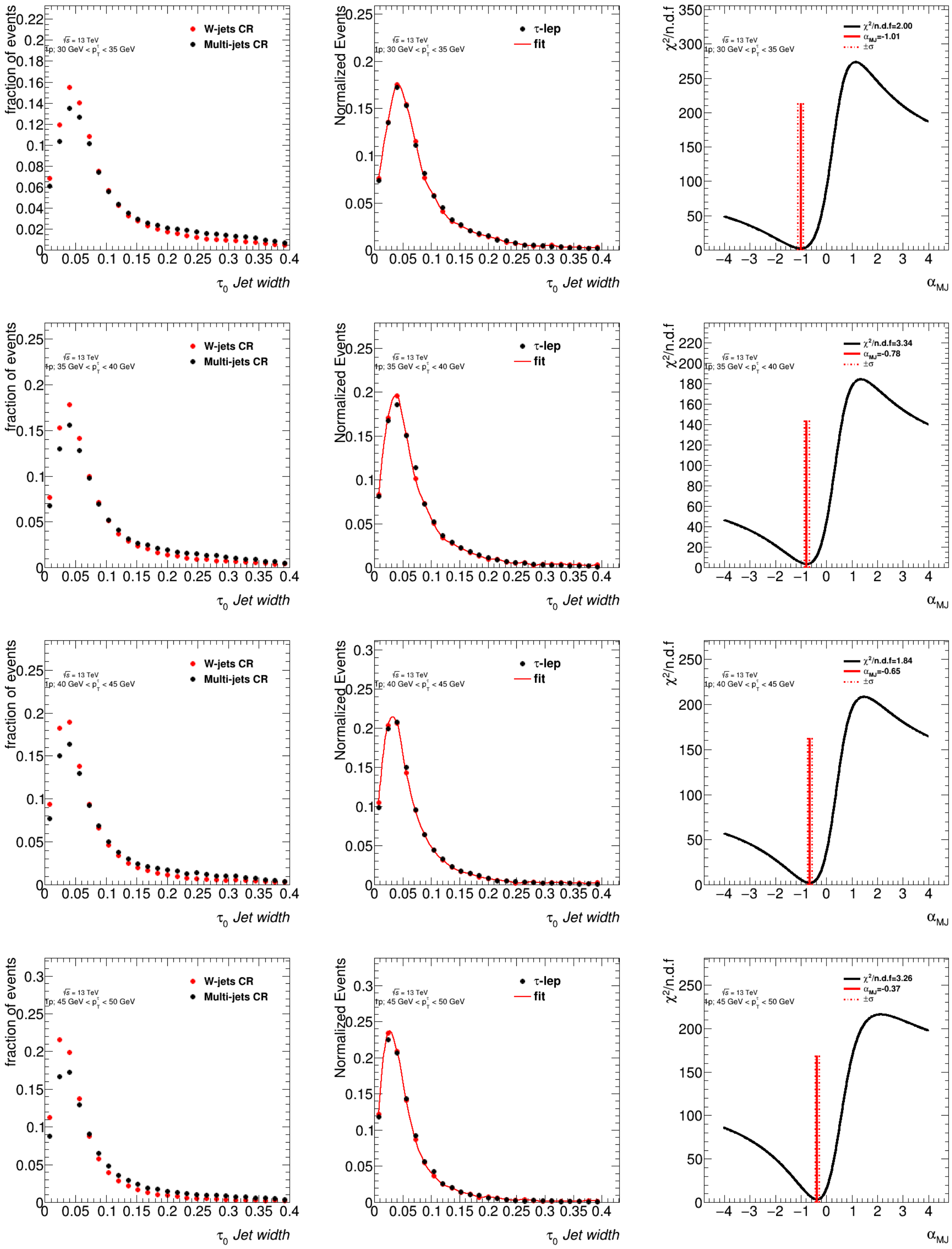


Figure 66: The procedure of $\alpha_{\mathrm{MJ}}$ estimation in the $\tau_{\mathrm{had-vis}}$+lepton SR for $p_{\mathrm{T}} \leq 50$ GeV 1-prong $\tau_{\mathrm{had-vis}}$ candidates. Left-hand side: measured templates of the discriminating variable for multi-jet and $W$+jets CRs in various $\tau_{\mathrm{had-vis}}$ $p_{\mathrm{T}}$ bins. Center: template of the discriminating variable obtained in the SR and fitted combination of the two CRs shapes using $\alpha_{\mathrm{MJ}}$ parameter. Right-hand side: $\chi^2$/ndf of the fit as a function of $\alpha_{\mathrm{MJ}}$, the $\alpha_{\mathrm{MJ}}$ uncertainty is determined by the band at $\chi^2_{\mathrm{min}}/\mathrm{ndf} + \sqrt{\frac{2}{\mathrm{ndf}}}$.

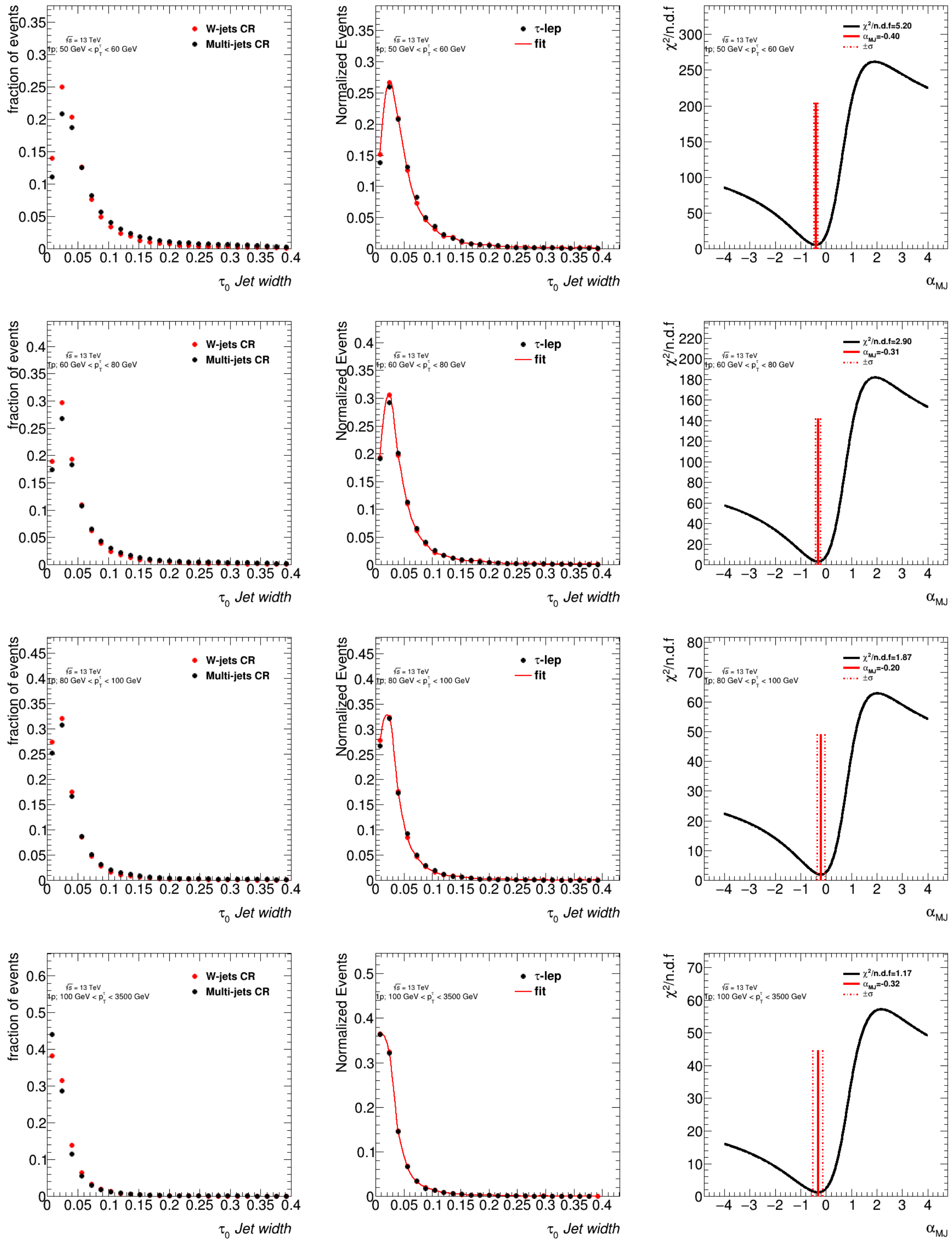


Figure 67: The procedure of $\alpha_{\mathrm{MJ}}$ estimation in the $\tau_{\mathrm{had-vis}}$+lepton SR for $p_{\mathrm{T}} \geq 50$ GeV 1-prong $\tau_{\mathrm{had-vis}}$ candidates. Left-hand side: measured templates of the discriminating variable for multi-jet and $W$+jets CRs in various $\tau_{\mathrm{had-vis}}$ $p_{\mathrm{T}}$ bins. Center: template of the discriminating variable obtained in the SR and fitted combination of the two CRs shapes using $\alpha_{\mathrm{MJ}}$ parameter. Right-hand side: $\chi^2$/ndf of the fit as a function of $\alpha_{\mathrm{MJ}}$, the $\alpha_{\mathrm{MJ}}$ uncertainty is determined by the band at $\chi^2_{\mathrm{min}}/\mathrm{ndf} + \sqrt{\frac{2}{\mathrm{ndf}}}$.

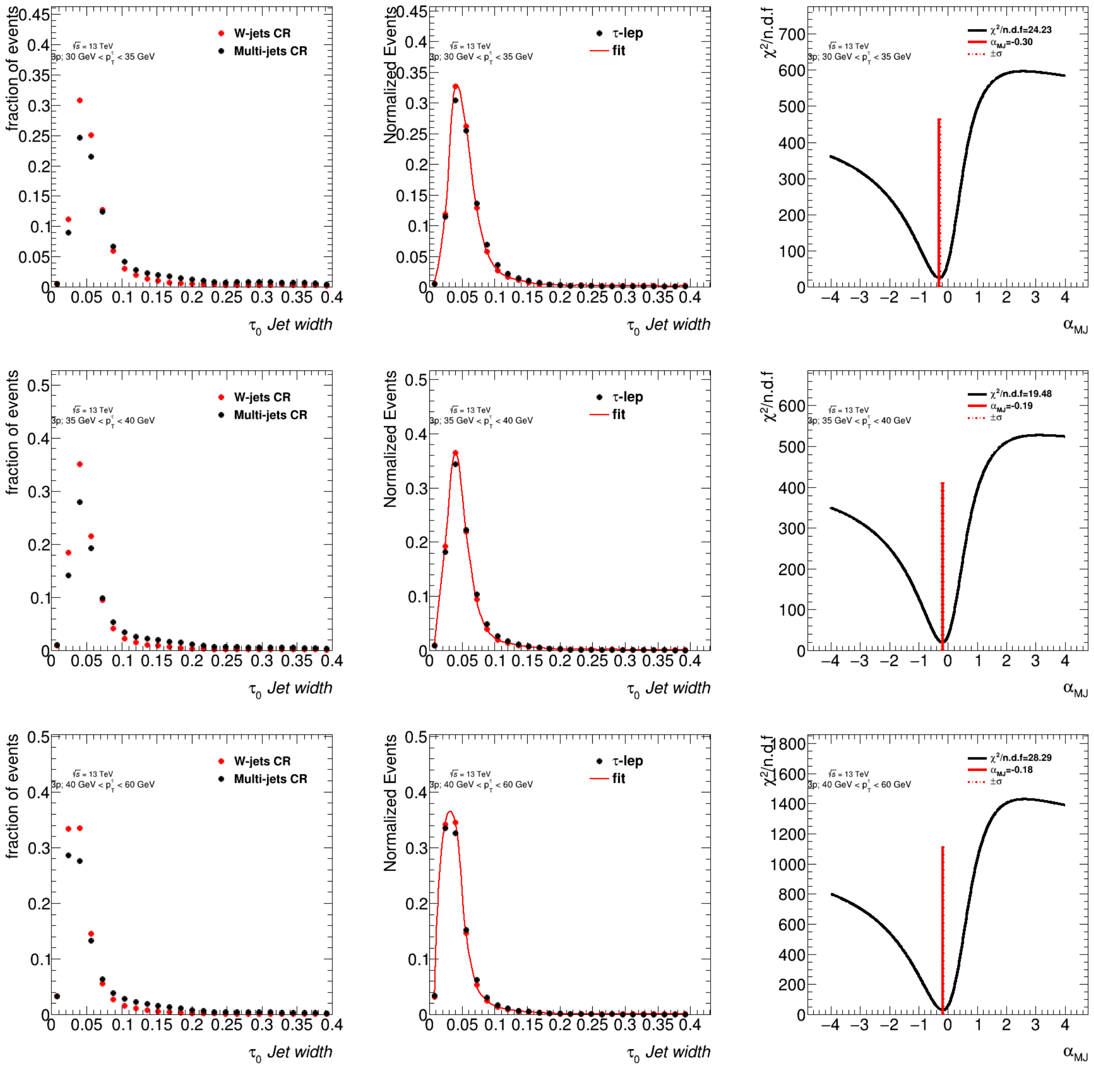


Figure 68: The procedure of $\alpha_{\mathrm{MJ}}$ estimation in the $\tau_{\mathrm{had-vis}}$+lepton SR for $p_{\mathrm{T}} \leq 60$ GeV 3-prong $\tau_{\mathrm{had-vis}}$ candidates. Left-hand side: measured templates of the discriminating variable for multi-jet and $W$+jets CRs in various $\tau_{\mathrm{had-vis}}$ $p_{\mathrm{T}}$ bins. Center: template of the discriminating variable obtained in the SR and fitted combination of the two CRs shapes using $\alpha_{\mathrm{MJ}}$ parameter. Right-hand side: $\chi^2$/ndf of the fit as a function of $\alpha_{\mathrm{MJ}}$, the $\alpha_{\mathrm{MJ}}$ uncertainty is determined by the band at $\chi^2_{\mathrm{min}}/\mathrm{ndf} + \sqrt{\frac{2}{\mathrm{ndf}}}$.

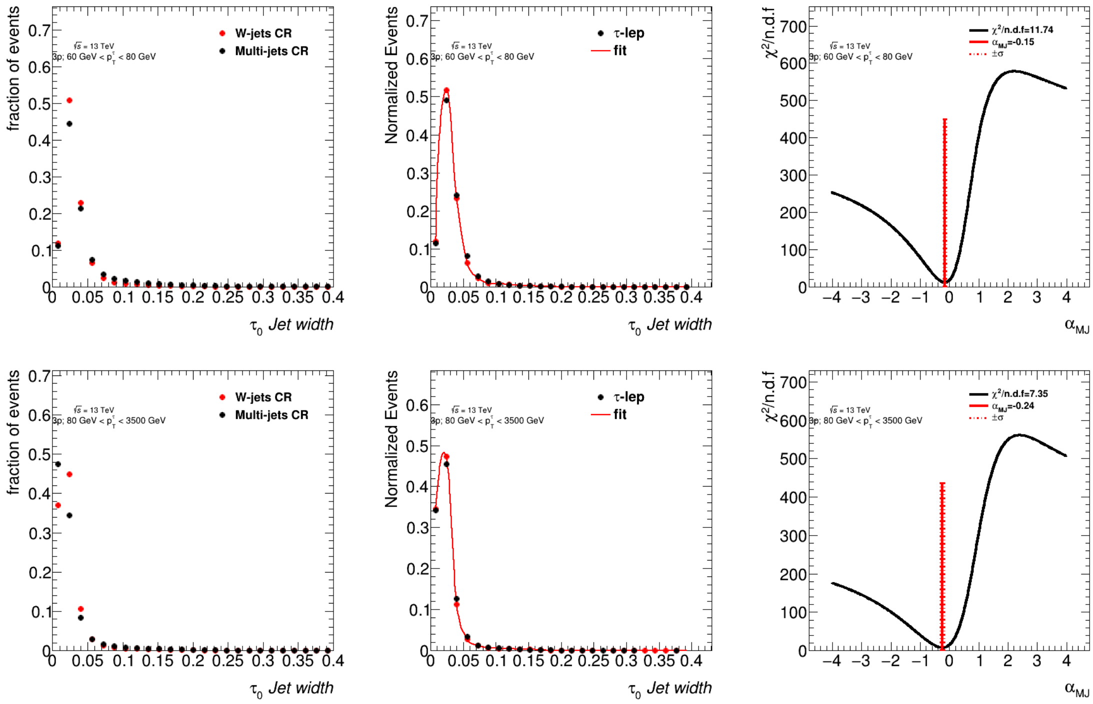


Figure 69: The procedure of $\alpha_{\mathrm{MJ}}$ estimation in the $\tau_{\mathrm{had-vis}}$+lepton SR for $p_{\mathrm{T}} \geq 60$ GeV 3-prong $\tau_{\mathrm{had-vis}}$ candidates. Left-hand side: measured templates of the discriminating variable for multi-jet and $W$+jets CRs in various $\tau_{\mathrm{had-vis}}$ $p_{\mathrm{T}}$ bins. Center: template of the discriminating variable obtained in the SR and fitted combination of the two CRs shapes using $\alpha_{\mathrm{MJ}}$ parameter. Right-hand side: $\chi^2$/ndf of the fit as a function of $\alpha_{\mathrm{MJ}}$, the $\alpha_{\mathrm{MJ}}$ uncertainty is determined by the band at $\chi^2_{\mathrm{min}}/\mathrm{ndf} + \sqrt{\frac{2}{\mathrm{ndf}}}$.

Table 14: The fitted $\alpha_{\mathrm{MJ}}$ values for different signal regions.

| 1-prong $\tau_{\mathrm{had-vis}}$ candidates | | |
|---|---|---|
| $p_{\mathrm{T}}$ range of $\tau_{\mathrm{had-vis}}$ candidates | $\tau_{\mathrm{had-vis}}$+jets SR | $\tau_{\mathrm{had-vis}}$ +lepton SR |
| 30-35 GeV | - | -1.01 |
| 35-40 GeV | - | -0.78 |
| 40-45 GeV | -0.09 | -0.65 |
| 45-50 GeV | 0.21 | -0.37 |
| 50-60 GeV | 0.03 | -0.40 |
| 60-80 GeV | 0.12 | -0.31 |
| 80-100 GeV | 0.33 | -0.20 |
| 100-3500 GeV | 0.22 | -0.32 |
| 3-prong $\tau_{\mathrm{had-vis}}$ candidates | | |
| $p_{\mathrm{T}}$ range of $\tau_{\mathrm{had-vis}}$ candidates | $\tau_{\mathrm{had-vis}}$+jets SR | $\tau_{\mathrm{had-vis}}$ +lepton SR |
| 30-35 GeV | - | -0.30 |
| 35-40 GeV | - | -0.19 |
| 40-60 GeV | 0.25 | -0.18 |
| 60-80 GeV | 0.10 | -0.15 |
| 80-3500 GeV | 0.35 | -0.24 |

### 6.5.5 Validation of the Method

The estimation of the differences in fractions between gluon- and quark-initiated jets, performed using the FF method, is validated in dedicated control regions depleted in signal events. There are three of them: the $\tau_{\mathrm{had-vis}}$+jets $b$-veto $m_{\mathrm{T}} > 100$ CR, as well as $\tau$+$e$ and $\tau$+$\mu$ $b$-veto CRs. The obtained $\alpha_{\mathrm{MJ}}$ values and the combined fake-factors for the $\tau_{\mathrm{had-vis}}$+jets $b$-veto $m_{\mathrm{T}} > 100$ CR and $\tau$+$e$ SR, as well as for the $\tau_{\mathrm{had-vis}}$+electron(muon) $b$-veto control CRs and $\tau_{\mathrm{had-vis}}$+lepton SR are presented in Figure 70 and Figure 71, respectively. The validation plots for the three additional regions mentioned above, shown in Figures 72 and 73, indicate good modelling of the fake $\tau_{\mathrm{had-vis}}$ objects. The ratio plots include systematic uncertainties stemming from the FF method, the assessment of which is detailed in Section 6.5.9.

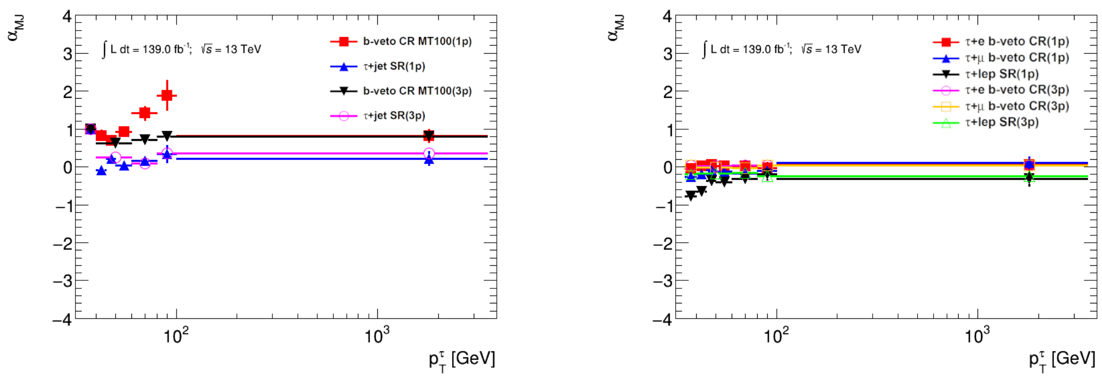


Figure 70: Estimated $\alpha_{\mathrm{MJ}}$ values for the $\tau_{\mathrm{had-vis}}$+jets $b$-veto $m_{\mathrm{T}} > 100$ control region, $\tau_{\mathrm{had-vis}}$+jets signal region, $\tau_{\mathrm{had-vis}}$+electron(muon) with $b$-veto control region and the $\tau_{\mathrm{had-vis}}$+lepton signal region. Error bars represent uncertainties due to the $\alpha_{\mathrm{MJ}}$ fitting using the template-fit method.

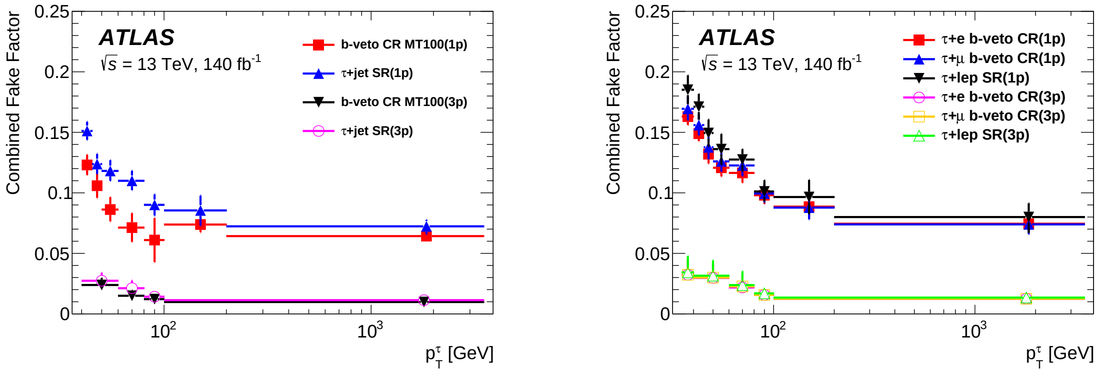


Figure 71: Combined fake-factors for the $\tau_{\mathrm{had-vis}}$+jets $b$-veto $\mathrm{m_T}$ >100 control region, $\tau_{\mathrm{had-vis}}$+jets signal region, $\tau_{\mathrm{had-vis}}$+electron(muon) with $b$-veto control region, and the $\tau_{\mathrm{had-vis}}$+lepton signal region. Error bars represent the full systematic uncertainties of the method.

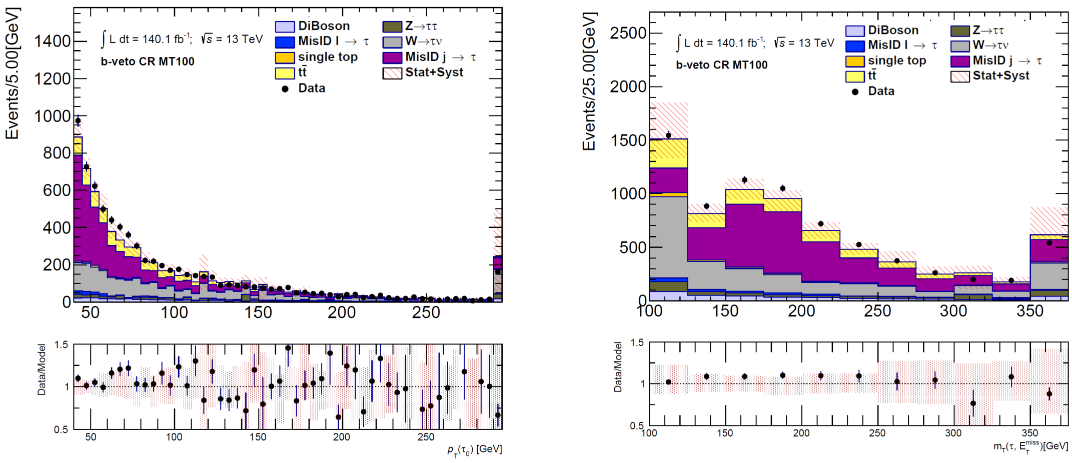


Figure 72: jet→ $\tau_{\mathrm{had-vis}}$ background validation plots for $\tau_{\mathrm{had-vis}}$+jets $b$-jet veto $\mathrm{m_T}$ >100 CR. Jets misidentified as $\tau_{\mathrm{had-vis}}$ are estimated from data using the FF method. The $l \to \tau$ background includes all processes with e or $\mu$ reconstructed and identified as the $\tau_{\mathrm{had-vis}}$. All other SM backgrounds are derived from MC simulation. Error bars represent statistical and systematic uncertainties.

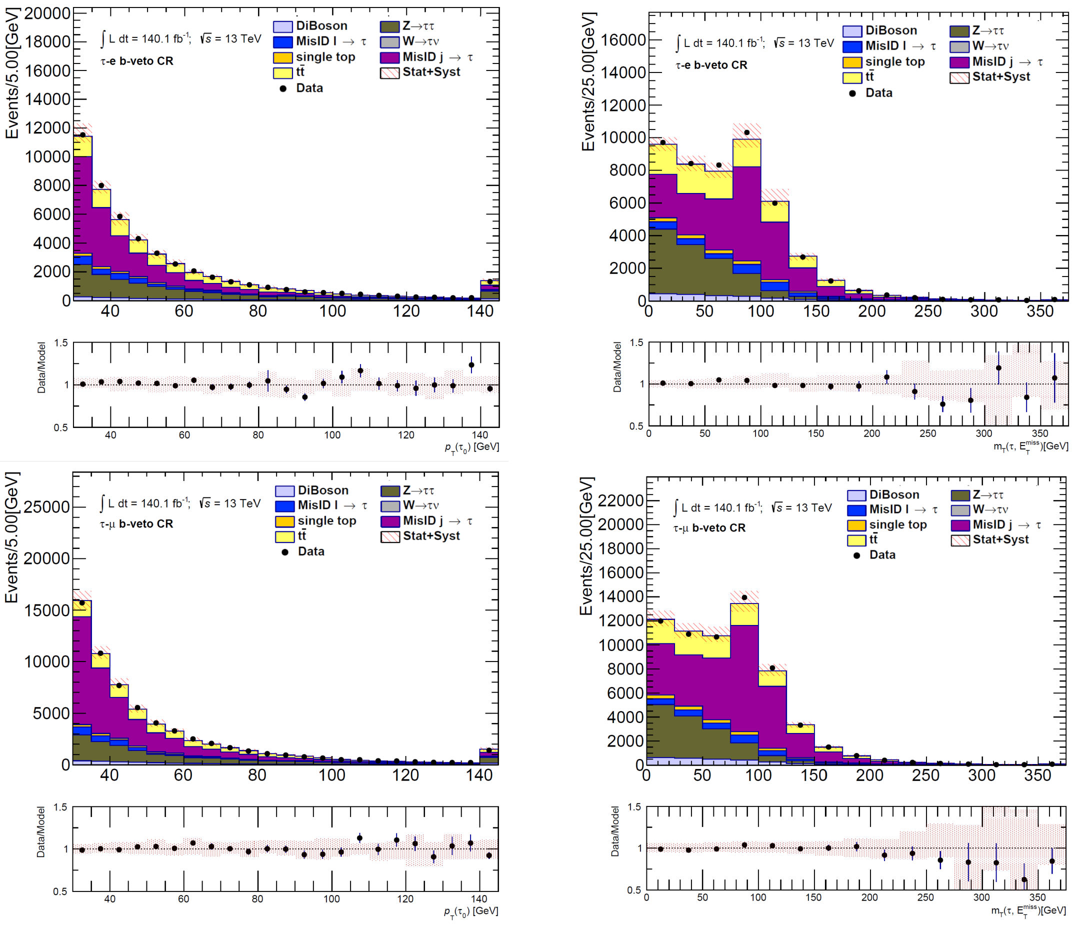


Figure 73: jet→ $\tau_{\text{had-vis}}$ background validation plots: $\tau_{\text{had-vis}}$+electron $b$-jet veto CR (top) and $\tau_{\text{had-vis}}$+muon $b$-jet veto CR (bottom). Jets misidentified as $\tau_{\text{had-vis}}$ are estimated from data using the FF method. The $l \to \tau$ background includes all processes with e or $\mu$ reconstructed and identified as the $\tau_{\text{had-vis}}$. All other SM backgrounds are derived from MC simulation. Error bars represent statistical and systematic uncertainties.

### 6.5.6 Study of the Heavy-Flavour Fake Factors

Fake-factors usually strongly depend on the type of jets. In the computation of the combined fake-factors, described in Section 6.5.4, the parameter $\alpha_{\mathrm{MJ}}$ is extracted from the fit of fake-$\tau_{\mathrm{had-vis}}$ templates in the SR. The computed value of $\alpha_{\mathrm{MJ}}$ takes into account the differences in jet composition between the regions where the fake-factors are extracted and where they are applied. As mentioned earlier, the fake-factors are computed in two control regions - the multi-jet CR with both gluon- or light-quark-initiated jets being misidentified as $\tau_{\mathrm{had-vis}}$, and W+jets CR dominated by the light-quark-initiated jets misidentified as $\tau_{\mathrm{had-vis}}$. These regions, however, have only a small fraction of heavy-quark-initiated jet.

Therefore, this might lead to a systematic bias in the evaluation of the fake-$\tau_{\mathrm{had-vis}}$ background in the signal regions, which are expected to have a significant contribution from heavy-flavor jets. The impact of the heavy-flavor jet contamination on the fake-factor method is studied here.

The dependence of the fake-factors on the type of jet faking the $\tau_{\mathrm{had-vis}}$ object was studied using $t\bar{t}$ MC samples, where the *PartonTruthLabelID* attribute (providing information about the PDG ID of the highest energy parton matched to the reconstructed jet) is utilized to identify the quark from which the jet originates. As a first step, the new Inclusive control region, with only the basic selection requirements for the $\tau_{\mathrm{had-vis}}$ candidates, was defined to ensure that each jet origin sample has a high number of events necessary for the FFs estimation procedure. The selection criteria are:

- at least one reconstructed $\tau_{\mathrm{had-vis}}$ candidate with one or three associated tracks is considered, passing *medium* working point,
- $p_{\mathrm{T}}^{\tau}$ of at least 30 GeV,
- $\tau_{\mathrm{had-vis}}$ candidate has $|\eta| < 2.3$ ($1.37 < |\eta| < 1.52$ is excluded).

The measured FFs for different jet sources (gluon, light-quark, $b$-quark and $c$-quark) misidentified as $\tau_{\mathrm{had-vis}}$ in the Inclusive CR are depicted in Figure 74, separately for 1-prong (black lines) and 3-prong (green lines) $\tau_{\mathrm{had-vis}}$ candidates. A clear dependence of the fake-factor values on the jet origin and $\tau_{\mathrm{had-vis}}$ $p_{\mathrm{T}}$ is observed, with generally higher misidentification rates at low $p_{\mathrm{T}}$. Gluon-initiated jets (a) exhibit relatively flat and low fake-factors across the full $p_{\mathrm{T}}$ range, particularly for 1-prong candidates. Light-quark jets (b) show similar fake-factors for 3-prong $\tau_{\mathrm{had-vis}}$ candidates, but the 1-prong fake-factors are the highest among all jet types, indicating the greatest likelihood of misidentification. Jets originating from $b$-quark (c) display a strong $p_{\mathrm{T}}$ dependence, with significantly higher fake-factors at low $p_{\mathrm{T}}$ values. In contrast, $c$-quark jets (d) yield consistently higher fake-factors for 3-prong candidates across all $p_{\mathrm{T}}$ bins, which can be attributed to the $D$-meson lifetime being comparable to that of the $\tau$ lepton. These differences highlight the importance of accounting for the jet flavour when applying fake-factor corrections in background estimation.

In order to test the impact of the population of heavy-flavor jets in the SRs, two extreme variants of the combined fake-factors are extracted:

- $\mathrm{FF}_{\mathrm{light}}^{\mathrm{gluon}}$ - only gluon- and light-quarks-initiated jets misidentified as $\tau_{\mathrm{had-vis}}$ are considered.
- $\mathrm{FF}_{\mathrm{light/b/c}}^{\mathrm{gluon}}$ - gluon- and light/b/c-quarks-initiated jets misidentified as $\tau_{\mathrm{had-vis}}$ are considered.

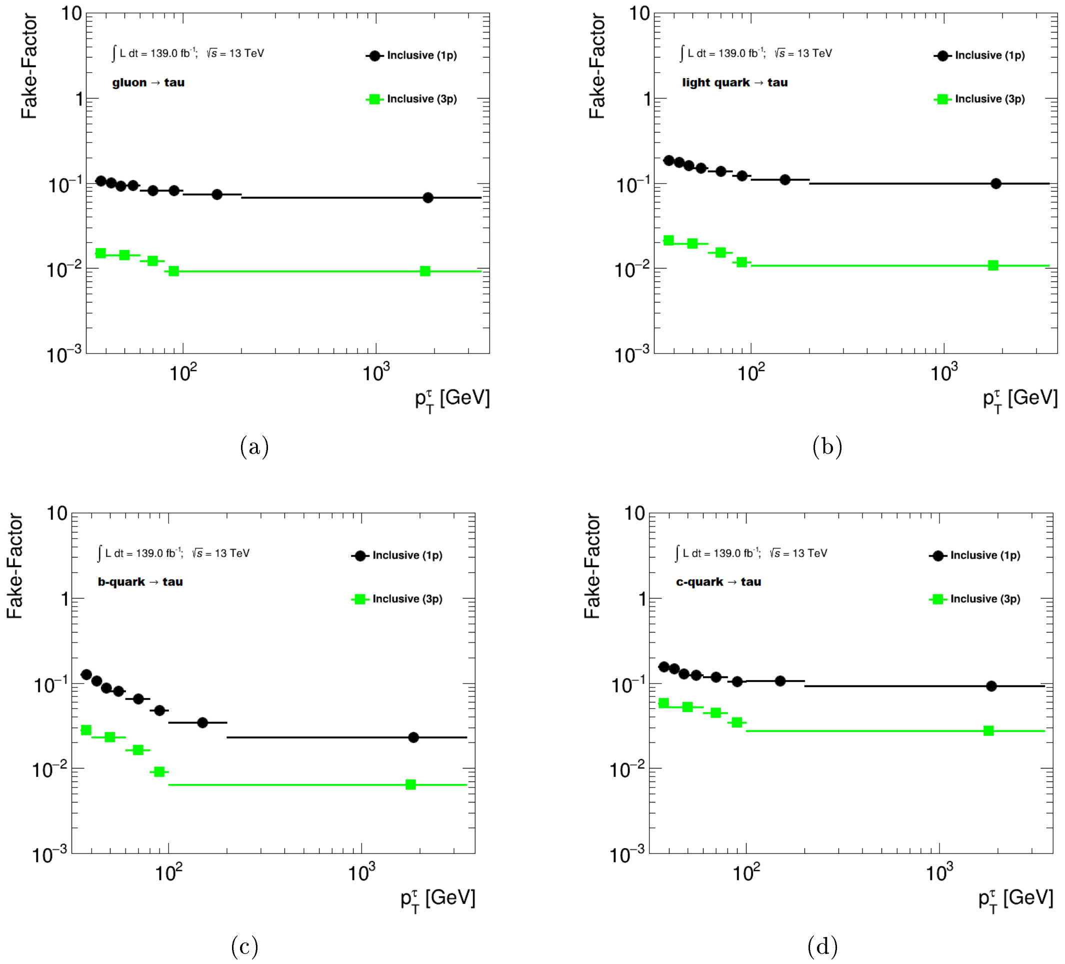


Figure 74: Fake-factors used in the estimation of the $j \to \tau_{\mathrm{had-vis}}$ background, for different types of jet origins: gluon (a), light-quark (b), $b$-quark (c) and $c$-quark (d). The association between the jet and the initial parton is made using the PartonTruthLabelID variable in the jet container. In the plots, fake-factors are shown for 1-prong and 3-prong $\tau_{\mathrm{had-vis}}$ candidates separately with statistical errors only. A MC16c $t\bar{t}$ sample was used to produce these plots.

From the fact that this study is based on the $t\bar{t}$ MC sample, the information about jet origin provided by the *PartonTruthLabelID* attribute can be used to determine the jet composition in the SRs, instead of the template-fit method used for experimental data. In order to calculate the two variants of the combined FFs, the FFs for individual jet sources (gluon or light/b/c-quark) were weighted according to the measured jet composition (percentage values of anti-$\tau_{\mathrm{had-vis}}$ events per each jet origin) in the SRs simulated in the $t\bar{t}$ MC sample, according to the formula:

$$\mathrm{FF}^{\mathrm{gluon}}_{\mathrm{light}} = f_{\mathrm{gluon}} \times \mathrm{FF}_{\mathrm{gluon}} + f_{\mathrm{light-quark}} \times \mathrm{FF}_{\mathrm{light-quark}}. \tag{74}$$

$$\mathrm{FF}^{\mathrm{gluon}}_{\mathrm{light/b/c}} = f_{\mathrm{gluon}} \times \mathrm{FF}_{\mathrm{gluon}} + f_{\mathrm{light}} \times \mathrm{FF}_{\mathrm{light}} + f_{\mathrm{b-quark}} \times \mathrm{FF}_{\mathrm{b-quark}} + f_{\mathrm{c-quark}} \times \mathrm{FF}_{\mathrm{c-quark}}. \tag{75}$$

Here, $f_{\mathrm{origin}}$ represents a fraction of the specific jet origin (gluon, light-quark, $b$-quark and $c$-quark) measured in the event sample with SR criteria using the $t\bar{t}$ MC sample, as well as the $FF_{origin}$ is the fake-factor calculated in Inclusive CR for a specific jet origin.

As a result, one obtains the actual combined FFs, not biased by the experimental $\alpha_{MJ}$ fitting procedure. The measured values of $FF^{gluon}_{light}$ and $FF^{gluon}_{light/b/c}$ are depicted in Figure 75. It can be observed that for 1-prong $\tau_{had-vis}$ events discrepancies between $FF^{gluon}_{light/b/c}$ and $FF^{gluon}_{light}$ increases with the $p_T$ of $\tau_{had-vis}$ candidate, while fake-factors for 3-prong $\tau_{had-vis}$ events differ substantially in bins with $p_T$ below 100 GeV.

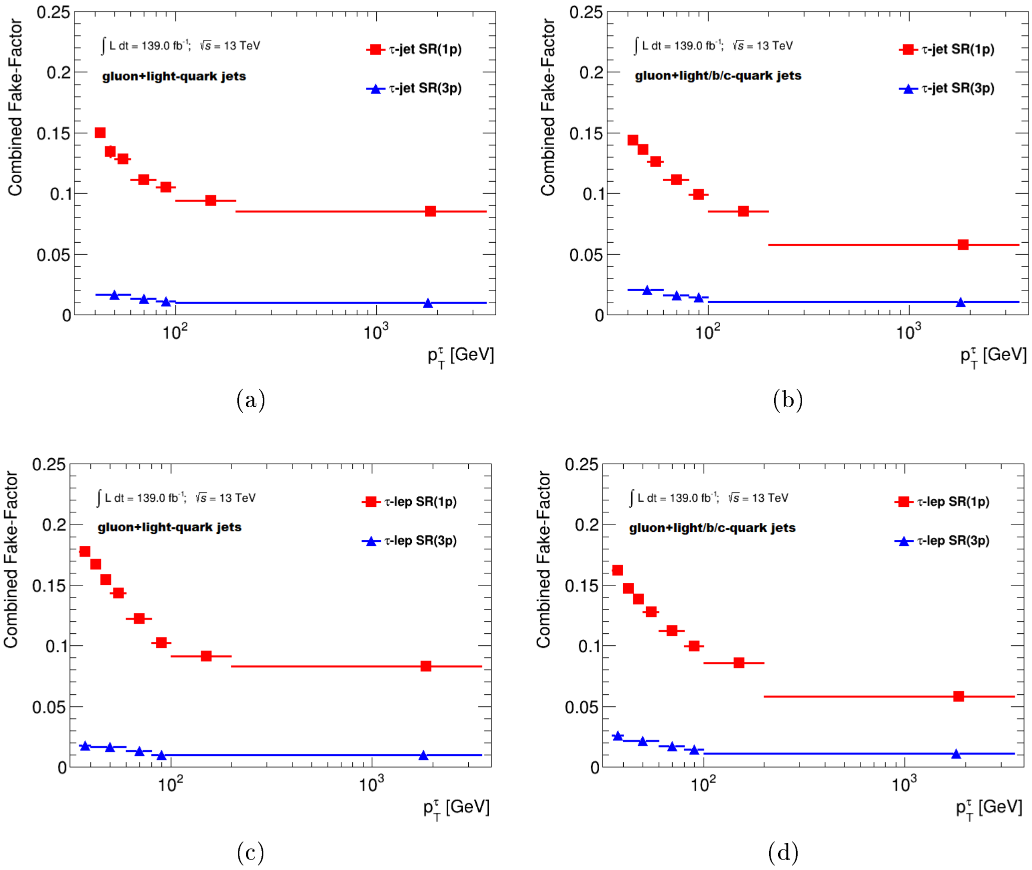


Figure 75: Combined fake-factors for gluon+light-quark templates (left) and gluon+light/b/c-quark templates (right) for the $\tau_{had-vis}$SRs. Error bars present only statistical uncertainty.

To establish the final systematic uncertainty related to heavy-flavour FFs, dedicated scale factors ($SF_{HF-FF}$), calculated as a ratio of $FF^{gluon}_{light/b/c}$ and $FF^{gluon}_{light}$, are applied to the nominal combined fake-factors. Taking into consideration that the background coming from the $t\bar{t}$ processes is a main source of the heavy-flavour uncertainty, the scale factors were additionally corrected by the coefficient reflecting the percentage fraction of $t\bar{t}$ processes in data - estimated as a ratio of the anti-$\tau_{had-vis}$ candidates from the $t\bar{t}$ MC sample ($N^{anti-\tau}_{t\bar{t}}(MC)$) to the number of the same events measured in data ($N^{anti-\tau}_{SR}(data)$) per each $\tau_{had-vis}$ $p_T$ bin. The final formula for the HF-SFs is as follows:

$$SF_{HF-FF} = \frac{FF^{gluon}_{light/b/c}}{FF^{gluon}_{light}} \times \frac{N^{anti-\tau}_{t\bar{t}}(MC)}{N^{anti-\tau}_{SR}(data)} \tag{76}$$

Calculated values of $SF_{HF-FF}$ per different $\tau_{had-vis}$ $p_T$ bins for $\tau_{had-vis}$+jet and $\tau_{had-vis}$+lep SRs are depicted in Figure 76, confirming that Heavy-Flavour FFs systematic has the biggest impact among 3-prong $\tau_{\mathrm{had-vis}}$ candidates.

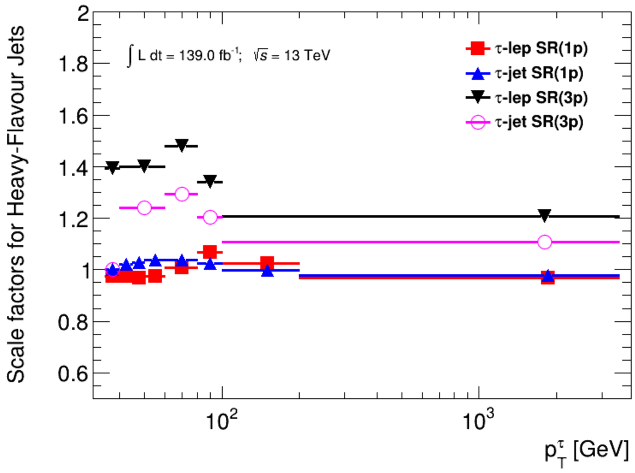


Figure 76: The obtained HF-FFs scale factors for $\tau_{\mathrm{had-vis}}$+jets and $\tau_{\mathrm{had-vis}}$+lepton SRs.

### 6.5.7 Optimization of the $\alpha_{MJ}$ Estimation

A template-fit approach used for the determination of jet composition in the signal regions, described in Section 6.5.4, highly depends on the templates' properties used for the $\alpha_{\mathrm{MJ}}$ estimation, hence one needs to ensure the proper optimization of the method. The templates can be prepared for various $p_{\mathrm{T}}$ ranges of $\tau_{\mathrm{had-vis}}$ candidates and with different numbers of bins in the distribution of the discriminating variable.

In the standard approach used in the analysis, the $\tau_{\mathrm{had-vis}}$ candidates with the highest $p_{\mathrm{T}}$ (>100 GeV $p_{\mathrm{T}}$ for 1-prong and >80 GeV $p_{\mathrm{T}}$ for 3-prong events) are combined into one bin to ensure sufficient statistics. This strategy enables to achieve higher quality of $\alpha_{\mathrm{MJ}}$ fitting procedure at the expense of precision of the background estimation for high $p_{\mathrm{T}}$ $\tau_{\mathrm{had-vis}}$ candidate. To evaluate the impact of different fitting strategies, the $\alpha_{\mathrm{MJ}}$ estimation was repeated for separate high $p_{\mathrm{T}}$ bins of $\tau_{\mathrm{had-vis}}$ (100-200 GeV and 200–3500 GeV) in 1-prong events. The statistics for 3-prong events were too low to allow for such a test. In addition, the number of bins in distributions of the discriminating variable used as templates was increased with regard to the standard approach (40 bins instead of 25).

Comparison of the calculated $\alpha_{\mathrm{MJ}}$, as well as the obtained combined FFs, utilizing the separate high $\tau_{\mathrm{had-vis}}$ $p_{\mathrm{T}}$ bins fitting strategy and the standard strategy is shown in Figure 77 and Figure 78, respectively.

Generally, the $\alpha_{\mathrm{MJ}}$ fitting utilizing the separate high $\tau_{\mathrm{had-vis}}$ $p_{\mathrm{T}}$ bins strategy has lower efficiency and the estimation uncertainties are bigger than in the case of the standard approach. While discrepancies in the values of $\alpha_{\mathrm{MJ}}$ and the combined fake factors are small in both signal regions across various fitting strategies, the most significant differences occur for high $\tau_{\mathrm{had-vis}}$ $p_{\mathrm{T}}$ bins in $\tau_{\mathrm{had-vis}}$+jets $b$-veto $m_{\mathrm{T}}$ >100 CR. Also, in almost every region the lowest quality of the $\alpha_{\mathrm{MJ}}$ extraction procedure is obtained in the 100-200 GeV $\tau_{\mathrm{had-vis}}$ $p_{\mathrm{T}}$ bin, which supports the validity of the standard fitting strategy. On the other hand, maintaining the separate bins at high $\tau_{\mathrm{had-vis}}$ $p_{\mathrm{T}}$ should provide a more accurate estimation of the fake $\tau_{\mathrm{had-vis}}$ background for each $\tau_{\mathrm{had-vis}}$ $p_{\mathrm{T}}$ range. To compensate for the different $\alpha_{\mathrm{MJ}}$ values in the case of various $\alpha_{\mathrm{MJ}}$ fitting approaches, a new systematic error is introduced as a difference in the combined FFs calculated using the standard fitting strategy and the strategy with separate high $\tau_{\mathrm{had-vis}}$ $p_{\mathrm{T}}$ bins.

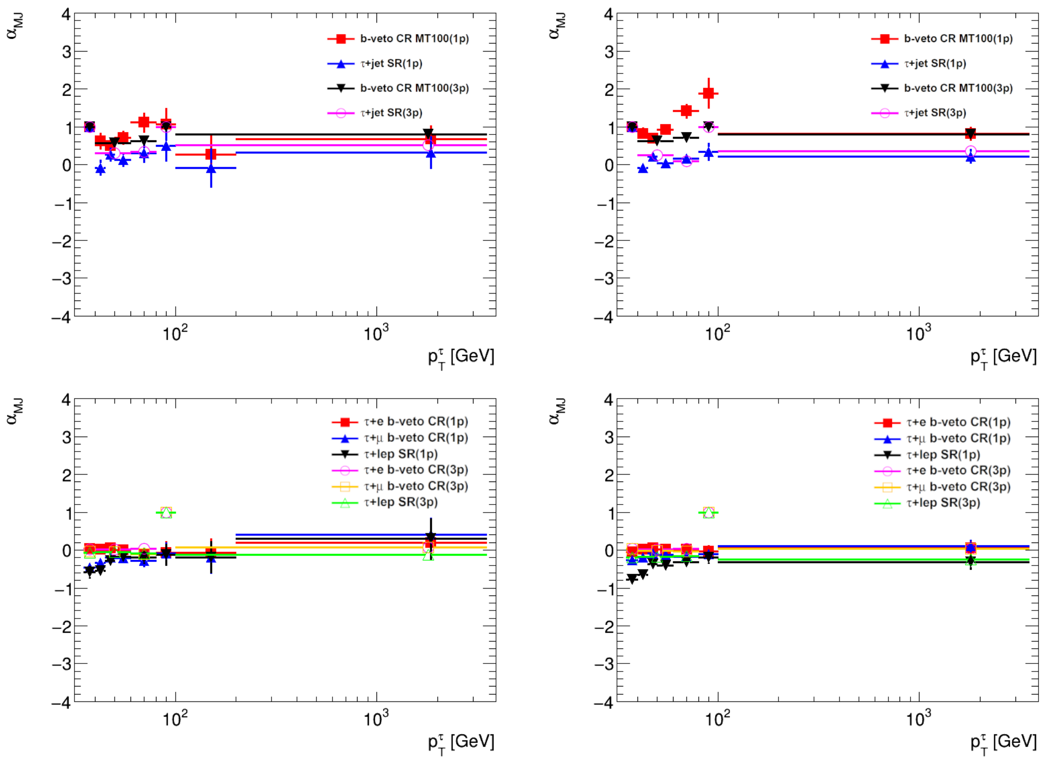


Figure 77: Corrected $\alpha_{\mathrm{MJ}}$ values using the separate high $\tau_{\mathrm{had-vis}}$ $p_{\mathrm{T}}$ bins fitting strategy (left-hand side) and the standard strategy (right-hand side) for the $\tau_{\mathrm{had-vis}}$+jets $b$-veto $\mathrm{m_T}$ >100 control region, $\tau_{\mathrm{had-vis}}$+jets signal region, $\tau_{\mathrm{had-vis}}$+electron(muon) $b$-veto control regions and the $\tau_{\mathrm{had-vis}}$+lepton signal region. Error bars represent the uncertainties due to the $\alpha_{\mathrm{MJ}}$ fitting using the template-fit method.

### 6.5.8 Correction of the $\Upsilon$ Variable

The identification of hadronically decaying $\tau$ leptons is achieved through the RNN model, which employs a variety of input variables, as described in Section 2.3.1. Notably, the leading-track momentum fraction, one of these input variables, possesses a significant correlation with the $\Upsilon$ variable. Consequently, a significant difference is observed in the distribution of the $\Upsilon$ variable between $\tau_{\mathrm{had-vis}}$ and anti-$\tau_{\mathrm{had-vis}}$ candidates. Proper modeling of the $\Upsilon$ distribution for $\tau_{\mathrm{had-vis}}$ candidates within the signal region is essential, as it is utilized as an input variable in the final PNN discriminant of the analysis. Due to the fact that there is no correlation between the $\Upsilon$ variable with the other variables employed as inputs to the final PNN discriminant, its distribution is adjusted using a Smirnov transformation [239]. Its first step involves obtaining the shapes of the $\Upsilon$ variable in both multi-jet and W+jets CRs for $\tau_{\mathrm{had-vis}}$ and anti-$\tau_{\mathrm{had-vis}}$ candidates. Next, these shapes are utilized to determine a cumulative distribution function (CDF), represented by $F(\Upsilon)$. The corrected value of $\Upsilon$ is:

$$\Upsilon_{\mathrm{corr}} = F_{\tau}^{-1}\left(F_{\mathrm{anti}-\tau}(\Upsilon)\right), \tag{77}$$

Here $F_{\tau}^{-1}(x)$ refers to the inverse of the cumulative distribution function of $\tau_{\mathrm{had-vis}}$ candidates and $F_{\mathrm{anti}-\tau}(x)$ is the cumulative distribution function of anti-$\tau_{\mathrm{had-vis}}$ candidates.

The distribution and the CDF of the $\Upsilon$ for 1-prong objects ($\Upsilon$ is not used in the training of the final PNN discriminant for 3-prong $\tau_{\mathrm{had-vis}}$ candidates) in the $W$+jets CR is presented in Figure 79.

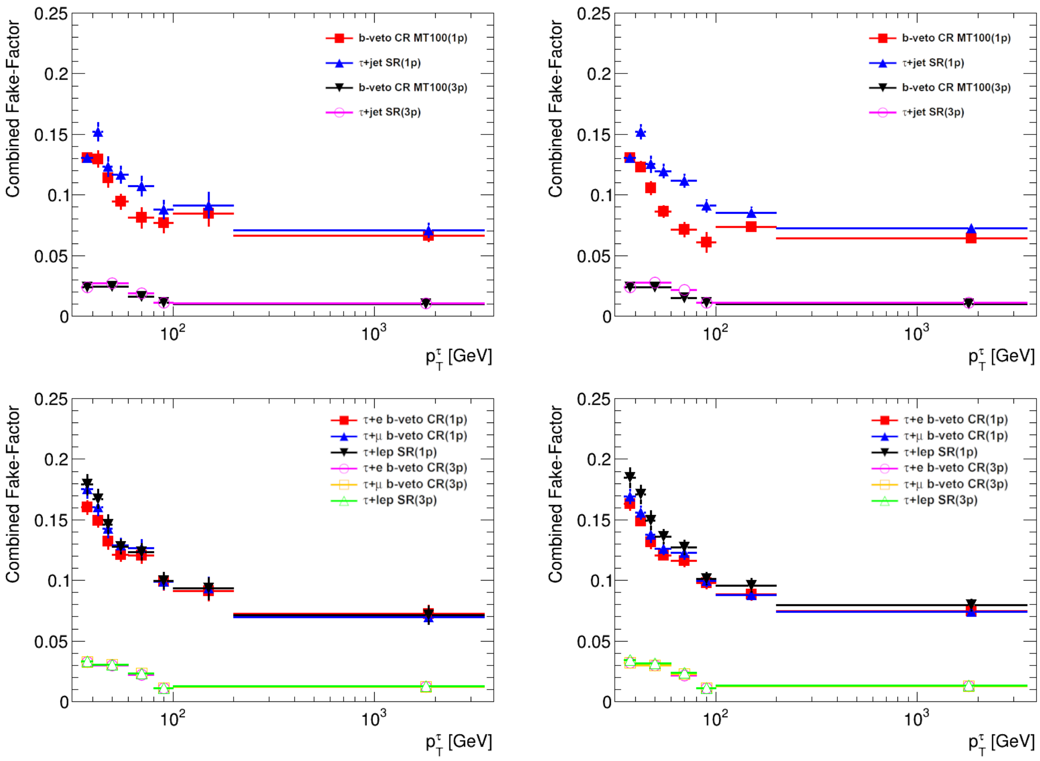


Figure 78: Combined fake-factors using separate high $\tau_{\mathrm{had-vis}}$ $p_{\mathrm{T}}$ bins fitting strategy (left-hand side) and standard strategy (right-hand side) for the $\tau_{\mathrm{had-vis}}$+jets b-veto $\mathrm{m_T}$ >100 control region, $\tau_{\mathrm{had-vis}}$+jets signal region, $\tau_{\mathrm{had-vis}}$+electron(muon) b-veto control regions and the $\tau_{\mathrm{had-vis}}$+lepton signal region. Error bars represent uncertainties due to the estimation of control regions FFs and $\alpha_{\mathrm{MJ}}$ fitting using the template-fit method.

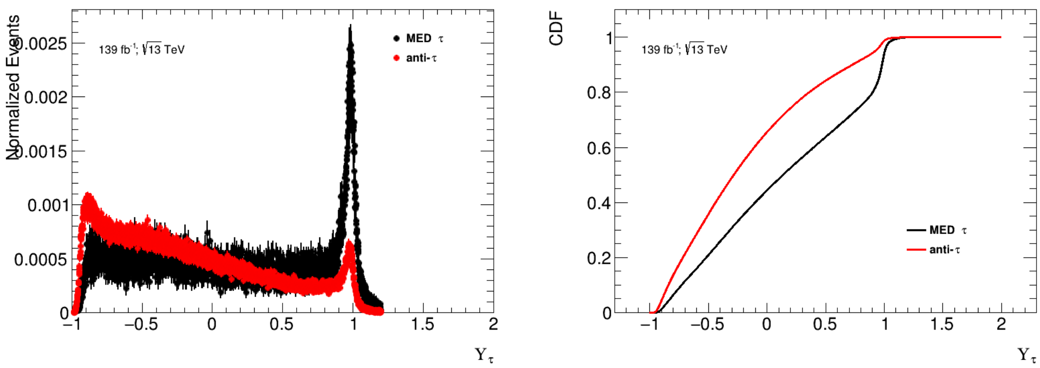


Figure 79: Left-hand side: Distribution of the $\Upsilon$ variable for $\tau_{\mathrm{had-vis}}$ (black) and anti-$\tau_{\mathrm{had-vis}}$ (red) candidates in the $W$+jets control region. Right-hand side: CDF of $\Upsilon$ for $\tau_{\mathrm{had-vis}}$ (black) and anti-$\tau_{\mathrm{had-vis}}$ (red) candidates in the $W$+jets control region.

The distributions of $\Upsilon$ after Smirnov transformation in the $\tau_{\mathrm{had-vis}}$+jets $b$-veto $\mathrm{m_T}$ >100 and $\tau_{\mathrm{had-vis}}$+electron(muon) $b$-veto control regions are shown in Figure 80.

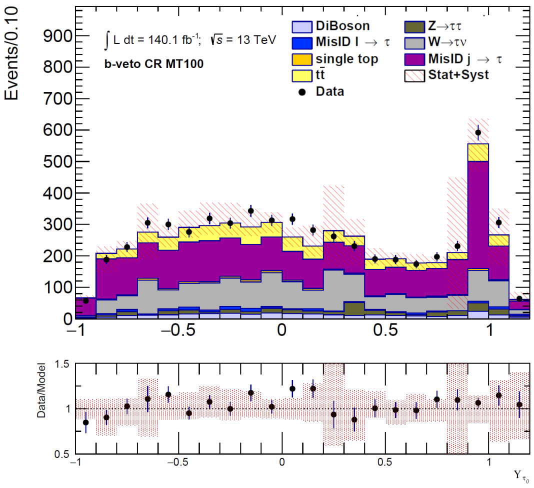


(a)

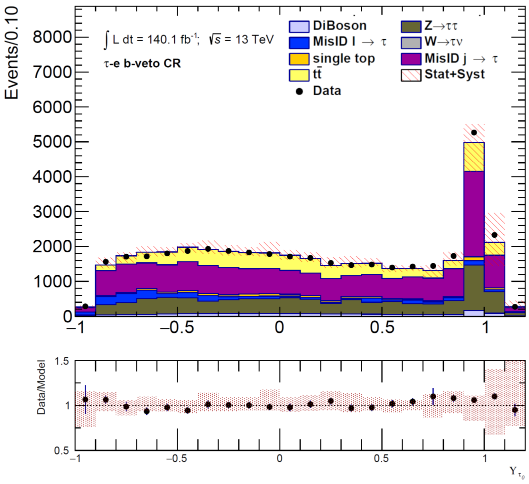


(b)

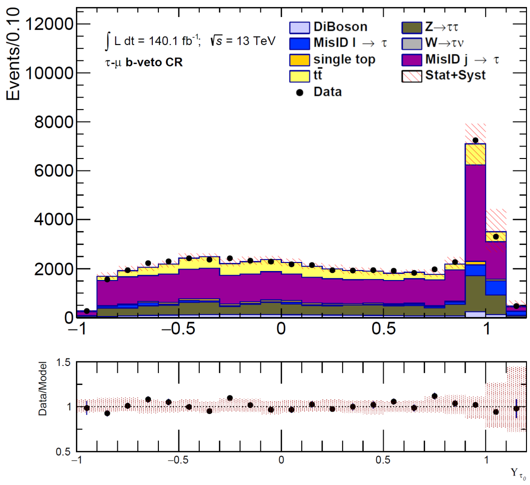


(c)

Figure 80: Distribution of $\Upsilon$ variable after Smirnov transformation in the $\tau_{\text{had-vis}}$+jets $b$-jet veto $m_T$ >100 CR (a), $\tau_{\text{had-vis}}$+electron $b$-jet veto CR (b) and $\tau_{\text{had-vis}}$+muon $b$-jet veto CR (c). Jets misidentified as $\tau_{\text{had-vis}}$ are estimated from data using the FF method. The $l \to \tau$ background includes all processes with e or $\mu$ reconstructed and identified as the $\tau_{\text{had-vis}}$. All other SM backgrounds are derived from MC simulation. Error bars represent statistical and systematic uncertainties.

### 6.5.9 Systematic Uncertainties of the FF Method

To correctly estimate the jet→ $\tau_{\text{had-vis}}$ background, it is crucial to consider various sources of the FF method systematic uncertainties. They can be categorized as follows:

1. the statistical uncertainty in the bins of the fake-factors, due to the control sample size;
2. the additional (conservative) uncertainty of 50% is applied on the amount of $\tau_{\text{had-vis}}$ candidates from a true hadronic $\tau$ decay that must be subtracted when computing $N^{\text{anti-}\tau}_{\text{fakes}}$:
$$N^{\text{anti-}\tau}_{\text{fakes}} = N^{\text{anti-}\tau}(\text{data}) - [0.5, 1.5] \times N^{\text{anti-}\tau}_{\text{true}}(\text{MC}) \tag{78}$$
3. the uncertainty arising from the MC modeling of true $\tau$ identification - scale factors error of 5% is implemented as follows:
$$N^{\tau\text{-id}} = N^{\tau\text{-id}}(\text{data}) - [0.95, 1.05] \times N^{\tau\text{-id}}(\text{MC}) \tag{79}$$
4. the error on $\alpha_{\text{MJ}}$ in the template-fit method (presented Section 6.5.4);
5. the uncertainty of the $\alpha_{\text{MJ}}$ fitting strategy (presented Section 6.5.7);
6. the uncertainty of Smirnov transformation for $\Upsilon$ (see Section 6.5.8);
7. the uncertainty from a possible bias as a result of different contamination of heavy-flavour jets between control and signal regions (summarised in Section 6.5.6).

A summary of the effect of the systematic uncertainties is given in Table 15.

Table 15: Effect on the shape variation and the yields of systematic uncertainties associated with the data-driven fake-factor method, used to estimate the jet→ $\tau$ background in the $\tau_{\text{had-vis}}$+jets and $\tau_{\text{had-vis}}$+lepton channel.

| | $\tau_{\text{had-vis}}$+jets | | $\tau_{\text{had-vis}}$+lepton | |
|---|---|---|---|---|
| Source of uncertainty | Effect on yield | Shape | Effect on yield | Shape |
| Fake factors: Statistical uncertainties | 3.9% | ✗ | 3.2% | ✗ |
| Fake-factors: True $\tau_{\text{had-vis}}$ in the anti-$\tau_{\text{had-vis}}$ CR | +3.4% -3.2% | ✗ | +4% -4.3% | ✗ |
| Fake factors: $\tau$ RNN Identification SF | 2.7% | ✗ | 2.7% | ✗ |
| Fake factors: $\alpha_{\text{MJ}}$ uncertainty | 3.6% | ✓ | 1.9% | ✓ |
| Fake factors: $\alpha_{\text{MJ}}$ fitting strategy | 1.6% | ✓ | 2.8% | ✓ |
| Fake factors: Smirnov transform | 0% | ✓ | 0% | ✓ |
| Fake factors: Heavy-flavour jet fraction | 5.9% | ✓ | 6.3% | ✓ |

The impact of these systematic uncertainties on the shape of the jet→ $\tau_{\text{had-vis}}$ background is illustrated in Figure 81 for the $\tau_{\text{had-vis}}$+jets SR, as well as in Figures 82-83 for the $\tau_{\text{had-vis}}$+electron and $\tau_{\text{had-vis}}$+muon SRs.

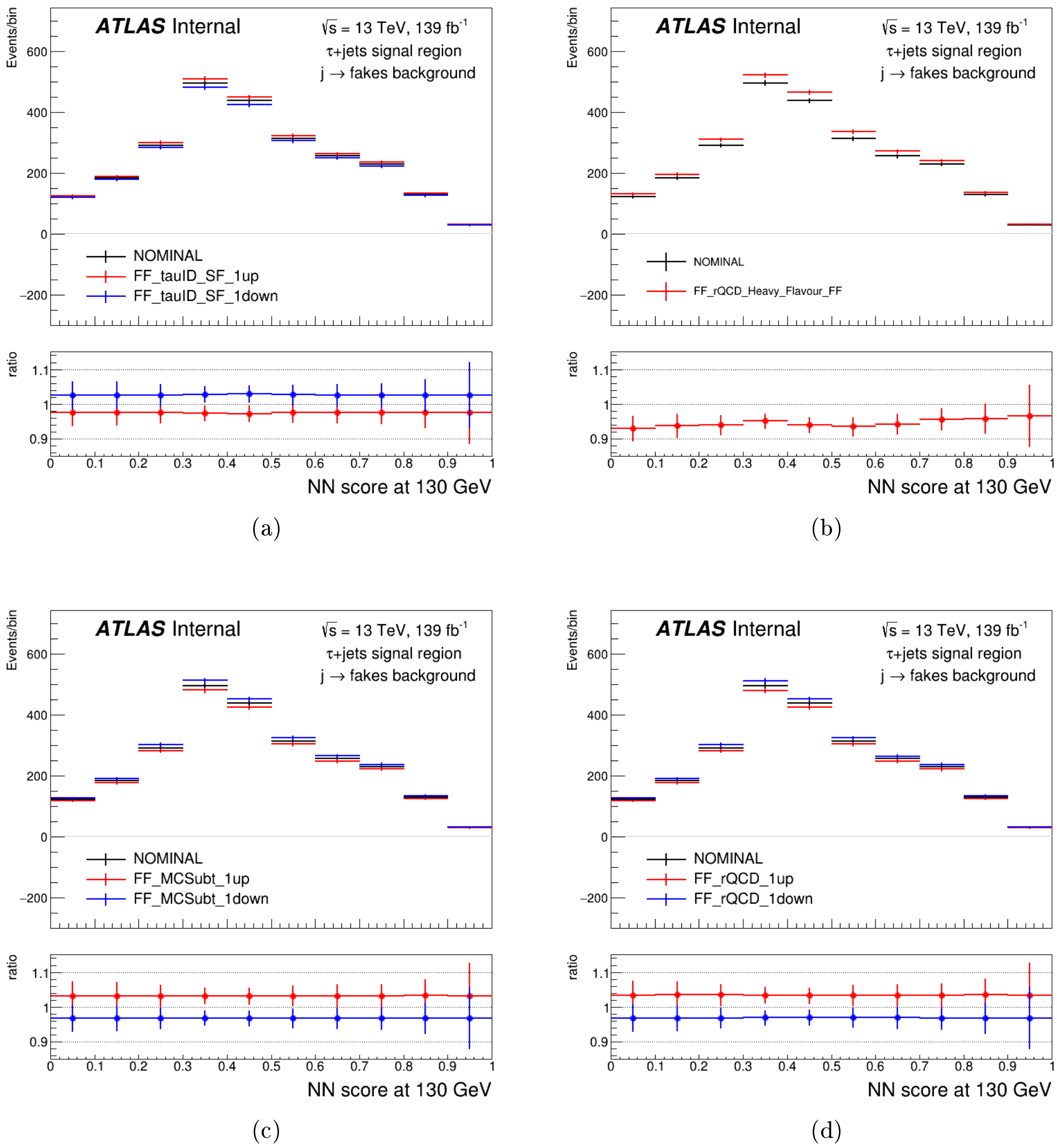


Figure 81: Effect of systematic variations on the PNN score in the $H^+$ mass point 130 GeV for the $\tau_{\text{had-vis}}$+jets SR from the following sources: the $\tau$ RNN identification scale factor (a), the heavy-flavour jet fraction (b), the true $\tau_{\text{had-vis}}$ contamination in the anti-$\tau_{\text{had-vis}}$ CR (c), the $\alpha_{\text{MJ}}$ template-fit method (d). The uncertainty bars in the ratio plots represent the statistical error in every bin of the PNN score.

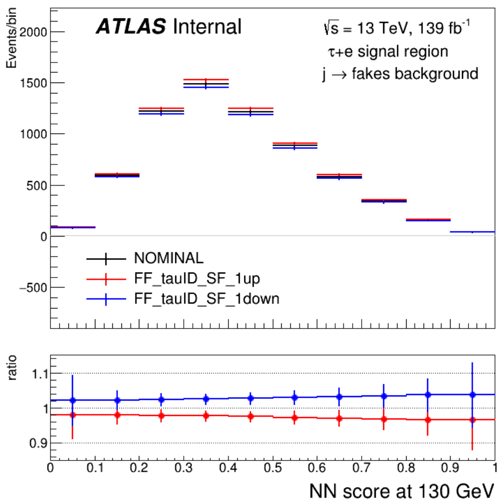


(a)

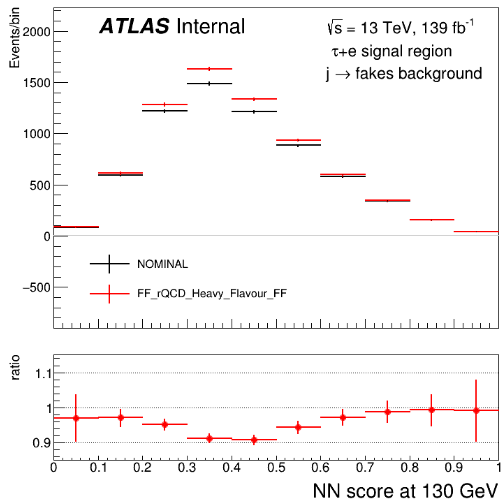


(b)

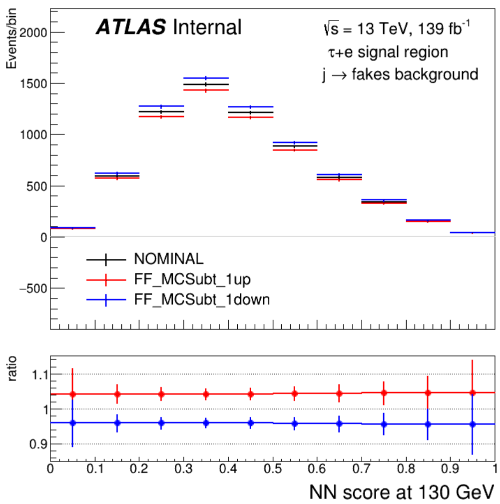


(c)

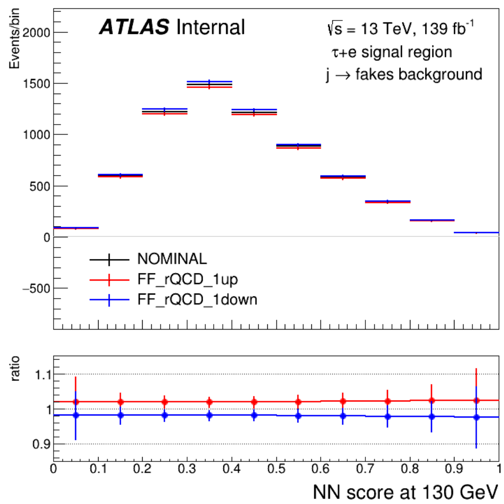


(d)

Figure 82: Effect of systematic variations on the PNN score in the $H^+$ mass point 130 GeV for the $\tau_{\text{had-vis}}$+electron SR from the following sources: the $\tau$ RNN identification scale factor (a), the heavy-flavour jet fraction (b), the true $\tau_{\text{had-vis}}$ contamination in the anti-$\tau_{\text{had-vis}}$ CR (c), the $\alpha_{\text{MJ}}$ template-fit method (d). The uncertainty bars in the ratio plots represent the statistical error in every bin of the PNN score.

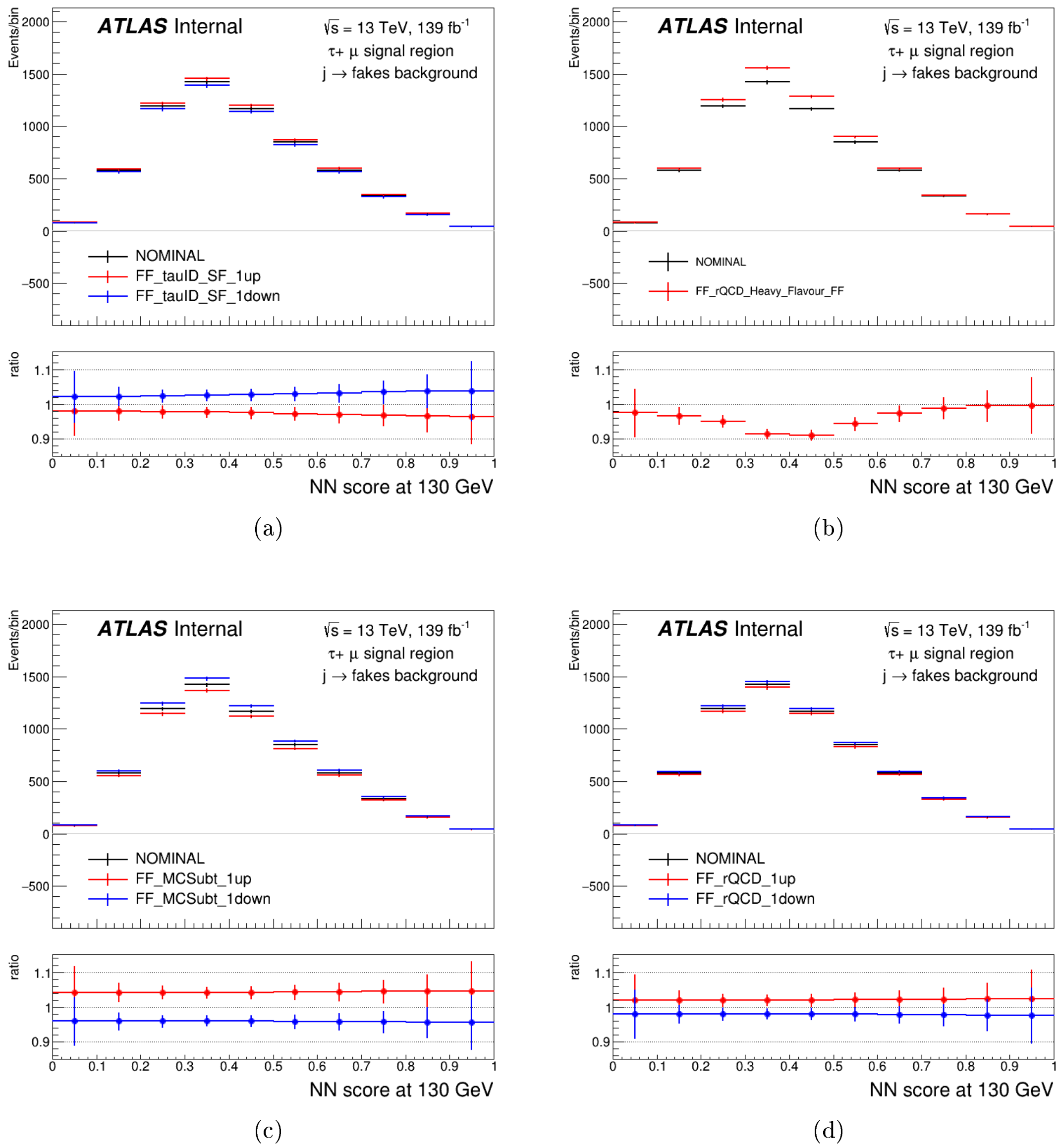


Figure 83: Effect of systematic variations on the PNN score in the $H^+$ mass point 130 GeV for the $\tau_{\text{had-vis}}$+muon SR from the following sources: the $\tau$ RNN identification scale factor (a), the heavy-flavour jet fraction (b), the true $\tau_{\text{had-vis}}$ contamination in the anti-$\tau_{\text{had-vis}}$ CR (c), the $\alpha_{\text{MJ}}$ template-fit method (d). The uncertainty bars in the ratio plots represent the statistical error in every bin of the PNN score.

## 6.6 Reweighting of $t\bar{t}$ and $W$+jets MC Samples

It has been observed that the $t\bar{t}$ Powheg+Pythia and $W$+jets Sherpa 2.2.1 generators exhibit limitations in accurately modeling the observed data at high jet multiplicities. To provide the data-to-simulation agreement, data-driven corrections are applied to the MC prediction as was done in References [240, 204]. Reweighting factors ($R(x)$) are determined by comparing the observed data and simulated predictions in dedicated control regions ($\tau_{\text{had-vis}}$+lepton $t\bar{t}$ CR, $\tau_{\text{had-vis}}$+jets $t\bar{t}$ CR and $W/Z$+jets CR), applied individually to the $t\bar{t}$ and $W$+jets MC samples, and can be formulated as:

$$R(x) = \frac{Data(x) - MC^{\text{non-t}\bar{\text{t}}\text{/non-W+jets}}(\text{x})}{MC^{\text{t}\bar{\text{t}}\text{/W+jets}}(\text{x})} \quad (80)$$

Here, $x$ represents the variable mismodeled by the MC simulation.

For $t\bar{t}$ backgrounds, the reweighting is performed in two separate channels:

- $\tau_{\text{had-vis}}$+lepton $t\bar{t}$ CR with variable $m_{\text{eff}} = \sum_{\text{jets}} p_T^{\text{jets}} + p_T^{\tau} + p_T^{\text{leptons}} + E_{\text{T}}^{\text{miss}}$,
- $\tau_{\text{had-vis}}$+jets $t\bar{t}$ CR with variable $m_{\text{eff}} = \sum_{\text{jets}} p_T^{\text{jets}} + p_T^{\tau} + E_{\text{T}}^{\text{miss}}$.

The $m_{\text{eff}}$ distributions are fitted with the function $a + b(m_{\text{eff}} + 30)\exp(-cm_{\text{eff}})$ in both channels. Fit results are shown in Table 16, and the associated uncertainties from the fit parameters are propagated as systematic errors.

Table 16: Results of the fits to the $m_{\text{eff}}$ weights distributions using $a + b(m_{\text{eff}} + 30)\exp(-cm_{\text{eff}})$ function.

| channel | a | b | c |
|---|---|---|---|
| $\tau_{\text{had-vis}}$+lepton | 0.6146 | 0.00179 | 0.00200 |
| $\tau_{\text{had-vis}}$+jets | 0.4907 | 0.00193 | 0.00177 |

The reweighting significantly improves the modeling of kinematic variables. As an example, the distributions of $E_{\text{T}}^{\text{miss}}$ are presented in Figure 84 and Figure 85, for both $\tau_{\text{had-vis}}$+lepton and $\tau_{\text{had-vis}}$+jets channels respectively.

For the $W$+jets background, reweighting is performed in the $W/Z$+jets CR of the $\tau_{\text{had-vis}}$+jets channel using the jet multiplicity, $n_{\text{jets}}$, as the reweighting variable. The derived weight distribution is fitted with a third-order polynomial, and the fit parameters are listed in Table 17. The resulting weights significantly improve the agreement between data and MC in $n_{\text{jets}}$ and other observables. As example, the effect of the reweighting on $E_{\text{T}}^{\text{miss}}$ is illustrated in Figure 86.

The $W$+jets reweighting has a negligible impact in the $\tau_{\text{had-vis}}$+lepton channel since this background plays only a minor role there, primarily contributing to fake lepton estimations. Overall, these data-driven corrections improve the modeling of key observables in both $t\bar{t}$ and $W$+jets backgrounds.

Table 17: Results of the fit to the $n_{\text{jets}}$ weights distributions using $a + bn_{\text{jets}} + cn_{\text{jets}}^2 + dn_{\text{jets}}^3$ function.

| channel | a | b | c | d |
|---|---|---|---|---|
| $\tau_{\text{had-vis}}$+jets | 0.8440 | 0.2062 | -0.0681 | 0.0049 |

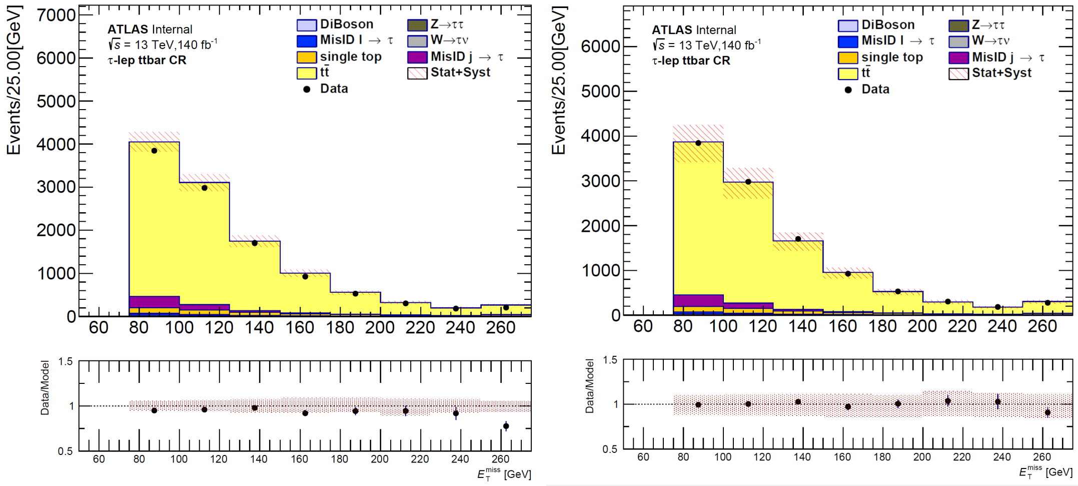


Figure 84: Comparison between the original (left-hand side) and $t\bar{t}$ MC reweighted (right-hand side) distributions of $E_{\mathrm{T}}^{\mathrm{miss}}$ in $\tau_{\mathrm{had-vis}}$+lepton $t\bar{t}$ CR. Jets misidentified as $\tau_{\mathrm{had-vis}}$ are estimated from data using the FF method. The $l \to \tau$ background includes all processes with e or $\mu$ reconstructed and identified as the $\tau_{\mathrm{had-vis}}$. All other SM backgrounds are derived from MC simulation. Error bars represent statistical and systematic uncertainties.

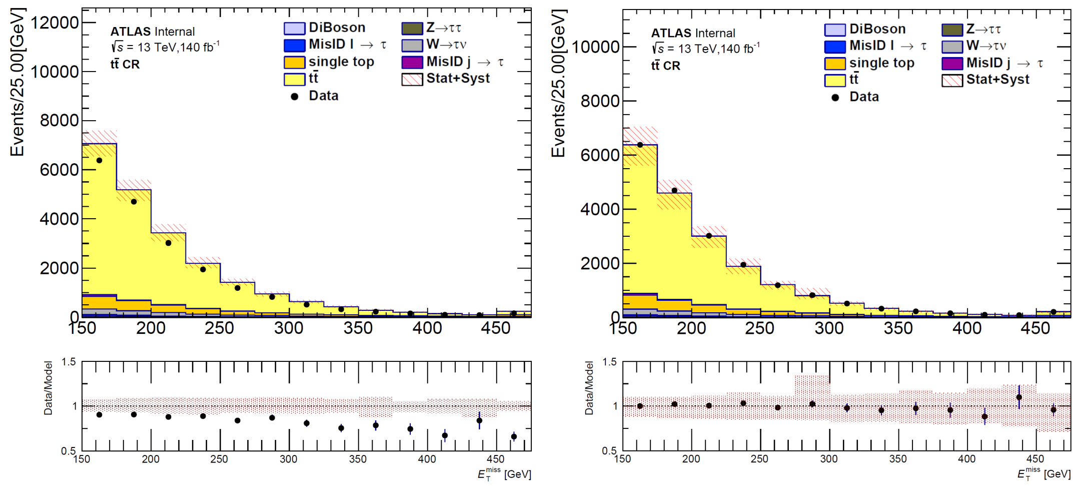


Figure 85: Comparison between the original (left-hand side) and $t\bar{t}$ MC reweighted (right-hand side) distributions of $E_{\mathrm{T}}^{\mathrm{miss}}$ in $\tau_{\mathrm{had-vis}}$+jets $t\bar{t}$ CR. Jets misidentified as $\tau_{\mathrm{had-vis}}$ are estimated from data using the FF method. The $l \to \tau$ background includes all processes with e or $\mu$ reconstructed and identified as the $\tau_{\mathrm{had-vis}}$. All other SM backgrounds are derived from MC simulation. Error bars represent statistical and systematic uncertainties.

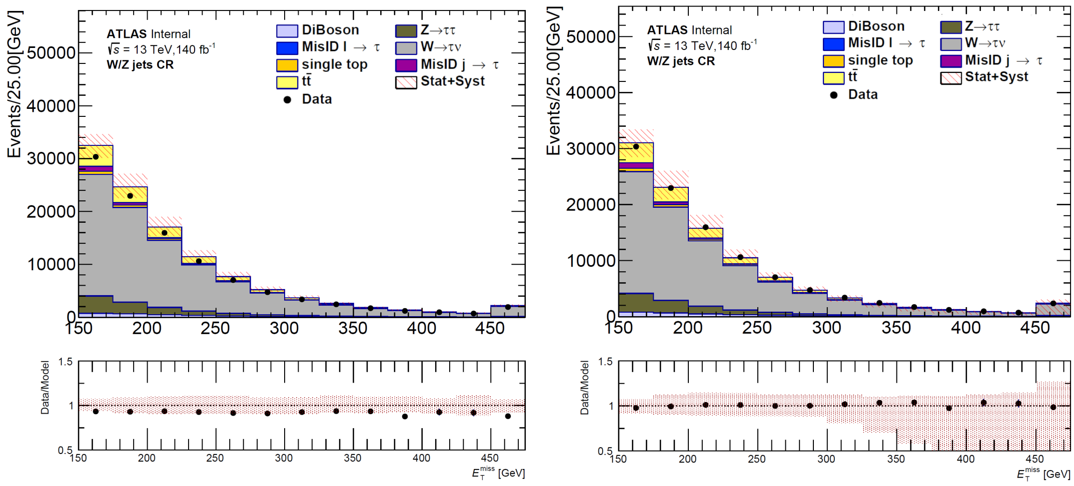


Figure 86: Comparison between the original (left-hand side) and $W$+jets MC reweighted (right-hand side) distributions of $E_T^{miss}$ in $W/Z$+jets CR of $\tau_{had-vis}$+jets channel. Jets misidentified as $\tau_{had-vis}$ are estimated from data using the FF method. The $l \to \tau$ background includes all processes with e or $\mu$ reconstructed and identified as the $\tau_{had-vis}$. All other SM backgrounds are derived from MC simulation. Error bars represent statistical and systematic uncertainties.

### 6.7 Systematic Uncertainties

In addition to the Fake-factor method uncertainties described in the previous Section 6.5.9, the remaining sources of systematic uncertainties are as follows:

- Systematic uncertainties from the detector setup stem from the simulation and reconstruction of electrons, muons, hadronic $\tau$ decays, $b$-jets, and missing transverse momentum, with their impact assessed by varying detector-related parameters within $\pm 1$ standard deviation. Additionally, variations in the scale factors associated with the efficiencies of reconstructing and identifying physics objects are also included. These uncertainties are propagated to both hard and soft components of the reconstructed missing energy [241]. Only systematic uncertainties with a significant impact, specifically those showing more than 0.5% deviation from the nominal value in any bin of the final discriminating variable, are included in the likelihood function used for the statistical analysis.

- In the $\tau_{\text{had-vis}}$+ jets channel, systematic uncertainties on the trigger efficiency include the statistical uncertainty from the erf fit to data, variations in $\tau_{\text{had-vis}}$ and electron identification criteria (*loose*, *medium*, *tight*), requirements on jet and $b$-jet multiplicities, and subtraction of fake $\tau$ leptons estimated using the Fake-factor method. Changes in the binning of $E_T^{miss}$ histograms used in the fit have negligible impact. The statistical uncertainties from the erf fit parameters are converted into eigenmodes of the covariance matrix and treated as independent.

- Theoretical uncertainties related to the main MC-simulated backgrounds - $V$+jets, single-top, and $t\bar{t}$ - are evaluated in both $\tau_{\text{had-vis}}$+jets and $\tau_{\text{had-vis}}$+lepton channels. The key sources include QCD scale, parton shower, hadronization model, initial state radiation (ISR), final state radiation (FSR) and PDF uncertainties, with reweighting applied to all variations but PDFs to avoid double counting. In the $\tau_{\text{had-vis}}$+lepton channel, where $W$+jets background is negligible, a 50% normalization uncertainty is assigned to $W$+jets, $Z$+jets, and diboson backgrounds. The methods employed for modeling ISR and FSR, as well as the treatment of renormalization and factorization scales, are dependent on the specific event generator used. However, a common approach involves scaling the resummation damping factor by a factor of two, to assess the associated uncertainties. To avoid double counting of uncertainties, dedicated reweighting procedures are applied to the $t\bar{t}$ and $W$+jets MC samples for each variation considered.

- Systematic uncertainties related to the reweighting of $t\bar{t}$ and $W$+jets MC samples include: statistical uncertainties in the fitted values of the reweighting function parameters, potential signal contamination in control regions, estimated using the expected $m_{H^+} = 90\,\text{GeV}$ cross-section limit, and uncertainties from extrapolation of reweighting factors to other regions. For $t\bar{t}$, the last uncertainty is assessed by comparing reweighting factors between the $\tau_{\text{had-vis}}$+lepton and $\tau_{\text{had-vis}}$+jets channels. For $W$+jets, where no alternative control region is available, a 50% uncertainty is considered. The total reweighting systematic corresponds to approximately 7% (6%) of the background yield in the $\tau_{\text{had-vis}}$+lepton (jets) channel for $t\bar{t}$, and 0.5% for $W$+jets in the jets channel, with extrapolation uncertainties being dominant.

- Signal uncertainties arise mainly from generator-level filters, which can reduce acceptance after analysis cuts - especially in the $\tau_{\text{had}-\text{vis}}$+jets channel at low $m_{H^+}$, due to the cut on $E_{\text{T}}^{\text{miss}}$. Additional uncertainties stem from PDFs and scale variations ($\mu_R$ and $\mu_F$), with effects on acceptance evaluated using event-by-event envelopes and rescaling procedures to preserve the nominal cross-section.

- The uncertainty associated with the measured integrated luminosity is estimated to be 0.83% [242]. This value was obtained through primary luminosity measurements performed using the LUCID-2 detector [243], complemented by additional measurements from the Inner Detector and calorimeters. This luminosity-related uncertainty impacts the normalization of all simulated samples employed in the analysis.

## 6.8 Results

The statistical analysis of this study relies on a simultaneous binned likelihood fit that estimates the signal strength parameter $\mu = \sigma(pp \to tbH^+) \times \mathcal{B}(H^+ \to \tau\nu)$ and incorporates nuisance parameters $\theta$ to account for statistical and systematic uncertainties through the minimization of the negative log-likelihood function. The likelihood function $\mathcal{L}(\mu, \theta)$ is constructed as the product of Poisson probability terms corresponding to each bin in signal regions. A profile likelihood ratio test statistic $\tilde{q}_\mu$ [244, 245] is used to compare the signal-plus-background and background-only hypotheses, computed as:

$$\tilde{q}_\mu = \begin{cases} -2\ln\dfrac{\mathcal{L}(\mu,\hat{\hat{\theta}}(\mu))}{\mathcal{L}(0,\hat{\hat{\theta}}(0))}, & \hat{\mu} < 0 \\ -2\ln\dfrac{\mathcal{L}(\mu,\hat{\hat{\theta}}(\mu))}{\mathcal{L}(\hat{\mu},\hat{\theta})}, & 0 \le \hat{\mu} \le \mu \\ 0, & \hat{\mu} > \mu \end{cases} \tag{81}$$

where $\hat{\mu}$ and $\hat{\theta}$ represent the values of the parameters that maximize the likelihood function, while $\hat{\hat{\theta}}(\mu)$ refers to the values of the nuisance parameters that maximize the likelihood function for a given value of the signal strength $\mu$. This test statistic is employed for the measurement of the data compatibility with the signal+background hypothesis for a signal strength equal to $\mu$. The $p$-value representing this compatibility is estimated by integrating the distribution of $\tilde{q}_\mu$ above the observed value $\tilde{q}_{\mu,\text{obs}}$. Upper limits on the signal production cross section are derived with the $\mathrm{CL_s}$ method [246]: for a given signal hypothesis, values of the production cross section times branching fraction $\sigma(pp \to btH^+) \times \mathrm{Br}(H^+ \to \tau\nu)$ yielding $\mathrm{CL_s} < 0.05$ are excluded at the 95% confidence level. The asymptotic approximation [247] is used throughout the statistical analysis.

The fit is performed across three signal regions ($\tau_{\text{had-vis}}$+jets, +electron, +muon), using optimized binning to balance statistical uncertainty and discriminating power.

One-sided nuisance parameters are symmetrized (except for $E_{\mathrm{T}}^{\mathrm{miss}}$ filter efficiency), and shape/normalization components are pruned if they contribute less than 0.5% variation. Workspace Maker and RooFit are used to prepare workspaces and perform the final fits.

The PNN score distributions for the 170 GeV and 1000 GeV $m_{H^+}$ mass parameters in different signal regions are depicted in Figures 87-88. All plots are obtained after the statistical fitting procedure with the background-only hypothesis. The binning shown in the figures is used in the statistical analysis, but drawn with uniform width to improve readability.

The expected number of events for all SM processes and the measured event yields in the combined signal regions are depicted in Table 18, prior to using the multivariate discriminant and applying the statistical fitting procedure. Additionally, the contributions from hypothetical charged Higgs bosons are shown, assuming a mass of 170 GeV or 1000 GeV, and with $\sigma(pp \to tbH^+) \times \mathcal{B}(H^+ \to \tau\nu)$ set to the prediction from the hMSSM scenario for $\tan\beta = 40$, as computed using References [69] and [248, 249, 250, 251, 252] for the production cross section and HDECAY [253] for the branching fraction. The data is found to be consistent with the sum of all background processes.

Figure 89 presents the expected and observed exclusion limits as a function of the charged Higgs boson mass hypothesis in the case of the $\tau_{\mathrm{had-vis}}$+jets and $\tau_{\mathrm{had-vis}}$ +lepton signal regions being combined. The observed data are compatible with the background-only hypothesis, with the lowest $p_0$-value found near 250 GeV (0.145). Exclusion limits at 95% CL are set on $\sigma(pp \to tbH^+) \times \mathcal{B}(H^+ \to \tau\nu)$, ranging from 4.51 pb to 0.4 fb across the entire probed mass range. In the 80–130 GeV mass region, this corresponds to limits on $\mathcal{B}(t \to bH^+) \times \mathcal{B}(H^+ \to \tau\nu)$ down to 0.04%.

The impact from the various sources of systematic uncertainty is estimated by comparing the expected 95% CL limits on $\sigma(pp \to tbH^+) \times \mathcal{B}(H^+ \to \tau\nu)$ in the combined signal regions channel when taking only statistical uncertainties into account and those obtained when a certain set of systematic uncertainties is added in the limit-setting procedure, as summarised in Table 19 for $H^+$ masses of 170 GeV and 1000 GeV.

Figure 90 presents the 95% CL exclusion combined limits on $\tan\beta$ as a function of the charged Higgs boson mass in the context of the hMSSM and the $m_h^{\text{mod-}}$ scenario of the MSSM discussed in Section 2.2.3. The analysis showed that for $\tan\beta$ values of 60, above which theoretical predictions become unreliable, the $m_{H^+}$ up to 1400 GeV is excluded. Figures 89 and 90, in addition to the results of this analysis, display limits established using the dataset collected in 2015 and 2016, with an integrated luminosity of 36.1 $\mathrm{fb}^{-1}$ [70], marked as red lines and areas in the plots. A substantial improvement can be observed in all tested models, in particular in the parameter space corresponding to high charged Higgs mass and high $\tan\beta$ .

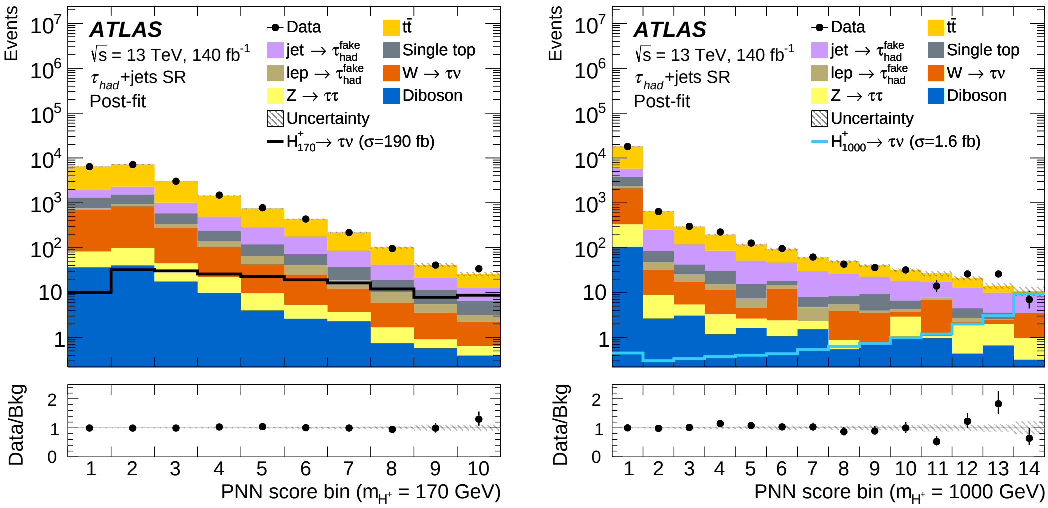


(a) (b)

Figure 87: PNN score distributions in the $\tau_{\text{had-vis}}$+jets signal region, for the 170 GeV (a) and 1000 (b) GeV $m_{H^+}$ hypotheses, after a fit to the data with the background-only hypothesis ("Post-fit"). The ratio between the observed data and the predicted SM background is displayed in the lower panel of each plot. The uncertainty bands incorporate all statistical and systematic uncertainties. The solid black or blue lines represent the signal distribution for the 170 GeV or 1000 GeV charged Higgs boson mass hypothesis, respectively, with the signal distribution scaled to the expected 95% CL limit [11].

Table 18: Expected event yields for the backgrounds and a hypothetical $H^+$ signal after applying all $\tau_{\text{had-vis}}$ + jets selection criteria, and comparison with 140 fb$^{-1}$ of data. All yields are evaluated prior to using the PNN discriminant and applying the statistical fitting procedure. The reported signal values assume charged Higgs boson masses of 170 GeV and 1000 GeV, with a cross-section times branching fraction $\sigma(pp \to tbH^+) \times \mathcal{B}(H^+ \to \tau\nu)$ of 1 pb. Both statistical and systematic uncertainties are provided [11].

| **Sample** | **Event yields and uncertainties** | | |
|---|---|---|---|
| | $\tau_{\text{had}}$+jets | $\tau_{\text{had}} + e$ | $\tau_{\text{had}} + \mu$ |
| **True $\tau_{\text{had}}$** | | | |
| $t\bar{t}$ | $13400 \pm 2000$ | $39000 \pm 6000$ | $39000 \pm 5000$ |
| Single top quark | $1600 \pm 400$ | $2900 \pm 400$ | $3630 \pm 330$ |
| $Z \to \tau\tau$ | $220 \pm 110$ | $900 \pm 500$ | $800 \pm 400$ |
| $W \to \tau\nu$ | $1770 \pm 270$ | $2.4 \pm 2.0$ | $0.07 \pm 0.21$ |
| Diboson ($WW$, $WZ$, $ZZ$) | $120 \pm 60$ | $70 \pm 35$ | $80 \pm 40$ |
| Misidentified jet $\to \tau_{\text{had-vis}}$ | $2430 \pm 200$ | $8500 \pm 700$ | $8200 \pm 700$ |
| Misidentified $e$, $\mu \to \tau_{\text{had-vis}}$ | $280 \pm 170$ | $1000 \pm 500$ | $1000 \pm 500$ |
| All backgrounds | $19800 \pm 2100$ | $52000 \pm 6000$ | $53000 \pm 6000$ |
| $H^+$ (170 GeV), $\sigma \times \mathcal{B} = 1$ pb | $980 \pm 150$ | $580 \pm 70$ | $690 \pm 80$ |
| $H^+$ (1000 GeV), $\sigma \times \mathcal{B} = 1$ pb | $13000 \pm 800$ | $940 \pm 60$ | $1040 \pm 70$ |
| Data | $19650 \pm 140$ | $51500 \pm 230$ | $52730 \pm 230$ |

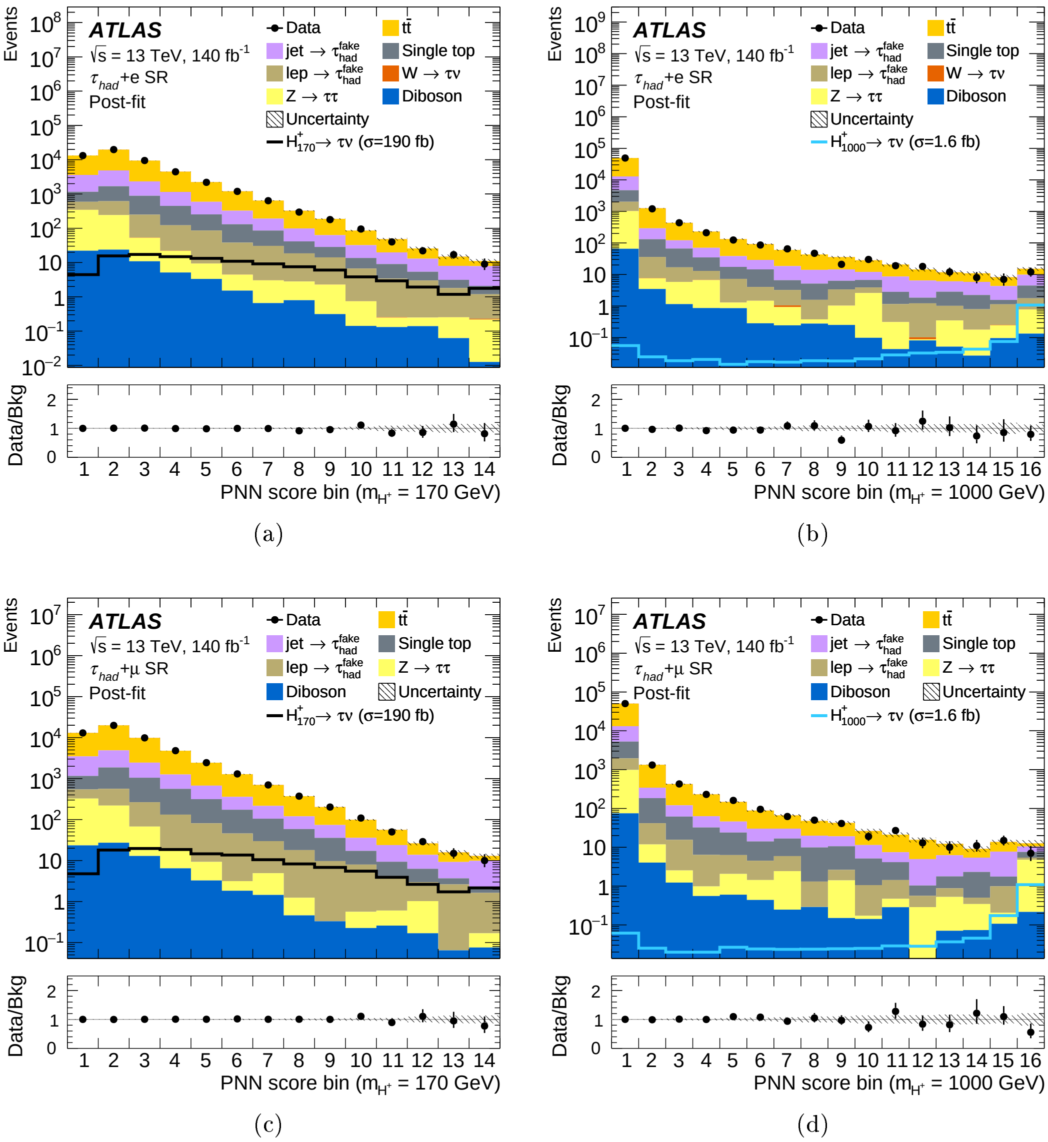


Figure 88: PNN score distributions in the $\tau_{\text{had-vis}}$+electron SR for the 170 GeV $m_{H^+}$ hypothesis (a), $\tau_{\text{had-vis}}$+electron SR for the 1000 GeV $m_{H^+}$ hypothesis (b), $\tau_{\text{had-vis}}$+muon SR for the 170 GeV $m_{H^+}$ hypothesis (c) and $\tau_{\text{had-vis}}$+muon SR for the 1000 GeV $m_{H^+}$ hypothesis (d), after a fit to the data with the background-only hypothesis ("Post-fit"). The ratio between the observed data and the predicted SM background is displayed in the lower panel of each plot. The uncertainty bands incorporate all statistical and systematic uncertainties. The solid black or blue lines represent the signal distribution for the 170 GeV or 1000 GeV charged Higgs boson mass hypothesis, respectively, with the signal distribution scaled to the expected 95% CL limit [11].

Table 19: Impact of systematic uncertainties on $\sigma_{\hat{\mu}}$ (the $\hat{\mu}$ 1 sigma uncertainty), obtained in 95% CL limit on $\sigma(pp \to tbH^+) \times \mathcal{B}(H^+ \to \tau\nu)$, for two $H^+$ mass hypotheses: 170 GeV and 1000 GeV in the combined channel. The impact is obtained by taking the difference in quadrature of the uncertainty ($\sigma_{\hat{\mu}}$) on $\hat{\mu}$ obtained when computing the expected limit considering ALL statistical uncertainties, with the $\sigma_{\hat{\mu}}$ obtained when computing the expected limit while a certain set of systematic uncertainties is removed in the limit-setting procedure. The impact is defined as, Impact $= \frac{(\sigma(\hat{\mu}_{\mathrm{ALL}})^2 - \sigma(\hat{\mu}_{\mathrm{group}})^2) \cdot 100}{\sigma(\hat{\mu}_{\mathrm{ALL}})}$. The row "Total" is obtained by computing the normalized difference in quadrature of the expected uncertainty when all systematics are added in the limit setting procedure [70].

| **Source of systematic uncertainty** | **Impact on $\sigma(\hat{\mu})$ [%]** | |
|---|---|---|
| | $m_{H^+} = 170$ GeV | $m_{H^+} = 1000$ GeV |
| **Experimental** | | |
| Luminosity | 1.0 | 1.0 |
| Trigger | 12 | 4.1 |
| $\tau_{\text{had-vis}}$ | 12 | 8.3 |
| Jet | 27 | 17 |
| Electron | 1.9 | 4.0 |
| Muon | 9.3 | 2.2 |
| $E_{\mathrm{T}}^{\mathrm{miss}}$ | 35 | 3.3 |
| Fake-factor method | 21 | 16 |
| **Signal and background models** | | |
| $t\bar{t}$ modeling | 20 | 14 |
| Single-top-quark modeling | 46 | 2.6 |
| $W/Z$+jets modeling | 13 | 51 |
| Cross-sections ($W/Z/VV/t$) | 2.3 | 15 |
| $H^+$ signal modeling | 8.5 | 1.0 |
| Total | 84 | 70 |

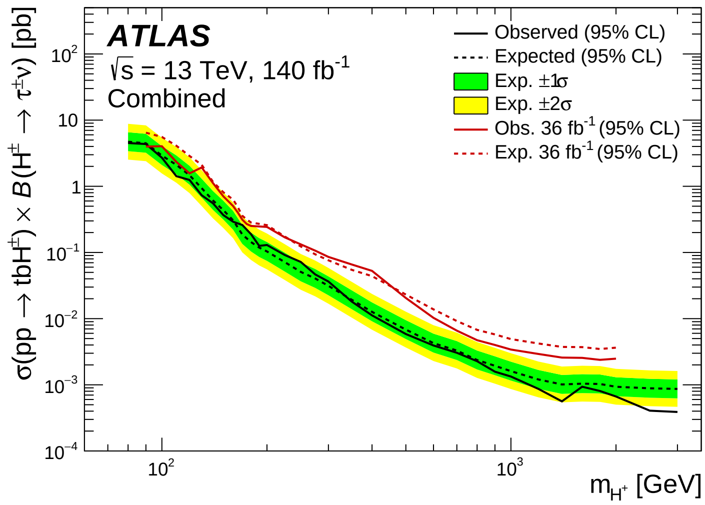


Figure 89: The observed and expected 95% CL exclusion limits on $\sigma(pp \to tbH^+) \times \mathcal{B}(H^+ \to \tau\nu)$ as a function of the charged Higgs boson mass, for the combination of the $\tau_{\mathrm{had-vis}}$+jets and the $\tau_{\mathrm{had-vis}}$+lepton SRs. The one-standard-deviation (green) and two-standard-deviation (yellow) uncertainty bands are also shown. As a comparison, the red lines present the observed and expected exclusion limits based on the dataset of 36.1 $\mathrm{fb}^{-1}$ collected in 2015 and 2016 at $\sqrt{s} = 13$ TeV [70].

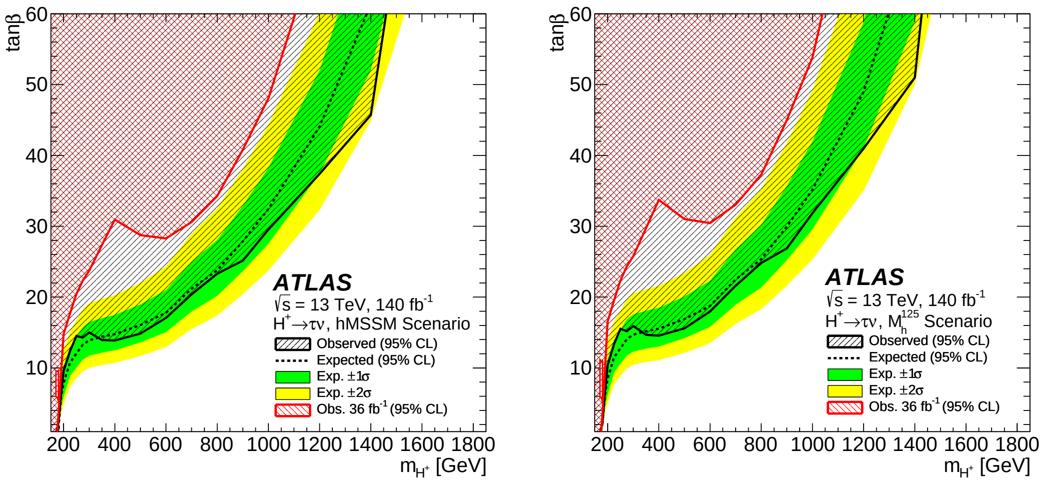


(a) (b)

Figure 90: The 95% CL exclusion limits on $\tan\beta$ as a function of $m_{H^+}$, shown in the context of (a) the hMSSM and (b) the $m_h^{\text{mod-}}$ scenario of the MSSM, for the regions in which theoretical predictions are available ($0.5 \leq \tan\beta \leq 60$). In the case of the expected limits, one-standard-deviation (green) and two-standard-deviation (yellow) uncertainty bands are also shown. As a comparison, the red curves present the observed and expected exclusion limits based on the dataset of 36.1 $\mathrm{fb}^{-1}$ collected in 2015 and 2016 at $\sqrt{s} = 13$ TeV [70].

## 6.9 Conclusions

A search for the $H^+ \to \tau\nu$ process, in which the $H^+$ originates from top-quark decays or is produced in association with a top-quark, was performed. Two distinctive channels were targeted according to the parallel decays of the $W$ boson: the $\tau_{\text{had}}$+jets and $\tau_{\text{had}}$+lepton channels. The analysis was based on the $pp$ collisions dataset at $\sqrt{s} = 13$ TeV, collected with the ATLAS experiment in LHC Run-2, corresponding to an integrated luminosity of 140 fb$^{-1}$. The investigated mass range of the charged Higgs boson was 80–3000 GeV.

My contribution to the analysis was the fake $\tau_{\text{had-vis}}$ background estimation originating from the gluon- or quark-initiated jets employing a data-driven Fake-factor method. The method has been adjusted to the analysis needs and the FFs for multi-jet and $W$+jets control regions were extracted. Then, a template-fit method was utilized to combine the FFs for CRs according to the proper gluon/quark-originating jet composition in the sought signal regions. The obtained combined FFs for SRs were validated in the dedicated control regions enriched with fake $\tau_{\text{had-vis}}$ background, showing a good estimation performance. Next, additional studies were conducted to assess different sources of the systematic uncertainties corresponding to the FF method, which revealed the biggest contribution from the heavy-flavour jets misidentified as $\tau_{\text{had-vis}}$ in the signal regions. The estimation of the fake jets$\to \tau_{\text{had-vis}}$ background is an important source of systematic uncertainties for the whole $H^+$ masses spectrum.

The experimental results are consistent with the background-only hypothesis. Upper limits at the 95% confidence level are set on the production cross-section of the charged Higgs boson times the branching fraction $\mathcal{B}(H^+ \to \tau\nu_\tau)$ in the range 4.51 pb–0.4 fb. In the mass range 80–130 GeV, assuming the Standard Model cross-section for $t\bar{t}$ production, this corresponds to upper limits between 0.27% and 0.04% for the branching fraction $\mathcal{B}(t \to bH^+) \times \mathcal{B}(H^+ \to \tau\nu)$.

# 7 Summary

This thesis presents a multi-faceted investigation contributing to searches for new physics within the scalar sector using advanced $\tau$ lepton reconstruction and identication techniques, as well as developments in detector operations at the ATLAS experiment.

The first part of the thesis focused on detector-related work on the ATLAS SCT detector and the upgrade of the Inner Detector for the HL-LHC. The environmental control system of the SCT was migrated to a modern quasar-based OPC UA architecture, improving maintainability and security. Contribution to the development of the readout system for pre-production of ITk Strips PP2 in Cracow, employing the EMCI and EMP devices, will lay the foundation for future control and monitoring applications in the HL-LHC phase of the ATLAS Experiment operation.

The second part of the thesis documents the study of $\tau$ lepton polarization in $Z \to \tau\tau$ decays using various MC samples employed in ATLAS analyses. While samples generated with Sherpa 2.2.11 and Powheg+Pythia8 showed good agreement with the LEP-measured polarization value ($P \approx -0.145$), the MadGraph+Pythia8 FxFx samples exhibited a small excess. A new Rivet routine was developed to validate $\tau$ polarization and spin correlations, revealing the absence of longitudinal spin correlations in Sherpa 2.2.11 samples, and transverse spin correlations in both Sherpa and Powheg+Pythia8 samples. These findings were reported to the ATLAS Tau CP Group. Additionally, minor deviations from Particle Data Group (PDG) values in $\tau$ hadronic branching ratios were observed. Comparisons of reconstructed $\tau$ identification variables using the new RNN and the legacy BDT algorithms showed consistent performance, further improved by $\tau$ $p_T$ reweighting. These comparisons and validations align with ATLAS's broader strategy of using multiple MC generators to assess theoretical uncertainties, validate detector modeling, and ensure that results do not depend excessively on a single simulation framework.

The final part of the thesis was dedicated to the search for a charged Higgs boson in the $H^+ \to \tau\nu$ decay channel. Events were studied in both the $\tau_{\mathrm{had}} + \mathrm{jets}$ and $\tau_{\mathrm{had}} +$ lepton final states using the full Run-2 ATLAS dataset at $\sqrt{s} = 13$ TeV, corresponding to 140 fb$^{-1}$ of integrated luminosity. The analysis probed a wide mass range of 80–3000 GeV. The author's contribution focused on estimating backgrounds from jets misidentified as hadronically decaying $\tau$ leptons using a data-driven Fake-Factor (FF) method. FFs were derived for multijet and $W + \mathrm{jets}$ control regions and combined using a template fit that accounted for the jet flavour composition of signal regions. The method was validated and systematic uncertainties assessed, with the largest contributions stemming from heavy-flavour jet component. Accurate estimation of the background contribution from fake jets that are misidentified as $\tau_{\mathrm{had-vis}}$ candidates is crucial, as it represents a substantial source of systematic uncertainties across the entire investigated mass range of $H^+$.

Results of the search revealed the data to be consistent with the background-only hypothesis. Upper limits at the 95% confidence level were set on the product of the charged Higgs boson production cross-section and the branching ratio $\mathcal{B}(H^+ \to \tau\nu)$, ranging from 4.51 pb to 0.4 fb across the investigated mass spectrum. In the 80–130 GeV region, this corresponds to limits on $\mathcal{B}(t \to bH^+) \times \mathcal{B}(H^+ \to \tau\nu)$ of 0.27%–0.04%, assuming Standard Model top-quark pair production. While no significant excess above the SM expectation was observed, the results significantly extend previous exclusion limits, provide important input for ongoing searches in the Higgs sector, as well as highlight the importance of $\tau$ lepton final states in searches for physics beyond the Standard Model.

# References


[1] ATLAS Collaboration. "The ATLAS experiment at the CERN Large Hadron Collider". In: *JINST* 3 (2008), S08003.

[2] CMS Collaboration. "The CMS experiment at the CERN LHC". In: *JINST* 3 (2008), S08004.

[3] L. R. Evans and P. Bryant. "LHC Machine". In: *JINST* 3 (2008), S08001.

[4] G.C. Branco et al. "Theory and phenomenology of two-Higgs-doublet models". In: *Phys. Rep.* 516.1–2 (2012), pp. 1–102.

[5] H. E. Haber and G. L. Kane. "The Search for Supersymmetry: Probing Physics Beyond the Standard Model". In: *Phys. Rep.* 117 (1985), p. 75.

[6] MSSM Working Group collaboration. "The Minimal Supersymmetric Standard Model: Group Summary Report". In: *Proceedings of the GDR (Groupement De Recherche) — Supersymétrie*. Montpellier, France, 1998.

[7] S. Dittmaier et al. "Handbook of LHC Higgs Cross Sections: 1. Inclusive Observables". In: (2011).

[8] K. Lantzsch et al. "The ATLAS Detector Control System". In: *Journal of Physics: Conference Series* 396.1 (2012), p. 012028.

[9] O. Brüning and L. Rossi. "The High-Luminosity Large Hadron Collider". In: *Nature Reviews Physics* 1 (2019), pp. 232–234.

[10] L. Gonella. "The ATLAS ITk Detector System for the Phase-II LHC Upgrade". In: *Nucl. Instrum. Methods Phys. Res., A* 1045 (2023), p. 167597.

[11] ATLAS Collaboration. "Search for charged Higgs bosons produced in top-quark decays or in association with top quarks and decaying via $H^\pm \to \tau^\pm \nu_\tau$ in 13 TeV $pp$ collisions with the ATLAS detector". In: *Phys. Rev. D* 111 (7 2025), p. 072006.

[12] S. L. Glashow. "Partial Symmetries of Weak Interactions". In: *Nuclear Physics* 22 (1961), p. 579.

[13] S. Weinberg. "A Model of Leptons". In: *Phys. Rev. Lett.* 19 (1967), p. 1264.

[14] A. Salam. "Weak and Electromagnetic Interactions". In: *Proceedings of the 8th Nobel Symposium*. Conf. Proc. C 680519. 1968, p. 367.

[15] S. L. Glashow, J. Iliopoulos, and L. Maiani. "Weak Interactions with Lepton-Hadron Symmetry". In: *Phys. Rev. D* 2 (1970), p. 1285.

[16] F. Englert and R. Brout. "Broken Symmetry and the Mass of Gauge Vector Mesons". In: *Phys. Rev. Lett.* 13 (1964), p. 321.

[17] P. W. Higgs. "Broken Symmetries and the Masses of Gauge Bosons". In: *Phys. Rev. Lett.* 13 (1964), p. 508.

[18] P. W. Higgs. "Spontaneous Symmetry Breakdown without Massless Bosons". In: *Physical Review* 145 (1966), p. 1156.

[19] E. Fermi. "Zur Quantelung des idealen einatomigen Gases". German. In: *Zeitschrift für Physik* 36.11–12 (1926), pp. 902–912.

[20] P. Dirac. "On the Theory of Quantum Mechanics". In: *Proc. R. Soc. Lond. Series A, Containing Papers of a Mathematical and Physical Character* 112.762 (1926), pp. 661–677.

[21] S. Bose. "Plancks Gesetz und Lichtquantenhypothese". In: *Zeitschrift für Physik* 26.1 (1924), pp. 178–181.

[22] A. Einstein. "Quantentheorie des einatomigen idealen Gases". In: *Sitzungsberichte der Preussischen Akademie der Wissenschaften, Physikalisch-mathematische Klasse* (1924), pp. 261–267.

[23] D. Galbraith and C. Burgard. *UX: Standard Model of the Standard Model.* `https://davidgalbraith.org/portfolio/ux-standard-model-of-the-standard-model/`. 2012.

[24] LHCb Collaboration. *Exotic hadron naming convention.* 2023. arXiv: `2206.15233 [hep-ex]`.

[25] P. Mohr et al. "CODATA recommended values of the fundamental physical constants: 2022". In: *Rev. Mod. Phys.* 97 (2025), p. 025002.

[26] T. Nakano and K. Nishijima. "Charge Independence for V Particles". In: *Progress of Theoretical Physics* 10.5 (1953), pp. 581–582.

[27] K. Nishijima. "Charge Independence Theory of V Particles". In: *Progress of Theoretical Physics* 13.3 (1955), pp. 285–304.

[28] M. Gell-Mann. "The Interpretation of the New Particles as Displaced Charged Multiplets". In: *Il Nuovo Cimento* 4 (1956), p. 848.

[29] D. J. Gross and F. Wilczek. "Ultraviolet Behavior of Nonabelian Gauge Theories". In: *Phys. Rev. Lett.* 30 (1973), pp. 1343–1346.

[30] H. D. Politzer. "Reliable Perturbative Results for Strong Interactions?" In: *Phys. Rev. Lett.* 30 (1973), pp. 1346–1349.

[31] D. J. Gross and F. Wilczek. "Asymptotically Free Gauge Theories - I". In: *Phys. Rev. D* 8 (1973), pp. 3633–3652.

[32] G. P. Salam. "Elements of QCD for Hadron Colliders". In: *2009 European School of High-Energy Physics.* 2010.

[33] N. Rougier. *Higgs Potential.* `https://tikz.net/higgs-potential/`. Accessed: 2025-06-19.

[34] ATLAS Collaboration. "Observation of a new particle in the search for the Standard Model Higgs boson with the ATLAS detector at the LHC". In: *Phys. Lett. B* 716 (2012), pp. 1–29.

[35] CMS Collaboration. "Observation of a new boson at a mass of 125 GeV with the CMS experiment at the LHC". In: *Phys. Lett. B* 716 (2012), pp. 30–61.

[36] ATLAS Collaboration. "Combination of searches for Higgs boson pairs in pp collisions at $\sqrt{s} = 13$ TeV with the ATLAS detector". In: *Phys. Lett. B* 800 (2020), p. 135103.

[37] CMS Collaboration. "Combination of searches for Higgs boson pair production in proton-proton collisions at $\sqrt{s} = 13$ TeV". In: *Phys. Rev. Lett.* 122 (2019), p. 121803.

[38] J. Goldstone, A. Salam, and S. Weinberg. "Broken Symmetries". In: *Physical Review* 127 (1962), pp. 965–970.

[39] P. A. Zyla et al. "Review of Particle Physics, 2020-2021. RPP". In: *Prog. Theor. Exp. Phys.* 2020 (2020), p. 083C01.

[40] A. Einstein. "Die Grundlage der allgemeinen Relativitätstheorie". In: *Annalen der Physik* 354 (1916), p. 769.

[41] B. P. Abbott et al. "Observation of Gravitational Waves from a Binary Black Hole Merger". In: *Phys. Rev. Lett.* 116 (6 2016), p. 061102.

[42] L. Smolin. “What Are We Missing in Our Search for Quantum Gravity?” In: *Foundations of Mathematics and Physics One Century After Hilbert: New Perspectives*. Springer International Publishing, 2018, pp. 287–304.

[43] J. Lesgourgues et al. “Neutrino Cosmology”. In: *Contemporary Physics* 54 (2013), p. 178.

[44] S. Gariazzo et al. “Neutrino masses and their ordering: global data, priors and models”. In: *J. Cosmol. Astropart. Phys.* 03 (2018), p. 011.

[45] E. Majorana. “Teoria simmetrica dell’elettrone e del positrone”. In: *Nuovo Cim.* 14 (1937), pp. 171–184.

[46] M. J. Dolinski, A. W. Poon, and W. Rodejohann. “Neutrinoless Double-Beta Decay: Status and Prospects”. In: *Annu. Rev. Nucl. Part. Sci.* 69 (2019), p. 219.

[47] D. S. Pereira et al. “Baryogenesis: A Symmetry Breaking in the Primordial Universe Revisited”. In: *Symmetry* 16.1 (2023), p. 13.

[48] A. D. Sakharov. “Violation of CP Invariance, C asymmetry, and baryon asymmetry of the universe”. In: *Pisma Zh. Eksp. Teor. Fiz.* 5 (1967), p. 32.

[49] F. Zwicky. “Republication of: The redshift of extragalactic nebulae”. In: *Gen. Relativ. Gravit.* 41 (2009), p. 207.

[50] Planck Collaboration. “Planck 2013 results. I. Overview of products and scientific results”. In: *Astron. Astrophys.* 571 (2014), A1.

[51] R. Massey, T. Kitching, and J. Richard. “The dark matter of gravitational lensing”. In: *Rep. Prog. Phys.* 73 (2010), p. 086901.

[52] Planck Collaboration. “Planck 2015 results. XIII. Cosmological parameters”. In: *Astron. Astrophys.* 594 (2016), A13.

[53] E.V. Linder. “Dark Energy, Expansion History of the Universe, and SNAP”. In: *AIP Conference Proceedings*. Vol. 655. AIP, 2003, pp. 193–207.

[54] S. P. Martin. “A Supersymmetry Primer”. In: *Adv. High Energy Phys.* 18 (1998), p. 1.

[55] S. P. Martin. “A Supersymmetry Primer”. In: *Adv. High Energy Phys.* 21 (2010), p. 1.

[56] Y. Wu and L. Wolfenstein. “Sources of CP violation in the two Higgs doublet model”. In: *Phys. Rev. Lett.* 73 (1994), pp. 1762–1764.

[57] L. Lavoura. “Signatures of discrete symmetries in the scalar sector”. In: *Phys. Rev. D* 50 (1994), pp. 7089–7092.

[58] S. L. Glashow and S. Weinberg. “Natural Conservation Laws for Neutral Currents”. In: *Phys. Rev. D* 15.7 (1977), pp. 1958–1965.

[59] S. Ferrara and B. Zumino. “Supergauge invariant Yang-Mills theories”. In: *Nucl. Phys. B* 79 (1974), p. 413.

[60] J. Wess and B. Zumino. “Supergauge invariant extension of quantum electrodynamics”. In: *Nucl. Phys. B* 78 (1974), p. 1.

[61] J. Wess and B. Zumino. “Supergauge transformations in four dimensions”. In: *Nucl. Phys. B* 70 (1974), p. 39.

[62] A. Salam and J. Strathdee. “Super-symmetry and non-Abelian gauges”. In: *Phys. Lett. B* 51 (1974), p. 353.

[63] R. Ball. “Chiral gauge theory”. In: *Phys. Rep.* 182 (1989), p. 1.

[64] S. Heinemeyer. "MSSM Higgs physics at higher orders". In: *Int. J. Mod. Phys. A* 21 (2006), p. 2659.

[65] P. Slavich et al. "Higgs-mass predictions in the MSSM and beyond". In: *Eur. Phys. J. C* 81 (2021), p. 450.

[66] M. Carena et al. "MSSM Higgs boson searches at the LHC: benchmark scenarios after the discovery of a Higgs-like particle". In: *Eur. Phys. J. C* 73, 2552 (2013).

[67] A. Djouadi et al. "The post-Higgs MSSM scenario: habemus MSSM?" In: *Eur. Phys. J. C* 73 (2013), p. 2650.

[68] A. Djouadi et al. "Fully covering the MSSM Higgs sector at the LHC". In: *JHEP* 06 (2015), p. 168.

[69] C. Degrande et al. "Accurate predictions for charged Higgs production: Closing the $m_{H^\pm} \sim m_t$ window". In: *Phys. Lett. B* 772 (2017), p. 87.

[70] ATLAS Collaboration. "Search for charged Higgs bosons decaying via $H^\pm \to \tau^\pm \nu_\tau$ in the $\tau$+jets and $\tau$+lepton final states with 36 fb$^{-1}$ of $pp$ collision data recorded at $\sqrt{s} = 13$ TeV with the ATLAS experiment". In: *JHEP* 09 (2018), p. 139.

[71] M. Flechl. "Charged Higgs boson production around the top quark mass threshold". In: *Proceedings of Prospects for Charged Higgs Discovery at Colliders — PoS(CHARGED2016)*. Vol. 286. 2017, p. 013.

[72] M. L. Perl. *The Discovery of the Tau Lepton*. SLAC Report SLAC-PUB-5937. 1992. URL: https://inspirehep.net/literature/340184.

[73] S. Navas et al. "Review of particle physics". In: *Phys. Rev. D* 110.3 (2024), p. 030001.

[74] ATLAS Collaboration. "Measurement of Tau Polarization in $W \to \tau\nu$ Decays with the ATLAS Detector in pp Collisions at $\sqrt{s} = 7$ TeV". In: *Eur. Phys. J. C* 72 (2012), p. 2062.

[75] ALEPH Collaboration et al. "Precision electroweak measurements on the Z resonance". In: *Phys. Rep.* 427 (2006), p. 257.

[76] S. Bedikian. "A Search for the Charged Higgs: Using Tau Polarimetry with Proton-Proton Collisions at the ATLAS Detector". Presented on 04 Mar 2013. Yale U. URL: https://repository.cern/records/bdwh3-twa28/preview/CERN-THESIS-2013-019.pdf.

[77] K. Hagiwara, A. Martin, and D. Zeppenfeld. "Tau polarization measurements at LEP and SLC". In: *Phys. Lett. B* 235 (1990), p. 198.

[78] A. Rouge. "Polarization observables in the 3 pi neutrino decay mode". In: *Z. Phys. C* 48 (1990), p. 75.

[79] S. Berge, W. Bernreuther, and S. Kirchner. "Determination of the Higgs CP-mixing angle in the tau decay channels at the LHC including the Drell–Yan background". In: *Eur. Phys. J. C* 74.11 (2014).

[80] Burton Richter. "The LEP Experiment". In: *Science* 218.4567 (1982), pp. 8–8.

[81] J. Lettry et al. "Overview of the Status and Developments on Primary Ion Sources at CERN". In: *Conf. Proc. C* 110904 (2011). Ed. by Christine Petit-Jean-Genaz, pp. 3474–3476.

[82] CERN. *Linear Accelerator 4*. https://home.cern/science/accelerators/linear-accelerator-4. Accessed: 2025-03-25.

[83] CERN. *The Proton Synchrotron Booster*. https://home.cern/science/accelerators/proton-synchrotron-booster. Accessed: 2025-03-25.

[84] CERN. *The Proton Synchrotron*. https://home.cern/science/accelerators/proton-synchrotron. Accessed: 2025-03-25.

[85] CERN. *The Super Proton Synchrotron*. https://home.cern/science/accelerators/super-proton-synchrotron. Accessed: 2025-03-25.

[86] H. Bartosik and G. Rumolo. *Performance of the LHC injector chain after the upgrade and potential development*. 2022. eprint: arXiv.2203.09202.

[87] J. Caron. "Cross section of LHC dipole. Dipole LHC: coup transversale." AC Collection. Legacy of AC. Pictures from 1992 to 2002. 1998. URL: https://cds.cern.ch/record/841539.

[88] CERN. *Linear Accelerator 3*. https://home.cern/science/accelerators/linear-accelerator-3. Accessed: 2025-03-25.

[89] CERN. *Low Energy Ion Ring (LEIR)*. https://home.cern/science/accelerators/low-energy-ion-ring. Accessed: 2025-03-25.

[90] The ALICE Collaboration. "The ALICE experiment at the CERN LHC". In: *JINST* 3 (2008), S08002.

[91] LHCb Collaboration. "The LHCb Detector at the LHC". In: *JINST* 3 (2008), S08005.

[92] G. Anelli et al. "The TOTEM experiment at the CERN Large Hadron Collider". In: *JINST* 3 (2008), S08007.

[93] O. Adriani et al. "The LHCf detector at the CERN Large Hadron Collider". In: *JINST* 3 (2008), S08006.

[94] J. Pinfold. "The MoEDAL experiment at the LHC". In: *EPJ Web of Conferences* 145 (2017). Ed. by B. Pattison, p. 12002.

[95] Henso Abreu et al. "The FASER detector". In: *JINST* 19 (2024), P05066.

[96] CERN. *SND@LHC Experiment*. https://home.cern/science/experiments/sndlhc. Accessed: 2025-03-25.

[97] ATLAS Collaboration. "The ATLAS experiment at the CERN Large Hadron Collider: a description of the detector configuration for Run 3". In: *JINST* 19.05 (2024), P05063.

[98] ATLAS Collaboration. *ATLAS Luminosity Public Results for Run 3*. https://twiki.cern.ch/twiki/bin/view/AtlasPublic/LuminosityPublicResultsRun3. Accessed: 2025-03-25.

[99] G. Strong. "On the impact of selected modern deep-learning techniques to the performance and celerity of classification models in an experimental high-energy physics use case". In: *Mach. learn.: sci. technol.* 1 (2020), p. 045006.

[100] ATLAS IBL Collaboration. "Production and integration of the ATLAS Insertable B-Layer". In: *JINST* 13 (2018), T05008.

[101] ATLAS Collaboration. "Alignment of the ATLAS Inner Detector in Run-2". In: *Eur. Phys. J. C* 80 (2020), p. 1194.

[102] ATLAS Collaboration. *ATLAS Schematics Resources*. https://atlas.cern/Resources/Schematics. Accessed: 2025-03-25.

[103] J. Guillermo P. Vazquez. "The ATLAS Data Acquisition System in LHC Run 2". In: *J. Phys. Conf. Ser.* 898 (2017), p. 032017.

[104] ATLAS Collaboration. "Operation of the ATLAS trigger system in Run 2". In: *JINST* 15.10 (2020), p. 10004.

[105] CERN. *CERN-EX-1301009-01.* https://cds.cern.ch/images/CERN-EX-1301009-01. Accessed: 2025-03-25.

[106] ATLAS Collaboration. "Performance of the ATLAS track reconstruction algorithms in dense environments in LHC Run 2". In: *Eur. Phys. J. C* 77.10 (2017).

[107] G. Borissov et al. *ATLAS strategy for primary vertex reconstruction during Run-2 of the LHC.* Tech. rep. ATL-PHYS-PUB-2015-026. CERN, 2015. URL: https://cds.cern.ch/record/2037717/.

[108] ATLAS Collaboration. "Jet reconstruction and performance using particle flow with the ATLAS Detector". In: *Eur. Phys. J. C* 77 (2017), p. 466.

[109] ATLAS Collaboration. "Electron reconstruction and identification efficiency measurements with the ATLAS detector using the 2011 LHC proton-proton collision data". In: *Eur. Phys. J. C* 74 (2014), p. 2941.

[110] ATLAS Collaboration. "Electron and photon energy calibration with the ATLAS detector using LHC Run 1 data". In: *Eur. Phys. J. C* 74 (2014), p. 3071.

[111] ATLAS Collaboration. "Muon reconstruction performance of the ATLAS detector in proton-proton collision data at $\sqrt{s} = 13$ TeV". In: *Eur. Phys. J. C* 76 (2016), p. 292.

[112] M. Cacciari, G. P. Salam, and G. Soyez. "The anti-$k_T$ jet clustering algorithm". In: *JHEP* 04 (2008), p. 063.

[113] JetEtmiss Group. *Jet Recommendations.* https://twiki.cern.ch/twiki/bin/view/AtlasProtected/JetEtmissRecommendationsR21. Accessed: 2025-03-25.

[114] A. Coccaro. "Track reconstruction and $b$-jet identification for the ATLAS trigger system". In: *J. Phys. Conf. Ser.* 368 (2012), p. 012034.

[115] ATLAS Collaboration. *Expected performance of the ATLAS b-tagging algorithms in Run-2.* Tech. rep. ATL-PHYS-PUB-2015-022. CERN, 2015. URL: https://cds.cern.ch/record/2037697.

[116] ATLAS Collaboration. "Identification and energy calibration of hadronically decaying tau leptons with the ATLAS experiment in $pp$ collisions at $\sqrt{s} = 8$ TeV". In: *Eur. Phys. J. C* 75.7 (2015).

[117] ATLAS Collaboration. *Identification of hadronic tau lepton decays using neural networks in the ATLAS experiment.* Tech. rep. 2019. URL: https://cds.cern.ch/record/2688062/.

[118] ATLAS Collaboration. *Reconstruction, Energy Calibration, and Identification of Hadronically Decaying Tau Leptons in the ATLAS Experiment for Run-2 of the LHC.* Tech. rep. CERN, 2015. URL: https://cds.cern.ch/record/2064383/.

[119] ATLAS Collaboration. *$E_T^{miss}$ performance in the ATLAS detector using 2015-2016 LHC pp collisions.* Tech. rep. CERN, 2018. URL: https://cds.cern.ch/record/2625233/.

[120] HL-LHC Approval by CERN Council. https://council.web.cern.ch/en/content/181. Accessed: 2025-04-03.

[121] O. Aberle et al. *High-Luminosity Large Hadron Collider (HL-LHC): Technical design report.* CERN Yellow Reports: Monographs. 10/2020. URL: https://cds.cern.ch/record/2749422?ln=pl.

[122] CERN. *High-Luminosity Large Hadron Collider (HL-LHC) Project.* https://hilumilhc.web.cern.ch/content/hl-lhc-project. Accessed: 2025-04-03.

[123] CERN. *HL-LHC Schedule and Plots.* https://lhc-commissioning.web.cern.ch/schedule/HL-LHC-plots.html. Accessed: 2025-04-03.

[124] A. Dainese et al. *Report on the Physics at the HL-LHC, and Perspectives for the HL-LHC.* Tech. rep. 7/2019. URL: https://cds.cern.ch/record/2703572.

[125] L. Gonella. "The ATLAS ITk detector system for the Phase-II LHC upgrade". In: *Nucl. Instrum. Methods Phys. Res. A* 1045 (2023), p. 167597.

[126] F. Lasagni Manghi. "ATLAS upgrade for the HL-LHC". In: *Nucl. Instrum. Meth. A* 1069 (2024), p. 169917.

[127] A. Paramonov. "FELIX: the Detector Interface for the ATLAS Experiment at CERN". In: *EPJ Web of Conferences* 251 (Jan. 2021), p. 04006.

[128] OPC Foundation. *OPC UA Online Reference - Released Specifications.* https://reference.opcfoundation.org/. Accessed: 2025-05-27.

[129] O. Beltramello et al. "The Detector Safety System of the ATLAS experiment". In: *JINST* 4 (2009), P09012.

[130] CAN (Controller Area Network) in Automation. http://www.can-cia.org/. Accessed: 2025-04-29.

[131] A. Daneels and W. Salter. "Selection and evaluation of commercial SCADA systems for the controls of the CERN LHC experiments". In: *Proceedings of the 7th International Conference on Accelerator and Large Experimental Physics Control Systems (ICALEPCS 1999).* Trieste, Italy, 1999.

[132] ETM professional control GmbH. *WinCC Open Architecture - Product Information.* https://www.winccoa.com/product-information.html. Accessed: 2025-04-03.

[133] A. Barriuso Poy et al. "Hierarchical Control for the ATLAS Experiment". In: *Europhys. Conf. Abstr.* Vol. 29J. 2005, TU2.4–20.

[134] O. Holme et al. "The JCOP Framework". In: *ECA*. Vol. 29J. CERN-OPEN-2005-027. 2005, WE2.1–6O.

[135] B. Hallgren et al. "The Embedded Local Monitor Board (ELMB) in the LHC Front-End I/O Control System". In: *7th Workshop on Electronics for LHC Experiments - LEB 2001: Proceedings.* CERN-2001-005. 2001, p. 325.

[136] International Electrotechnical Commission. *OPC Unified Architecture - Part 1: Overview and concepts.* Tech. Rep. IEC TR 62541-1:2016. 2016. URL: https://webstore.iec.ch/publication/25997.

[137] P. Nikiel. "Automating software development for distributed control systems with the OPC UA standard". Presented on 22 Dec 2022. AGH-UST, 2022. URL: https://cds.cern.ch/record/2850424.

[138] ATLAS Collaboration. *ATLAS Public Plots: Detector Control System (DCS).* https://twiki.cern.ch/twiki/bin/view/AtlasPublic/ApprovedPlotsDCS. Accessed: 2025-04-03.

[139] A. Robichaud-Véronneau. "Measurement of the Production Cross-Section of J/psi Mesons Decaying into Electron-Positron Pairs in Proton-Proton Interactions at a Collision Energy of 10 TeV, using a detailed Simulation of the ATLAS Detector at the CERN LHC". Presented on 25 Nov 2010. Geneva U., 2010. URL: https://cds.cern.ch/record/1322645.

[140] A. Sfyrla et al. "The Detector Control System for the ATLAS Semiconductor Tracker Assembly Phase". In: *IEEE Trans. Nucl. Sci.* 52.4 (2005), pp. 938–943.

[141] P. Nikiel. *CANopen amp; ELMB software for LHC experiment controls as seen in 2022*. Tech. rep. CERN-OPEN-2022-012. CERN, 2022. URL: https://cds.cern.ch/record/2834805.

[142] ATLAS Collaboration. *Expected tracking and related performance with the updated ATLAS inner tracker layout at the high-luminosity LHC*. Tech. rep. ATL-PHYS-PUB-2021-024. CERN, 2021. URL: https://cds.cern.ch/record/2776651.

[143] ATLAS Collaboration. *Technical Design Report for the ATLAS ITk Strips Detector*. Tech. rep. CERN-LHCC-2017-005. CERN, 2016. URL: https://cds.cern.ch/record/2257755.

[144] ATLAS Collaboration. *ATLAS DCS Requirement Document for HL-LHC*. Tech. rep. ATU-GE-ES-0004. CERN, 2019. URL: https://edms.cern.ch/ui/#!master/navigator/document?D:100514080:100514080:subDocs.

[145] T. C. Gosart et al. "Quality Control Testing of the AMAC ASIC for the HL-LHC ATLAS ITk Strip Detector". In: *JINST* 18 (2023).

[146] M. Dyndał et al. "Development of the radiation and magnetic field tolerant DC/DC converter system for the ATLAS ITk Strip Detector". In: *JINST* 18.01 (2023), p. C01007.

[147] EMCI-EMP team. *Embedded Monitoring Processor*. https://edms.cern.ch/ui/file/2631648/1/EMP_hardware_specifications_v1.4_docx_cpdf.pdf. Accessed: 2025-04-29.

[148] N. Guettouche et al. "The lpGBT production testing system". In: *JINST* 17 (2022), p. C03040.

[149] Xilinx. *Zynq UltraScale+ MPSoC Data Sheet: Overview*. https://docs.amd.com/v/u/en-US/ds891-zynq-ultrascale-plus-overview. Accessed: 2025-04-29.

[150] Trenz Electronic. *Trenz Electronic TE0807 MPSoC Modules with AMD Zynq™ UltraScale+™*. https://shop.trenz-electronic.de/en/Products/Trenz-Electronic/TE08XX-Zynq-UltraScale/TE0807-Zynq-UltraScale/. Accessed: 2025-04-29.

[151] D. Ecker et al. "EMCI-EMP: developments and experience with the novel detector control solution". In: *JINST* 20.01 (2025), p. C01020.

[152] M. Dudek. "Control system for pre-production testing of the ATLAS ITk PP2". In: *Proceedings of the 31st Cracow Epiphany Conference on Physics at the Electron–Ion Collider and Future Facilities (January 2025)*. To appear in Acta Physica Polonica B.

[153] InfluxData. *InfluxData*. https://www.influxdata.com/. Accessed: 2025-04-29.

[154] Grafana Labs. *Grafana*. https://grafana.com/. Accessed: 2025-04-29.

[155] ATLAS Collaboration. *TauAnalysisTools – Tau ID tools within the ATLAS Athena framework*. https://gitlab.cern.ch/atlas/athena/-/tree/21.2/PhysicsAnalysis/TauID/TauAnalysisTools. Accessed: 2025-05-19.

[156] URL: https://rivet.hepforge.org/.

[157] A. Buckley et al. "General-purpose event generators for LHC physics". In: *Phys. Rep.* 504.5 (2011), pp. 145–233.

[158] A. Valassi et al. "Challenges in Monte Carlo Event Generator Software for High-Luminosity LHC". In: *Comput. Softw. Big. Sci.* 5.1 (2021), p. 12.

[159] R. K. Ellis, W. J. Stirling, and B. R. Webber. *QCD and Collider Physics*. Vol. 8. Cambridge Monographs on Particle Physics, Nuclear Physics and Cosmology. Cambridge University Press, 1996, pp. 1–435.

[160] S. Hoche. "Introduction to parton-shower event generators". In: URL: `https://api.semanticscholar.org/CorpusID:119291985`.

[161] M. Botje et al. *The PDF4LHC Working Group Interim Recommendations*. 2011. URL: `https://arxiv.org/abs/1101.0538`.

[162] A. Buckley et al. "LHAPDF6: parton density access in the LHC precision era". In: *Eur. Phys. J. C* 75.3 (2015), p. 132.

[163] E. Bothmann et al. "Event Generation with Sherpa 2.2". In: *SciPost Physics* 7 (2019), p. 034.

[164] T. Gleisberg et al. "SHERPA 1., a proof-of-concept version". In: *JHEP* 2004.02 (2004), pp. 056–056.

[165] J. Alwall et al. "The automated computation of tree-level and next-to-leading order differential cross sections, and their matching to parton shower simulations". In: *JHEP* 2014.7 (2014).

[166] S. Alioli et al. "A general framework for implementing NLO calculations in shower Monte Carlo programs: the POWHEG BOX". In: *JHEP* 1006 (2010), p. 043.

[167] J. Bellm et al. "Herwig 7.0/Herwig++ 3.0 release note". In: *Eur. Phys. J. C* 76.4 (2016), p. 196.

[168] T. Sjöstrand. "The Pythia event generator: Past, present and future". In: *Comput. Phys. Commun.* 246 (2020), p. 106910.

[169] ATLAS Collaboration. "Modelling and computational improvements to the simulation of single vector-boson plus jet processes for the ATLAS experiment". In: *JHEP* 2022.8 (2022), p. 089.

[170] T. Gleisberg and S. Höche. "Comix, a new matrix element generator". In: *JHEP* 12 (2008), p. 039.

[171] Z. Bern et al. "Next-to-Leading Order W + 5-Jet Production at the LHC". In: *Phys. Rev. D* 88 (2013), p. 014025.

[172] T. Sjöstrand, S. Mrenna, and P. Skands. "A Brief Introduction to PYTHIA 8.1". In: *Comput. Phys. Commun.* 178 (2008), pp. 852–867.

[173] URL: `https://its.cern.ch/jira/browse/ATLMCPROD-8930`.

[174] T. Sjöstrand et al. "An introduction to PYTHIA 8.2". In: *Comput. Phys. Commun.* 191 (2015), pp. 159–177.

[175] ATLAS Collaboration. *ATLAS Pythia 8 tunes to 7 TeV data*. Tech. rep. ATL-PHYS-PUB-2014-021. CERN, 2014. URL: `https://cds.cern.ch/record/1966419`.

[176] R. Frederix and S. Frixione. "Merging meets matching in MC@NLO". In: *JHEP* 12 (2012), p. 061.

[177] A. Kaczmarska et al. "Application of TauSpinner for Studies on $\tau$-Lepton Polarization and Spin Correlations in $Z$, $W$ and $H$ Decays at the LHC". In: *Acta Phys. Pol. B* 45.10 (2014), p. 1921.

[178] S. Jadach and Z. Was. "QED $O(\alpha^3)$ Radiative Corrections to the Reaction $e^+e^- \rightarrow \tau^+\tau^-$ Including Spin and Mass Effects". In: *Acta Phys. Pol.* B15 (1984), p. 1151.

[179] The ALEPH Collaboration. "Measurement of the Tau Polarisation at LEP". In: *Eur. Phys. J. C* 20.3 (2001), pp. 401–430.

[180] URL: `https://root.cern/manual/fitting/#using-the-fit-method`.

[181] N. Davidson et al. "Universal interface of TAUOLA: Technical and physics documentation". In: *Comput. Phys. Commun.* 183.3 (2012), pp. 821–843.

[182] M. Tanabashi et al. “Review of Particle Physics”. In: *Phys. Rev. D* 98 (3 2018), p. 030001.

[183] J. Krzysiak. “Searching for Beyond-the-Standard-Model Physics Using Signatures with Tau Leptons in the Final State at the ATLAS Experiment”. Presented on 25 Jan 2022. IFJ PAN, 2021. URL: https://cds.cern.ch/record/2803965.

[184] ATLAS Collaboration. “ATLAS $b$-jet identification performance and efficiency measurement with $t\bar{t}$ events in $pp$ collisions at $\sqrt{s} = 13$ TeV”. In: *Eur. Phys. J. C* 79 (2019), p. 970.

[185] S. Agostinelli et al. “Geant4 – a simulation toolkit”. In: *Nucl. Instrum. Meth. A* 506 (2003), pp. 250–303.

[186] ATLAS Collaboration. *Identification of hadronic tau lepton decays using neural networks in the ATLAS experiment*. Tech. rep. ATL-PHYS-PUB-2019-033. CERN, 2019. URL: https://atlas.web.cern.ch/Atlas/GROUPS/PHYSICS/PUBNOTES/ATL-PHYS-PUB-2019-033/.

[187] ALEPH, DELPHI, L3, OPAL and LEP Collaborations. “Search for charged Higgs bosons: combined results using LEP data”. In: *Eur. Phys. J. C* 73 (2013), p. 2463.

[188] ATLAS Collaboration. “Search for charged Higgs bosons decaying via $H^{\pm} \to \tau\nu$ in $t\bar{t}$ events using $pp$ collision data at $\sqrt{s} = 7\,\mathrm{TeV}$ with the ATLAS detector”. In: *JHEP* 06 (2012), p. 039.

[189] ATLAS Collaboration. “Search for charged Higgs bosons through the violation of lepton universality in $t\bar{t}$ events using $pp$ collision data at $\sqrt{s} = 7\,\mathrm{TeV}$ with the ATLAS experiment”. In: *JHEP* 03 (2013), p. 076.

[190] ATLAS Collaboration. “Search for charged Higgs bosons decaying via $H^{\pm} \to \tau^{\pm}\nu$ in fully hadronic final states using $pp$ collision data at $\sqrt{s} = 8\,\mathrm{TeV}$ with the ATLAS detector”. In: *JHEP* 03 (2015), p. 088.

[191] CMS Collaboration. “Search for a light charged Higgs boson in top quark decays in $pp$ collisions at $\sqrt{s} = 7\,\mathrm{TeV}$”. In: *JHEP* 07 (2012), p. 143.

[192] CMS Collaboration. “Search for a charged Higgs boson in $pp$ collisions at $\sqrt{s} = 8\,\mathrm{TeV}$”. In: *JHEP* 11 (2015), p. 018.

[193] ATLAS Collaboration. “Search for a light charged Higgs boson in the decay channel $H^{+} \to c\bar{s}$ in $t\bar{t}$ events using $pp$ collisions at $\sqrt{s} = 7\,\mathrm{TeV}$ with the ATLAS detector”. In: *Eur. Phys. J. C* 73 (2013), p. 2465.

[194] CMS Collaboration. “Search for a light charged Higgs boson decaying to $c\bar{s}$ in $pp$ collisions at $\sqrt{s} = 8\,\mathrm{TeV}$”. In: *JHEP* 12 (2015), p. 178.

[195] ATLAS Collaboration. “Search for charged Higgs bosons in the $H^{+} \to tb$ decay channel in $pp$ collisions at $\sqrt{s} = 8$ TeV using the ATLAS detector”. In: *JHEP* 03 (2016), p. 127.

[196] ATLAS Collaboration. “Search for a charged Higgs boson produced in the vector-boson fusion mode with decay $H^{\pm} \to W^{\pm}Z$ using $pp$ collisions at $\sqrt{s} = 8$ TeV with the ATLAS experiment”. In: *Phys. Rev. Lett.* 114 (2015), p. 231801.

[197] CMS Collaboration. “Search for charged Higgs bosons in the $H^{+} \to \tau^{+}\nu_{\tau}$ decay channel in proton–proton collisions at $\sqrt{s} = 13$ TeV”. In: *JHEP* 07 (2019), p. 142.

[198] ATLAS Collaboration. “Search for charged Higgs bosons decaying into a top quark and a bottom quark at $\sqrt{s} = 13$ TeV with the ATLAS detector”. In: *JHEP* 06 (2021), p. 145.

[199] CMS Collaboration. “Search for charged Higgs bosons decaying into a top and a bottom quark in the all-jet final state of $pp$ collisions at $\sqrt{s} = 13$ TeV”. In: *JHEP* 07 (2020), p. 126.

[200] ATLAS Collaboration. “Search for resonant $WZ$ production in the fully leptonic final state in proton–proton collisions at $\sqrt{s} = 13$ TeV with the ATLAS detector”. In: *Phys. Lett. B* 787 (2018), pp. 68–86.

[201] CMS Collaboration. “Search for charged Higgs bosons produced in vector boson fusion processes and decaying into vector boson pairs in proton–proton collisions at $\sqrt{s} = 13$ TeV”. In: *Eur. Phys. J. C* 81 (2021), p. 723.

[202] CMS Collaboration. “Search for a charged Higgs boson decaying into a heavy neutral Higgs boson and a W boson in proton-proton collisions at $\sqrt{s} = 13$ TeV”. In: *JHEP* 09 (2023), p. 032.

[203] ATLAS Collaboration. “Search for a heavy charged Higgs boson decaying into a W boson and a Higgs boson in final states with leptons and b-jets in $\sqrt{s} = 13$ TeV $pp$ collisions with the ATLAS detector”. In: *JHEP* 02 (2025), p. 143.

[204] ATLAS Collaboration. “Search for a light charged Higgs boson in $t \to H^+b$ decays, with $H^+ \to cb$, in the lepton+jets final state in proton–proton collisions at $\sqrt{s} = 13$ TeV with the ATLAS detector”. In: *JHEP* 09 (2023), p. 004.

[205] CMS Collaboration. “Search for a light charged Higgs boson in the $H^+ \to cs$ channel in proton–proton collisions at $\sqrt{s} = 13$ TeV”. In: *Phys. Rev. D* 102 (2020), p. 072001.

[206] ATLAS Collaboration. “Search for a light charged Higgs boson in $t \to H^+b$ decays, with $H^+ \to cs$, in $pp$ collisions at $\sqrt{s} = 13$ TeV with the ATLAS detector”. In: *Eur. Phys. J. C* 85 (2025), p. 153.

[207] ATLAS Collaboration. “Search for additional heavy neutral Higgs and gauge bosons in the ditau final state produced in 36 fb$^{-1}$ of $pp$ collisions at $\sqrt{s} = 13$ TeV with the ATLAS detector”. In: *JHEP* 01 (2018), p. 055.

[208] CMS Collaboration. “Search for additional neutral MSSM Higgs bosons in the $\tau\tau$ final state in proton–proton collisions at $\sqrt{s} = 13$ TeV”. In: *JHEP* 09 (2018), p. 007.

[209] Heavy Flavor Averaging Group (HFLAV). *HFLAV semileptonic HF results: $R(D)$ and $R(D^*)$ ratios.* `https://hflav-eos.web.cern.ch/hflav-eos/semi/moriond24/html/RDsDsstar/RDRDs.html`. Accessed: 2024-05-27.

[210] J. Hernandez-Sanchez et al. “Off-diagonal terms in Yukawa textures of the type-III 2-Higgs doublet model and light charged Higgs boson phenomenology”. In: *JHEP* 07 (2013), p. 044.

[211] S. Iguro and K. Tobe. “$R(D^{(*)})$ in a general two Higgs doublet model”. In: *Nucl. Phys. B* 925 (2017), pp. 560–574.

[212] W. Altmannshofer, P. S. Bhupal Dev, and A. Soni. “$R(D^{(*)})$ anomaly: A possible hint for natural supersymmetry with R-parity violation”. In: *Phys. Rev. D* 96 (2017), p. 095010.

[213] ATLAS Collaboration. “Luminosity determination in $pp$ collisions at $\sqrt{s} = 13$ TeV using the ATLAS detector at the LHC”. In: *Eur. Phys. J. C* 83 (2023), p. 982.

[214] ATLAS Collaboration. “The ATLAS Simulation Infrastructure”. In: *Eur. Phys. J. C* 70 (2010), pp. 823–874.

[215] S. Frixione, P. Nason, and G. Ridolfi. “A Positive-Weight Next-to-Leading-Order Monte Carlo for Heavy Flavour Hadroproduction”. In: *JHEP* 09 (2007), p. 126.

[216] C. Oleari S. Alioli P. Nason and E. Re. "A general framework for implementing NLO calculations in shower Monte Carlo programs: the POWHEG BOX". In: *JHEP* 06 (2010), p. 043.

[217] R. D. Ball et al. "Parton distributions for the LHC Run II". In: *JHEP* 04 (2015), p. 040.

[218] P. Artoisenet et al. "Automatic spin-entangled decays of heavy resonances in Monte Carlo simulations". In: *JHEP* 03 (2013), p. 015.

[219] ATLAS Collaboration. *A study of optimal parameter setting for aMC@NLO + Pythia8 matched setup*. Tech. rep. CERN, 2015. URL: https://cds.cern.ch/record/2103221.

[220] D. J. Lange. "The EvtGen particle decay simulation package". In: *Nucl. Instrum. Meth. A* 462 (2001), pp. 152–155.

[221] M. Czakon and A. Mitov. "Top++: A Program for the Calculation of the Top-Pair Cross-Section at Hadron Colliders". In: *Comput. Phys. Commun.* 185 (2014), pp. 2930–2938.

[222] N. Kidonakis. "Next-to-next-to-leading-order collinear and soft gluon corrections for t-channel single top quark production". In: *Phys. Rev. D* 83 (2011), p. 091503.

[223] N. Kidonakis. "NNLL resummation for s-channel single top quark production". In: *Phys. Rev. D* 81 (2010), p. 054028.

[224] N. Kidonakis. "Two-loop soft anomalous dimensions for single top quark associated production with a $W^-$ or $H^-$". In: *Phys. Rev. D* 82 (2010), p. 054018.

[225] T. Gleisberg et al. "Event generation with SHERPA 1.1". In: *JHEP* 02 (2009), p. 007.

[226] C. Anastasiou et al. "High precision QCD at hadron colliders: Electroweak gauge boson rapidity distributions at NNLO". In: *Phys. Rev. D* 69 (2004), p. 094008.

[227] K. Melnikov and F. Petriello. "Electroweak gauge boson production at hadron colliders through $\mathrm{O}(\alpha_s^2)$". In: *Phys. Rev. D* 74 (2006), p. 114017.

[228] F. Petriello R. Gavin Y. Li and S. Quackenbush. "FEWZ 2.0: A code for hadronic Z production at next-to-next-to-leading order". In: *Comput. Phys. Commun.* 182 (2011), pp. 2388–2403.

[229] ATLAS Collaboration. "Measurement of the Z boson transverse momentum distribution in *pp* collisions at 7 TeV with the ATLAS detector". In: *JHEP* 2014 (2014), p. 055.

[230] M. Wiesemann C. Degrande M. Ubiali and M. Zaro. "Heavy charged Higgs boson production at the LHC". In: *JHEP* 10 (2015), p. 145.

[231] ATLAS Collaboration. "Performance of the missing transverse momentum triggers for the ATLAS detector during Run-2 data taking". In: *JHEP* 08 (2020), p. 080.

[232] ATLAS Collaboration. "Performance of electron and photon triggers in ATLAS during LHC Run 2". In: *Eur. Phys. J. C* 80 (2020), p. 47.

[233] ATLAS Collaboration. "Performance of the ATLAS muon triggers in Run 2". In: *JINST* 15 (2020), P09015.

[234] ATLAS Collaboration. "The ATLAS inner detector trigger performance in pp collisions at 13 TeV during LHC Run 2". In: *Eur. Phys. J. C* 82 (2022), p. 206.

[235] P. Baldi et al. "Parameterized neural networks for high-energy physics". In: *Eur. Phys. J. C* 76 (2016), p. 235.

[236] F. Chollet. *Keras*. `https://github.com/fchollet/keras`. Accessed: 2024-05-27. 2015.

[237] M. Abadi et al. *TensorFlow: Large-Scale Machine Learning on Heterogeneous Systems*. `https://www.tensorflow.org`. Accessed: 2024-04-26. 2015.

[238] R. Andrae, T. Schulze-Hartung, and P. Melchior. *Dos and Don'ts of Reduced Chi-Squared*. 2010. arXiv: `1012.3754 [astro-ph.IM]`.

[239] L. Devroye. *Non-Uniform Random Variate Generation*. Springer, 1986.

[240] ATLAS Collaboration. "Search for charged Higgs bosons decaying into a top quark and a bottom quark at $\sqrt{s} = 13$ TeV with the ATLAS detector". In: *JHEP* 06 (2021), p. 145.

[241] ATLAS Collaboration. "The performance of missing transverse momentum reconstruction and its significance with the ATLAS detector using 140 fb$^{-1}$ of $\sqrt{s} = 13$ TeV $pp$ collisions". In: *Eur. Phys. J. C* 85.6 (2025), p. 606.

[242] ATLAS Collaboration. "Luminosity determination in $pp$ collisions at $\sqrt{s} = 13$ TeV using the ATLAS detector at the LHC". In: *Eur. Phys. J. C* 83 (2023), p. 982.

[243] G. Avoni et al. "The new LUCID-2 detector for luminosity measurement and monitoring in ATLAS". In: *JINST* 13 (2018), P07017.

[244] G. Cowan et al. "Asymptotic formulae for likelihood-based tests of new physics". In: *Eur. Phys. J. C* 71 (2011), p. 1554.

[245] G. Cowan et al. "Erratum to: Asymptotic formulae for likelihood-based tests of new physics". In: *Eur. Phys. J. C* 73 (2013), p. 2501.

[246] A. L. Read. "Presentation of search results: The CLS technique". In: *J. Phys. G* 28 (2002), pp. 2693–2704.

[247] G. Cowan et al. "Asymptotic formulae for likelihood-based tests of new physics". In: *Eur. Phys. J. C* 71 (2011). Erratum: Eur. Phys. J. C 73 (2013) 2501, p. 1554.

[248] J. R. Andersen et al. *Handbook of LHC Higgs Cross Sections: 3. Higgs Properties*. Ed. by S. Heinemeyer et al. 2013.

[249] C. Degrande et al. "Heavy charged Higgs boson production at the LHC". In: *JHEP* 10 (2015), p. 145.

[250] M. Flechl et al. "Improved cross-section predictions for heavy charged Higgs boson production at the LHC". In: *Phys. Rev. D* 91 (2015), p. 075015.

[251] S. Dittmaier et al. "Charged-Higgs-boson production at the LHC: Next-to-leading-order supersymmetric QCD correction". In: *Phys. Rev. D* 83 (2011), p. 055005.

[252] E. L. Berger et al. "Associated production of a top quark and a charged Higgs boson". In: *Phys. Rev. D* 71 (2005), p. 115012.

[253] A. Djouadi, J. Kalinowski, and M. Spira. "HDECAY: a program for Higgs boson decays in the Standard Model and its supersymmetric extension". In: *Comput. Phys. Commun.* 108 (1998), pp. 56–74.